GEOMAR REPORT

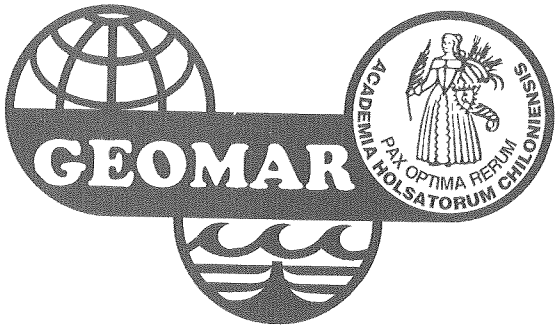

INGO A. PECHER

SEISMIC STUDIES OF BOTTOM SIMULATING REFLECTORS AT THE CONVERGENT MARGINS OFFSHORE PERU AND COSTA RICA

Nature and Formation: Results from full Waveform Inversion
Heat Flux from the Depth of Bottom Simulating Reflectors

47

GEOMAR REPORT

INGO A. PECHER

SEISMIC STUDIES OF BOTTOM SIMULATING REFLECTORS AT THE CONVERGENT MARGINS OFFSHORE PERU AND COSTA RICA

Nature and Formation: Results from full Waveform Inversion
Heat Flux from the Depth of Bottom Simulating Reflectors

GEOMAR
Forschungszentrum
für marine Geowissenschaften
der Christian-Albrechts-Universität
zu Kiel

Kiel 1996

GEOMAR REPORT 47

GEOMAR
Research Center
for Marine Geosciences
Christian Albrechts University
in Kiel

Dissertation
zur Erlangung des Doktorgrades
der mathematisch-naturwissenschaftlichen Fakultät
der Christian-Albrechts-Universität zu Kiel
Zum Druck genehmigt am 15.11.1995

Redaktion der Serie:	Gerhard Haass	Managing Editor:	Gerhard Haass
Umschlag:	Kerstin Kreis, Harald Gross, GEOMAR Technologie GmbH	Cover:	Kerstin Kreis, Harald Gross, GEOMAR Technologie GmbH

GEOMAR REPORT
ISSN 0936 - 5788

GEOMAR REPORT
ISSN 0936 - 5788

GEOMAR
Forschungszentrum
für marine Geowissenschaften
D-24148 Kiel
Wischhofstr. 1-3
Telefon (0431) 600-2555, 600-2505

GEOMAR
Research Center
for Marine Geosciences
D-24148 Kiel / Germany
Wischhofstr. 1-3
Telephone (49) 431 / 600-2555, 600-2505

Contents

1 Zusammenfassung, Abstract 4

2 Introduction 9

3 Previous studies of bottom simulating reflectors 14
3.1 Nature and formation of BSRs 14
3.2 Heat flux from the depth of BSRs 15

4 Methods 16
4.1 Full waveform inversion of reflection seismic data 16
4.1.1 Theory of the full waveform inversion technique 16
4.1.2 Flow pattern of the inversion strategy 17
4.1.3 Data pre-processing 17
4.1.4 Reflectivity of the seafloor and source wavelet 19
4.1.5 Starting model 19
4.1.6 Full waveform inversion 20
4.2 Modeling P-wave velocity as a function of water saturation 21
4.3 Determination of heat flux from the depth of the BSR 22

5 Geology of the central Peruvian margin 23
5.1 Bore hole stratigraphy 23
5.2 Seismic studies 27
5.2.1 Reflection data from 12° S 27
5.2.2 Reflection data from 9° S 31
5.3 Development of the accretionary prism 31
5.4 Organic carbon, hydrocarbon gases and gas hydrates 36
5.5 BSR analysis 37
5.6 Heat flux 37

6 Geology of the convergent margin off Costa Rica 38
6.1 Tectonic setting and bathymetry 38
6.2 Seismic studies 39
6.2.1 Reflection seismic lines 8, 9, and 5 39
6.2.2 Nature of the rough surface 39
6.3 DSDP Site 565: Sediment composition, hydrocarbon gases and gas hydrates 44
6.4 Heat flux 44

7 Nature of BSRs off Peru and Costa Rica 46
7.1 Full waveform inversion scheme applied to Peru line 1018 CMP 1126 46
7.1.1 Data pre-processing 46
7.1.2 Reflectivity of the seafloor and source wavelet 48
7.1.3 Starting model 50
7.1.4 Full waveform inversion 50

7.1.5 Modeling P-wave velocity as a function of water saturation 54
7.2 Nature of the BSR at Peru line 1018 CMP 1514 54
7.3 Nature of the BSR at Peru line 1018 CMP 1594 59
7.4 Nature of the BSR at Peru line 1017 CMP 3790 63
7.5 Distribution of BSRs at the central Peruvian margin 67
7.5.1 Reflection data from 12° S 67
7.5.2 Reflection data from 9° S 70
7.6 Nature of the BSR off the Nicoya Peninsula, Costa Rica line 9 CMP 1410 72
7.7 Distribution of BSRs at the Costa Rican convergent margin 78

8 Heat flux from the depth of the BSR **84**
8.1 Heat flux at the central Peruvian margin 84
8.1.1 Velocity, density, and thermal conductivity 84
8.1.2 Estimate of heat flux at Nazca Plate 84
8.1.3 Heat flux from BSRs at 12° S 88
8.1.4 Heat flux from BSRs at 9° S 93
8.2 Heat flux at the Costa Rican margin 96
8.2.1 Velocity, density, and thermal conductivity 96
8.2.2 Heat flux 96

9 Discussion, conclusions and outlook **101**
9.1 Inversion scheme 101
9.2 Geophysical nature of the BSR 105
9.3 Possible sources of free gas at BSRs and hydrates off Peru and Costa Rica 108
9.3.1 Peruvian margin 108
9.3.2 Costa Rica margin 110
9.3.3 Implications on hydrate formation and distribution 111
9.4 Temperature and heat flux 112
9.4.1 Reliability of the method 112
9.4.2 Peruvian margin 112
9.4.3 Margin off Costa Rica 113
9.5 Outlook 116

10 Acknowledgments **119**

A Gas hydrates in sediments **127**
A.1 Chemistry of gas hydrates 127
A.2 Chemical markers of hydrates in sediments 128
A.3 Physical properties of hydrates and hydrated sediments 129
A.4 Implications on sedimentological properties 130
A.5 Formation mechanisms for methane, hydrates, and BSRs 130
A.5.1 Formation of methane 130
A.5.2 Models for the formation of hydrates in sediments 130
A.5.3 Possible formation mechanisms for BSRs 132

A.6 Identification and quantification of oceanic hydrates in sediments 132
A.6.1 Seismic methods 133
A.6.2 Drilling oceanic hydrates: Evidence from cores and logging 133
A.7 Significance of natural gas hydrates 134
A.7.1 Potential energy reservoir 134
A.7.2 Geologic hazard and slope stability 134
A.7.3 Hydrates and environment 135

B Amplitude corrections **137**
B.1 Determination of the energy from the seafloor 137
B.2 Computation of theoretical energies 137
B.2.1 Directivities 137
B.2.2 Reflectivity versus angle-of-incidence 138

C Starting model **138**
C.1 Gradient velocity model 138
C.2 Density and shear wave velocity 139

D Elastic waves in porous media **139**
D.1 Homogeneous media 139
D.2 Porous media 140
D.3 Physical properties of methane gas 141
D.3.1 Deviation from ideal gas and density 141
D.3.2 Bulk modulus 141
D.4 Modeling P-wave velocity versus water saturation 142
D.5 Limitations 143

E Pre-stack depth migration **144**

F Phase boundary of methane hydrate **149**

G Miscellaneous parameters and equations **149**

H Abbreviations and symbols **151**

1 Zusammenfassung, Abstract

Zusammenfassung

Ein großer Teil des Wissens über die weltweite Verteilung von ozeanischen Gashydraten stammt aus der Beobachtung von "Bottom Simulating Reflectors (BSRs)". In dieser Arbeit werden die Natur und Bildung von BSRs an konvergenten Kontinentalrändern durch die Anwendung von seismischen Inversionstechniken auf BSRs in reflexionsseismischen Daten von den Küsten Perus und Costa Ricas untersucht. Diese Ergebnisse werden im Zusammenhang mit lokalen tektonischen Prozessen ausgewertet.

Um der Frage nachzugehen, ob *freies Gas* in der Tiefe von BSRs vorhanden ist, wurde die Feinstruktur der Kompressionswellengeschwindigkeit durch Anwendung von seismischen Inversionsmethoden untersucht. Die langwelligen Merkmale der seismischen Geschwindigkeitsvariationen wurden in mehreren Schritten bestimmt. Durchschnittsgeschwindigkeiten wurden mittels einer "Global-Grid"-Suche entlang elliptischer Trajektorien in der Interzeptzeit-Langsamkeit-Domäne gefunden. Diese Durchschnittsgeschwindigkeiten wurden in Intervallgeschwindigkeiten umgewandelt. Die Genauigkeit der Intervallgeschwindigkeiten wurde mit einer globalen Monte-Carlo-Suche auf maximale Energie verbessert. Anschließend erfolgte eine lokale Suche mittels der Simplex-Methode. Diese Geschwindigkeiten wurden verwendet, um ein Startmodell für eine Wellenforminversion in der Frequenz-Langsamkeit-Domäne zu konstruieren, welche ein detailliertes Geschwindigkeits/Tiefen-Modell in der Umgebung des BSRs ergab.

Die Geschwindigkeitsfeinstruktur wurde an vier Lokationen vor *Peru* bei 12° S untersucht. An drei dieser Lokationen wird der BSR durch eine deutliche $6-18m$ mächtige Schicht niedriger Geschwindigkeit verursacht. Der scharfe Abfall der Geschwindigkeit wird als klares Anzeichen für das Vorhandensein von wenigen Prozent freien Gases im Porenraum interpretiert. Keine deutliche Schicht niedriger Geschwindigkeit wird an der vierten Lokation beobachtet, die nahe an der landwärtigen Begrenzung des BSRs liegt. Daher wird dort wesentlich weniger, wenn überhaupt, freies Gas erwartet. Die Qualität von seismischen Daten aus einem Gebiet weiter nördlich bei 9° S erlaubte keine Inversion. Basierend auf den Resultaten aus dem südlichen Gebiet, kann jedoch auf das Vorhandensein von freiem Gas an BSRs, die in diesen Daten erkennbar sind, geschlossen werden.

Vor Peru wurde der Nazca-Rücken nicht-senkrecht subduziert. Er bewegte sich lateral von Norden nach Süden entlang des Kontinentalrandes. Die Subduktion führte zu tektonischer Erosion des alten Akkretionskeils. Danach begann die Bildung eines neuen Keils, was bei 12° S zu schneller Hebung am äußeren Kontinentalrand führt. Weiter im Norden ist das Wachstum des Akkretionskeils fast abgeschlossen. Es wird daraus geschlossen, daß nur wenig Hebung stattfindet. Die meisten Grabensedimente werden subduziert. Das Yaquina-Becken weiter hangaufwärts ist weitgehend stabil oder wird sogar leicht gehoben im Gegensatz zum Lima-Becken, das noch absinkt. Bei Bohrungen im Rahmen von ODP Leg 112 wurden Hydrate geborgen. Aufgrund ihrer Zusammensetzung und von Informationen über Isotopenverhältnisse wird angenommen, daß die Hydrate biogenen Ursprungs sind. Der hohe Anteil an organischem Kohlenstoff am äußeren Kontinentalrand ermöglicht eine in-situ Bildung von Hydraten innerhalb der Stabilitätszone.

Starke und kontinuierliche BSRs werden über den gesamten unteren Hang im südlichen Gebiet beobachtet, wohingegen BSRs im Akkretionskeil fehlen. Dieses Muster ändert sich nach Norden, wo BSRs im Akkretionskeil beobachtet werden. Im Lima-Becken wurden entlang der für die vorliegende Studie untersuchten seismischen Profile keine BSRs identifiziert, obwohl berichtet wurde, daß BSRs im Lima-Becken weiter nördlich auftreten. Im Gegensatz dazu wurde ein starker BSR im Yaquina-Becken identifiziert.

Basierend auf der Verteilung von BSRs am äußeren Kontinentalrand, wird angenommen, daß beide Mechanismen, die im allgemeinen für eine Bildung von freiem Gas an BSRs vorgeschlagen werden, nämlich Methanrecycling durch Zerfall von Hydraten an der Basis der Hydratstabilitätszone und Aufwärtsmigration von Methan, am peruanischen Kontinentalrand auftreten können. Im südlichen Gebiet, wo das Vorhandensein von BSRs mit Regionen tektonischer Hebung verbunden zu sein scheint, dürf-

te Methanrecycling über Gasansammlung durch aufwärts migrierende Fluide dominieren. Dieses Muster verändert sich, wenn man sich weiter nach Norden begibt. Hier ist das Vorhandensein von BSRs am Fuß des Akkretionskeils ein Anzeichen für eine starke Verbindung zwischen Fluidmigration und BSR-Bildung. Freies Gas an der Basis der Hydratstabilitätszone im Yaquina-Becken kann durch Zerfall von Hydraten in Sedimenten, die aufgrund von Kompaktion absinken, entstanden sein. Ein besseres Verständnis der BSR-Bildung am oberen Hang erfordert jedoch weitere Untersuchungen.

Vor der Küste *Costa Ricas* wird zur Zeit eine Gruppe von Seamounts zwischen dem Fisher-Seamount und dem Quepos-Plateau subduziert. Nordwestlich dieser Region ist der Meeresboden relativ eben. Dort werden BSRs über fast den gesamten Hang beobachtet bis zu der Linie, an der die Hydratstabilitätszone den Meeresboden schneidet. In dem Seamount-Gebiet sind in den meisten Regionen, die durch Hangrutschungen beeinflußt worden sind, keine BSRs vorhanden. BSRs sind südöstlich vom Quepos-Plateau weitverbreitet. Seismische Inversion im Gebiet nordwestlich des Fisher-Seamounts deutet wiederum auf das Vorhandensein einer geringen Menge freien Gases in einer dünnen Schicht an der Basis der Stabilitätszone hin. Die tektonische Situation ist noch nicht eindeutig bekannt. Einige Interpretationen bevorzugen das Vorhandensein von ophiolitischem Gestein unter neogenen Sedimenten am oberen Hang in diesem Gebiet. Eine andere Möglichkeit wäre ein alter Akkretionskeil aus dem Eozän.

Das Fehlen von BSRs in durch Hangrutschungen beeinflußten Gebieten kann durch das Entweichen von freiem Gas während der Rutschung erklärt werden. Das Auftreten von flachen BSRs liefert einen Hinweis auf eine Beteiligung der Migration von Fluiden an der Bildung von BSRs und folglich Hydraten, da hohe in-situ Produktionsraten von Methan notwendig wären, um Hydrate oberhalb einer flachen Basis der Hydratstabilitätszone zu bilden. Eine bessere Kenntnis der detaillierten Hebungs- und Senkungsgeschichte und der Natur der Gesteine unterhalb der BSRs ist notwendig, um mögliche Bildungsmechanismen von BSRs und Hydraten in diesem Gebiet herauszufinden.

Die *Wärmeflußdichte* am Meeresboden wurde aus der Tiefe von BSRs berechnet. Vor *Peru* wurden die Intervallgeschwindigkeiten als Funktion der Zweiweglaufzeit zwischen Meeresboden und BSR durch Fokussierungsanalysen während einer Tiefenmigration vor dem Stapeln von zwei Linien aus dem südlichen Gebiet erhalten. Diese Geschwindigkeiten wurden verwendet, um die Zweiweglaufzeit zum BSR in Tiefe zu konvertieren. Die Daten aus dem nördlichen Gebiet erlaubten keine Fokussierungsanalysen, hauptsächlich wegen einer kürzeren Streamerlänge. Deshalb wurde die Geschwindigkeitsfunktion aus dem südlichen Gebiet verwendet, um die Tiefe von BSRs aus Anrissen in Zeitsektionen zu berechnen. Der Porendruck am BSR wurde als hydrostatisch angenommen und wurde, basierend auf dem Phasendiagramm für Hydrate in einem reinen Wasser/Methan-System, in Temperatur konvertiert. Der thermische Gradient wurde mittels der Tiefe des BSRs und der Temperatur am Meeresboden berechnet und in Wärmeflußdichte umgerechnet. Hierbei wurde ein Durchschnittswert von Meßergebnissen, die im Rahmen von ODP Leg 112 gewonnen worden waren, als Wärmeleitfähigkeit verwendet.

Das generelle Wärmeflußdichtemuster am äußeren peruanischen Kontinentalhang wird durch eine Abnahme der Wärmeflußdichte von $\sim 40-60 mW/m^2$ auf $\sim 20-30 mW/m^2$ entlang des unteren Hangs zum Akkretionskeil hin dominiert. Innerhalb des Akkretionskeils scheint die Wärmeflußdichte wieder in Richtung der Grabenachse zuzunehmen bis auf Werte um $\sim 30-40 mW/m^2$. Sowohl Reibungswärme an der subduzierten Platte als auch radiogene Wärme aus dem metamorphen Körper, der unter dem unteren Hang liegt, könnten solch ein Muster hervorbringen. Fluidaustritt kann zusätzlich die Wärmeflußdichte im Akkretionskeil beeinflussen. Ohne weitere Studien können die Wärmequellen allerdings nicht genauer eingegrenzt werden.

Erste Untersuchungen wurden an BSRs vor der Küste *Costa Ricas* in drei seismischen Linien durchgeführt, von denen zwei nordwestlich vom Fisher Seamount liegen, die andere südöstlich vom Quepos Plateau. Geschwindigkeitsinformationen waren nur von einer dieser Linien vorhanden. Die Durchschnittsgeschwindigkeit entlang dieser Linie wurde auch verwendet, um Anrisse des BSRs in Zeitsektionen der anderen Linien in Tiefen zu konvertieren. Diese vorläufigen Ergebnisse deuten darauf hin, daß

die Wärmeflußdichte generell im südöstlichen Gebiet höher zu sein scheint. Es gibt eine Zunahme der Wärmeflußdichte mit abnehmender Distanz zur Grabenachse bis auf Werte $> 150 mW/m^2$. Etwa $5 km$ entfernt von der Grabenachse entlang der südöstlichen Linie kann ein Maximum der Wärmeflußdichte als Anzeichen für Fluidaustritt interpretiert werden. Wiederum ist eine bessere Kenntnis der Geologie des costaricanischen konvergenten Kontinentalrandes notwendig, um das Wärmeflußmuster in dieser Region besser zu verstehen. Ergebnisse von konventionellen Messungen, die entlang eines Teils der westlichsten Linie durchgeführt wurden, stimmen gut mit der BSR-Wärmeflußdichte überein, was auf die Verläßlichkeit der indirekten Methode zur Berechnung der Wärmeflußdichte aus der Tiefe des BSRs in diesem Untersuchungsgebiet hinweist.

Abstract

Much of our knowledge of the world wide distribution of oceanic gas hydrates comes from seismic observations of Bottom Simulating Reflectors (BSRs). In this thesis, the nature and formation of BSRs at convergent continental margins is investigated by applying seismic inversion techniques to BSRs in reflection seismic data from offshore Peru and Costa Rica. These results are evaluated in the context of local tectonic processes.

To address the question of whether *free gas* is present at BSRs, their compressional (P-) wave velocity fine structure was determined by applying a combination of seismic inversion techniques. The long-wavelength features of seismic velocity variations were determined in several steps. Root-mean-square (RMS) velocities between major reflectors were obtained from a global grid search for maximum energy along elliptical trajectories in the intercept time-slowness domain. RMS velocities were transformed into interval velocities. Accuracy of interval velocities was enhanced using a global Monte Carlo search for maximum energy followed by a local search using the simplex method. These velocities were used to form a starting velocity model for a full waveform inversion in the frequency-slowness domain, which yielded a detailed velocity/depth model in the vicinity of the BSR.

The fine velocity structure of BSRs at four locations offshore *Peru* at 12° S was investigated using this inversion scheme. At three of these locations, the BSR is caused by a distinct $6 - 18m$ thick low velocity layer (LVL). The sharp drop of velocity is interpreted as clear evidence for the presence of a few percent of free gas in the pore space. No clear LVL is observed at the fourth location, which is close to the landward termination of the BSR. Thus, considerably less gas, if any, is predicted there. Quality of seismic data from an area further north at 9° S did not allow inversion. However, the presence of free gas at BSRs observed in these data may be inferred from the results from the southern area.

Offshore Peru, Nazca Ridge was subducted obliquely, sweeping the margin from north to south. Subduction led to tectonic erosion of the old accretionary wedge. Formation of a new wedge leads to rapid uplift at the outer margin at 12° S. Further north, development of the accretionary prism has almost been completed and only slight uplift is inferred to take place. Most of the trench sediment is subducted. Yaquina Basin further upslope is essentially stable or even slightly uplifted in contrast to Lima Basin in the south, which still is subsiding. Hydrates have been recovered during drilling of ODP Leg 112. From their composition and from isotopic information, they are believed to be of biogenic origin. The high organic carbon content at the outer margin allows in situ formation of hydrates within the hydrate stability zone.

Strong and continuous BSRs are observed all over the lower slope in the southern area, whereas BSRs are absent in the accretionary prism. This pattern changes towards the north where BSRs are observed in the accretionary wedge. No BSRs were identified in Lima Basin along the seismic lines, which were investigated for the present study, although BSRs have been reported to occur in Lima Basin further north. In contrast, a strong BSR could be identified in Yaquina Basin.

Based on the knowledge of BSR distribution at the outer margin, it is suggested that both mechanisms commonly proposed for free gas at BSRs, i.e. methane recycling due to a dissociation of hydrates at the base of the hydrate stability zone and upward migration of methane, may occur at the Peruvian margin. In the southern area, where the presence of BSRs appears to be linked to regions of uplift, methane recycling mainly due to decompression caused by uplift, may dominate over gas accumulation from rising fluids. This pattern changes as one moves further to the north. Here, the presence of BSRs at the toe of the accretionary wedge gives evidence for a strong link between upward fluid migration and BSR formation. Free gas at the base of the hydrate stability zone in Yaquina Basin may have been produced by dissociation of hydrates in sediments subsiding due to compaction. However, a better understanding of BSR formation at the upper slope requires further investigation.

Offshore *Costa Rica*, a series of seamounts is currently being subducted between Fisher Seamount

and Quepos Plateau. Northwest of this region, the ocean floor is relatively smooth. There, BSRs are observed over most of the slope up to where the hydrate stability zone intersects the seafloor. In the seamount area, BSRs are not present in most areas which have been affected by slumps. BSRs are wide-spread southeast of Quepos Plateau. Seismic inversion at a location in the area northwest of Fisher Seamount again indicates the presence of a small amount of free gas in a thin layer beneath the hydrate stability zone. The tectonic setting is still unresolved. Some interpretations favor the presence of an ophiolitic rock beneath Neogene sediments in the upper slope of this area. Another possibility would be an old Eocene accretionary wedge.

The lack of BSRs in areas affected by slumping may be explained by an escape of free gas during slumping. The occurrence of shallow BSRs provides evidence for an involvement of fluid migration in BSR and subsequently hydrate formation, since high in-situ production rates of methane would be required to form hydrates above a shallow base of the hydrate stability zone. A better knowledge of the detailed tectonic uplift/subsidence history and the nature of the rocks underlying BSRs is required to discriminate between possible formation mechanisms of BSRs and hydrates in this area.

Heat flux was computed from the depth of BSRs. Offshore *Peru*, interval velocities as a function of two-way-traveltime (TWT) between seafloor and BSR were obtained from focusing analyses during pre-stack depth migration of two lines from the southern area. These velocities were used to convert TWT to the BSR to depth. Data from the northern area did not allow accurate focusing analyses mainly due to a smaller maximum offset. Therefore, the velocity function from the southern area was used to compute the depth of BSRs from time picks. Pore pressure at the BSR was assumed to be hydrostatic and was converted to temperature based on the phase diagram for hydrates in a pure water/methane system. The thermal gradient was computed from the depth of the BSR together with temperature at the seafloor and converted to heat flux using an average thermal conductivity obtained from measurements during ODP Leg 112. Some tests were also performed to estimate the effect of assuming lithostatic instead of hydrostatic pressure as the other end-member of pore pressure.

The general heat flux pattern at the outer Peruvian margin is dominated by a decrease of heat flux from $\sim 40-60 mW/m^2$ to $\sim 20-30 mW/m^2$ along the lower slope as one approaches the accretionary wedge. Within the accretionary wedge, heat flux appears to increase again slightly towards the trench axis reaching values of $\sim 30-40 mW/m^2$. Both frictional heat at the subducting plate and radiogenic heat from the metamorphic body underlying the lower slope might produce this pattern. Fluid expulsion may also affect heat flux in the accretionary prism. Heat sources cannot be distinguished without further studies.

First investigations were performed along BSRs in three lines offshore *Costa Rica*, two of which are located northwest of Fisher Seamount, the other southeast of Quepos Plateau. Velocity information was available only for one of these lines. An average velocity obtained from this line was also used to convert time picks at the BSR to depth in the other lines. The preliminary results indicate that heat flux in general appears to be higher in the southeastern area. There is an increase of heat flux with decreasing distance from the trench axis reaching values of $> 150 mW/m^2$. A maximum of heat flux about $5 km$ away from the trench axis in the southeastern line may be interpreted as evidence for fluid expulsion. Again, an enhanced knowledge of the geology of the Costa Rican convergent margin is needed to better understand the heat flux pattern in this region. Results from conventional measurements conducted along a segment of the westernmost line compare well with BSR heat flux indicating the reliability of the indirect method of computing heat flux from the depth of BSRs in this study area.

2 Introduction

Natural gas hydrates are ice-like crystalline structures of water molecules surrounding molecules of hydrate forming gases. In sediments, the gas is usually methane (ref. section A.1). It is obvious from the phase diagram of methane hydrates (fig. 1) that in the Earth they are stable in two regions, permafrost regions at low temperatures (continental hydrates) and deep sea sediments at higher temperatures and pressures (oceanic hydrates). In those regions, solid-phase hydrates may replace part of the pore water or they may be present as macroscopic nodules, layers, or as massive bodies (ref. also section A.5.2).

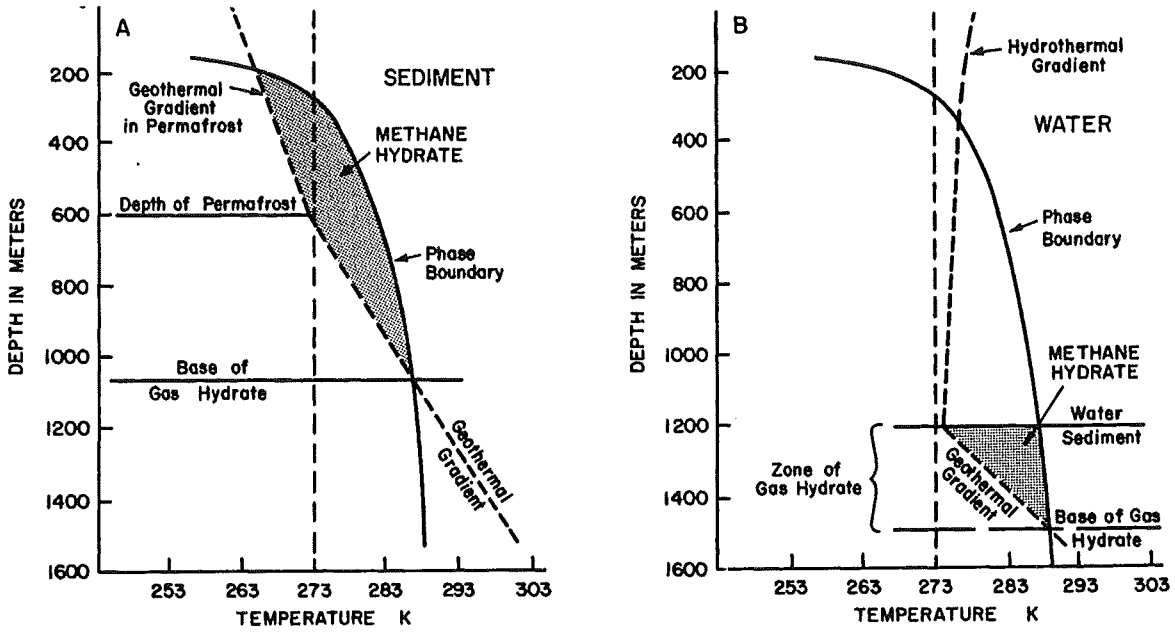

Figure 1: Simplified phase diagram of hydrates in a pure water/methane-system adapted to typical situations expected in permafrost (A) and in deep sea sediments (B). This diagram qualitatively demonstrates that hydrates are stable within sediments in these two regions (grey areas). Pressure was converted to depth assuming hydrostatic pore pressure. From Sloan (1990) after Kvenvolden (1988).

Fig. 2 displays locations of known and inferred gas hydrates (Kvenvolden, 1994). Several new discoveries of BSRs and hydrates have been reported since, such as hydrate samples from offshore Nigeria (Brooks et al., 1994) and BSRs elsewhere.

Two mechanisms have been proposed for the generation of methane in marine sediments: thermogenic formation at temperatures above $\sim 100°C$ and biogenic formation at lower temperatures, which involves the microbial breakdown of organic matter (Claypool and Kaplan, 1974). Biogenic formation may take place both in situ within the hydrate stability zone (HSZ, ref. also table 12 for abbreviations) or below the HSZ. The latter process as well as a thermogenic generation of methane requires that methane migrates upward into the HSZ for hydrate formation (ref. section A.5.2 for details). It is commonly assumed that methane concentration in the pore water must locally exceed the saturation level before hydrates may form (e.g. Sloan, 1990).

The significance of natural hydrates is largely due to the huge amount of carbon which is assumed to be stored as hydrates. As a direct consequence, a quantification of the formation and dissociation of natural hydrates is of importance for assessing the global carbon budget. Since knowledge about hydrate distribution in the Earth is relatively poor, only rough estimates of the amount of hydrates have been made. Table 1 lists some of these estimates. Note that the volume of oceanic hydrates in table 1 is estimated to be ~ 100 times above that of continental hydrates (ref. also section A.7 for details about

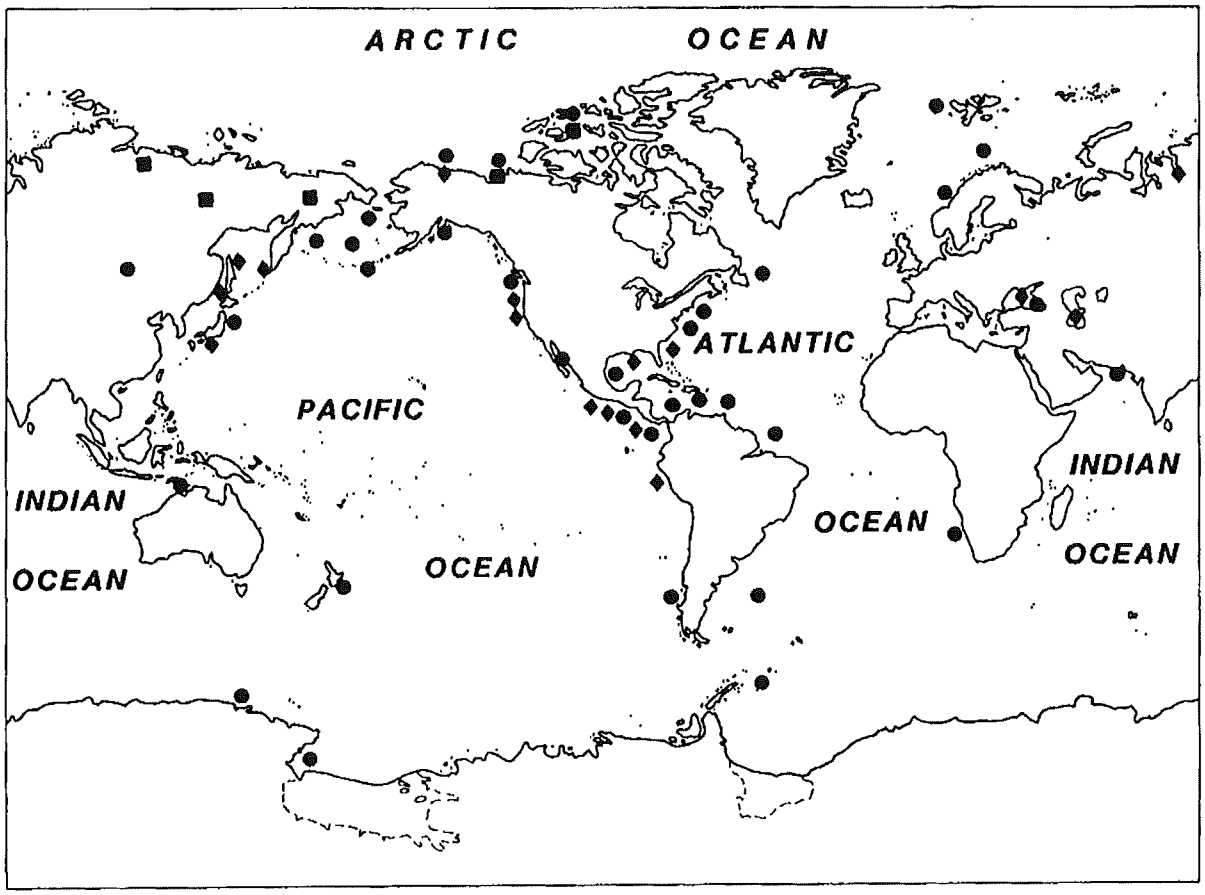

Figure 2: Worldwide locations of known and inferred hydrates. Squares: continental hydrates, circles: oceanic hydrates, inferred from BSRs, diamonds: locations where oceanic hydrates have been recovered. From Kvenvolden (1994).

those estimates). Table 2 shows an estimate of the distribution of organic carbon in the Earth, according to which the amount of carbon stored in hydrates exceeds that from fossil fuels by a factor of two.

cont. hydrates volume in $10^{13}m^3$	oceanic hydrates volume in $10^{15}m^3$	reference
5.7	5 – 25	Trofimuk et al. (1977)
3.1	3.1	McIver (1981)
1.4	-	Meyer (1981)
-	18	Kvenvolden (1988)
-	26.4 – 139.1	Gornitz and Fung (1994)

Table 1: Estimates of the amount of methane stored in hydrates worldwide. Compiled mainly after Sloan et al. (1990).

Reservoir	C_{org} $[10^{13}kg]$
Gas hydrates (on- and offshore)	10000
Fossil fuels (coal, oil, natural gas)	5000
Soil	1400
Dissolved organic matter in water	980
Land biota	830
Peat	830
Detrital organic matter	60
Atmosphere	3.6
Marine biota	3

Table 2: Estimated distribution of organic carbon in the Earth. Dispersed organic carbons such as kerogen and bitumen are not included. From Kvenvolden (1993).

Consequently, methane hydrates are a significant potential energy reservoir (e.g. Kvenvolden, 1993). The base of the gas hydrates stability zone (BHSZ) may represent a zone of weakness within the sediment column because hydrates may inhibit consolidation and excess pore pressure may build up at the BHSZ. Hence, hydrates may play an important role during slope failure (e.g. Booth et al., 1994). Since CH_4 is an important greenhouse gas – its warming potential exceeds that of CO_2 by a factor of 21 (Taylor, 1991) – an eventual release of methane from hydrates might also contribute to global warming. The amount of methane stored in hydrates is estimated to be $\sim$ 3000 the amount in the atmosphere (table 2). It is mostly assumed, however, that in general only continental and shallow water hydrates might considerably contribute to global warming (e.g. Kvenvolden, 1994; ref. also section A.7).

Prominent seismic reflectors, which are frequently observed in marine seismic reflection data from outer continental margins, are commonly believed to be associated with the BHSZ. These reflectors, known as bottom simulating reflectors (BSRs), are sub-parallel to the seafloor and cross dipping lithological boundaries indicating a non-sedimentary origin. They are characterized by a negative polarity with regard to the seafloor reflection caused by a decrease in seismic impedance (velocity multiplied by density) and hence most probably a decrease in velocity.

The negative impedance contrast at BSRs might be explained by the partial replacement of pore water by solid hydrates causing a velocity increase in the bulk sediment. Density of the bulk sediment is not expected to decrease considerably unless hydrates also replace part of the sediment matrix since hydrate has a density similar to that of water (ref. also table 8). Hydrates in the pore space of sediments are also believed to decrease permeability and thus, layers of hydrated sediments might act as gas traps. Replacing part of the pore water with free gas leads to a sharp drop in compressional wave velocity (V_p,

ref. also table 13 for symbols) (Domenico, 1976). Thus, a possible presence of free gas at the base of the hydrate stability zone might significantly contribute to the observed negative impedance contrast at BSRs.

Seismic methods aimed at investigating the nature of BSRs focus on delineating between the two principle V_p-models at the BSR shown in fig. 3. It is difficult, if not impossible, to resolve the base of a possible free gas zone beneath BSRs by applying conventional processing techniques including deconvolution to standard reflection seismic data, i.e. data with a frequency range of approximately $5 - 50Hz$. Higher resolution data combined with wide-angle measurements indicate, that velocity might increase gradually beneath a BSR rather than in a first-order velocity contrast (Katzmann et al., 1994). Such a velocity gradient could reflect a gradual decrease of gas concentration with depth.

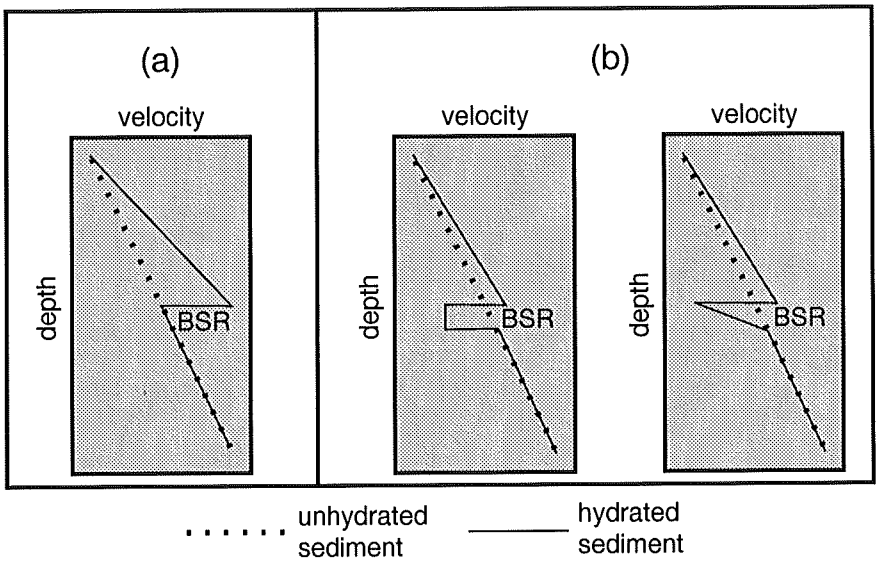

Figure 3: Compressional wave velocity structure of the BSR according to two principal models (a) not involving and (b) involving the presence of free gas. The free gas model may be a combination of two end-member models, a first-order velocity contrast at the base of the BSR (left) or a gradual increase of velocity beneath the BSR (right). Note that a much higher velocity, and thus presumably hydrate concentration, is required above the BSR than if assuming free gas at the BSR in order to produce a given reflectivity.

The geophysical nature of BSRs may be linked to formation mechanisms of hydrates. Whereas free gas is expected at the BHSZ if hydrates are formed in situ, the presence of free gas is not required if hydrates form exclusively from upward migrating methane-rich fluids (Hyndman and Davis, 1992) (ref. section A.5.3 for details).

The BSR plays an important role in heat flux studies because it may be regarded as well-defined temperature point within the sediment column. Assuming that it represents the base of the hydrate stability zone, the composition of hydrates and pore water is known, and the pressure at the BSR can be estimated, temperature can be read from the phase diagram for hydrates. Then, the depth of BSRs can be used to obtain heat flux through the sediment section above BSRs (e.g. Yamano et al., 1982).

Objectives of this study

Since drilling will not provide sufficient data to estimate the distribution and amount of natural hydrates, indirect methods have to be used to for this purpose. Much of the knowledge of the world wide distribution of submarine gas hydrates comes from seismic observations of BSRs (ref. also fig. 2). However, hydrate commonly occurs in areas where no BSRs can be observed. A better understanding of the conditions

required for BSR formation in addition to the presence of hydrates above them would be highly desirable for an assessment of the global distribution of hydrates. Geophysical studies of BSRs therefore focus on their nature and formation mechanisms.

A full waveform inversion scheme developed at the University of Cambridge (U.K.) (Singh et al., 1993; Minshull et al., 1994) proved to be a reliable method for investigating the nature of BSRs. The geology of the convergent margins off Costa Rica and Peru is being extensively studied at GEOMAR, University of Kiel. Seismic data from these areas frequently display BSRs. In this study, geophysical investigations of the nature and formation of BSRs at those margins together with heat flux obtained from the depths of BSRs are presented. In particular, the following questions are addressed:

- *Geophysical nature of bottom simulating reflectors:* The velocity structure of BSRs offshore Peru and Costa Rica is investigated using the 1-d full waveform inversion applied by Singh et al. (1993) and Minshull et al. (1994) to other locations. Those velocity structures allow a discrimination between the two end-member models for the nature of BSRs, one of which assumes the reflection is caused merely by elevated velocities above the BSR, the other involving the presence of free gas beneath the HSZ.

  On the Peruvian margin, ODP sites have been proposed for drilling through the hydrate layer and BSR (von Huene et al., 1995, unpubl.). BSRs at some locations along a reflections seismic line had been previously investigated by Miller et al. (1991) using a post-stack wavelet-modeling approach. Reliable knowledge concerning the occurrence of free gas is required for a risk analysis. Therefore, one of the goals of the studies presented here is to test and enhance those results prior to drilling by applying the more sophisticated pre-stack waveform inversion technique to data from the same seismic line. For this reason, several locations for waveform inversion are located close to those selected by Miller et al. (1991).

- *Formation mechanisms of BSRs:* Intensive studies of structure, tectonics, fluid flux and related topics have been conducted in recent years at the convergent margins offshore Peru and Costa Rica. Together with the knowledge of the nature of BSRs in both regions, possible formation mechanisms for BSRs are studied. Some of the questions, which are addressed, are:

  - Why do BSRs occur beneath hydrate layers in some areas, whereas they are absent in adjacent areas though the presence of hydrates in sediments from those areas is known or at least inferred?
  - Is there a link between the presence of BSRs and certain structures, especially structures which might control fluid migration?
  - May the development of BSRs be linked to tectonic uplift?
  - Is it possible to delineate sources of gas at the BSR based on geophysical evidence and existing information from drilling?

  The Costa Rican and Peruvian margin are regarded as case histories and may be representative for BSR formation at other convergent margins. Information about formation mechanisms of BSRs may also enhance the knowledge of gas hydrate formation in marine sediments.

- *Heat flux studies:* Heat flux is computed from the depth of BSRs, which are widespread in both study areas, focusing on the following points:

  - General patterns of heat flux are compared between Costa Rica, where a young oceanic plate is subducted, and Peru, where the downgoing plate is considerably older and thus colder.
  - Lateral variations of heat flux are investigated. The question of whether they may be related to fluid flow patterns was addressed.

3 Previous studies of bottom simulating reflectors

3.1 Nature and formation of BSRs

The nature of bottom simulating reflectors has been investigated by a number of authors since BSRs were associated with the base of the hydrate stability zone (e.g. Markl et al., 1970). Modeling of zero-offset reflection seismic data was performed in order to obtain the velocity structure of those reflectors: The velocity model was changed such that synthetic and real wavelets at the BSR match best. White (1977) and Shipley et al. (1979) predicted the presence of free gas at the BHSZ by investigating single-channel data. Miller et al. (1991) investigated a BSR in stacked multi-channel data off Peru and also concluded that the BSR may be best explained by the presence of a small amount of free gas at the BHSZ (ref. also section 5.5). Lee et al. (1994) applied an inversion scheme to zero-offset data from the southeastern U.S. continental margin. They used a classification of BSRs according to their waveform and apparent reflection coefficient R, so-called "strong BSRs" (S-BSRs, $R >\sim -0.1$), "weak BSRs" (W-BSRs, $R <\sim -0.05$) and inferred BSRs (I-BSRs), a classification introduced by Tucholke (1977). S-BSRs were interpreted as being caused by the presence of a thin gas layer. W-BSRs, which displayed considerably lower amplitudes, were related to only a very thin layer of free gas or merely the interface between hydrated sediments and water-saturated sediments. I-BSRs were mainly inferred from the updip termination of anomalously high amplitudes, which were interpreted as pockets of gas aligned parallel to sediment bedding.

Stacking traces in order to obtain zero-offset data causes a loss of offset dependent information. Amplitude performance as a function of source-receiver offset ("amplitude versus offset", AVO) may help to discriminate between gas bearing and fluid saturated sediments (Ostrander, 1984). Hyndman and Spence (1992) applied AVO forward-modeling to data from offshore Cascadia. The fit between real and synthetic data was best for a velocity model which consisted of a $10-30m$ thick high velocity layer above the BHSZ having a gradational top and a sharp base, the BSR. Subsequently, the authors preferred a model where no free gas occurred at the BSR. On the other hand, Minshull and White (1989) inferred from AVO performance of BSRs in data from the Makran accretionary complex that the BHSZ is underlain by free gas. Andreassen et al. (1995), applied a similar modeling technique to BSRs in the Beaufort Sea, explained zero-offset waveform and AVO performance in their data by assuming a thin layer of free gas.

Waveform inversion minimizes a key problem of forward-modeling, which is a certain subjectiveness since the changes in the velocity model are performed by the interpreter. Singh et al. (1993) applied a pre-stack full waveform inversion to data from a BSR off Vancouver Island, the same data set which had previously been investigated by Hyndman and Spence (1992) using AVO modeling. Singh et al. (1993) predicted free gas at the BHSZ in a $\sim 30m$ thick layer. Minshull et al. (1994) investigated BSRs off Colombia concluding that free gas is present beneath hydrates at the top of anticlines. Very little, if any, free gas was required to explain the velocity structure at a location at the flank of an anticline. This was interpreted as strong evidence for gas migration along the BHSZ. Wood et al. applied a similar waveform inversion technique to a BSR at Blake Ridge, concluding that it includes a $\sim 25m$ thick gas layer.

Those investigations were based on standard multichannel seismic (MCS) data which were acquired mainly to image the structure of the subsurface having frequencies in the range of approximately $5-50Hz$ (i.e. layers of less than $\sim 10-20m$ thickness could not be resolved). A few seismic experiments have recently been conducted which were designed to study BSRs and hydrated sediments. Rowe and Gettrust (1993) concluded from deep-towed MCS data using a high-frequency transducer ($250-650Hz$) that the BSR at Blake Ridge might be formed by a gas layer only $\sim 4m$ thick. They also reported offsets of up to $\sim 20m$ of the BSR across faults, which were interpreted as possible fluid migration paths. A decrease in reflectivity at the BSR as it intersects such faults is consistent with this interpretation (Rowe et al., 1995). Gas pockets at the BHSZ appear to be aligned along sediment bedding (Wood et al., 1995).

In order to investigate velocity variations within the hydrate layer together with the velocity structure of the BSR, a combination of wide-angle OBH data and high-resolution single channel data was acquired at Blake Ridge (Katzman et al., 1994), at Caroline Rise (Korenaga et al., 1995), and offshore Vancouver Island (Spence et al., in press). Those investigations indicate that the base of the BSR might be gradational rather than a first-order velocity step (Katzman et al., 1994). Also, Spence et al. (in press) observed that the BSR becomes less continuous the higher the frequency content of the source (i.e. the smaller the widths of the Fresnel zone) indicating lateral variations of its reflectivity within $\sim 200-400m$.

BSRs were first purposely penetrated during ODP Leg 141 at the Chile Triple Junction. Until then, drilling a BSR was regarded as hazardous and avoided in open-hole scientific drilling. Core investigations and especially logging provided valuable information about the nature and formation of BSRs.

A sonic log through the BHSZ at Leg 141 Site 859 showed that the BSR there is caused by a drop in V_p from $1.95km/s$ to an average of $1.6km/s$ in a $7m$ thick layer (Bangs et al., 1993). Within this layer, V_p reached a minimum value of $1.2km/s$, i.e. velocities less than that of water, which only can be reasonably explained by the presence of free gas in the pore space. Bangs et al. (1993) interpreted this velocity structure as evidence for a $7m$ thick gas layer containing an average of approximately 1% free gas in the pore space.

BSRs were also penetrated at Leg 146 Sites 889 and 892, during which VSP and sonic logs were obtained. At both locations, velocities indicate a small amount of free gas as the cause of the BSR. Moreover, V_p-profiles obtained from VSP data from Site 889 (MacKay et al., 1994) matched well with earlier results from waveform inversion (Singh et al., 1993) indicating the reliability of the waveform inversion approach.

Dissociation of hydrates has been suggested as a source of free gas in both regions off Chile and Cascadia/Vancouver Island. Chlorinity profiles in cores from Leg 146 gave strong evidence for a recent, i.e. interglacial, upward move of the BHSZ: low Cl^--concentrations at the BHSZ could be best explained by a moderate hydrate concentration together with an additional source of upward migrating low Cl^--fluid from a presumed paleo-hydrate zone (Kastner et al., in press). Such an upward shift of the BHSZ might be attributed e.g. to increased bottom-water temperatures after deglaciation (Kastner et al., in press).

3.2 Heat flux from the depth of BSRs

Heat flux values computed from the depth of BSRs and in-situ measurements matched fairly well if assuming a pure water/methane system at the Blake Bahama Outer Ridge (Site 533), at the Peru margin (Site 685), and at the Nankai accretionary prism (Site 808) (compiled by Hyndman et al., 1992). Discrepancies of theoretical and measured temperatures at the depth of the BSR however, have been reported from the Chilean margin (Leg 141 Site 859, e.g. Bangs et al., 1993) and offshore Vancouver (Leg 146 Sites 889 and 892, Westbrook et al., 1994). Temperatures at the BSR obtained from WSTP (water-sampling temperature profile) measurements were $\sim 2K$ lower than predicted from the phase diagram of methane hydrates from fresh water (e.g. Bangs et al., 1993, Westbrook et al., 1994) , i.e. the theoretical BHSZ was below the geophysically determined depth of the BSR. Adding 3.5% of NaCl would lead to a shift of the phase diagram of about $1.1K$ (Westbrook et al., 1994). Sloan (1990) warns that adding 24%NaCl (saturation is reached at 26%) to water shifts the phase diagram by as much as $13K$ towards lower temperatures at a given pressure. On the other hand, higher-molecular-weight hydrocarbons, which have been found at relatively high concentrations above BSRs at Sites 889 and 892 would shift the phase diagram into the opposite direction.

Relative lateral variations of heat flux, however, are in general not assumed to be considerably affected by discrepancies in the phase diagram. Mapping the depth of the BSR was used to infer small-

scale variations of heat flux. Heat flux variation inferred from changes in the depth of BSRs showed evidence for localized fluid expulsion in the Makran accretionary prism (Minshull et al., 1992). Hutchinson et al. (1995) observed upward deflections of BSRs in Lake Baikal of up to $75m$, which provided indirect evidence for circulation of presumed warm pore fluids.

4 Methods

4.1 Full waveform inversion of reflection seismic data

4.1.1 Theory of the full waveform inversion technique

Waveform inversion aims at finding a seismic model of the subsurface such that the sample-by-sample misfit between synthetic and observed data is minimized. The generalized least-squares method has been widely used in recent years as an approach to such seismic inverse problems. A good review of least-squares methods applied to seismic data is given by Santosa and Symes (1989). These nonlinear inverse problems can be solved using iterative gradient methods (Tarantola, 1984). Linearized inversion of seismic data (e.g. Clayton and Stolt, 1981) is possible if the starting model is close enough to the real Earth. Nonlinear approaches (e.g. McAuley, 1985) are less restrictive. However, since they are gradient-based, they still require a good a priori estimate of seismic parameters in order to minimize nonlinear effects (Kormendi and Dietrich, 1991).

The inversion technique used for these investigations is a 1-dimensional nonlinear conjugate gradient method, which was developed by Kormendi and Dietrich (1991) (ref. this article for a more detailed description of the technique). It solves the inverse problem for data in the frequency/slowness (ω, p)-domain assuming an elastic medium. The assumption of 1-dimensionality allowed to use an effective forward modeling scheme, the generalized reflection and transmission matrix method of Kennett and Kerry (1979). The method accounts for all nonlinear effects of Earth models such as multipathing and mode conversions. The Fréchet (or partial) derivatives of the plane wave response of the Earth model with respect to model parameters are computed using formulas from Dietrich and Kormendi (1990).

The inverse problem

A vector $\mathbf{d}$ contains the discrete samples of a plane-wave response of a stratified medium described by $\mathbf{m}$ which contains the model parameters. The Earth parameters $\mathbf{m}$ are nonlinearly related to the synthetic seismic data $\mathbf{d}$ via an operator $\mathbf{f}$, which maps the model space M into the data space D:

$$\mathbf{d} = \mathbf{f}(\mathbf{m}) \quad . \tag{1}$$

The misfit (or cost) function is then a sample-by-sample comparison of the observed seismic data $\mathbf{d}_{obs}$ with the synthetic data $\mathbf{d}$ together with the deviation of the current model $\mathbf{m}$ from the initial model $\mathbf{m_0}$ (Tarantola and Valette, 1982):

$$S(\mathbf{m}) = \frac{\|\mathbf{d} - \mathbf{d}_{obs}\|_D^2 + \|\mathbf{m} - \mathbf{m_0}\|_M^2}{2} \quad . \tag{2}$$

The norm $\|\cdot\|$ is the weighted L_2 norm, which is defined by

$$\|\mathbf{d}\|_D^2 = \mathbf{d}^\tau \underline{\mathbf{C}}_D^{-1} \mathbf{d} \qquad \text{and} \qquad \|\mathbf{m}\|_M^2 = \mathbf{m}^\tau \underline{\mathbf{C}}_M^{-1} \mathbf{m} \tag{3}$$

where $\underline{\mathbf{C}}_D$ and $\underline{\mathbf{C}}_M$ are the covariance matrices for data and the starting model, respectively, and $^\tau$ denotes the transpose of a matrix.

The inversion aims at minimizing S. A gradient-based technique can be used to find the minimum of S, if the starting model is close enough to the optimum model (i.e. $\mathbf{m_0}$ is in the vicinity of the global minimum of S). Gradient-based techniques iteratively improve the model starting from $\mathbf{m_0}$ by

determining a direction of descent $\mathbf{\Phi}$ and a length of descent μ to compute the model for iteration $n+1$ from iteration n:

$$\mathbf{m}_{n+1} = \mathbf{m}_n - \mu_n \mathbf{\Phi}_n \qquad \text{such that} \qquad S(\mathbf{m}_{n+1}) < S(\mathbf{m}_n) \quad . \tag{4}$$

Gradient-based inversions may get "trapped" in a local minimum of S rather than finding the global minimum and thus, the optimum model, if $\mathbf{m}_0$ is not close enough to the optimum model. Optimizing the fit of the seismic waveform by inverting for a high resolution velocity/depth function using such a technique therefore requires a good knowledge of the long-wavelength (i.e. large-scale) velocity distribution.

Good values for $\mathbf{\Phi}$ and μ may be determined with the conjugate gradient method. The Fréchet derivatives are defined by:

$$\underline{\mathbf{F}}_n = \left.\frac{\partial \mathbf{f}}{\partial \mathbf{m}}\right|_{\mathbf{m}=\mathbf{m}_n} \quad . \tag{5}$$

Element (i,j) of $\underline{\mathbf{F}}_n$ represents the first-order perturbation of the i'th sample of $\mathbf{d}$ caused by a infinitesimally small change of the j'th parameter of $\mathbf{m}$. The direction of steepest descent can then be computed as

$$\mathbf{\Gamma}_n = \underline{\mathbf{C}}_M \left.\frac{\partial S}{\partial \mathbf{m}}\right|_{\mathbf{m}=\mathbf{m}_n} = \underline{\mathbf{C}}_M \underline{\mathbf{F}}_n^{\tau} \underline{\mathbf{C}}_D^{-1} \left(\mathbf{f}(\mathbf{m}_n) - \mathbf{d}_{\mathbf{obs}}\right) + (\mathbf{m}_n - \mathbf{m}_0) \quad . \tag{6}$$

The direction of steepest descent is used for computing the conjugate direction of descent

$$\mathbf{\Phi}_n = \mathbf{\Gamma}_n + \sigma_n \mathbf{\Phi}_{n-1} \qquad \text{starting from} \qquad \mathbf{\Phi}_0 = \mathbf{\Gamma}_0 \quad . \tag{7}$$

The formula of Polak and Ribière (1969)

$$\sigma_n = \frac{(\mathbf{\Gamma}_n - \mathbf{\Gamma}_{n-1})^{\tau} \underline{\mathbf{C}}_M^{-1} \mathbf{\Gamma}_n}{\mathbf{\Gamma}_{n-1}^{\tau} \underline{\mathbf{C}}_M^{-1} \mathbf{\Gamma}_{n-1}} \tag{8}$$

gives σ_n. The optimum step width μ_n is obtained from a linear search along the direction of descent $\mathbf{\Phi}_n$ to find a value which minimizes the cost function: The cost function is computed for several (typically 3) values of μ_n. The optimum step width is then computed from a three-point parabolic inverse interpolation (ref. Kormendi and Dietrich, 1991, for details).

4.1.2 Flow pattern of the inversion strategy

Fig. 4 shows a flow pattern of the inversion scheme. The inversion strategy consisted of two main steps. At first, a long-wavelength velocity model was determined based on an accurate determination of interval velocities between discrete reflectors. This velocity model formed the basis for a starting model for the waveform inversion itself.

4.1.3 Data pre-processing

A CMP-gather from the location which was investigated was frequency filtered with a broad bandpass filter (typically $5 - 50Hz$). As a next step, the amplitude behavior of the channels had to be tested. For this purpose, energies of the reflection from the seafloor were determined for each trace in a $200ms$ window around the signal from the seafloor (ref. section. B.1).

These energies varied considerably within one CMP-gather in the data from off Costa Rica, due either to a varying strength of source signals or to differences in receiver sensitivities. Therefore, amplitude corrections were performed in a deterministic way: the theoretical energy-versus-offset function of the seafloor reflection, normalized to the mean energy of the seafloor reflection over all traces, was computed taking into account geometrical spreading, directivities and amplitude-versus-angle-of-incidence performance of the seafloor. Then, correction factors were computed for each trace by which the signals

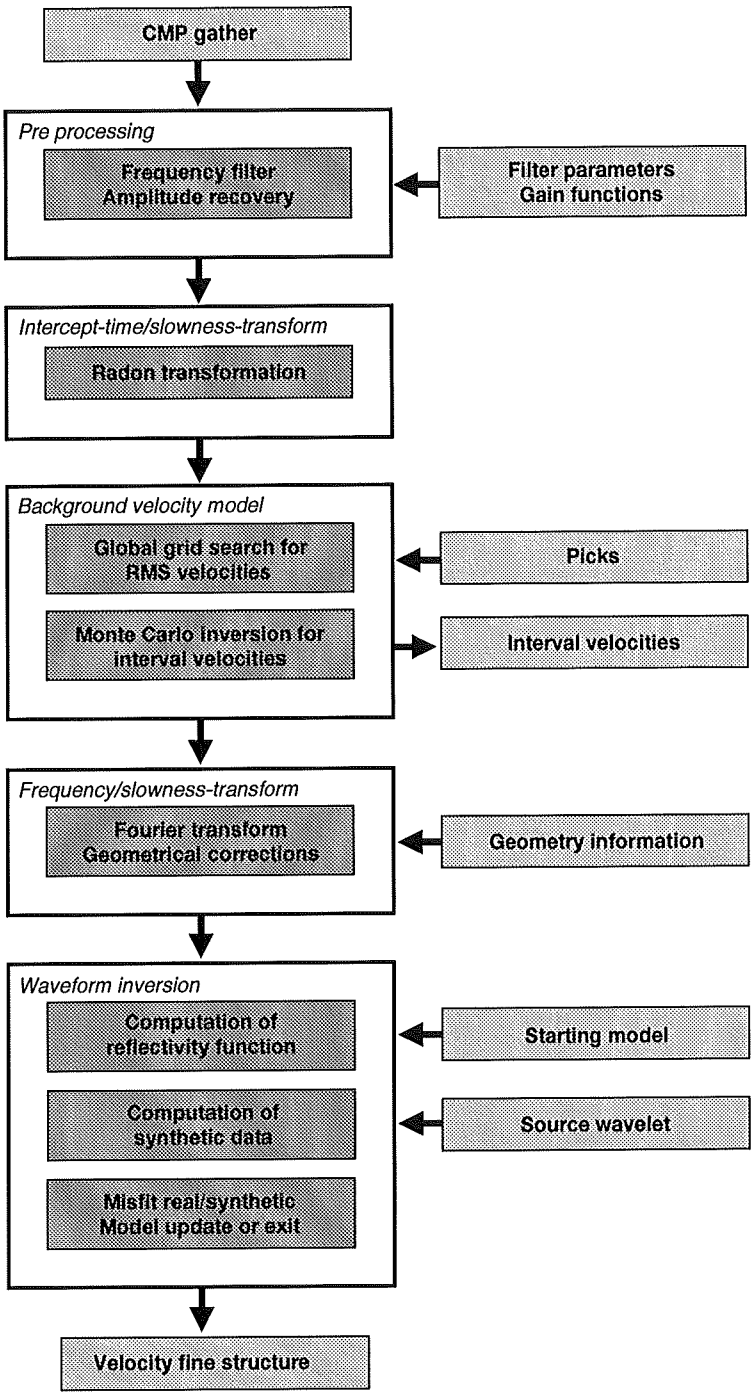

Figure 4: Flow pattern of the inversion strategy.

in the windows around the seafloor had to be multiplied in order to match theoretical energy-versus-offset performance. This factor was applied to the whole trace.

To test this deterministic approach, it has been applied to a data set off Peru, where the energy-versus-offset trend of the seafloor reflection did not show a strong variation between adjacent traces (except for one trace). At this data set, the theoretical, i.e. deterministically determined, energy function, roughly follows the general trend of energy of the data indicating that the assumptions made for computing the theoretical energy and thus, amplitude correction factors, were reasonable. This is important as waveform inversion implicitly accounts for amplitude-versus-offset variations of reflections.

The data set was transformed into the intercept-time/slowness (τ, p)-domain using the exact Radon transform (Chapman, 1981). In the (τ, p)-domain, reflections are characterized by elliptical trajectories. This data set was used to determine the long-wavelength velocity function. For the waveform inversion, the data were Fourier transformed into the (ω, p)-domain and directivity corrected (Sheriff and Geldart, 1982) (ref. also section B.2.1).

4.1.4 Reflectivity of the seafloor and source wavelet

The synthetic data set for the waveform inversion is computed by convolving the reflectivity function of the subsurface with a given source wavelet. This source wavelet was obtained from the seafloor reflection. A signal reflected at the seafloor at normal incidence, i.e. zero-offset, $A_s(t)$ is a convolution of the reflectivity series $R(t)$ at the seafloor with the source wavelet. $R(t)$ can be obtained by comparing the signal from the seafloor and its multiple $A_m(t)$: A Wiener shaping filter, which transforms $A_s(t)$ into $A_m(t)$ is equivalent to the reflectivity series $R(t)$ multiplied by -2. This is due to the reflection coefficient of -1 at the free air/water surface. The factor 2 is caused by geometrical spreading (e.g. Warner, 1990). If $R(t)$ is only one spike, i.e. the seafloor is a single reflector within the length of the source wavelet, the source signal is equivalent to the signal reflected from the seafloor. Then, the reflection coefficient of the seafloor can be computed from

$$R = (-2) \cdot \frac{A_m(t)}{A_s(t)} \quad . \tag{9}$$

In this case, signals from seafloor and multiple are identical (except for the scaling factor of $-2 \cdot R$).

To compare signals from seafloor and multiple, they were extracted from near-offset traces (as an approximation to zero-offsets) of several CMP-gathers (typically 20) and stacked in order to enhance the signal-to-noise ratio. At most locations which were investigated, both signals were almost identical (after scaling and multiplying the multiple signal by -1). At two locations, the reflectivity series was also determined, which turned out to be mainly a spike, as expected. The source wavelet then could be easily extracted by stacking traces in a window around the seafloor.

4.1.5 Starting model

An optimum long-wavelength velocity model was determined from the data set in the (τ, p)-domain in four steps. In the first step, a global grid search was used to determine upper and lower limits on root-mean-square (RMS) velocities between major reflectors (typically three reflectors: seafloor, BSR, and one reflection beneath the BSR). RMS velocities between the picked horizons were systematically varied and energies along the corresponding elliptical trajectories in the (τ, p)-gather were computed. The limits for RMS velocities in the i'th layer between two picked horizons were defined by their uncertainty computed from the energy-versus-velocity distribution according to Landa et al. (1991):

$$\delta V_{rms,i} = \sqrt{\frac{-2E_{min}}{\left(\frac{d^2E}{dV^2}\right)_{E_{max}}}} \tag{10}$$

where E_{min} denotes the minimum value of the energy E summed along an elliptical trajectory. It represents an upper limit of the energy in the absence of any signal. In the denominator, $E(V_{rms})$ is evaluated in the vicinity of its maximum value E_{max}.

RMS velocities were then transformed into interval velocities using the Dix equation. Applying this equation to $\delta V_{rms,i}$ gives uncertainties in interval velocities $\delta V_{int,i}$ as:

$$\delta V_{int,i} = \frac{\Delta t_i V_{rms,i} \delta V_{rms,i} + \Delta t_{i-1} V_{rms,i-1} \delta V_{rms,i-1}}{(t_i - t_{i-1}) \cdot V_{int,i}} \tag{11}$$

where $V_{int,i}$ is the interval velocity in the i'th layer, Δt_i the two way traveltime between the i'th and the $(i-1)$'th reflector.

Within these velocity limits, in the next step, a Monte Carlo (random) search (e.g. Singh and Minshull, 1994) was simultaneously applied to all interval velocities to enhance accuracy of the interval velocities. The a priori probability distribution form the Monte Carlo inversion was defined as:

$$P(V) = \begin{cases} \text{constant} & \text{if} \quad |V - V_{int,i}| < \delta V_{int,i} \\ 0 & \text{otherwise} \end{cases}, \tag{12}$$

The procedure started with 50 random models and 50 iterations per model. In each iteration, the velocity of one layer was randomly changed. The new model was accepted if energies along the elliptical trajectories were increased by the change. After 50 iterations, the interval velocity model had sufficiently converged to a few local maxima of the energy functions. In the third step, the best of the 50 final models was optimized by a local search using the Simplex method (e.g. Singh and Minshull, 1994).

Minshull et al. (1994) estimate uncertainties for velocities at about $0.1 km/s$. These uncertainties should be about the same for the investigations performed for the present studies since depths relative to the maximum source-receiver distances are similar.

This interval velocity model was finally transformed into a gradient model in such a manner that (1) vertical traveltime between two picked horizons was kept constant, and (2) there was no velocity contrast at the seafloor; the seafloor reflection is produced by a change in density (ref. section C.1). At the Peruvian margin, the latter approximation was justified by results from ODP Leg 112 Site 688, at the Costa Rican margin by results from measurements during DSDP Leg 84 Site 565. Also, P-wave measurements e.g. on box cores indicate that this assumption seems to be a good approximation for deep sea sediments in general (Philipp, 1989).

Other seismic properties which were required to model the subsurface were density (ρ), shear wave velocity (V_s), and seismic quality factors for P-waves (Q_p) and shear waves (Q_s), describing attenuation. Density of the water column was set to $1.035 g/cm^3$. In the sediment column, ρ was computed using Hamilton's relations between ρ and V_p (Hamilton, 1978) (ref. section C.2 for formula) . V_s was estimated from Castagna's et al. (1985) relationships between V_s and V_p in siliceous sediments (ref. section C.2 for formula). This calculation yielded a shear wave velocity in sediments at the seafloor of $0.1 km/s$, which is a realistic value compared to in-situ measurements (e.g. Whitmarsh and Miles, 1991). Q_p was estimated to be 10,000 (i.e. effectively infinite) in the water column and 200 in the sediment. Q_s was set to 100 throughout the sediment (Minshull and Singh, 1993). Finally, seismic properties for the starting model were sampled at $6m$ intervals and smoothed using a running average operator.

4.1.6 Full waveform inversion

Starting model, source wavelet, and real data were used as input for the full waveform inversion, which is described in section 4.1.1. The principle flow pattern of this technique is shown in fig. 5.

All model parameters but V_p were kept fixed. The goal of these investigations was to address the question of whether a thin layer of free gas is present beneath the hydrate zone. Free gas significantly decreases V_p, however, neither ρ nor V_s are considerably affected by the replacement of part of the pore

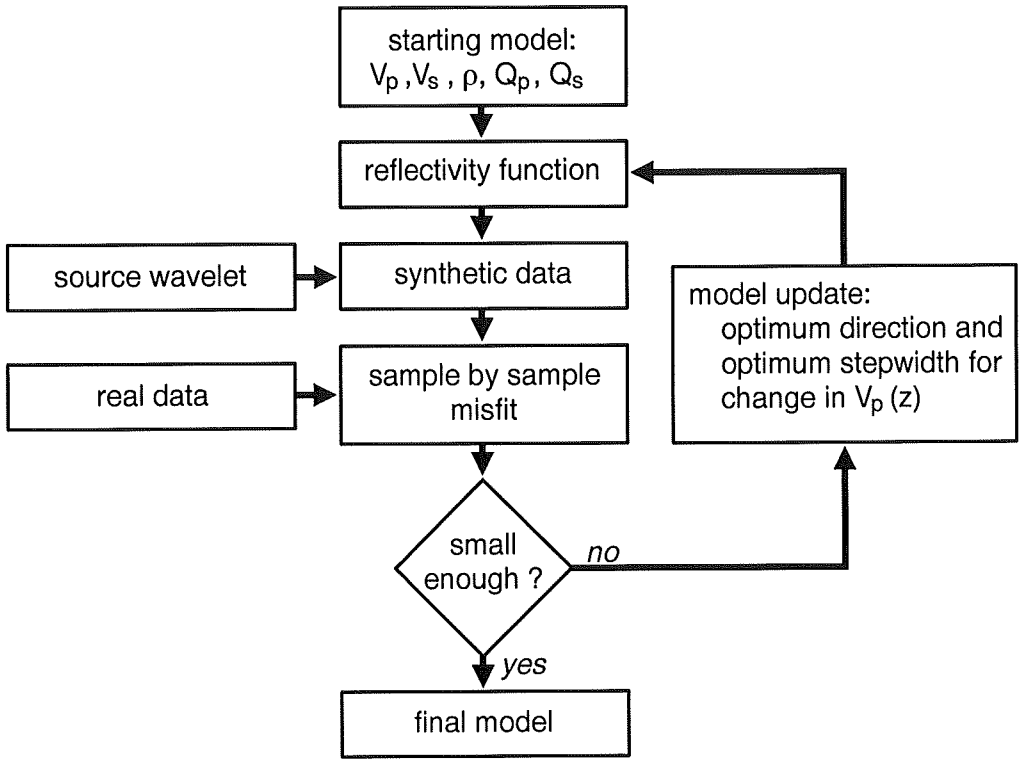

Figure 5: Flow pattern of the waveform inversion. The model update is performed using a conjugate gradient technique.

water by gas (Biot, 1956a). Allowing a second free parameter in the inversion, such as ρ, would make results, i.e. an optimum Earth model, less stable. The Poisson's ratio, which is often used as an indication for free gas, is varied indirectly by changing V_p (ref. eq. 27). The entire sediment column above the BSR was modeled, because the BSR waveform is affected by transmission through these sediments, down to some distance beneath it.

Each inversion consisted of several runs, during which 5 iterations were performed. The final model from each run was used as a starting model for the next run, except that a part of the old starting model around the seafloor was copied into it. This was done to keep scaling at the seafloor constant and to stop the inversion algorithm from concentrating on a best fit of the data around the strong seafloor reflection rather than the weaker BSR.

A major concern while applying gradient inversion methods is to avoid getting "trapped" in local minima of the misfit function. To ensure that the global minimum is reached, inversions were first performed at lower frequencies (typically, up to $30Hz$), and thus reduced resolution, before using the whole frequency range of the data (typically, up to $50Hz$). The final model from the low-frequency inversion was used as starting model for the high-frequency inversion. This approach allowed to first account for longer wavelength changes in the velocity/depth function, before determining the velocity fine structure. This strategy is a common technique to avoid gradient based inversions reaching a local minimum of the misfit function (e.g. Singh and Minshull, 1994). The misfit function changed little between successive iterations during the last runs of the high-frequency inversion, which indicated convergence of the model to minimum misfit.

4.2 Modeling P-wave velocity as a function of water saturation

Compressional wave velocity as a function of water saturation of the pore space in partially saturated sediments was modeled based on the equation of Gassmann (1951), Biot (1956a), and Geertsma (1961).

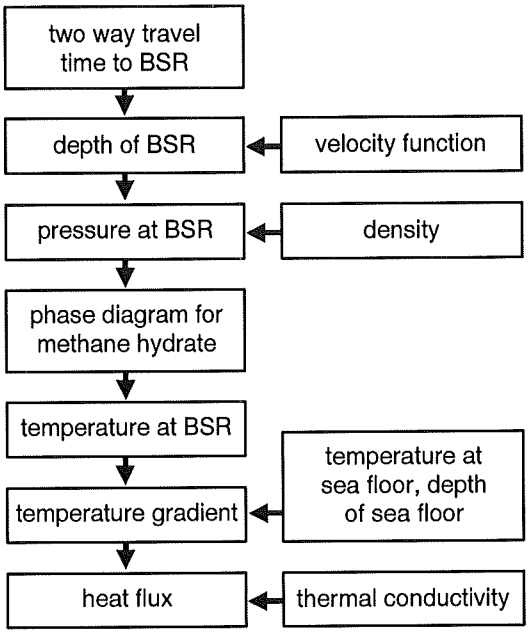

Figure 6: Determination of heat flux from the depth of the BSR. Instead of converting TWT to the BSR to depth using a velocity function, depth of the BSR could also be picked from pre-stack depth migrated sections at 12° S (ref. text for details).

For these studies, a version was used which allowed V_p and V_s at full saturation to be specified as input parameters. In order to estimate the error margin of the modeling, the model parameters were varied.

See section D.2 for the Biot-Geertsma equation. In section D.4 a description of the approach used for these investigations is given. To model V_p as a function of water saturation by applying the Biot-Geertsma equation assumes an even distribution of free gas within the pores, which seems to be a major limitation for this method (ref. section D.5).

4.3 Determination of heat flux from the depth of the BSR

Heat flux through the sediments above the BSR can be determined assuming that the BSR represents the base of the methane hydrate stability zone (Yamano et al., 1982). This method is based on the assumption that temperatures at the BSR may be obtained from the phase diagram for methane hydrate, if (pore) pressure at this depth is estimated. Fig. 6 describes how this method was applied to the data from offshore Peru and Costa Rica for the present studies.

Seismic data were pre-stack depth migrated using a package developed by DATAID TOTAL ('MIGPACK'). The migration is based on a downward continuation of shots and receivers in the shot-geophone-frequency (SGW) domain (Denelle et al., 1986). A velocity model is obtained iteratively from a focusing analysis (Audebert and Diet, 1990). Ref. to section E for some details.

Off Peru at 12° S, migrated depth sections were re-stretched to time. Two-way-traveltime (TWT) of seafloor and BSR was picked. An interval velocity-versus-TWT function was determined from both profiles, which was applied to obtain the depth of the BSR. To use a general velocity-versus-TWT function for the whole region instead of picks in the depth sections was considered to be more accurate due to small-scale artifacts in the position of the BSR caused by dip-effects during focusing analyses (ref. section 8.1.1). However, heat flux obtained from depth picks was also computed for comparison. Data from 9° S did not allow an accurate determination of interval velocities between seafloor and BSR, due

to their acquisition parameters (small maximum offset relative to the depth of the BSR) and a relatively weak BSR, which resulted in inaccurate ("smeary") and weak focuses. Therefore, the interval velocity-versus-TWT function determined at 12° S was used to convert picks in the time sections to depth. The procedure was similar for the Costa Rican data, where velocity information was available from only one of the three investigated lines.

Pressure at the BSR was computed assuming hydrostatic pressure, i.e. using water density. Tests with lithostatic pressure as the other end-member of possible pore pressure at the BSR were also performed. For this case, density/depth-relations based on results from measurements on cores from ODP Leg 112 (Suess et al., 1988) and DSDP Site 565 (von Huene et al., 1985b) were used for the Peruvian and Costa Rican data, respectively.

Temperature at the BSR was calculated based on the phase diagram for hydrates assuming a pure water/methane system. Ref. section F details. The temperature gradient can be easily computed from the depth of the BSR together with temperatures at BSR and seafloor. The latter is available from oceanographic data.

Finally, heat flux is defined by:

$$H = K \cdot \frac{\Delta T}{\Delta z} \tag{13}$$

where K is the thermal conductivity, $\Delta T/\Delta z$ the temperature gradient. An average value from core measurements during ODP Leg 112 was used for K. Since no depth dependence of K could be observed, (which should exist if porosity is depth dependent), no depth corrections were applied. Off Costa Rica, thermal conductivity was computed by applying a geometric mean relation between sea water and grain conductivity (p. 151 eq. 54).

Minshull and White (1989) estimated error margins in similar heat flux computations at the Makran accretionary prism at $\sim$ 10%. However, they stress that this value does not account for possible systematic errors from inaccuracies in the phase diagram. For the present studies, error margins are expected to be in the same order of magnitude perhaps having a more accurate velocity information from pre-stack depth migration but less control over thermal conductivities.

5 Geology of the central Peruvian margin

The recent geology of the central Peruvian convergent margin was greatly influenced by subduction of Nazca Ridge. Tectonic processes in that area have been intensely studied and include drilling of ODP Leg 112. Fig. 7 shows the locations of these drill sites and the seismic profiles used for the present study.

Nazca Plate is subducted beneath the South American Plate at a current rate of $78mm/a$ (De Mets et al., 1990). At 15° S the Nazca Ridge enters the subduction zone. It is assumed to have an approximate mirror-image symmetry to Tuamotu Ridge, since both ridges are believed to originate from the same melting anomaly on the East Pacific Rise (Pilger and Handschuhmacher, 1981). Nazca Ridge is subducted obliquely to the trench migrating north to south along the margin. Its subduction affected tectonics along the margin to about 8° S, where its frontal part was subducted about $8Ma$ before present (Cande, 1985). A reconstruction of this movement along the margin is shown in fig. 8.

5.1 Bore hole stratigraphy

Most of the Leg 112 drill sites at the central Peruvian margin are located approximately along two transects at about 9° S and 12° S (fig. 7). Some results from two industry holes, Ballena and Delfin were also available for scientific purposes.

Eocene sediments were drilled at three locations, Sites 682, 683, and 688 (figs. 9 and 10). They are cut by the Incaic-Quechua (IQ) unconformity. This hiatus spans Eocene, Oligocene and lower Miocene

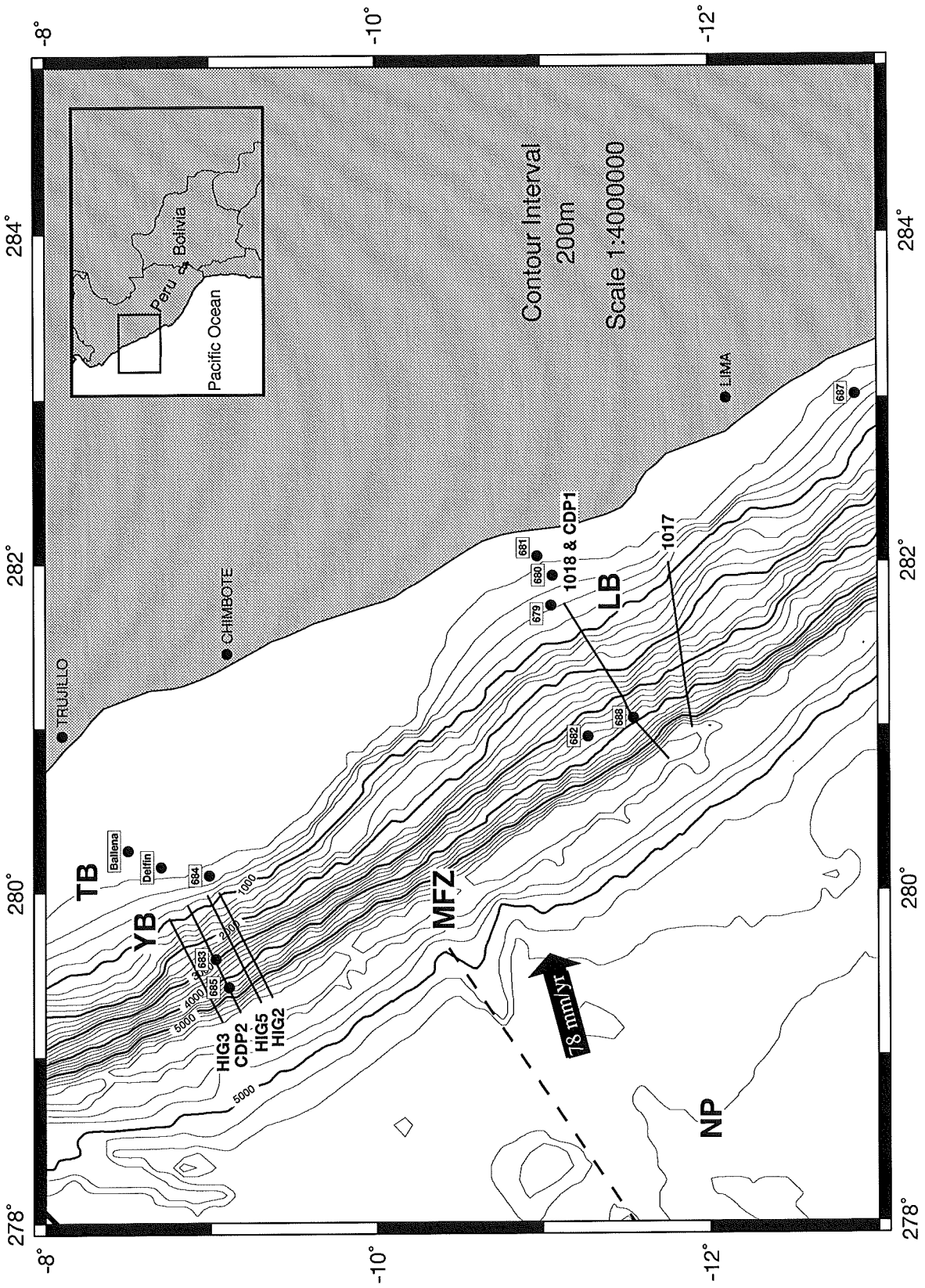

Figure 7: Location of drill sites and seismic lines at the Peruvian convergent margin. NP: Nazca Plate, MFZ: Mendaña Fracture Zone, LB: Lima Basin, TB: Trujillo Basin, YB: Yaquina Basin. Locations of seismic lines are only approximate due to a lack of exact navigational data. Tracks of CDP1 and 1018 are almost identical except at the lower slope, where CDP1 is located slightly north of 1018. Circles denote drill sites, numbered sites are ODP Leg 112 sites, Ballena and Delfin are industry sites. HIG2-5, CDP2, 1017, and 1018 are reflection seismic profiles.

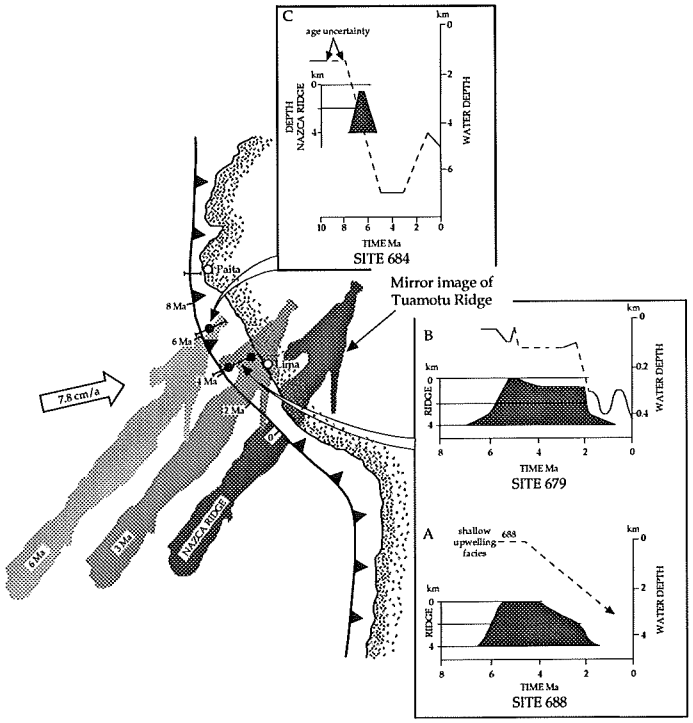

Figure 8: Movement of Nazca Ridge from north to south along the margin based on the assumption that its topography mirror-images that of Tuamotu Ridge. Insets show paleobathymetric reconstructions at ODP Leg 112 Sites 679, 684, and 688. The lines in the insets display water depth as a function of age at these sites (dashed lines indicate that the exact age is uncertain). The shaded areas show the topography of Tuamotu Ridge along a trajectory beneath the corresponding ODP sites. Slightly modified from von Huene et al. (in press).

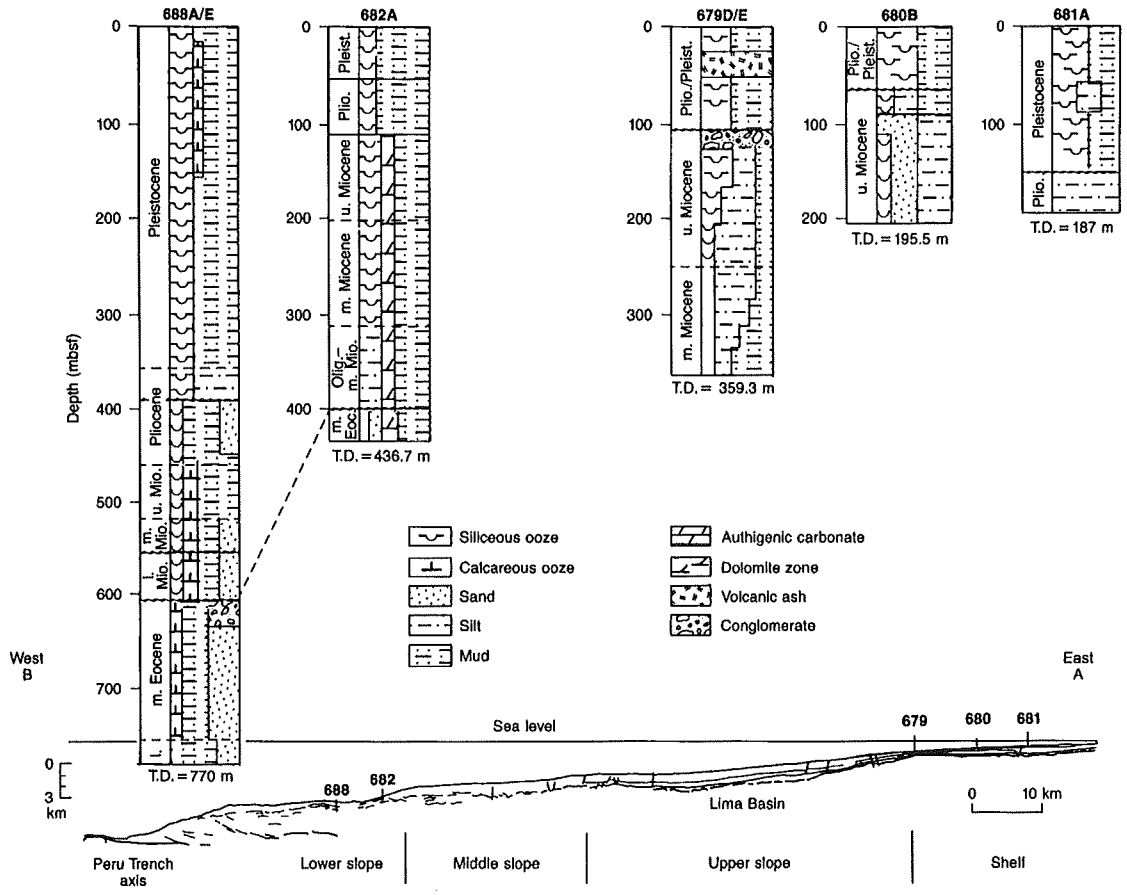

Figure 9: Columnar sections of ODP Leg 112 drill sites along the southern transect. From von Huene et al. (1988).

time ($40-25Ma$ B.P.). It coincides with the last Incaic and first Quechua tectonic and magmatic pulses and seems to have followed the landward shift of volcanism from close to the present coast to the Neogene Andean arc (Noble et al., 1979).

Miocene mudstone was deposited above the IQ unconformity. It contains abundant transported microfossils and in-situ benthic foraminiferal assemblages from middle to lower bathyal depth zones ($500-4000m$). Sedimentation rates increased at Site 682 during the middle and late Miocene and reworked components become abundant in this sections. Together with the presence of an unconformity which underlies Lima Basin, this indicates erosion at this time further upslope. At Site 688, the basal Pliocene includes coastal upwelling-facies, which are currently restricted to deposition in water $150-500m$ deep. Further upslope at Site 679, upper Miocene to Quaternary mud transported from the adjacent zone of coastal upwelling was recovered. This section overlies a regional hiatus in late Miocene/early Pliocene which is marked by a seismic unconformity beneath Lima Basin and spans a period of $4Ma$. The middle Miocene section at Site 683 in the northern area consists of mudstone deposited in middle bathyal depths. It is bounded by the IQ unconformity and an upper Miocene hiatus. Further downslope at Site 685, a $200m$ thick section of Pleistocene slope sediments consisting of mainly diatomaceous mud and containing abundant transported shelf microfossils overlies accreted sediment of late Miocene age. A hiatus of at least $4.3Ma$ separates both sections (von Huene et al., 1988).

The two industry drill holes in the northern area (fig. 10) penetrated the whole sedimentary sequence down to a metamorphic basement consisting of Paleozoic gneiss and schist (e.g. Kulm et al., 1985).

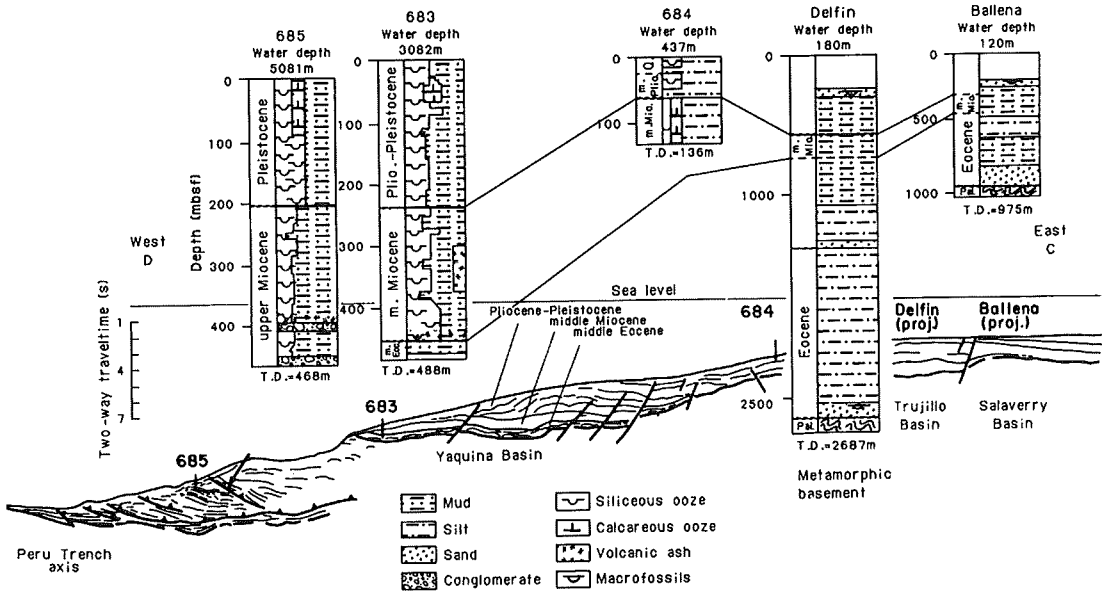

Figure 10: Columnar sections of ODP Leg 112 and industry drill sites along the northern transect. The line drawing is from a time section of CDP 2. From von Huene et al. (1988).

Uplift and subsidence history of the central Peruvian margin since Miocene time can be clearly linked to the oblique subduction of Nazca Ridge. The insets in fig. 8 give a draft description of uplift and subsidence history in both areas based on bore hole stratigraphy at Sites 684, 688, and 680. Nazca Ridge was subducted in late Miocene/early Pliocene time at 12° S. Lima Basin was uplifted probably to sea level in late Miocene time, when erosion caused the unconformity beneath it. Subsidence down to present depths implies subsidence rates of about $450m/Ma$. Benthic foraminifera indicate subsidence at a rate between 350 and $650m/Ma$ (Kulm et al., 1988). In the northern area, Nazca Ridge was subducted earlier. The age of accreted sediment drilled at Site 688 indicates a switch from tectonic erosion to accretion at latest in upper Miocene time.

5.2 Seismic studies

Seismic lines from the Peruvian convergent margin include several reflection lines in the areas of ODP Leg 112, some of which have been re-processed in recent years at GEOMAR. Processing included a pre-stack depth migration technique ('MIGPACK', ref. section E) to enhance the structural image of these tectonically complex areas. Velocity analysis together with pre-stack migration in the depth domain gave considerably more detailed structural information in areas of steepened dip than e.g. earlier pre-stack time migrated sections of lines 1017 and 1018 (von Huene and Miller, 1988).

5.2.1 Reflection data from 12° S

Reflection seismic profiles from the area of the southern ODP Leg 112 transect include data acquired by Shell Oil Co. (The Hague) in 1972 (lines 1017, 1018), data acquired as part of the Nazca Plate Project (CDP 1) as well as some data recorded by the Hawaii Institute of Geophysics (HIG). The two Shell lines have been re-processed at GEOMAR. These two lines showed the best image of the subsurface due to a tuned airgun array, close CMP spacing and a relatively long streamer. Data acquisition parameters are given in table 3.

The enhanced images of lines 1017 and 1018 have been re-interpreted together with lines from the northern area to allow a reconstruction of development of the accretionary prism (von Huene et al.,

Line	CMP spacing [m]	no. of airguns	total airgun volume [l]	no. of channels	maximum offset [m]
1017, 1018	25	13	20	60	3186
CDP 2	33.5	4	43	24	1600
HIG 2-5	33.33	2	13	24	1691

Table 3: Data acquisition parameters of seismic lines from offshore Peru which were used for these investigations. CMP spacing of the HIG lines has been re-sampled to half the original spacing by trace interpolation to avoid spatial aliasing during pre-stack migration.

in press, ref. also section 5.3).

Line 1017

The seaward part of the southernmost line 1017, which was re-processed for the present study, is displayed in fig. 11. Interpretation of the seismic data presented here is based on work by von Huene et al. (1985a), von Huene and Miller (1988), and von Huene et al. (in press).

The trench lacks turbidite filling. Part of the $300 - 350m$ thick oceanic pelagic/hemipelagic section is underthrust beneath the accretionary prism. The prism itself is characterized by a relatively steep dip of the seafloor and sequences of landward dipping reflections which can be traced down to about $1.5km$ below the seafloor. This pattern extends towards the continent up to a landward dipping tectonic boundary. Reflections from the subducted oceanic plate, subducted sediments and some underplated sediments are clearly visible beneath and landward of the accretionary complex.

The adjacent lower slope terrace displays fewer coherent reflections, but some landward verging thrusts can be identified. Strong high-amplitude reflections at the base of this unit are characteristic for the Eocene sediments drilled at Site 688. High amplitude reflections beneath the inferred Eocene sediments probably mark the top of a high velocity metamorphic complex presumed to be composed of similar rocks as drilled in the Ballena and Delfin bore holes as well as those dredged at 9° S (Kulm et al., 1988). This section is most probably identical with the low to high velocity boundary (up to about $5km/s$) observed in refraction data further north (Hussong and Wipperman, 1981). These data show a further gradual increase of velocities landward which might indicate that the complex beneath the lower slope terrace is fractured (Hussong et al., 1988). The exact location of the seaward boundary of this complex cannot be resolved from the seismic data, although a buttress is clearly marked by relatively continuous reflections dipping about 25°. Internal structures within this block are consistent with its inferred metamorphic character. Also, signs of some faults extending into the crystalline basement might be observed. A strong BSR is present beneath the lower slope terraces about $300 - 600m$ below the seafloor. Note that the track of this profile is not perpendicular to the trench axis. Therefore, horizontal distances have to be multiplied by 0.9 (i.e. $cos(25°)$, where 25° is the angle between the track of this profile and a line perpendicular to the trench axis) before comparing structures with e.g. line 1018.

Line 1018

Line 1018, re-processed for the studies of von Huene et al. (in press), is located close to the ODP Leg 112 southern transect. In principle, it shows the same structural features as line 1017. Fig. 12 displays the seaward part of a pre-stack migrated section of line 1018, which is located close to Leg 112 drill sites.

Thrust packages at the accretionary prism thicken at the base of the slope, which indicates that turbidites enter the trench. Landward dipping reflectors mark the accretionary wedge, the boundary of which is better resolved than in line 1017. The buttress again is characterized by reflections dipping about 25°. Landward verging thrusts beneath the lower slope terrace are better imaged than in line 1017, which

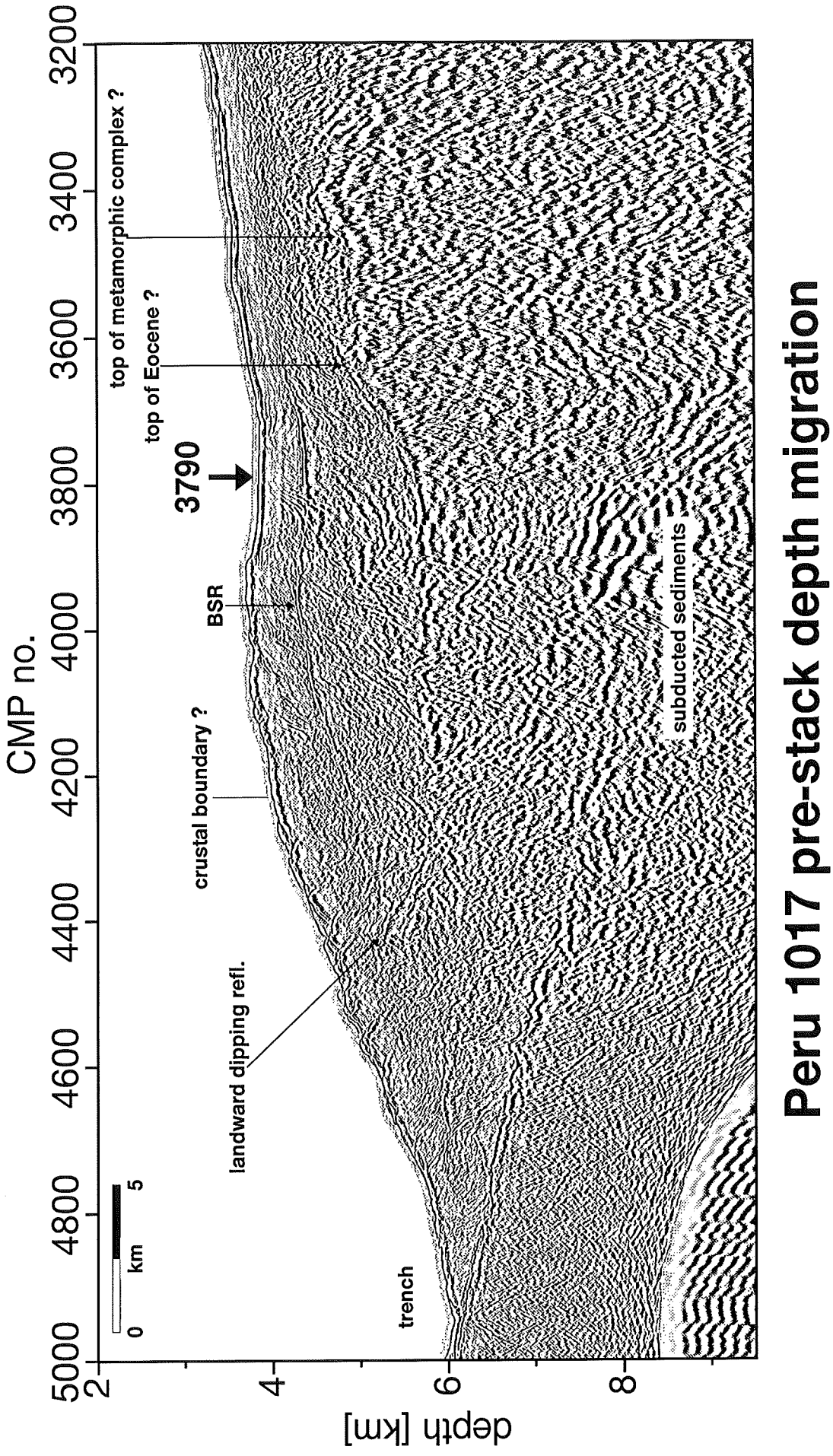

Figure 11: Pre-stack depth migrated section of the seaward part of Peru line 1017. CMP spacing is $25m$, vertical exaggeration is 3, AGC window is $1s$. The numbered arrow indicates the location at which the velocity structure of the BSR was investigated.

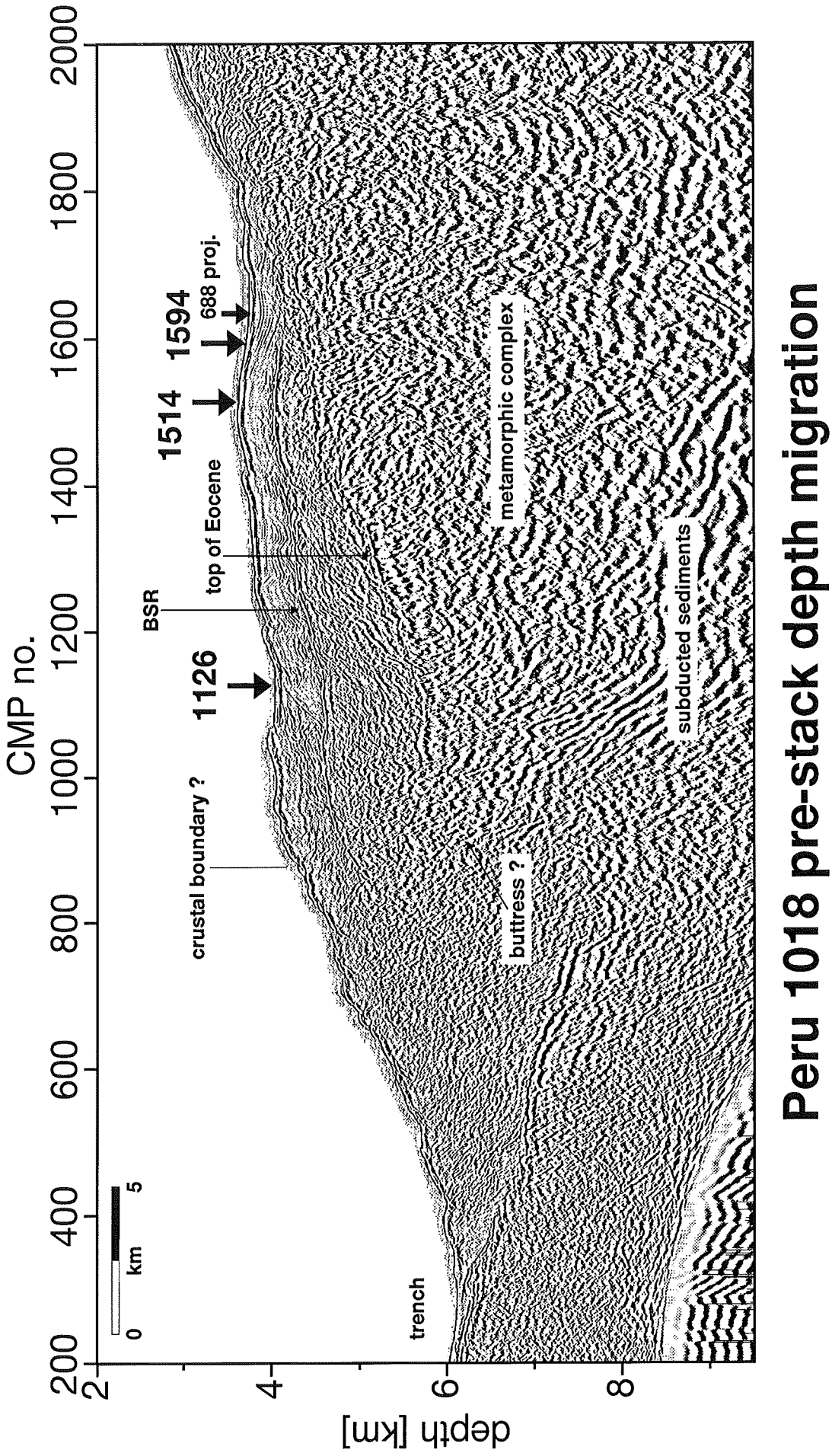

Figure 12: Pre-stack depth migrated section of the seaward part of Peru line 1018. CMP spacing is $25m$, vertical exaggeration is 3, AGC window is $1s$. Numbered arrows indicate locations at which the velocity structure if the BSR was investigated. Site 688 was drilled during ODP Leg 112.

gives clear evidence for compression. Eocene sediments at the base of the lower slope terrace were drilled at Site 688. This section of clastic shallow water sediments causes high-amplitude reflections above the metamorphic complex. Again, the exact position of the seaward termination of this complex cannot be resolved. Internal structures within this block as well as possibly some faults might be observed in the data. A strong and continuous BSR cuts sedimentary horizons all along the lower slope terrace.

The boundary between lower slope terrace and middle slope is marked by a distinct change in angle of dip at the sea floor. Normal faults are prevalent at the middle slope throughout sedimentary sequences which appear to extend into the metamorphic complex.

5.2.2 Reflection data from 9° S

Four seismic profiles from the area of the northern Leg 112 transect have been re-processed at GEOMAR, lines CDP 2, HIG 2, HIG 3, and HIG 5 (fig. 7). CDP 2 was acquired in 1973 in conjunction with the Nazca Plate Project. It turned out to be located across a laterally displaced basement ridge, which distorted 2-d seismic images. Therefore, several lines shot by the HIG as a part of ODP Leg 112 site surveys (Moore and Taylor, 1988) are used to show typical sections from this area.

The seaward part of CDP 2 (fig. 13) shows that the trench is filled with about $900m$ thick sediments. Landward dipping reflectors at the lower slope mark the accretionary complex (ref. also fig. 15). Buttress reflectors dip about 25° landward. Beneath the wedge, the oceanic plate is clearly imaged by high-amplitude reflections. A small ridge is currently being subducted. The presence of continental crystalline rocks is inferred from both refraction velocities and dredging of metamorphic rocks at the lower slope (Kulm et al., 1988). The BSR at the lower slope is confined to the accretionary wedge unlike in the area of the southern transect, where it is prominent further upslope.

At the upper slope in Yaquina Basin, Site 683 allowed a stratigraphic calibration of reflections in Yaquina Basin (fig. 14). The Oligocene hiatus may be traced well into Yaquina basin as a prominent unconformity. Metamorphic rocks were sampled by dredging slightly further upslope at the seaward flank of Trujillo Basin. A BSR can be clearly identified in the Yaquina Basin.

Only the seaward parts of profiles HIG 2, HIG 3, and HIG 5 have been pre-stack depth migrated. Due to low airgun volumes, larger CMP spacing and a relatively short streamer, penetration was less and data quality did not allow focusing analyses at reflections deeper than about $1km$. Therefore, velocity information from CDP 2 was utilized to form MIGPACK velocity models for the HIG lines. A structural interpretation of these sections is presented in fig. 15.

5.3 Development of the accretionary prism

The north to south movement of the crest of Nazca Ridge along the trench accompanied by erosion of the accretionary wedge and followed by the formation of a new wedge allowed a reconstruction of the development of the accretionary wedge in time (von Huene et al., in press). The structural images at 12° S and 9° S represent stages in the development of the wedge 4 and $6m.y.$, respectively, after subduction and the onset of accretion. Fig. 16 shows the principle stages of wedge development.

Between the first two stages (0 and $1-3m.y.$), the prism grew rapidly. The wedge beneath the apex of the margin was underplated. A lower slope terrace developed. The stage between $4-6m.y.$ is documented by lines 1017 and 1018. The margin wedge was uplifted causing back-thrusting. Above the uplifted margin wedge apex, a lower slope terrace was enlarged. The subduction fraction increased. At the final stage about $7-9m.y.$, accretion was arrested. Slope sediment covered most of the accretionary wedge. The margin wedge apex has reached a stable position.

An important aspect of these studies is the rapid decrease of the accreted fraction of sediments and thus, the increase of the subducted fraction. This fraction could be estimated because enhanced

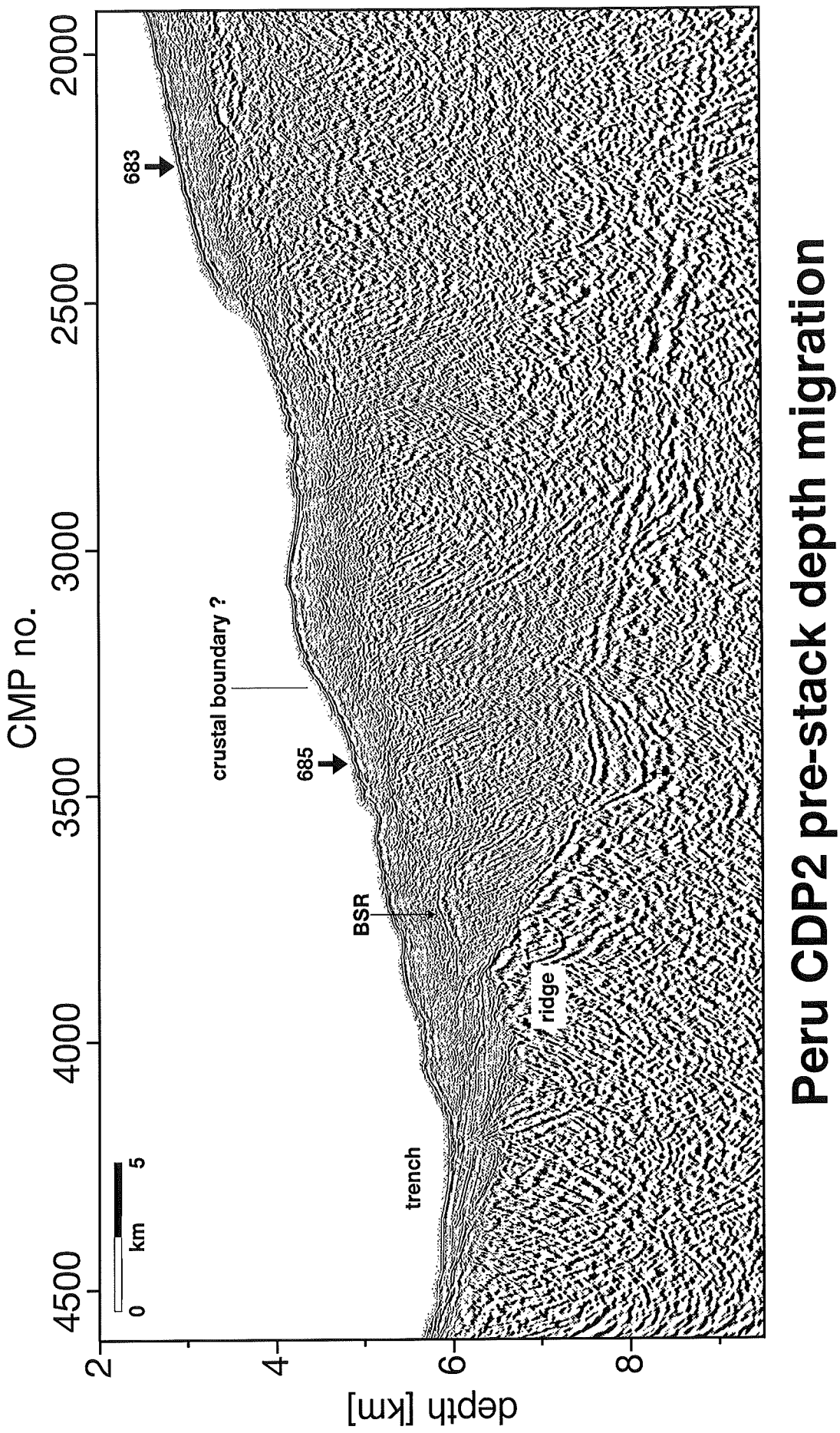

Figure 13: Pre-stack depth migrated section of the seaward part of Peru line CDP 2. CMP spacing is $16.75m$, vertical exaggeration is 3, AGC window is $1s$. Sites 685 and 683 were drilled during ODP Leg 112. The location of the crustal boundary is relatively well constrained. Note the subducted ridge beneath the accretionary wedge.

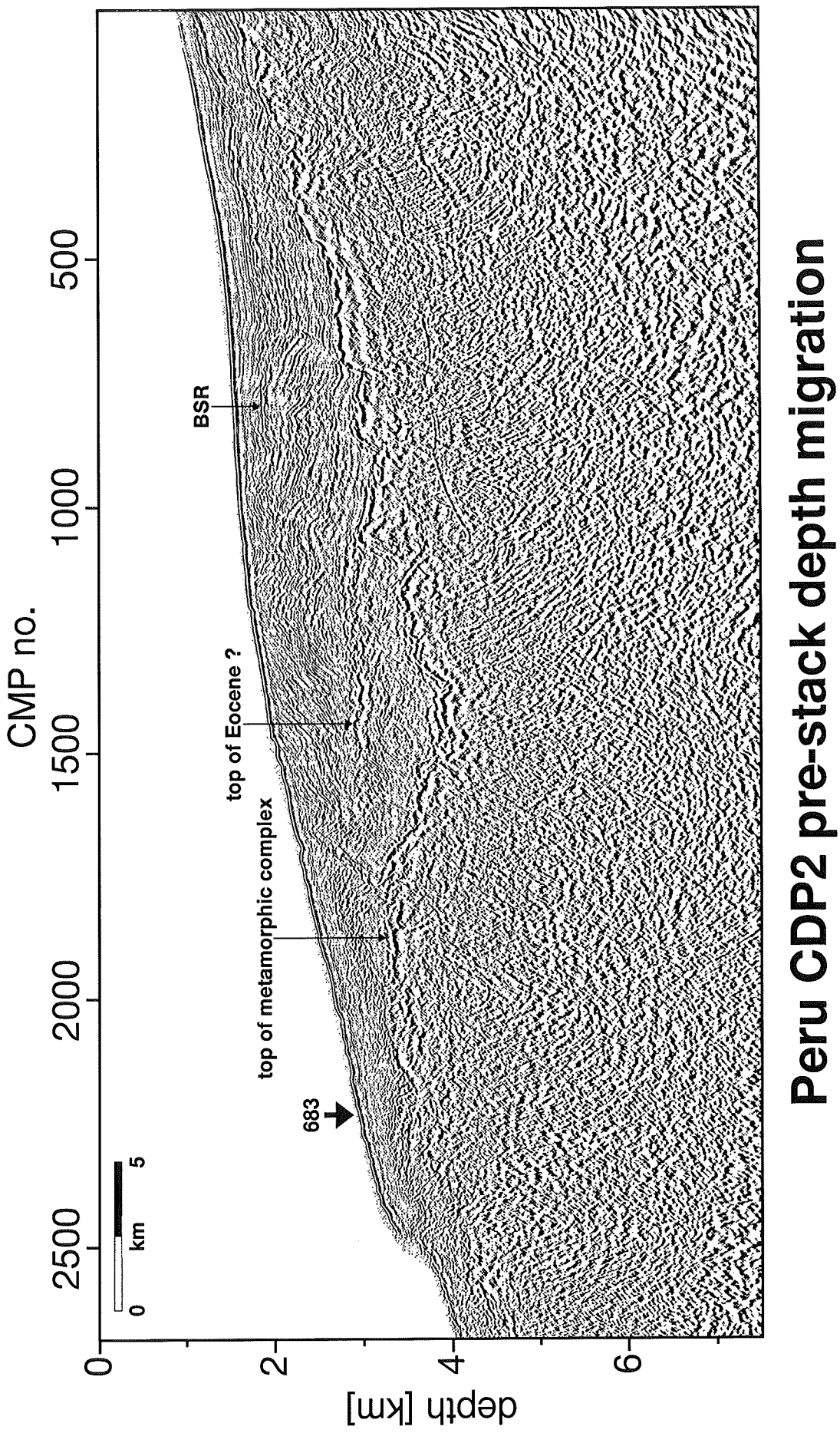

Figure 14: Pre-stack depth migrated section of the landward part of Peru line CDP 2. CMP spacing is $16.75m$, vertical exaggeration is 3, AGC window is $1s$. Site 683 was drilled during ODP Leg 112.

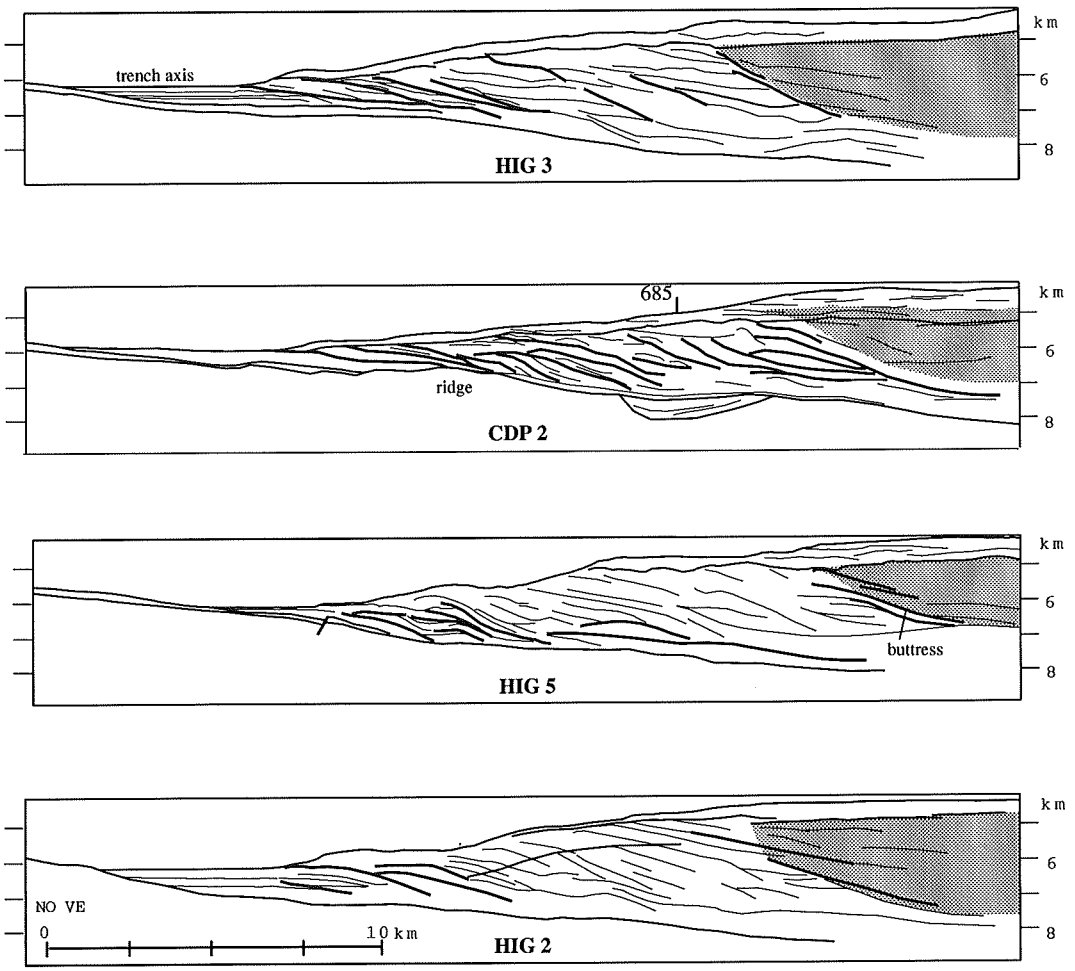

Figure 15: Line drawings of coherent reflectors from the profiles from the lower slope area at 9° S. The higher velocity buttress is shown in gray. From von Huene et al. (in press).

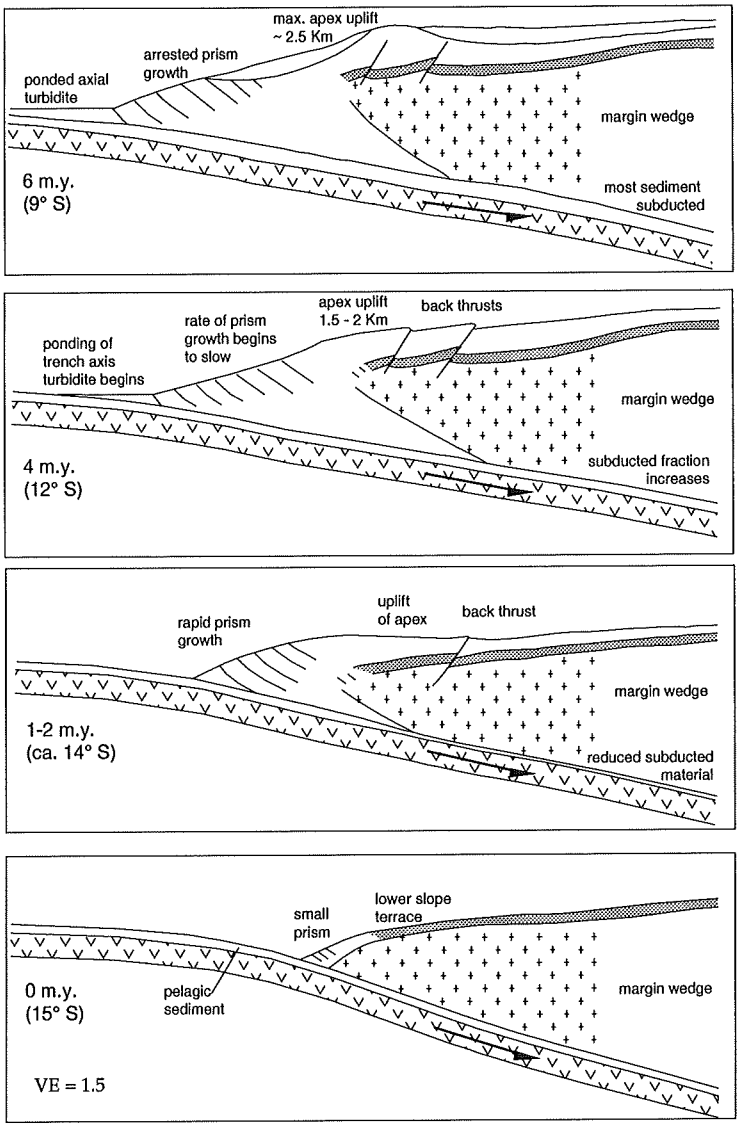

Figure 16: Four stages of the development of an accretionary wedge. The elapsed time after subduction corresponds to distance along the margin from the present location of the crest of Nazca Ridge, i.e. 15° S. The stage of $1-2m.y.$ is inferred. From von Huene et al. (in press).

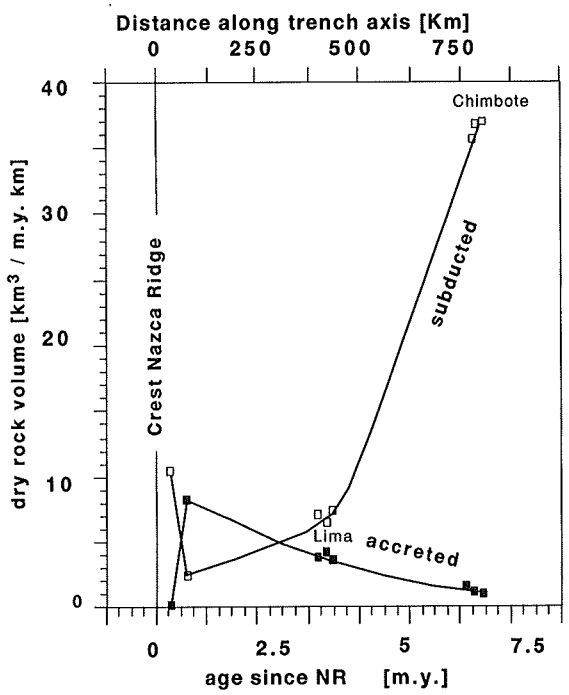

Figure 17: Top: Fraction of accreted and subducted sediments per m.y. as a function of distance from the crest of Nazca ridge and subsequently elapsed time after its subduction. Squares indicate approximate positions of the seismic lines (from left to right: 1017, 1018, CDP 1, HIG 2, HIG 5, HIG 3) used for these computations. CDP 2 was not suitable for volumetric considerations due to distortions caused by subduction of a small ridge. After von Huene et al. (in press).

seismic images allowed a reconstruction of sediment volumes within the accretionary wedge. This is illustrated by fig. 17. Despite an increased trench sediment supply, the accreted portion of sediments within the wedge decreases from about 60% to about 30% (von Huene et al., in press). Subsequently, the amount of subducted sediment per unit time increases and it is considerably larger at 9° S than at 12° S.

5.4 Organic carbon, hydrocarbon gases and gas hydrates

Sediments in cores from the Peru upwelling area are characterized by a high carbon concentration (e.g. von Breymann et al., 1990), which is common for upwelling regions. Organic carbon in the lower slope sediments usually exceeds about 2% reaching values up to 12%. The chemistry of hydrocarbon gases and gas hydrates was investigated at all ODP Leg 112 sites (Kvenvolden et al., 1990; Kvenvolden and Kastner, 1990). The concentrations of higher-molecular-weight hydrocarbons (C_2, C_3, $i-C_4$, and $n-C_4$) tend to increase with depth at all sites, however methane (C_1) in general constitutes more than 99% of hydrocarbon gases. This gives evidence for a microbial and early thermal formation of methane supporting the model of biogenic methane generation (Claypool and Kaplan, 1974).

Gas hydrates were recovered at Site 685 and at Site 688. At Site 685, they occurred at 99 mbsf and 166 mbsf as dark grey pieces which resembled mudstone. They felt cold to the touch and a bubbling foam could be seen at the edges. The volumetric ratio of methane to water was determined as 100 at one of the samples at 166 mbsf, which indicated either undersaturation or partial decomposition during core recovery (Kvenvolden and Kastner, 1990). At Site 688, gas hydrates were detected at about $141 mbsf$ in samples, which were composed of a mixture of gas-hydrates and dark-grayish black mud (Kvenvolden and Kastner, 1990).

Isotopic investigations of these gas hydrate samples confirmed the assumption of a mainly biogenic formation. $\delta^{13}C$ values were -65.0 and -59.6 $^{o}/_{oo}$ PDB in hydrate samples from Sites 685 and 688, respectively.

Water from gas hydrates should be devoid of salts. Chlorinity and salinity of liquid water formed during decomposition of one of the Site 685 samples were only about 9% and 11%, respectively, of that of sea water. Therefore, the decrease in chlorinity with depth, which can be observed at all the four lower slope sites, (fig. refchlorinity) indicates the presence of hydrates also at the two sites, where no direct evidence for gas hydrates was found (Kvenvolden and Kastner, 1990). Hydrates probably dissociated during core recovery and due to the time required for core preparation.

5.5 BSR analysis

The velocity structure of the BSR in line 1018 was first investigated by Miller et al. (1991) using a zero-offset wavelet modeling technique on stacked data. Except for one of the nine investigated locations, synthetic and real data matched best if a free gas layer is assumed at the BSR having a thickness of $5.5 - 17m$. The velocity structure was interpreted as indicating a concentration of at least 10% free gas in the pore space. At the location closest to the landward termination of the BSR, no evidence for the presence of free gas was found (ref. fig. 18).

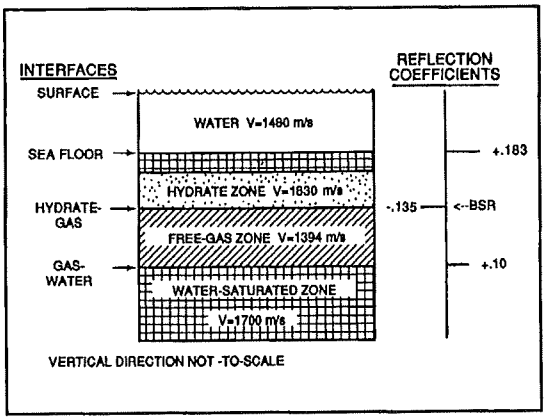

Figure 18: Seismic model at the BSR used by Miller et al. (1991) for investigating the velocity structure at the BSR. Thickness of the presumed gas layer was varied in order to obtain an optimum fit of real and synthetic data.

5.6 Heat flux

During site surveys and ODP Leg 112, heat flux values were determined (Yamano and Uyeda, 1990). Downhole measurements were compared to values obtained in 1985 using heat probes and older data. Yamano and Uyeda (1990) also applied the method of determining heat flux from the depth of the BSR which they had applied previously to data from the Middle America Trench (Yamano et al., 1982).

Measurements of heat flux at Sites 685 and 688 are of particular interest for the present investigations, because of the proximity of those locations to BSRs. At Site 685, temperature was determined from wireline logging at depths of 75 and $150mbsf$, at Site 688 using an advanced piston corer tool at $36.8mbsf$. Thermal conductivity was measured in sediment cores by applying the needle probe technique. Heat flux values from those measurements are listed in table 4. The discrepancy of heat flux within the depth ranges of $0 - 75mbsf$ and $75 - 150mbsf$, respectively, at Site 685 might be attributed to upward flow of pore water from the accretionary complex (Yamano and Uyeda, 1990). Such fluid venting

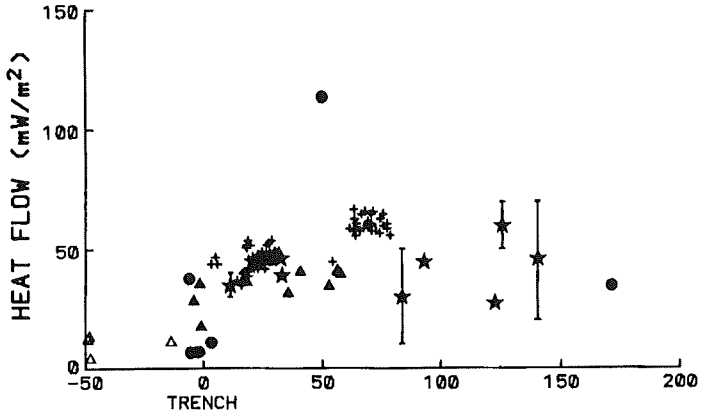

Figure 19: Compilation of heat flow values vs. distance from the trench obtained from heat flow probe measurements and in Leg 112 bore holes (stars). Closed and open triangles represent data obtained in 1985 and 1986, respectively, circles denote values from other measurements (Von Herzen, 1959; Von Herzen and Uyeda, 1963; Henry and Pollack, 1988). Crosses mark values obtained from the depth of the BSR. From Yamano and Uyeda (1990).

can increase surface thermal gradient, as observed e.g. on the Oregon accretionary wedge (Langseth and Hobart, 1984).

Site	depth range [mbsf]	heat flux $[mW/m^2]$
685	0-75	41
	75-150	28
688	0-36.8	46

Table 4: Heat flux from temperatures at Sites 685 and 688. Temperature at 0 mbsf is the bottom-water temperature. After Yamano and Uyeda (1990).

Heat flux data are plotted as a function of distance from the trench in fig. 19. The general pattern resembles that of other subduction zones (Yamano and Uyeda, 1988). Relatively low heat flux prevails at the trench. It increases rapidly towards the continent, reaching values of about $40-50mW/m^2$ at the slope. A decrease was observed again close to the continent at water depths of between $200-2000m$ which might be attributed to poor measurements: probe measurements might be unreliable above approximately $2500m$ depth due to temporal variations of bottom water temperature (Yamano and Uyeda, 1990). On the other hand, those values compare relatively well to on-shore data (Yamano and Uyeda, 1990).

6 Geology of the convergent margin off Costa Rica

6.1 Tectonic setting and bathymetry

At the Costa Rican Pacific margin, Cocos and Pacific Plates are subducted beneath the Caribbean Plate. Two centers of crustal generation formed the oceanic crust off Costa Rica: the northwest part was generated at the East Pacific Rise, whereas the southeast part was formed along the Cocos spreading center or the Galapagos Rift (Lonsdale and Klitgord, 1978). Fisher Seamount was extruded along the boundary of the two crustal provinces (von Huene et al., 1995), the so-called the "rough-smooth" boundary (Hey, 1977). Cocos Ridge is a third element and was formed by the Galapagos Hotspot.

During R/V "Sonne" cruises SO-76 and SO-81 in 1991 and 1992, swath-mapping and seismic

Line	CMP spacing [m]	no. of airguns	total airgun volume [l]	no. of channels	maximum offset [m]
Costa Rica 5, 8, and 9	25	20	51.2	48	2475

Table 5: Data acquisition parameters of seismic lines from offshore Costa Rica acquired during "Sonne" Legs SO-76 and 81.

studies were conducted in this area (Hinz et al., 1992). Three domains can be clearly delineated at the oceanic plate from seafloor morphology (fig. 20), which are mirrored by bathymetry further upslope. Northwest of Fisher Seamount, the smooth Pacific Plate is subducted opposite of Nicoya Peninsula leading to a relatively smooth morphology of the continental slope. The adjacent area of the oceanic plate to the southeast is covered with seamounts. The continental slope there is more rugged. Scars within the slope relief probably mark traces of subducted seamounts (von Huene et al., 1995). Further to the southeast, Cocos Ridge uplifts the margin at Osa Peninsula.

6.2 Seismic studies

6.2.1 Reflection seismic lines 8, 9, and 5

Seismic lines Costa Rica 8 and 9 are located northwest of Fisher Seamount and are relatively close to DSDP Site 565. Figs. 21 and 22 display migrated sections of these lines. Data acquisition parameters are given in table 5. Line 5 was acquired southeast of Quepos Plateau (fig. 23).

Interpretation of those lines follows Hinz et al. (in press). The oceanic plate is displaced along normal faults being flexed downward as it enters the trench. The igneous crust can be identified as a strong reflector, at which the character of reflectivity changes from sub-horizontal relatively continuous horizons to diffuse reflections. This boundary can be traced well beneath the accretionary complex. The accretionary prism is characterized by a series of landward dipping reflectors. Its landward termination can be delineated by a wedge-shaped unit, the top of which is marked by high-amplitude reflections. Three main seismic units characterize the middle and upper slope (Hinz et al., in press): (1) The slope sediments, which extend from the seafloor down to a strong and irregular horizon, the so-called "rough surface" (e.g. Shipley et al., 1992), (2) the margin wedge, a unit from the rough surface down to a sequence of sub-horizontal layered reflections, which displays a wedge-shaped cross-section towards the accretionary prism, and (3) a unit of layered high-amplitude reflections. The latter unit is interpreted as subducted sediments (Hinz et al., in press). The nature of the second unit, the margin wedge between the rough surface and the subducted sediments, is still controversial and a key question with regard to tectonic evolution of this part of the margin. Strong and continuous BSRs can be identified in the three profiles almost all over the slope down to the accretionary prism.

6.2.2 Nature of the rough surface

The Guatemalan margin was drilled down to a basement reflector similar to the rough surface which is observed off Costa Rica (von Huene et al, 1985b). Ophiolitic rock was recovered which lead to the conclusion that the Guatemala margin is largely composed of accreted ophiolite. Site 565, which was drilled off Nicoya Peninsula, did not penetrate the whole sedimentary section. However based on the results from the Guatemalan margin, von Huene et al. (1985) interpreted the rough surface in seismic sections from this region as a continuation of the Nicoya ophiolite, Jurassic to Cretaceous oceanic rocks that crop out on-shore. This hypothesis would require a change of tectonic processes since Eocene times, when the Nicoya Peninsula was uplifted form abyssal to neritic depth.

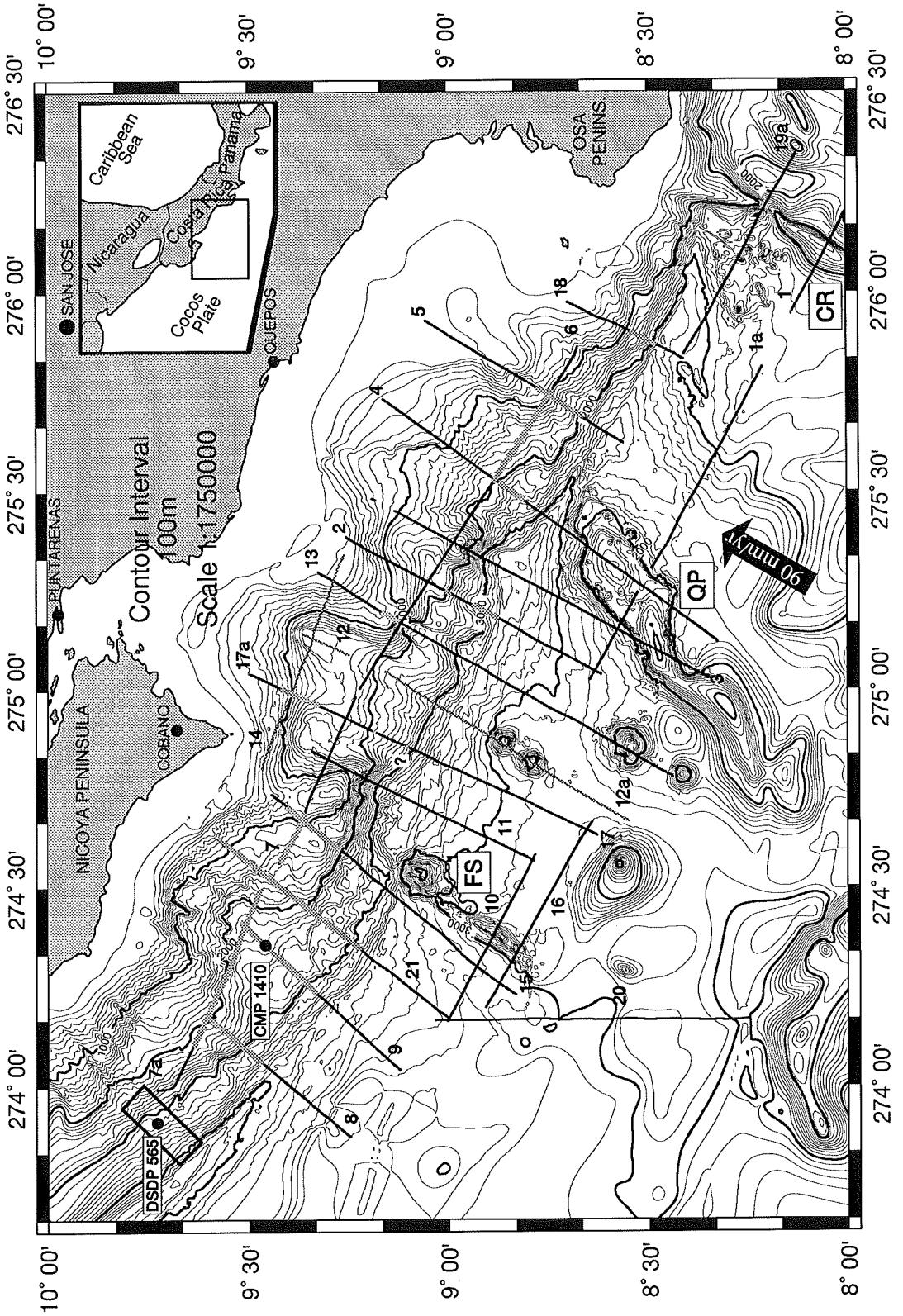

Figure 20: Tectonic setting, bathymetry, tracks of seismic lines, and occurrence of BSRs offshore Costa Rica. CR: Cocos Ridge, FS: Fisher Seamount, QP: Quepos Plateau. Site 565 was drilled during DSDP Leg 84 and the surrounding box denotes the location of a 3-d data set (Shipley et al., 1992). Lines mark tracks of seismic profiles acquired during "Sonne" cruise SO-76 and SO-81. Processing of lines 12, 12a, and 14 (in grey) has not yet been finished. Thick grey lines indicate sections in which BSRs could clearly be identified. The velocity structure of the BSR in line 9 was investigated at CMP 1410. After Hinz et al. (in press).

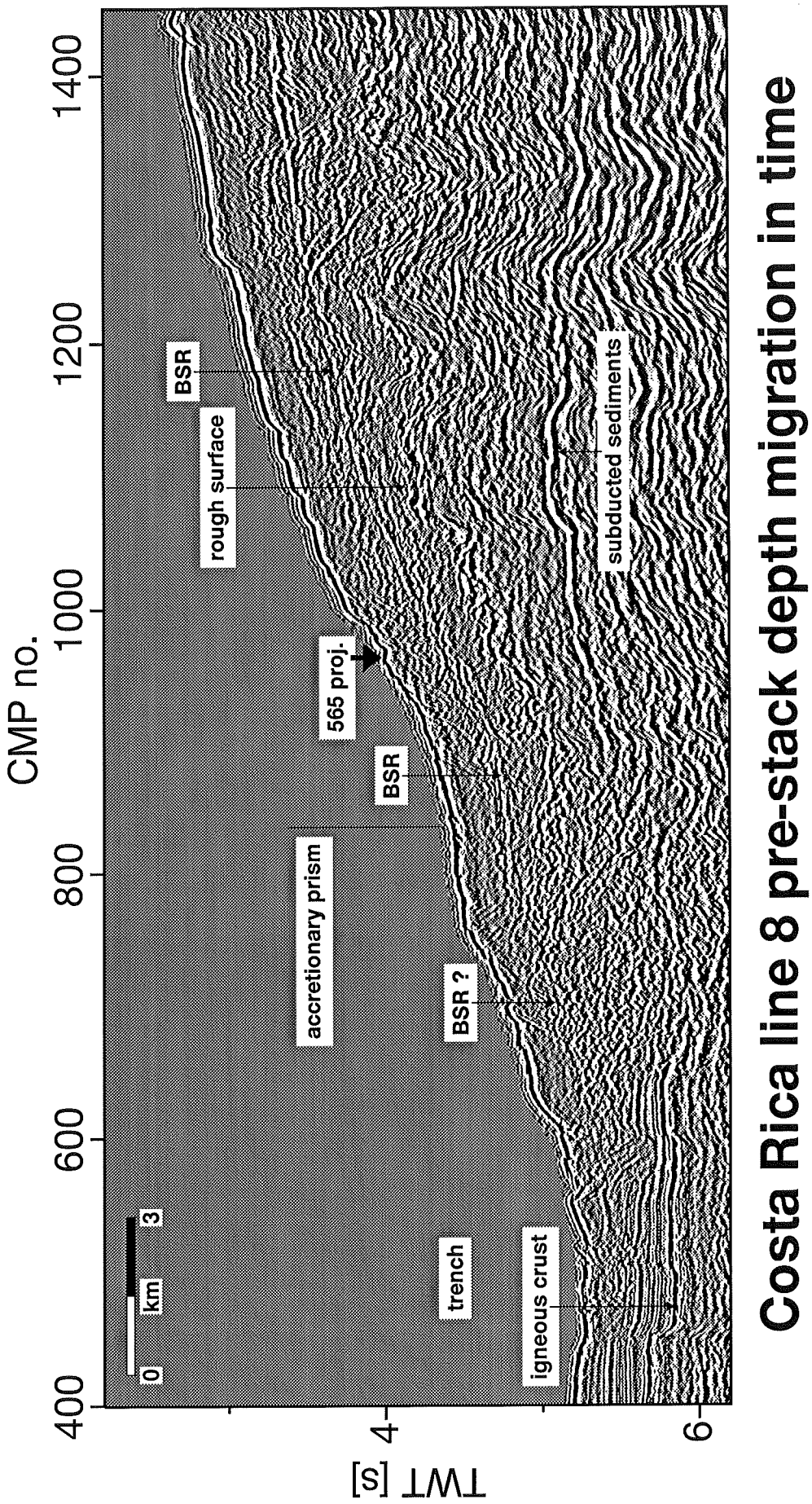

Figure 21: Pre-stack depth migrated section re-stretched to time of the landward part of Costa Rica line 8. CMP spacing is $25m$, AGC window is $1s$. Site 565, the location of which is projected into this line, was drilled during DSDP Leg 565. After Hinz et al.(in press).

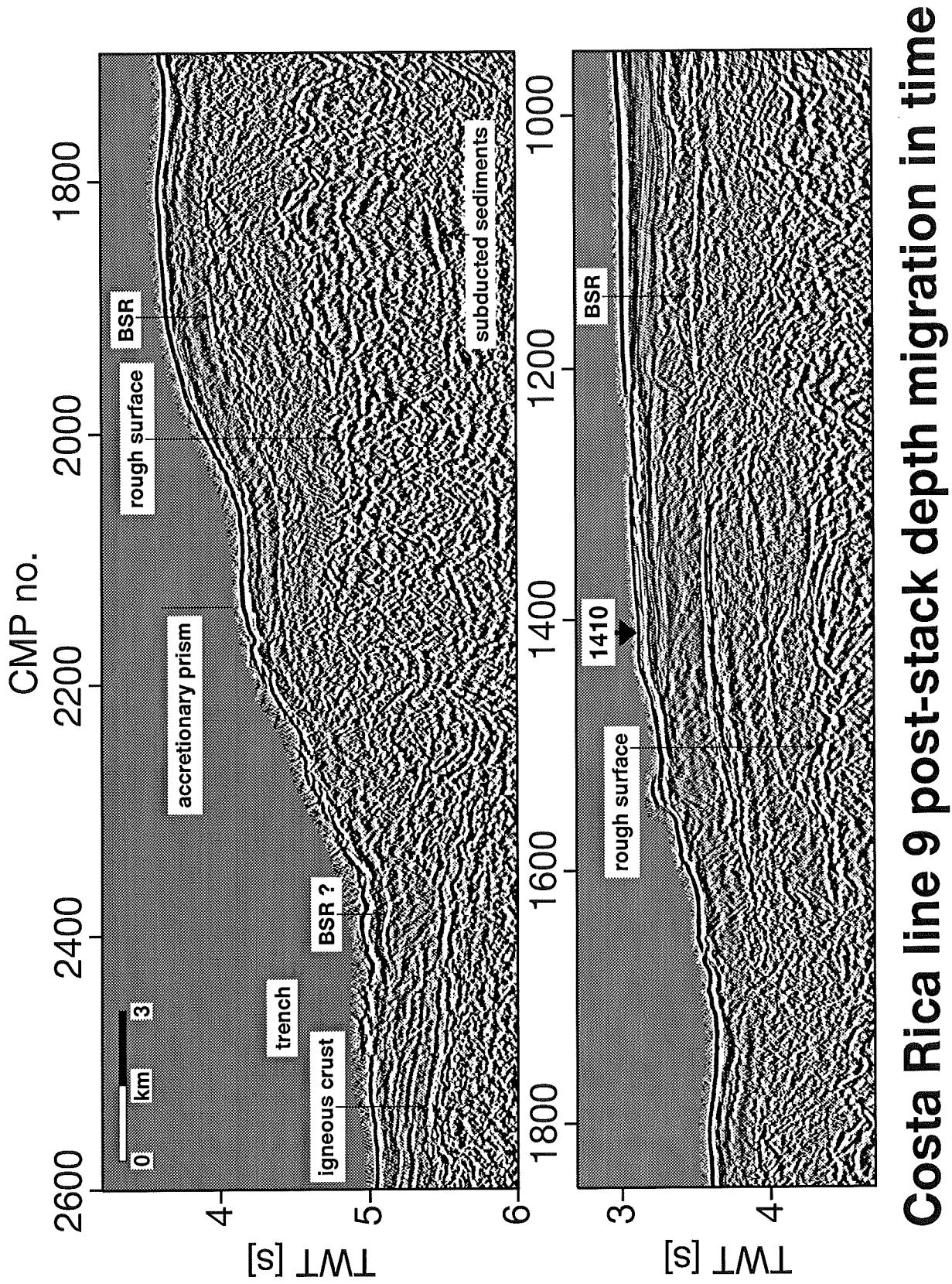

Figure 22: Post-stack depth migrated section re-stretched to time of the landward part of Costa Rica line 9. CMP spacing is $25m$, AGC window is $1s$. After Hinz et al.(in press).

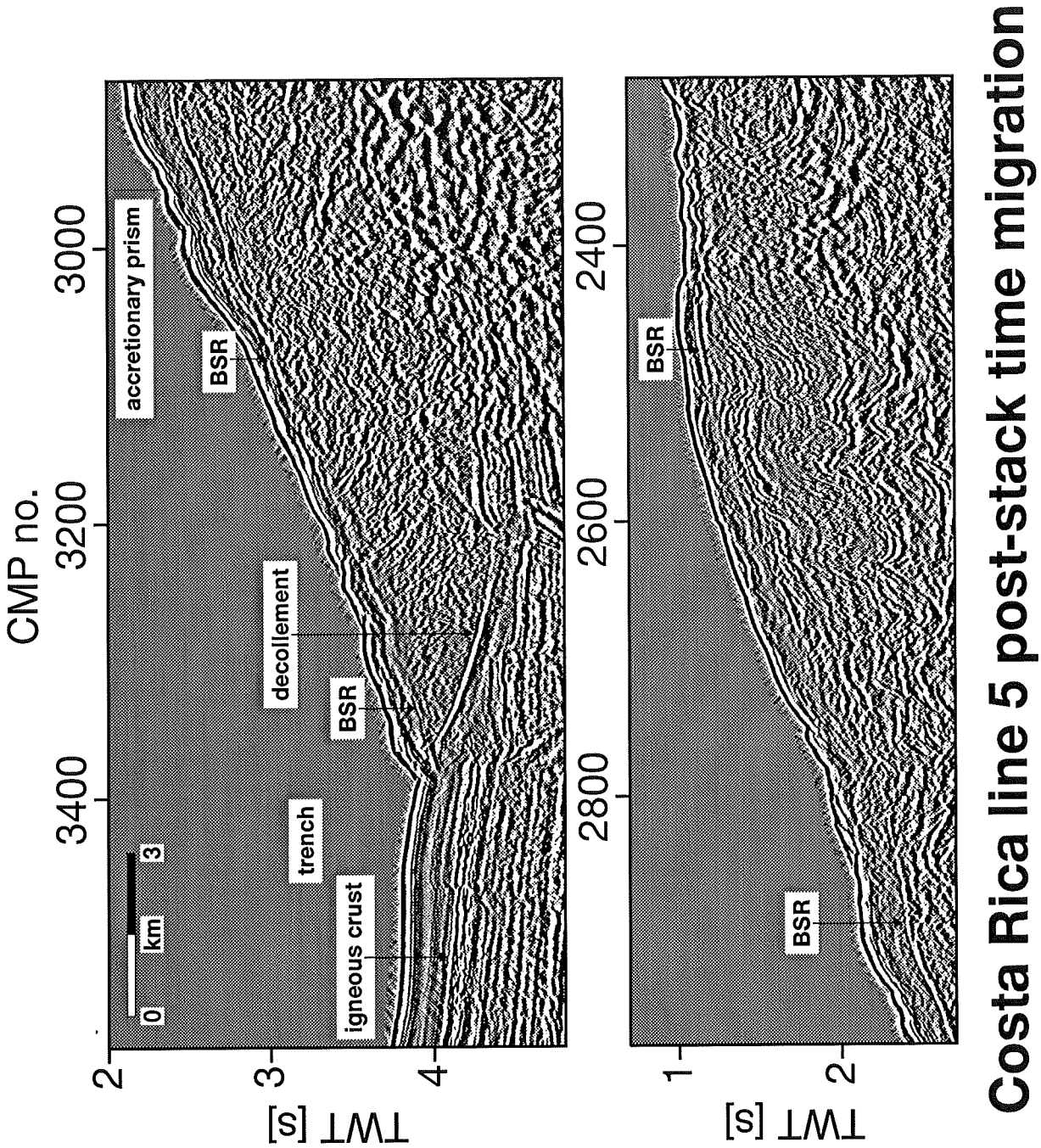

Figure 23: Post-stack time migrated section of the seaward part of Costa Rica line 5. CMP spacing is $25m$, AGC window is $1s$. After Hinz et al.(in press).

Alternatively, Shipley et al. (1992) interpret the margin wedge in a 3-d seismic record as an old accretionary wedge consisting of consolidated offscraped and underplated oceanic Eocene to Quaternary sediments. This model would imply a steady-state tectonic history since Eocene times.

Velocity information from refraction seismic data acquired during "Sonne" SO-76 expedition could not resolve this ambiguity: The velocity contrast at the rough surface from $2.0 - 2.5 km/s$ to over $4.5 km/s$ (Ye et al., in press) could be interpreted as a boundary between sediments and ophiolitic rock as well as a transition from relatively soft slope deposits overlying a body of highly consolidated accreted sediments. Hinz et al. (in press) favor the interpretation of the rough surface as being an extension of the Nicoya ophiolite, mainly because no boundary can be identified in seismic data between this ophiolitic complex and a presumed old accretionary wedge and because almost no landward dipping structures typical for accretionary complexes are displayed in the seismic data beneath the rough surface. However, the authors stress that final conclusions are withheld until after drilling of the prospected ODP Leg 170 at the Costa Rican margin in late 1996.

6.3 DSDP Site 565: Sediment composition, hydrocarbon gases and gas hydrates

One of the objectives of Site 565 was to drill the rough surface in order to investigate the nature of the margin wedge. However drilling had to be stopped at $328 mbsf$ because of the occurrence of gas hydrates. Down to this depth, Pliocene-Pleistocene sediments of generally massive dark olive gray to dark greenish gray mud and mudstone were recovered.

Organic carbon at this site in general was $0.5 - 2\%$. Concentration of C_1 - C_3 in hydrocarbon gases suggested a mainly microbial source for the formation of methane, though a general increase of higher-molecular-weight hydrocarbons with depth indicated additional lower-temperature diagenetic production at greater depths (Kvenvolden and McDonald, 1985).

Gas hydrates were recovered during Leg 84 at Sites 565 (off Costa Rica), 568, and 570 (both off Guatemala). They were encountered at Site 565 at 285 and $319 mbsf$ as white ice-like pieces. The sample from the lower position was chemically analyzed: decomposition of the sample released about 133 volumes of C_1 per volume of pore fluid. The amount of C_1 was more than 30 times higher than its solubility under in-situ conditions. Chlorinity of the pore fluid was only 0.051%. C_1/C_2 was 2000 (Kvenvolden and McDonald, 1985)). Close to the position of this hydrate sample, gas-releasing muddy sandstone was recovered, which probably contained hydrates.

6.4 Heat flux

Heat flux measurements were performed by Langseth and Silver (in press) during cruise A-131 of R/V "Atlantis II" in 1994 off Costa Rica using the 4 m long WHOI digital heat flow instrument. With the same instrument, thermal conductivity was measured in situ at each thermistor position using the continuous line source method. Several dives of D/V "Alvin" were conducted during this campaign. $1m$ temperature probes equipped with 5 thermistors could be deployed from the submersible. Within the area surveyed for Leg 170, profiles were measured approximately along strike at several given distances from the trench. Additional measurements were taken along the seismic profile Costa Rica line 8 (fig. 20), in which a BSR was observed.

A profile of heat flux versus distance from the trench axis is shown in fig. 24. In the trench, heat flux is extremely low, an average of $14 mW/m^2$. This is conflicting the value of about $100 mW/m^2$, which would be expected over $20 Ma$ oceanic crust currently subducted at this margin (Klitgord and Mammerickx, 1982). Heat flux then increases rapidly towards the continent until reaching values of about $30 mW/m^2$, which is still relatively low compared e.g. to the Peruvian margin.

The authors explain this low heat flux by thermal cooling of the upper oceanic crust down

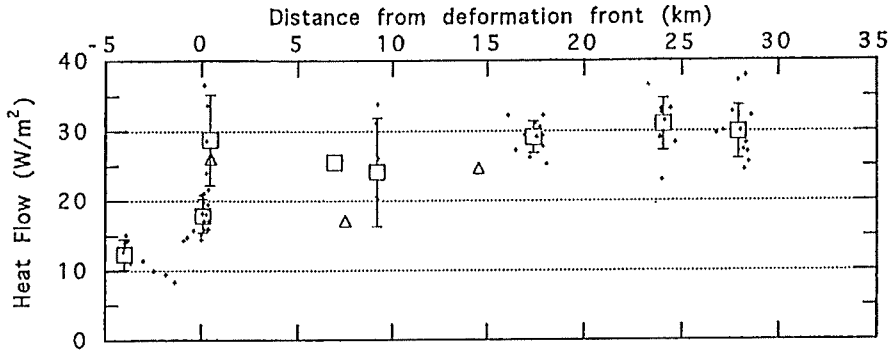

Figure 24: Heat flux vs. distance from the trench off the Nicoya Peninsula. The locations are approximately in the area of the seismic 3-d survey. Individual measurements are shown as dots, means of groups of measurements at a given distance from the trench axis as squares. Triangles are measurements obtained during dives of D/V "Alvin". Error bars are from computation of standard deviations. From Langseth and Silver (in press).

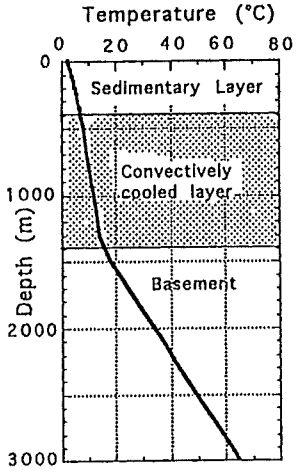

Figure 25: Temperature profile within oceanic crust cooled by the "sea water heat exchange" mechanism. From Langseth and Silver (in press).

to $400 - 1000mbsf$, the "sea water heat exchange" mechanism: Cold sea water enters the upper crust at basement exposures and flows horizontally absorbing heat before exiting again (e.g. Langseth et al., 1992). This leads to a decrease of the temperature gradient at shallower depths (fig. 25). Langseth and Silver also simulated the thermal regime at this margin using the modeling concept of Ferguson et al. (1993). This model explains both low heat flux values in the trench and the rapid increase landward. The authors point out that frictional heating at the décollement plays a major role in heat flux at the lower slope.

Further to the southeast, 7 measurements were conducted along Costa Rica line 8 from the $2760 - 2120m$ isobath (i.e. between CMPs 990 and 1260 in fig. 21), corresponding to distances of about between 17 and $24km$ from the trench. An average value of $46.2mW/m^2$ was measured with a standard deviation of about $4.1mW/m^2$. This value is considerably above heat flux values at the same distance from the trench in the survey area further to the north (ref. fig. 24), something, which Langseth and Silver (in press) attribute to increased frictional heating at the décollement.

7 Nature of BSRs off Peru and Costa Rica

7.1 Full waveform inversion scheme applied to Peru line 1018 CMP 1126

The waveform inversion scheme will be illustrated using a location along Peru Shell line 1018 as an example. Three locations were chosen for waveform inversion along this line, although it already had been investigated by applying a zero-offset modeling technique (Miller et al., 1991), because drilling might take place in this area. The limitations of the earlier zero-offset modeling approach include: (1) Offset-dependent information was lost by stacking. Only zero-offset reflection coefficients were used, which depend on the seismic impedance (i.e. velocity multiplied by density) contrast between two layers and do not permit absolute velocity determination of a single layer. Thus, this method allowed a determination of the velocity beneath the BSR only relative to the velocity of the hydrated layer above. (2) Another problem with stacking is, that if different reflectors (e.g. the sea bed and the BSR) have different amplitude variations with offset, their relative amplitudes when stacked will be a poor approximation to their relative amplitudes at zero-offset. (3) The forward modeling approach is subjective: It requires an input model from the interpreter who also performs changes in the model. Therefore, forward modeling cannot provide a quantitative measure of fitness of the real with synthetic data and may lead to a wrong final model, although for the Peruvian margin additional constraints were available from Leg 112 sites.

A location should meet the following criteria to be suitable for the 1-d full waveform inversion technique: (1) sea floor, BSR, and major reflectors should be sub-horizontal, and (2) they should be laterally continuous over at least the part of the profile through which seismic rays to the BSR travel at all offsets used for the inversion. Three CMPs, which matched those criteria, were chosen along line 1018 (ref. also fig. 12). At CMP 1126, reflectivity at the BSR appears to be strongest. Between CMPs 1514 and 1594, reflectivity decreases rapidly. Qualitatively, CMP 1514 might be regarded as "strong BSR", whereas CMP 1595 might be a typical "weak BSR" (ref. p. 14 for this classification). Comparing results from both locations may give evidence for the differences between these two suggested types of BSRs.

7.1.1 Data pre-processing

CMP 1126 was selected as a first suitable target off Peru. The BSR is characterized by its relatively strong amplitude. Fig. 26 displays a part of the pre-stack depth migrated section re-stretched to time around CMP 1126. CMP-gathers 1126 and 1127 were merged in order to get a CMP-super-gather which contains all shot-receiver offsets (which is referred to as CMP 1126 in the following text). Fig. 27 presents the neartrace and the raw CMP-(super)-gather 1126.

Fig. 28 displays energy of the signals from the sea floor together with the theoretical energy function to which the traces would be normalized if applying the method of amplitude recovery described in section B.1. The theoretical, i.e. deterministically computed, energy function, roughly follows the general trend of energy of the data. This indicates that the assumptions made for computing the theoretical energy and thus, amplitude correction factors, were realistic. This is important as waveform inversion implicitly accounts for AVO variations of reflections. In the Peruvian data (lines 1017 and 1018), only channel no. 54 ($1561m$ offset) displayed considerably lower amplitudes than the other channels. Therefore amplitudes of this channel were corrected by applying a trace normalization with respect to the two neighboring traces. Amplitudes of the other channels were not changed in order to reduce the risk of introducing an artificial AVO trend. However, since amplitudes in the Costa Rica data set varied much stronger, an amplitude recovery technique had to be applied to them. Therefore, it was important to test whether the assumptions behind this technique were reasonable as shown in fig. 28.

The amplitude spectra of neartrace and fartrace also displayed in fig. 28 show that the main frequencies of the signals are between 10 and $40Hz$. A bandpass filter of $5-50Hz$ was applied to eliminate high-frequency noise. The pre-processed CMP-gather and the data set in the (τ, p)-domain are shown in

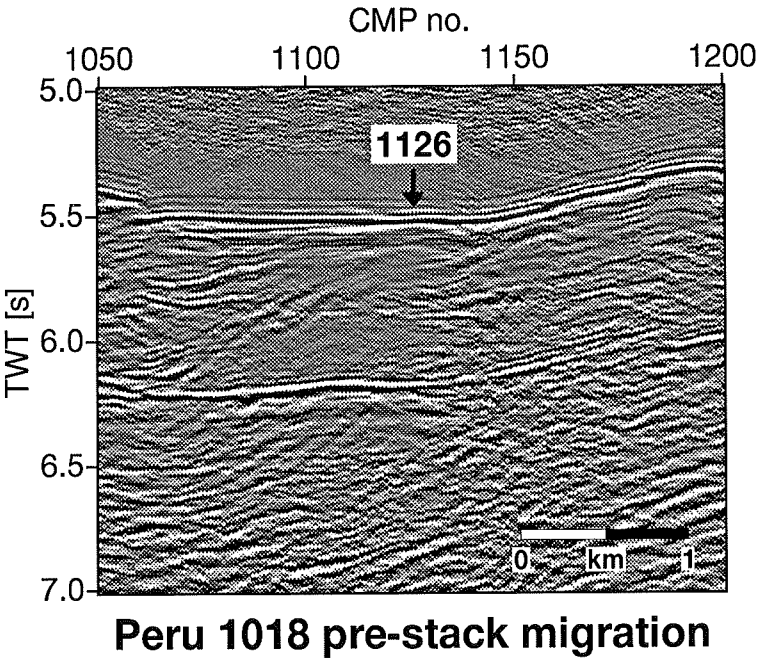

Figure 26: Pre-stack depth migrated section re-stretched to time of Peru line 1018 around CMP 1126. Processing included signature deconvolution. The AGC window is 1*s*. The arrow indicates the exact position of the location chosen for inversion.

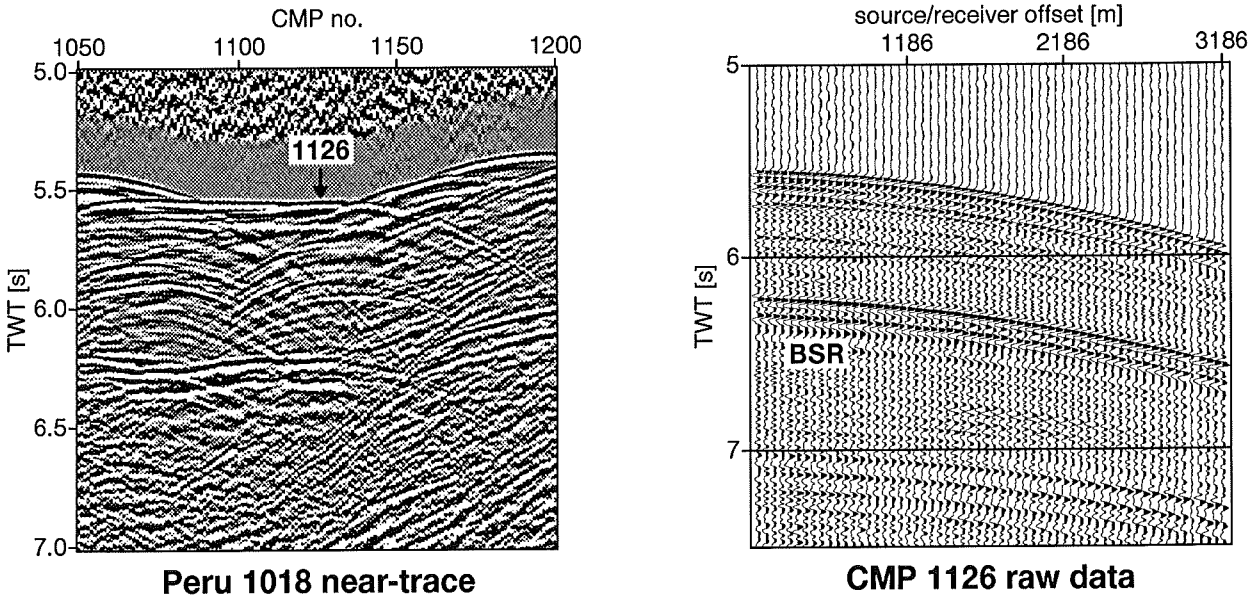

Figure 27: Neartrace and CMP 1126 super-gather of raw data. No AGC was applied for plotting. The arrow in the neartrace indicates the exact position of the location chosen for inversion.

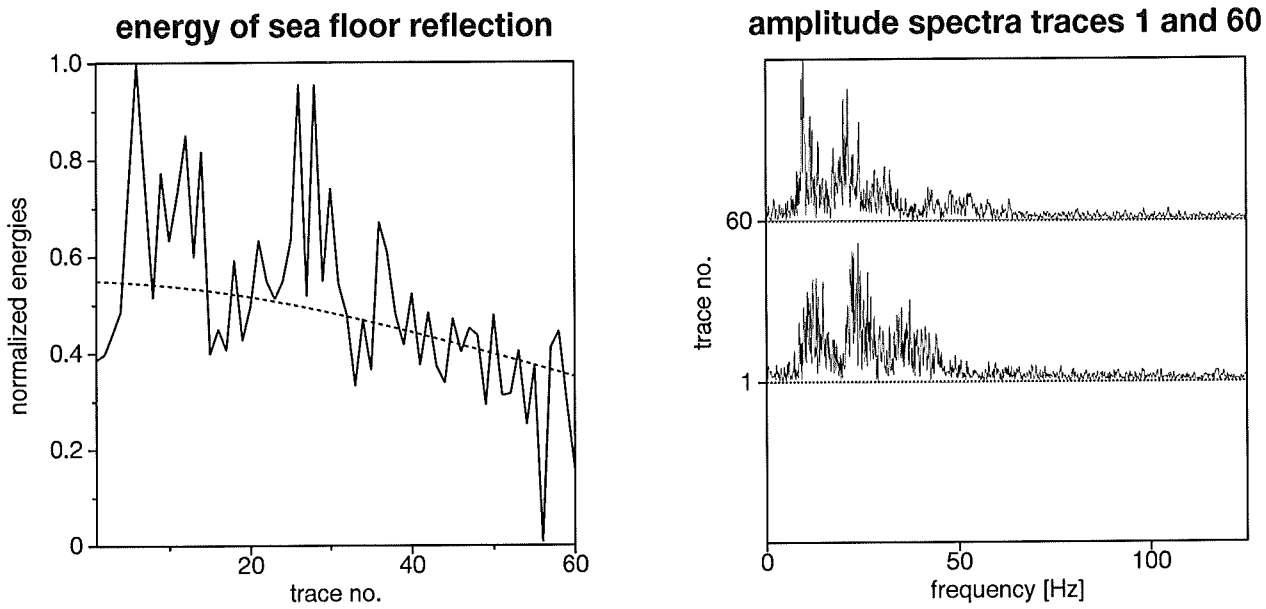

Figure 28: Left: Energies of the seafloor reflection together with the theoretical energy-versus-offset function (dashed line). Right: Amplitude spectra of neartrace and fartrace.

fig. 29. This data set was finally Fourier-transformed into the (ω, p)-domain.

7.1.2 Reflectivity of the seafloor and source wavelet

To obtain the reflectivity series at the seafloor, 20 traces around CMP 1126 were stacked. Then, the Wiener filter operator which transformed the signal of the seafloor reflection to that of the multiple, was determined. This operator is equivalent to the reflectivity series (in this case, normalized to the energy of the signals). The normalized reflectivity function is displayed in fig. 30 together with signals from seafloor and multiple.

The reflectivity series at the seafloor is approximately a spike. This means, that the shape of the multiple in fig. 30 should be the same as that of the seafloor reflection. The reflection coefficient can then be easily computed by comparing amplitudes of seafloor reflection and multiple (eq. 9). It was 0.14 at this location. For the other Peru locations, only the shape of seafloor signal and multiple were compared to check whether the seafloor is a single reflector.

The source wavelet is then equivalent to the response from the seafloor. It was extracted by stacking traces in the (τ, p)-gather in a window around the seafloor after correcting for water velocity and shifting those traces such that the cross-correlation of adjacent traces in the window around the seafloor was maximum. This wavelet is in fact a superposition of a wavelet which had been reflected at the sea floor and its ghost from the free water/air surface above the streamer. Using stacked (τ, p)-transformed traces over the whole range of offsets had the advantage that tuning effects created by increasing differences in travel paths for direct signals from the sea floor and ghost signals with increasing offset were averaged out. Therefore, corrections for receiver ghost directivity effects in the data were not required. The source wavelet was Fourier-transformed to be used for computing synthetic data in the (ω, p)-domain.

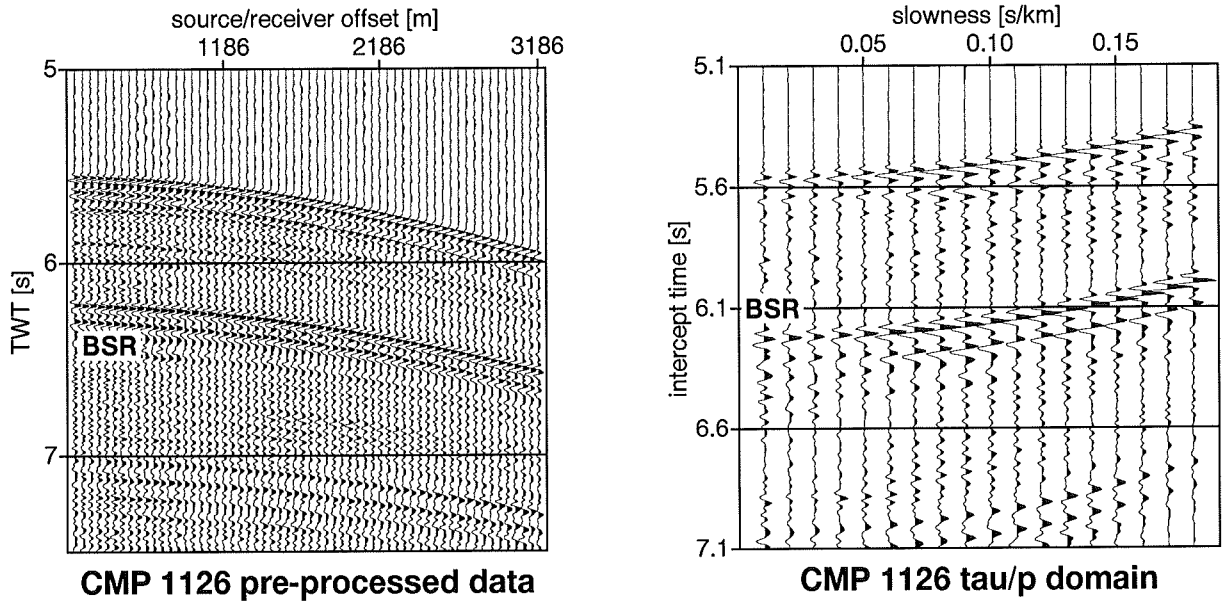

Figure 29: Pre-processed CMP-gather together with (τ, p)-gather. Refer text for details about processing. No AGC was applied for plotting.

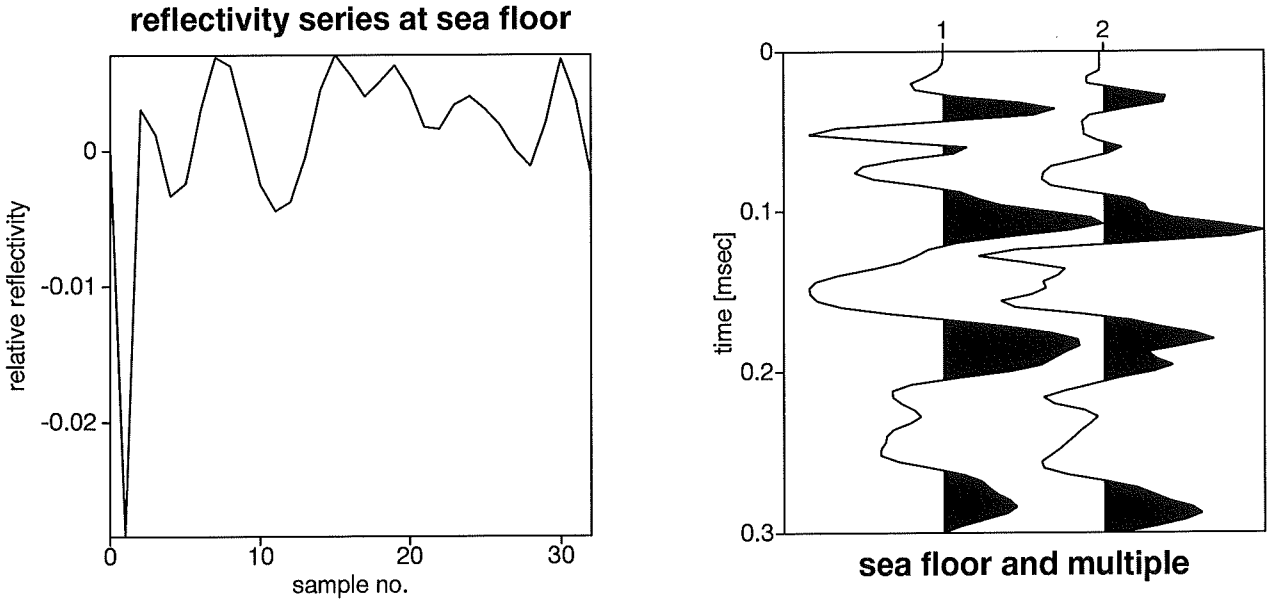

Figure 30: CMP 1126. Left: reflectivity series at the seafloor relative to the energy of the signal within the window which was chosen for the Wiener filter (left). Right: Signal from seafloor (left) and multiple (right). The signal from the multiple was multiplied by -1 and scaled such that peak-to-peak amplitudes from both seafloor and multiple are approximately the same.

7.1.3 Starting model

An optimum large-scale velocity model was determined from the data set in the (τ, p)-domain by applying the Monte Carlo inversion technique as described in section 4.1.5. Fig. 31 presents the random starting models for the Monte Carlo inversion, the final models from it, the final models from the Simplex optimization, and the resulting velocity model, together with velocity histograms for the layers above and below the BSR.

The interval velocity model was transformed into a gradient model such that vertical traveltime between two picked horizons was kept constant and there was no velocity contrast at the seafloor. Other seismic properties (V_s, ρ, Q_p, and Q_s) were computed as described in section 4.1.5. Fig. 32 shows the functions for V_p, V_s, and ρ obtained from this method (Q_p and Q_s are constant within the sediment column). Note that the reflection coefficient at the seafloor is caused by a step in the density function from $1.035 g/cm^3$ to $1.386 g/cm^3$. The average bulk density within the first $12m$ (i.e. two depth samples for the inversion procedure) in cores from Site 688 is $1.433 g/cm^3$. Though this location is more than $12km$ away from CMP 1126, this should justify the approach that the seafloor reflection coefficient was attributed to a change in density rather than P-wave velocity.

7.1.4 Full waveform inversion

The starting model, the real data set in the (ω, p)-domain, and the source wavelet were used as input for the full waveform inversion program, in which V_p was varied such that an optimum fit between the real data and synthetic data computed from source wavelet and reflectivity function was achieved (ref. section 4.1.6). Each inversion consisted of several runs, during which 5 iterations were performed. Inversions were first performed at lower frequencies. The final model from the low-frequency inversion runs was used as starting model for the high-frequency inversion. 5 runs of 5 iterations at lower frequencies ($2/8-20/30 Hz$) and 10 runs of 5 iterations using the whole frequency range ($2/8-30/50 Hz$) were performed. After that, the misfit function changed only little ($\sim 0.23\%$ for this data set) between successive iterations, which indicated convergence.

The resulting velocity structure from the full waveform inversion is presented in fig. 33 together with starting and final model from the low-frequency inversion and a plot showing the development of the misfit functions for both the low and the high-frequency runs.

Fig. 34 presents real data in the (τ, p)-domain from this location together with synthetic data for the final velocity model as well as residuals (real data minus synthetic data). Down to well below the BSR most residual energy is incoherent noise, which indicates that the velocity function is an adequate model for the velocity structure in the vicinity of the BSR.

At the BSR, a sharp decrease from about $2.15 km/s$ down to an average of $1.67 km/s$ in a layer of $18m$ thickness and a minimum velocity of $1.57 km/s$ in a $6m$ interval is observed. The sharp drop in V_p within a thin layer to well below values of neighboring sediment is a clear indication for the presence of free gas. Thus, the low velocity layer (LVL) is interpreted as a free gas zone with a thickness of between $6-18m$.

Shortly above the BSR at about $4.55 km$, velocity increases with regard to the starting model. This might be interpreted as the top of a layer containing an elevated concentration of hydrates in the pore space. Such effects however, may also be artifacts. In order to match reflectivity at the BSR, the conjugate gradient algorithm which updates the model may both decrease V_p at the BSR and increase V_p above it. Offset dependent waveform variations, which contain absolute velocity information in the vicinity of the BSR, have also to be accommodated for by the inversion. Thus, the inversion scheme is expected to favor only a velocity decrease if the BSR consists only of a LVL. The smaller maximum offset compared to the depth of the BSR, however, the less absolute velocity information is available. This effect is equivalent to the lack of low-frequency information while inverting seismic zero-offset data for

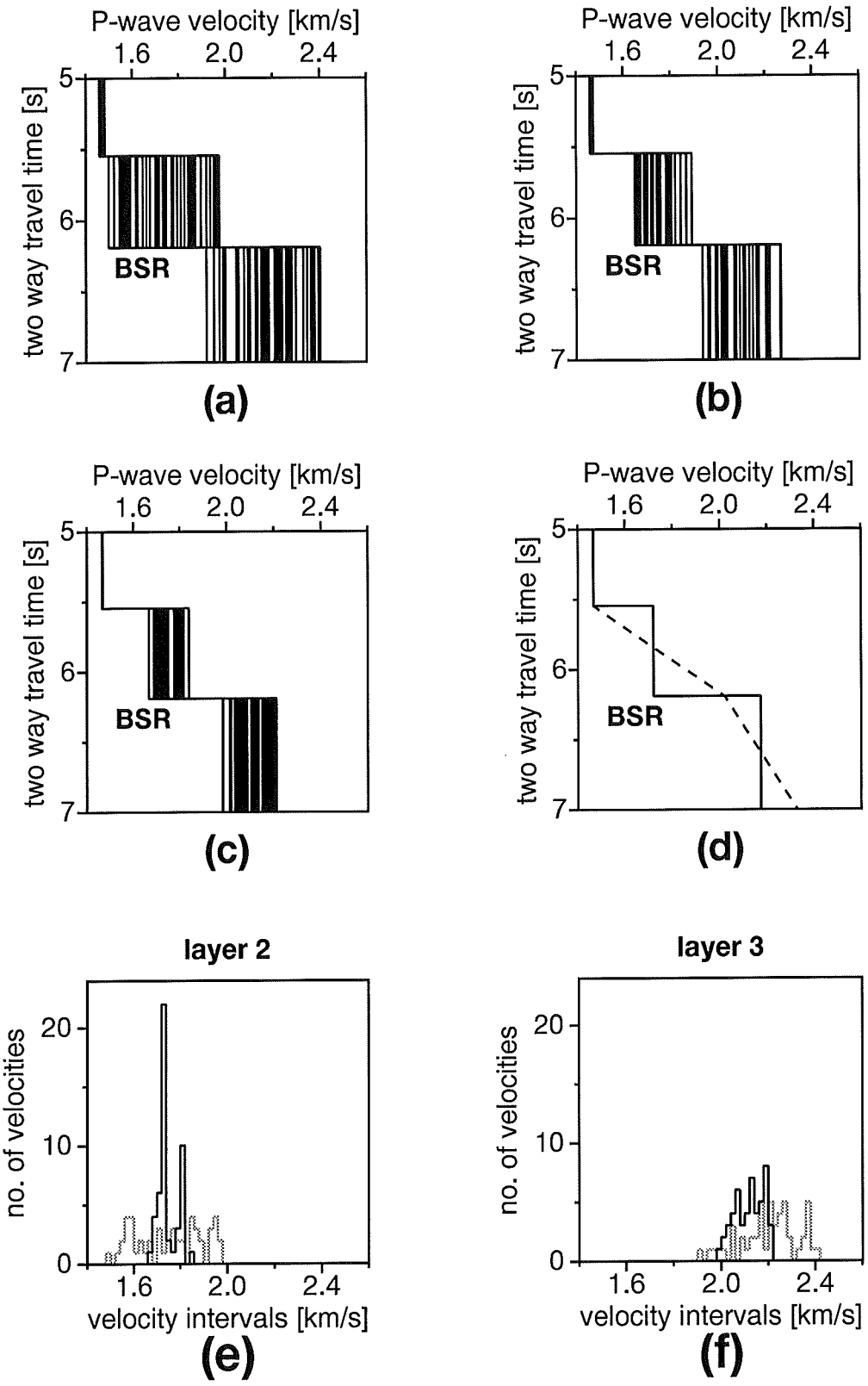

Figure 31: Starting velocity model for CMP 1126. (a) 50 random models for the Monte Carlo inversion. (b) Models after 50 Monte Carlo steps. (c) Models after Simplex optimization. (d) Resulting interval velocity model (solid) and gradient model (dashed). (e) Velocity histograms for steps (a) (grey line) and (c) (black line) in the layer above the BSR. The velocity bin is $0.01 km/s$. (f) Velocity histograms for steps (a) (grey line) and (c) (black line) in the layer below the BSR. The velocity bin is $0.01 km/s$.

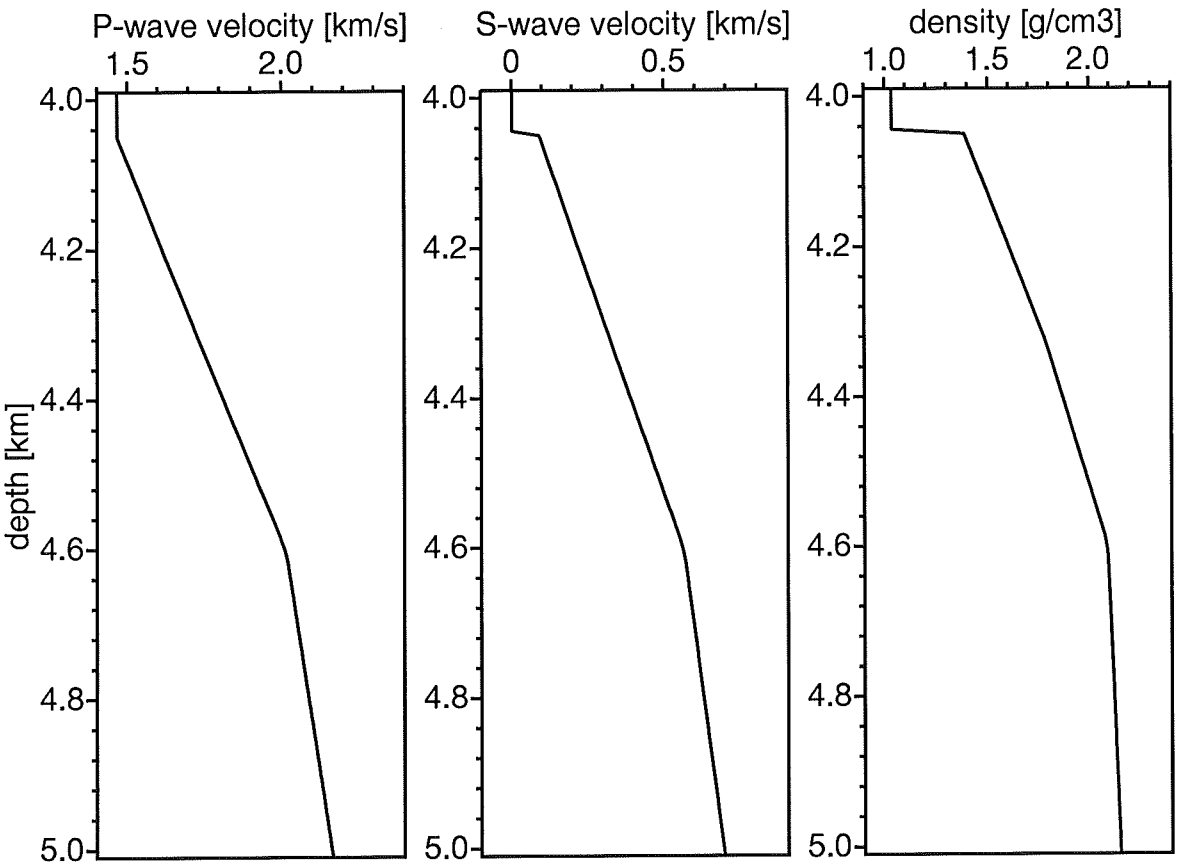

Figure 32: Starting model for the full waveform inversion at CMP 1126. Values for Q are constant: $Q_p = 10000$ in the water column, $Q_p = 200$ and $Q_s = 100$ in the sediment.

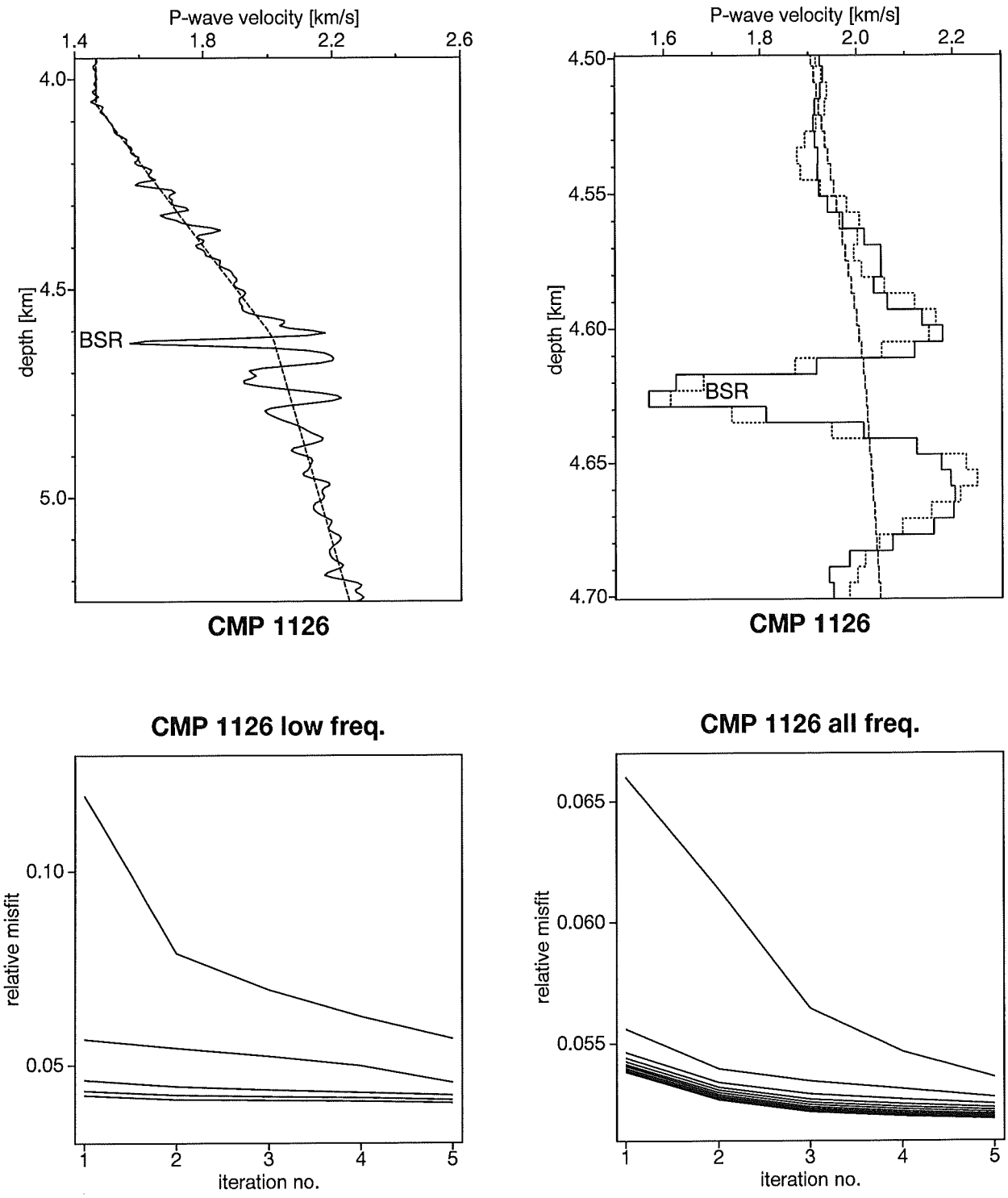

Figure 33: Velocity models obtained from full waveform inversion (top). The right plot shows a blow-up around the BSR. Depth intervals are $6m$. Dashed line: starting model, dotted line: final model from the low-frequency runs, solid line: final model using the whole frequency range. Development of the misfit function (bottom) using low frequencies (left) and all frequencies (right). Misfits in the two plots are not comparable with each other because of different scaling of the data.

reflectivity (e.g. Santosa and Symes, 1989). Wood (pers. com., 1995) reported similar phenomena during waveform inversion of MCS data from off the U.S. east coast (Wood et al., 1994). Thus, assuming that higher velocities above the BSR are caused by hydrates may result in an over-interpretation of the data. These effects are even more pronounced at most other locations which were investigated off Peru.

Beneath the BSR, undulations in the V_p-function probably are caused by problems with the source wavelet. Weak reflectors beneath the seafloor within the depth range which corresponds to the length of the source signal lead to a distortion of the source wavelet if using the seafloor response as source signal. However, this is not expected to affect the velocity structure obtained from waveform inversion at the BSR itself, as long as (1) no strong reflectors are present within one wavelength of the source signal beneath the seafloor, which has been checked by comparing the waveform with the multiple, (2) the first part of the source signature over a time window corresponding to one main period of the signal (i.e. one wavelength in depth) has been properly obtained from the seafloor, and (3) no stronger reflections occur slightly above the BSR. This will be demonstrated at the Costa Rica line 9 CMP 1410 data set.

7.1.5 Modeling P-wave velocity as a function of water saturation

In order to estimate the concentration of free gas in the pore space, compressional wave velocity as a function of water saturation of the pore space in partially saturated sediments was modeled as described in section 4.2. The properties of the model sediment are listed in tables 10 and 11. In order to estimate the error margin of this modeling, model parameters were varied. Variation of (or erroneous assumptions on) V_p at full water saturation ($V_{p,0}$) had by far the strongest effect on the velocity-versus-water saturation function. Therefore, the dashed lines in fig. 35, which displays the V_p-versus-water saturation functions for three given values of $V_{p,0}$, approximately represent an estimate for the error margins of these calculations. It is obvious from the results that, given a P-wave velocity of $1.67 km/s$, water saturation of the pore space is below about 97% (i.e. gas content is above approximately 3% of pore volume). However, V_p depends only slightly on water saturation below this value, which makes it impossible to further constrain the gas content beneath the BSR. Thus, the maximum concentration would theoretically be 100% of the pore space.

7.2 Nature of the BSR at Peru line 1018 CMP 1514

CMPs 1514 and 1594 were two other suitable targets off Peru. These locations are relatively close to ODP Site 688 (about $1.1 km$ from CMP 1594). Fig. 36 shows a part of the pre-stack depth migrated section re-stretched to time around those CMPs. Whereas at CMP 1514 the BSR displays a relatively strong amplitude, amplitudes are considerably weaker around CMP 1594, which is close to the landward termination of the BSR. The decrease of reflectivity of the BSR between both locations may be equivalent with a transition from a "strong BSR" to a "weak BSR" (classification by Lee et al., 1993).

Again, two CMP-gathers were merged to obtain all offsets. Pre-processing was similar to that of CMP 1126. The resulting CMP-super-gather is displayed together with direct and multiple signals from the seafloor in fig. 37. The shapes of the direct and multiple signals are quite similar, indicating that the seafloor reflectivity series again consists mainly of a spike. The reflection coefficient is 0.18.

A starting model for the full waveform inversion was determined by applying a Monte Carlo inversion to reflections from the layers above the BSR. Since no stronger and relatively flat reflector could be identified closely beneath the BSR to determine the velocities in this region, velocities from pre-stack depth migration were used for that purpose. Fig. 38 displays the resulting seismic starting model. Bulk density at the sea floor is $1.489 g/cm^3$.

The final velocity structure from the full waveform inversion is displayed in fig. 39. Fig. 40 shows real and synthetic data in the (τ, p)-domain from this location together with the residuals. Low amplitudes of the residuals again indicate that the velocity function obtained from waveform inversion is

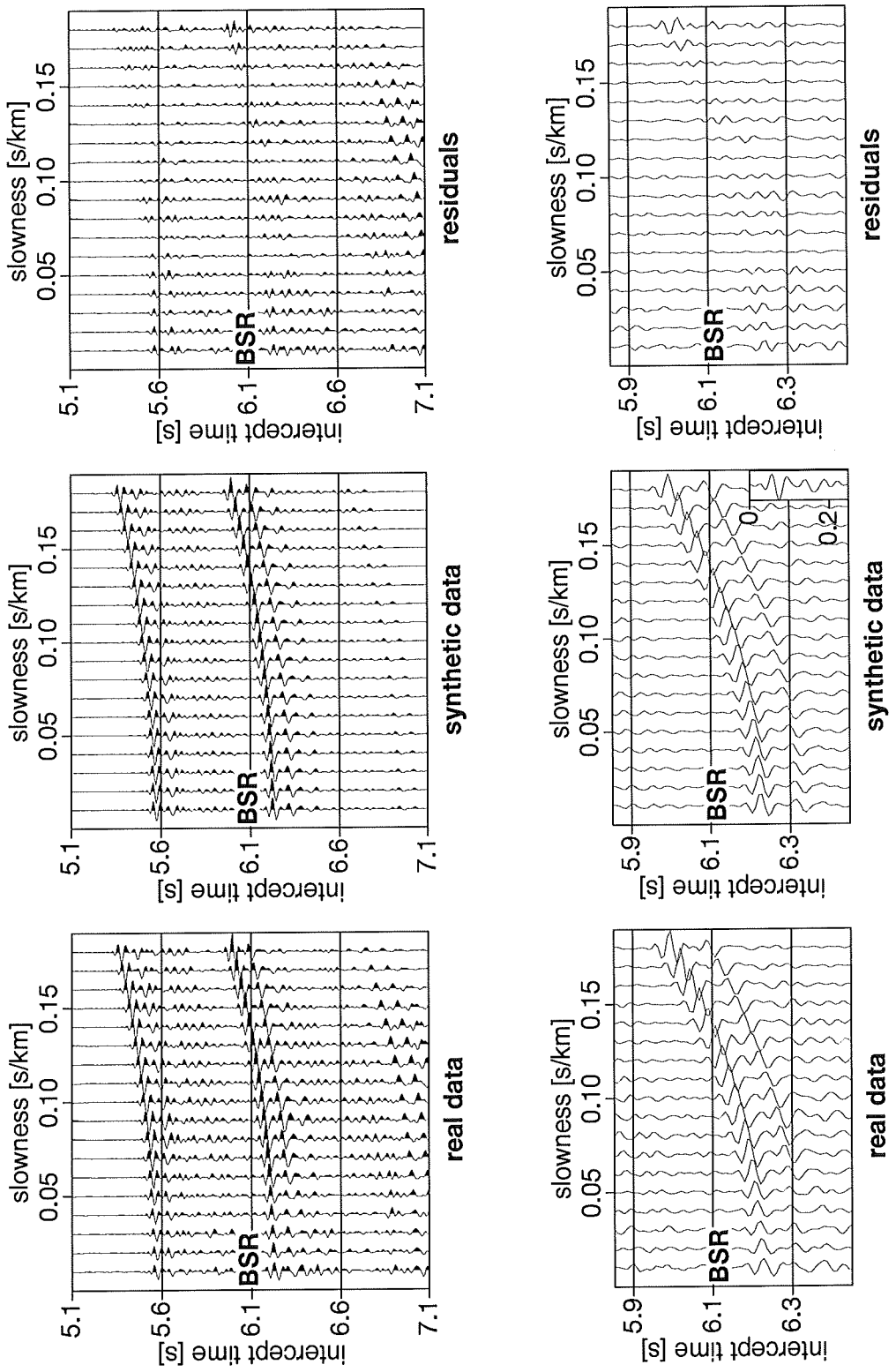

Figure 34: Real data in the (τ, p)-domain compared to synthetic data computed from the final model from the waveform inversion and residuals (real minus synthetic data) at CMP 1126. Lower figures: blow-up around BSR. The inset in the synthetic data displays the source signature.

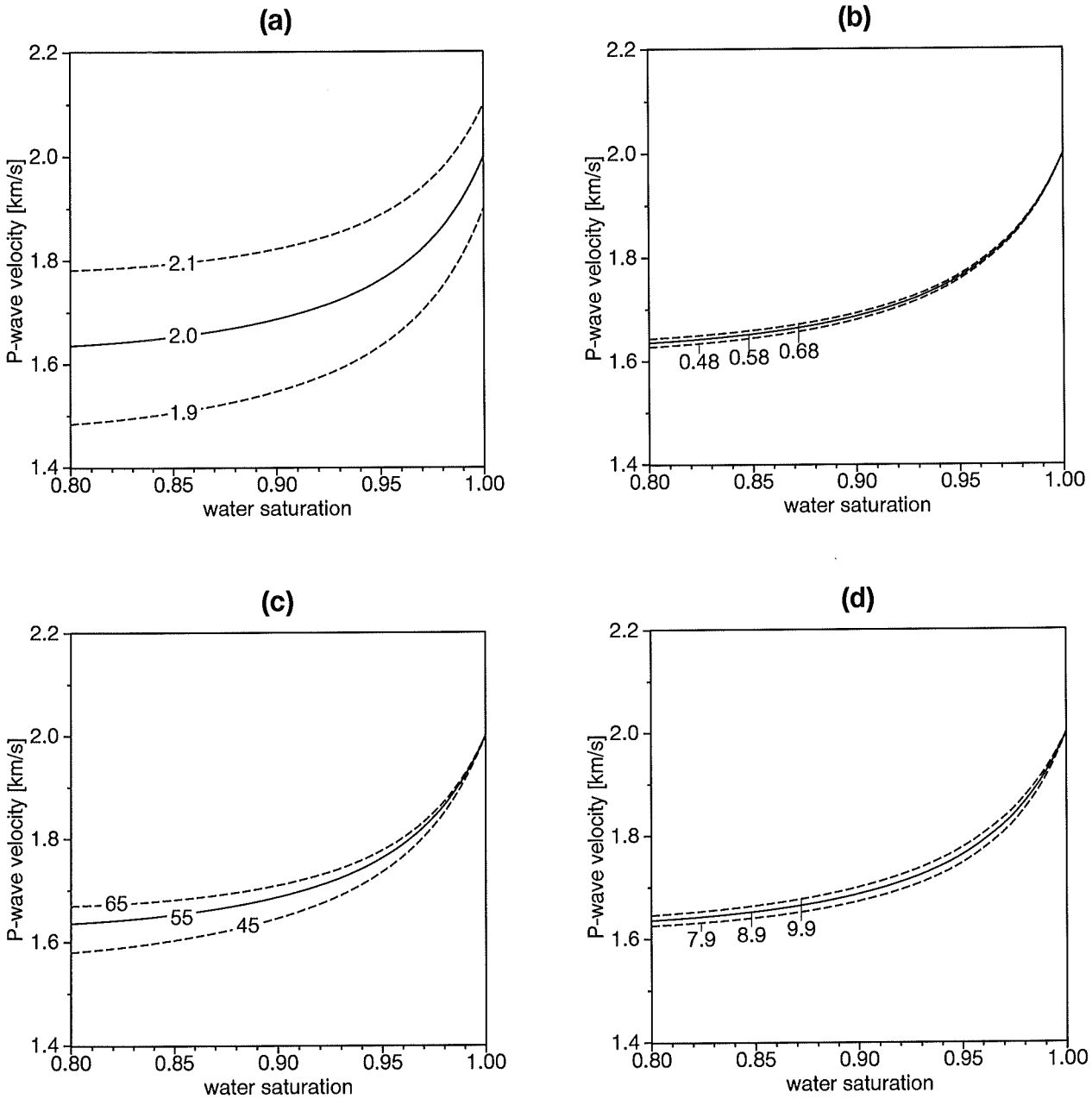

Figure 35: Compressional wave velocity as a function of water saturation. Variation with (a) $V_{p,0}$, (b) $V_{s,0}$ (b), (c) Φ, and (c) K_g (d). Values for those properties are given in the graphs, units: $V_{p,0}$, $V_{s,0}$ in km/s, Φ in percent, and K_g in $10^7 Pa$. Those variations represent the approximate error margins for the assumed model parameters. Variation of other parameters did not significantly affect the V_p-versus-water saturation function. Note, that water saturation is given in percent of pore volume, not of the bulk sediment.

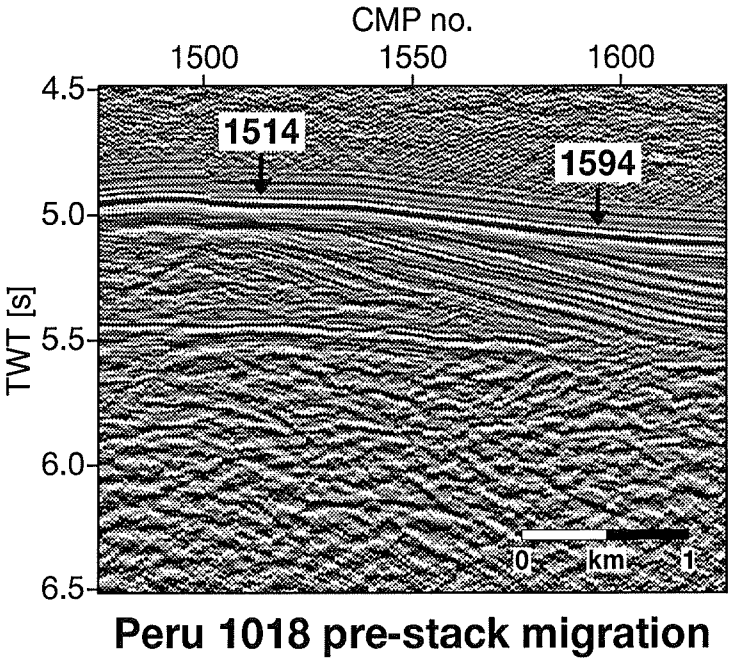

Figure 36: Pre-stack depth migrated section re-stretched to time of Peru line 1018 around CMPs 1514 and 1594. Processing included signature deconvolution. The AGC window is 1s. The arrows indicate the exact positions of the locations chosen for inversion.

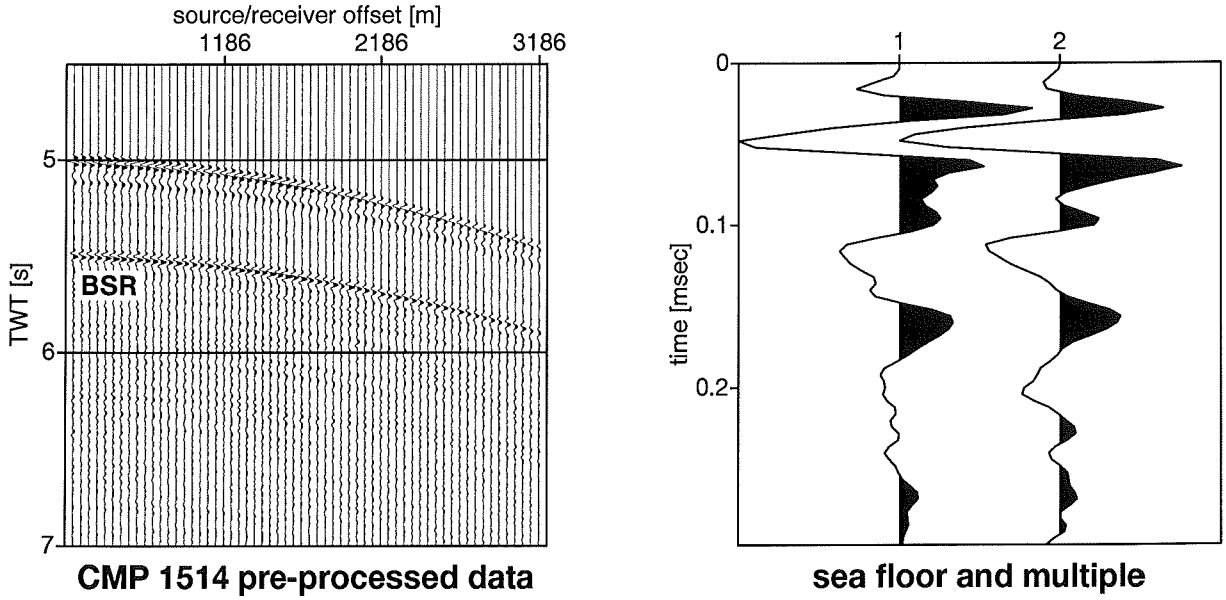

Figure 37: Left: CMP 1514 super-gather after pre-processing, no AGC. Right: Signals from seafloor and multiple, the multiple was multiplied by -1 and scaled such that peak-to-peak amplitudes from both direct and multiple signal are approximately the same.

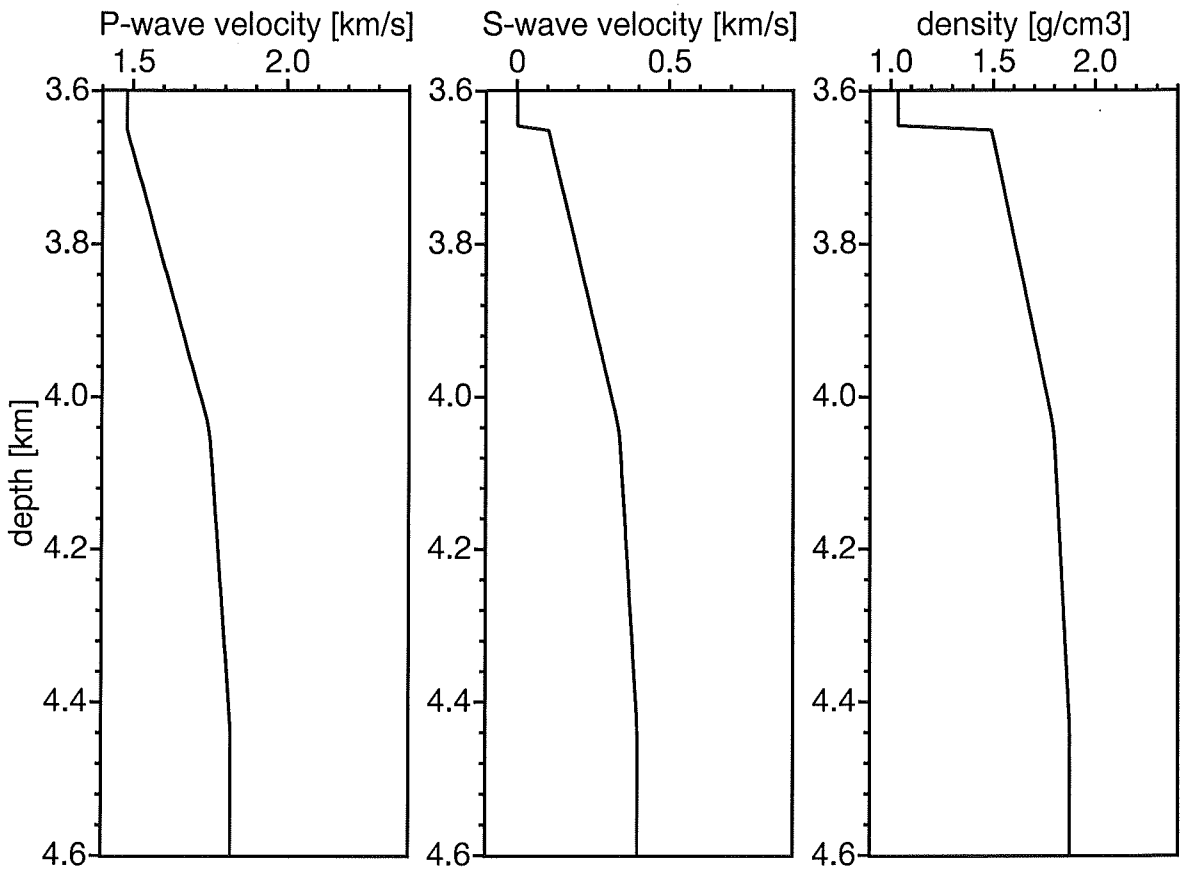

Figure 38: Starting model for the full waveform inversion at CMP 1514.

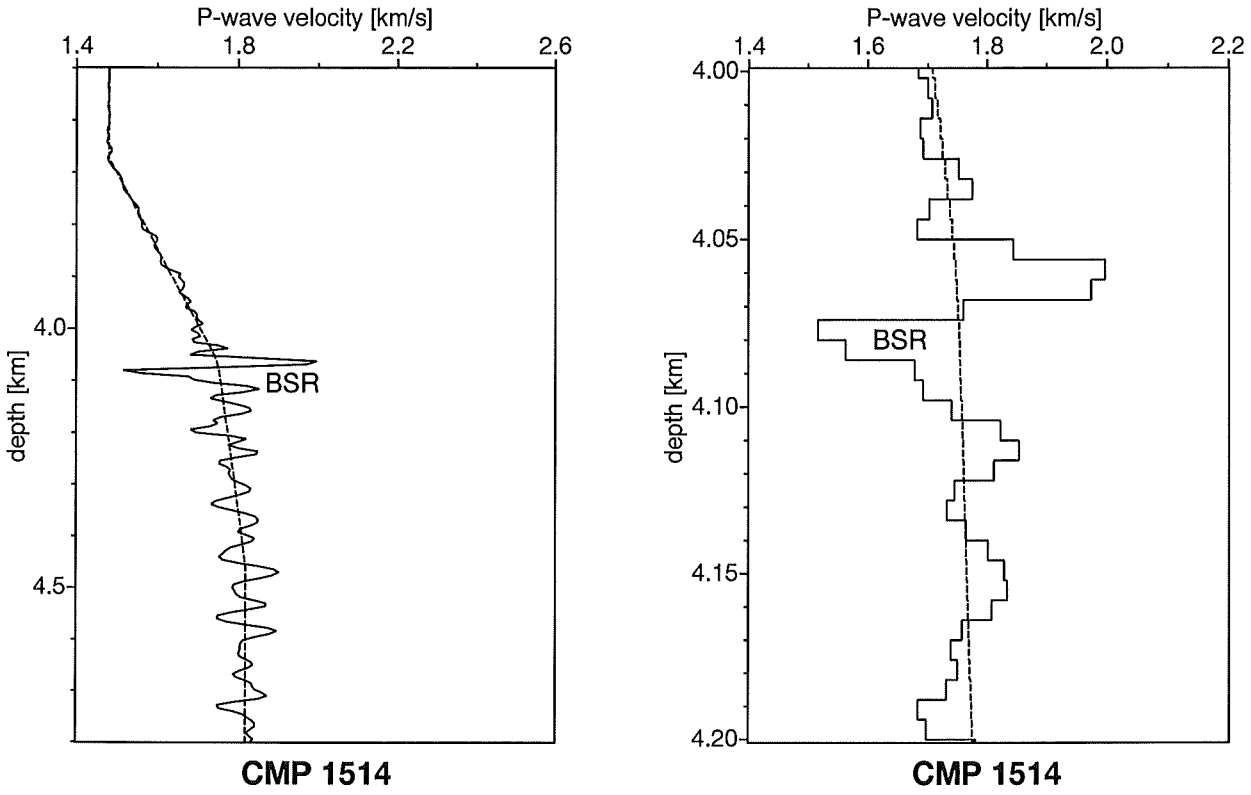

Figure 39: Velocity models obtained from full waveform inversion. The right plot shows a blow-up around the BSR. Depth intervals are $6m$. Dashed line: starting model, solid line: final model.

an adequate model for the velocity structure in the vicinity of the BSR. The BSR is characterized by a sharp decrease in V_p from about $2.0km/s$ down to $1.55km/s$ in a $12m$ thick layer. Again, this drop in velocity can only be explained by the presence of free gas. Fig. 41 shows the V_p-versus-water saturation function adapted to the depth of the BSR at this location. A P-wave velocity of $1.54km/s$ could be explained by a gas content of at least 1% of pore volume.

7.3 Nature of the BSR at Peru line 1018 CMP 1594

The BSR is considerably weaker at CMP 1594 than at all other locations which were investigated for the present study (fig. 36). Fig. 42 shows the CMP-super-gather together with signals from seafloor and multiple. The shape of the two signals is not very similar. Probably, this is due to the presence of reflections slightly beneath the seafloor, which can also be seen in the migrated section in fig. 36. Therefore, source signal and direct signal from the seafloor may not be regarded as being equivalent and a reflection coefficient at the seafloor cannot be computed by merely comparing peak-to-peak amplitudes of direct and multiple signal. Both reflection coefficient and source signal from CMP 1514 were therefore used assuming that both do not change much over a distance of 80 CMP, i.e. $2km$ (a reflection coefficient computed from comparing the amplitudes of the first phase of seafloor and multiple would be 0.16).

The starting model was determined as for CMP 1514: a Monte Carlo inversion was applied to reflections from the layers above the BSR. Velocities from pre-stack depth migration were used beneath the BSR, since the only strong reflection there (at abt. $6.0s$ TWT) has a relatively steep dip (ref. fig. 36). Fig. 43 shows the seismic starting model. The density step at the seafloor is (of course) the same as for CMP 1514.

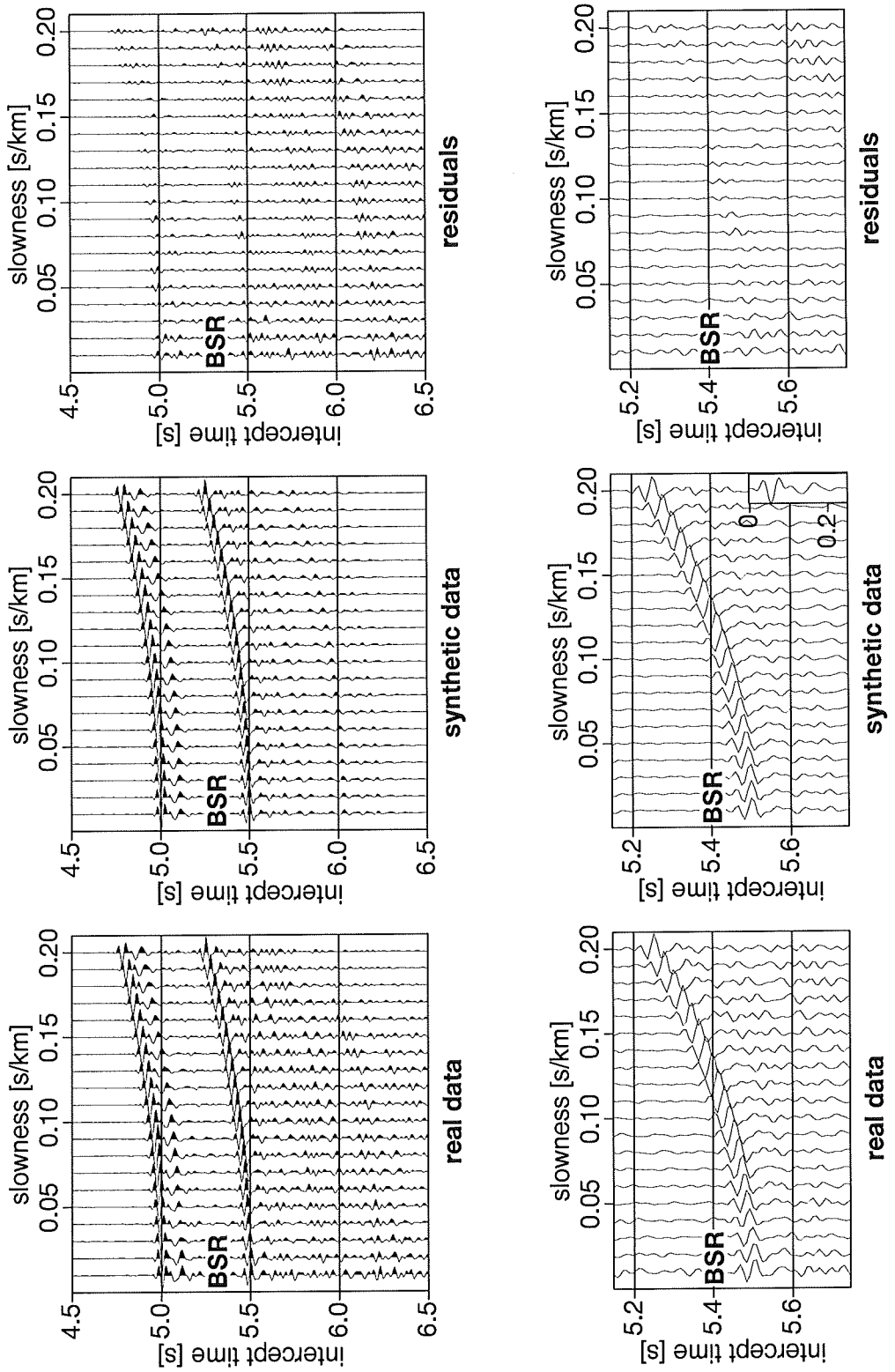

Figure 40: Real data in the (τ, p)-domain compared to synthetic data computed from the final model from the waveform inversion and residuals at CMP 1514. Lower figures: blow-up around BSR. The inset in the synthetic data displays the source signature.

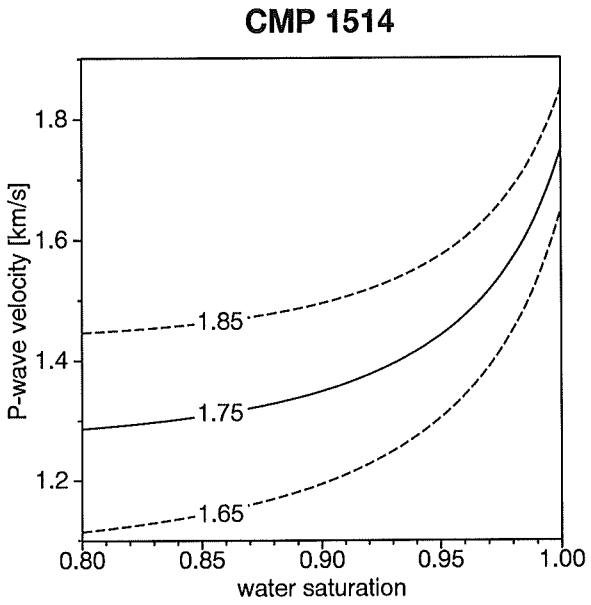

Figure 41: Compressional wave velocity as a function of water saturation at the depth of the BSR at locations Peru 1018 CMPs 1514 and 1594. Variation of $V_{p,0}$ as given in the graph represents the approximate error margin for this modeling.

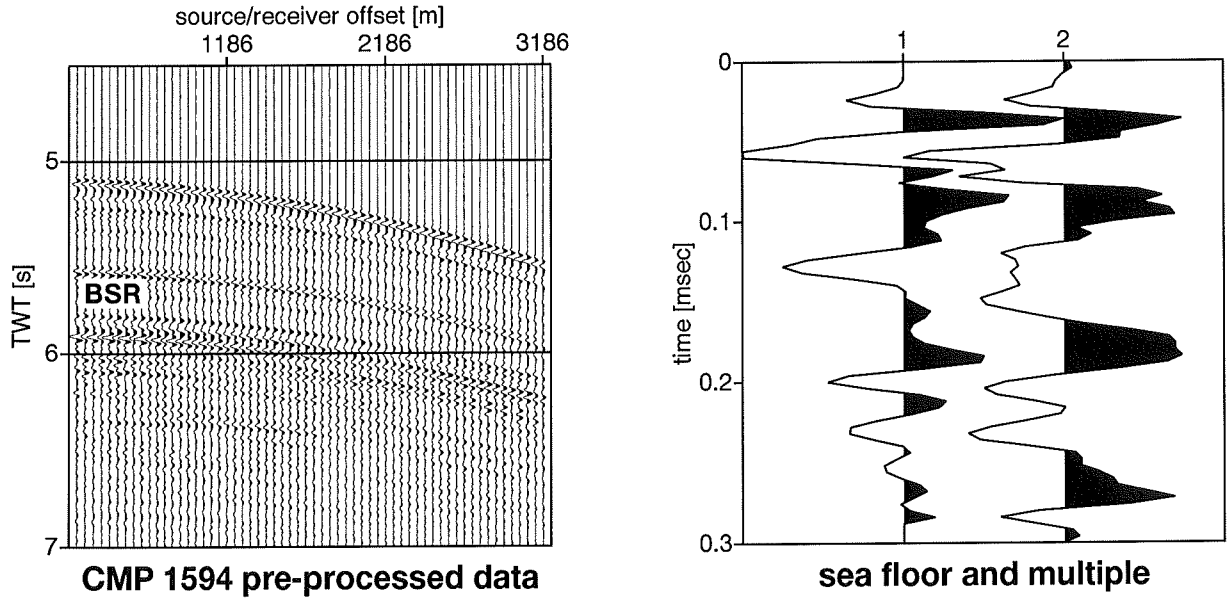

Figure 42: Left: CMP 1594 super-gather after pre-processing. Right: Signals from seafloor and multiple, the multiple was multiplied by -1 and scaled such that peak-to-peak amplitudes from both direct and multiple signal are approximately the same.

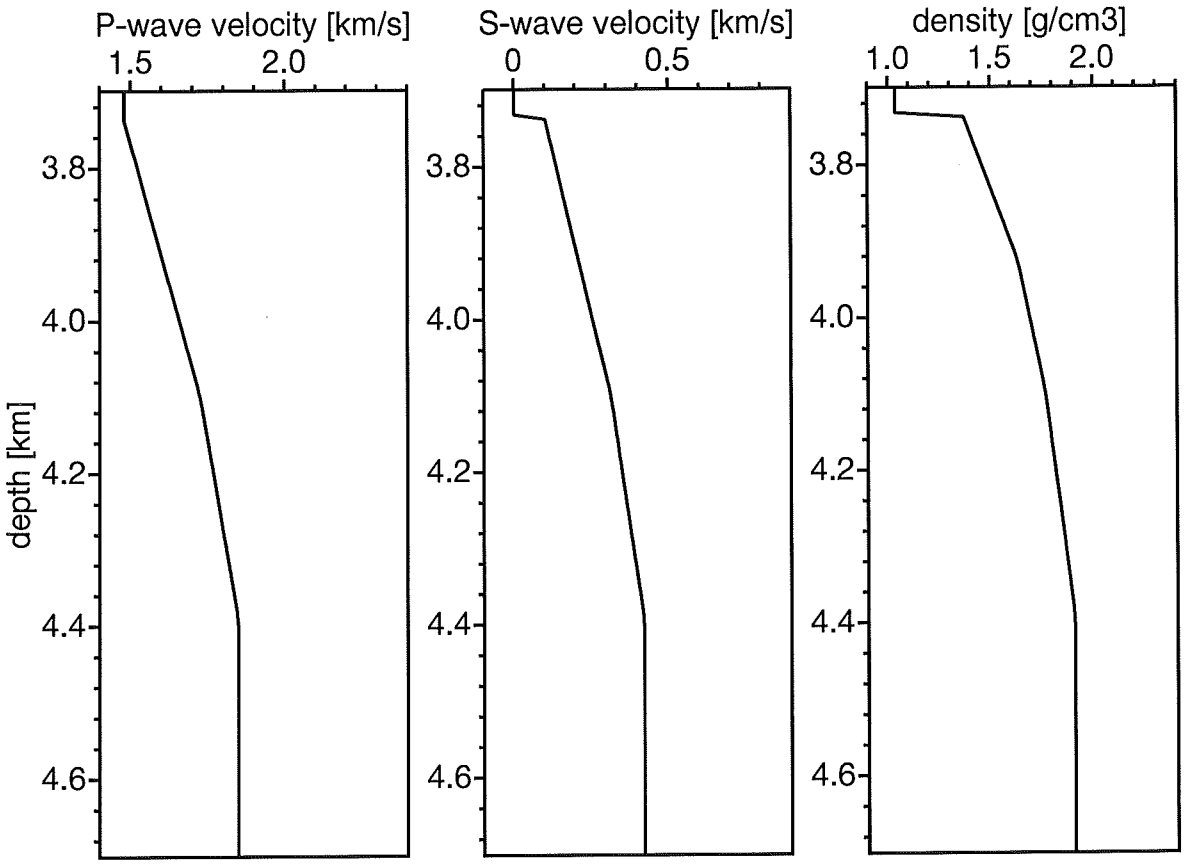

Figure 43: Starting model for the full waveform inversion at CMP 1594.

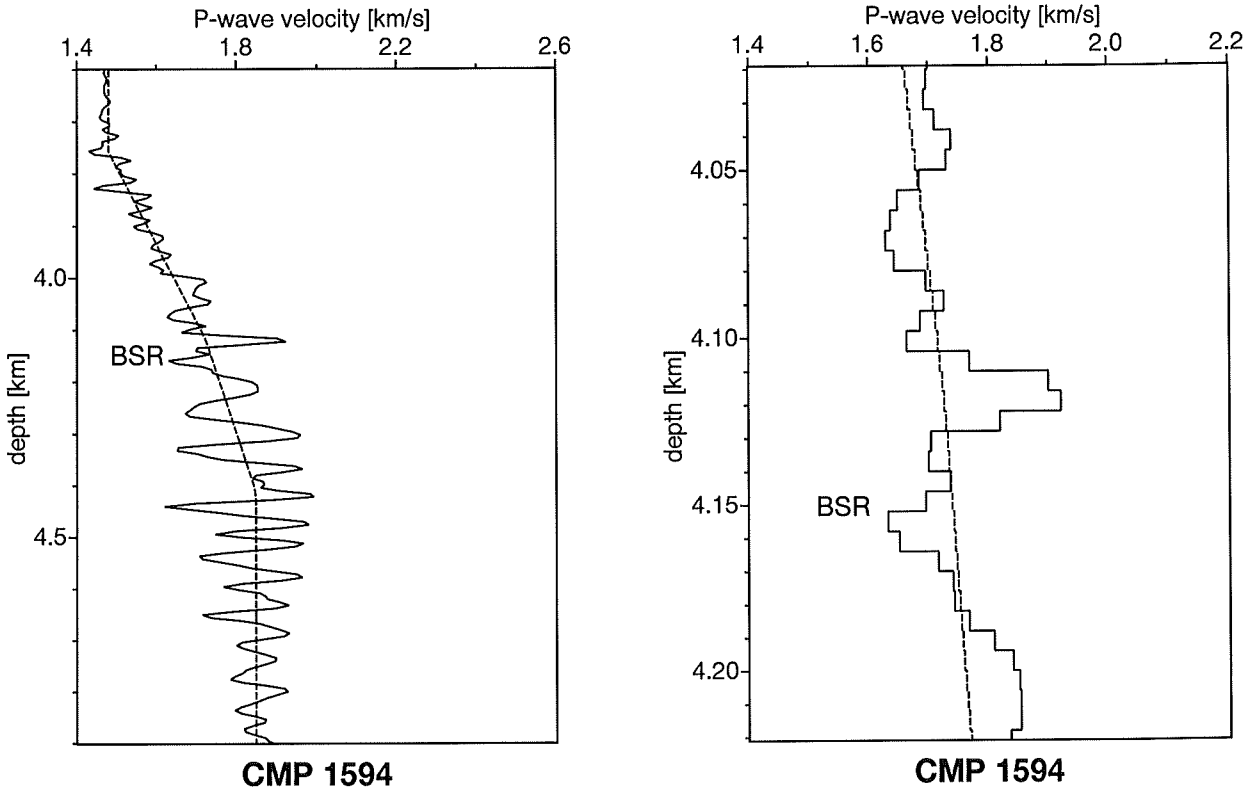

Figure 44: Velocity models obtained from full waveform inversion. The right plot shows a blow-up around the BSR. Depth intervals are $6m$. Dashed line: starting model, solid line: final model.

The fine velocity structure from full waveform inversion is shown in fig. 44. The BSR is caused by relatively slight drop in V_p. This small decrease in velocity does not indicate the presence of much (if any) free gas. Slightly elevated V_p above the BSR may be artificial. However since this increase of V_p is clearly more pronounced than the decrease at the BSR itself, this effect may be at least partly real, possibly indicating a hydrated layer. Undulations of the V_p-structure a few hundred meters beneath the BSR are probably caused by a high-velocity crystalline basement at this depth, which was not accounted for in the starting model. The aim of the present investigations was to determine the velocity structure at the BSR. Trying to fit the model for deeper layers would have required much more effort and would have been made quite difficult because basement reflectors are not horizontal. Fig. 45 displays real and synthetic data as well as residuals. Again, residuals show that the velocity function is adequate down to well below the BSR. Beneath the BSR, strong residual energy indicates that no proper model was obtained for higher velocity rocks.

7.4 Nature of the BSR at Peru line 1017 CMP 3790

Further to the south along line 1017, CMP 3790 was selected as another target for full waveform inversion. The BSR there appears to be reflective and continuous in the pre-stack migrated section (fig. 46). CMP-super-gather and direct and multiple signals from the seafloor are displayed in fig. 47. Note the strong amplitude of the seafloor reflection with respect to the other reflectors including the BSR, though the BSR is relatively strong compared to other parts of the pre-stack migrated sections (e.g. figs. 11 and 46). Signals from seafloor and multiple are quite similar and thus, the seafloor can be regarded as a single layer again. The reflection coefficient was computed as 0.31, which is rather high compared to the

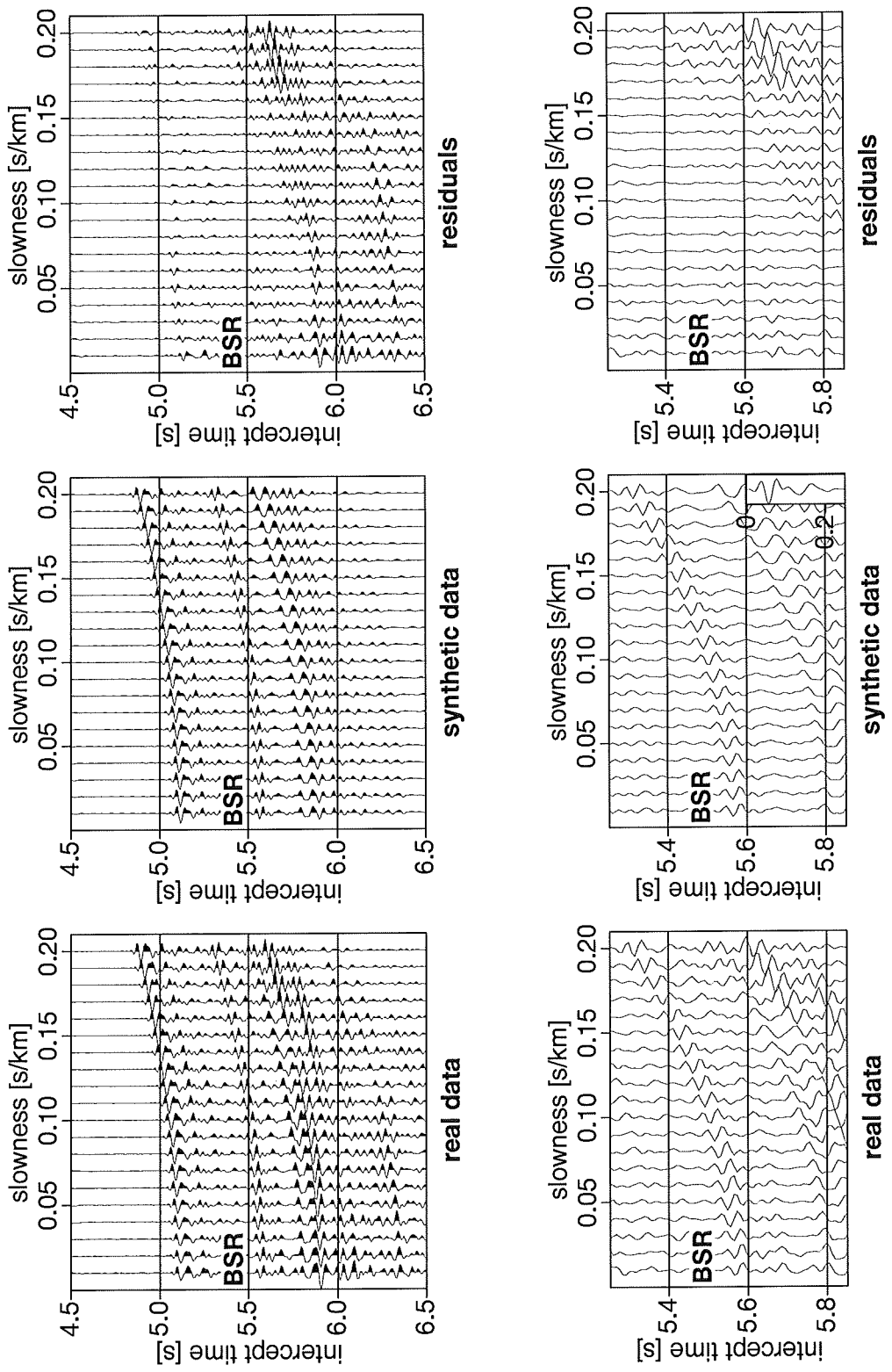

Figure 45: Real data in the (τ, p)-domain compared to synthetic data computed from the final model from the waveform inversion and residuals at CMP 1594. Lower figures: blow-up around BSR. The inset in the synthetic data displays the source signature, which is from CMP 1514.

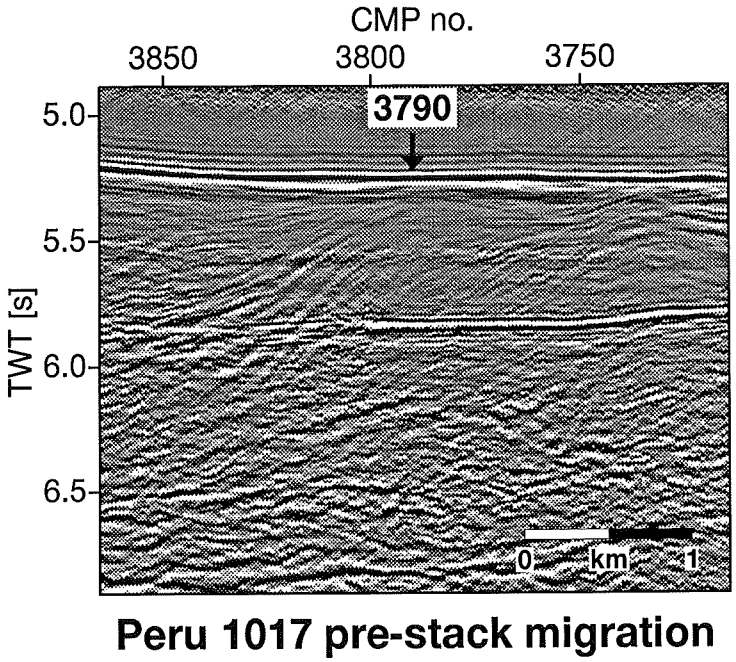

Figure 46: Pre-stack depth migrated section re-stretched to time of Peru line 1017 around CMP 3790. Processing included spiking deconvolution. The AGC window is $1s$. The arrow indicates the exact position of the location chosen for inversion.

other locations to which waveform inversion was applied and explains the strong seafloor reflection in the CMP-gather.

For the starting model, a Monte Carlo inversion was applied to reflections from the layers above the BSR. Again, velocities from pre-stack depth migration were used below the BSR. Stronger reflections there at about 6.9 s TWT have a relatively steep dip (ref. fig. 46) and therefore velocities from 'MIGPACK' were believed to be more reliable than those from the Monte Carlo inversion which assumes one-dimensionality. Fig. 48 presents the seismic starting model.

A density of over $1.9g/cm^3$ at the seafloor is due to the assumption that the high reflectivity is merely caused by a change in density. This density value is certainly too high and consequently, part of the reflection coefficient should be assigned to a velocity contrast at the seafloor. Since no additional constraints were available however, an estimate of this velocity contrast would be highly arbitrary. A higher value for V_p at the seafloor would lead to a lower velocity gradient within the sediments above the BSR in order to keep the TWT to the BSR constant. Subsequently, this would yield lower values of V_p in the vicinity of the BSR. To avoid artificially low in the background velocities at the BSR, the gradient velocity model was therefore generated as for the other locations by assuming that V_p at the seafloor was the same as that in the water column. V_p was by far more important a parameter for the waveform inversion scheme than ρ, since it was only inverted for V_p. The value of V_p in the starting model at the BSR is $2.05km/s$ compared to $2.02km/s$ at CMP 1126 in line 1018. Depths of the BSR beneath the seafloor are $0.56km$ and 0.52 at lines 1017 CMP 3790 and 1018 CMP 1126, respectively. Thus, velocities at the BSR may be expected to be similar, which justifies our approach for generating a starting model at CMP 3790, keeping in mind that the goal of the inversion strategy is a most accurate V_p-versus-depth function in the vicinity of the BSR.

The final velocity function obtained from full waveform inversion is shown in fig. 49. Again,

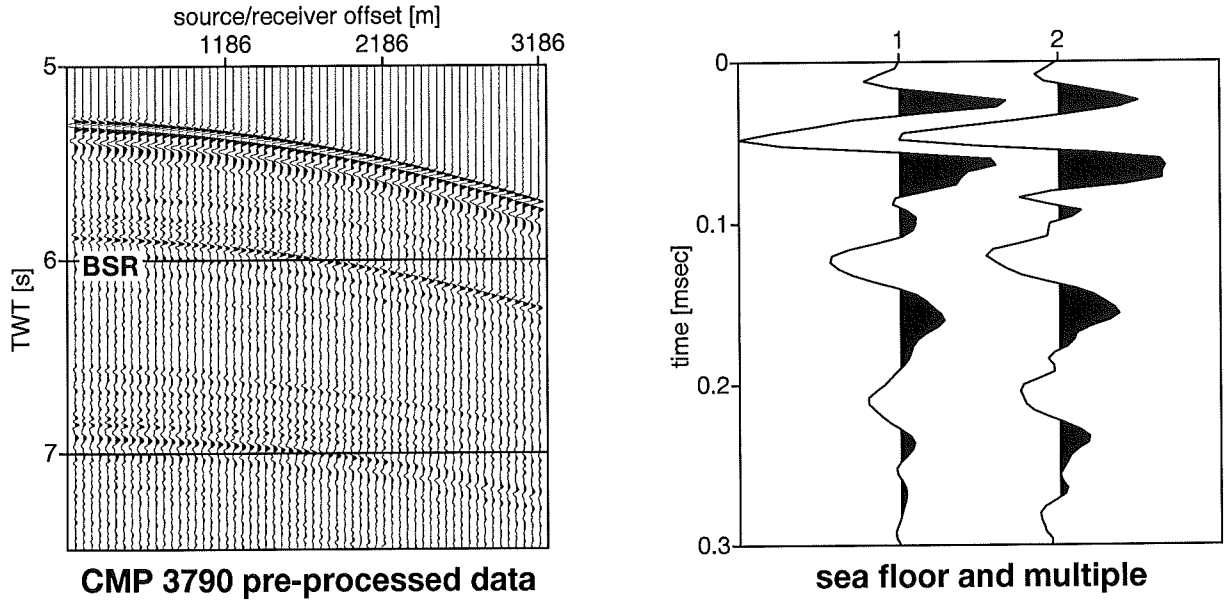

Figure 47: Left: CMP 3790 super-gather after pre-processing. Right: Signals from seafloor and multiple, the multiple was multiplied by -1 and scaled such that peak-to-peak amplitudes from both direct and multiple signal are approximately the same.

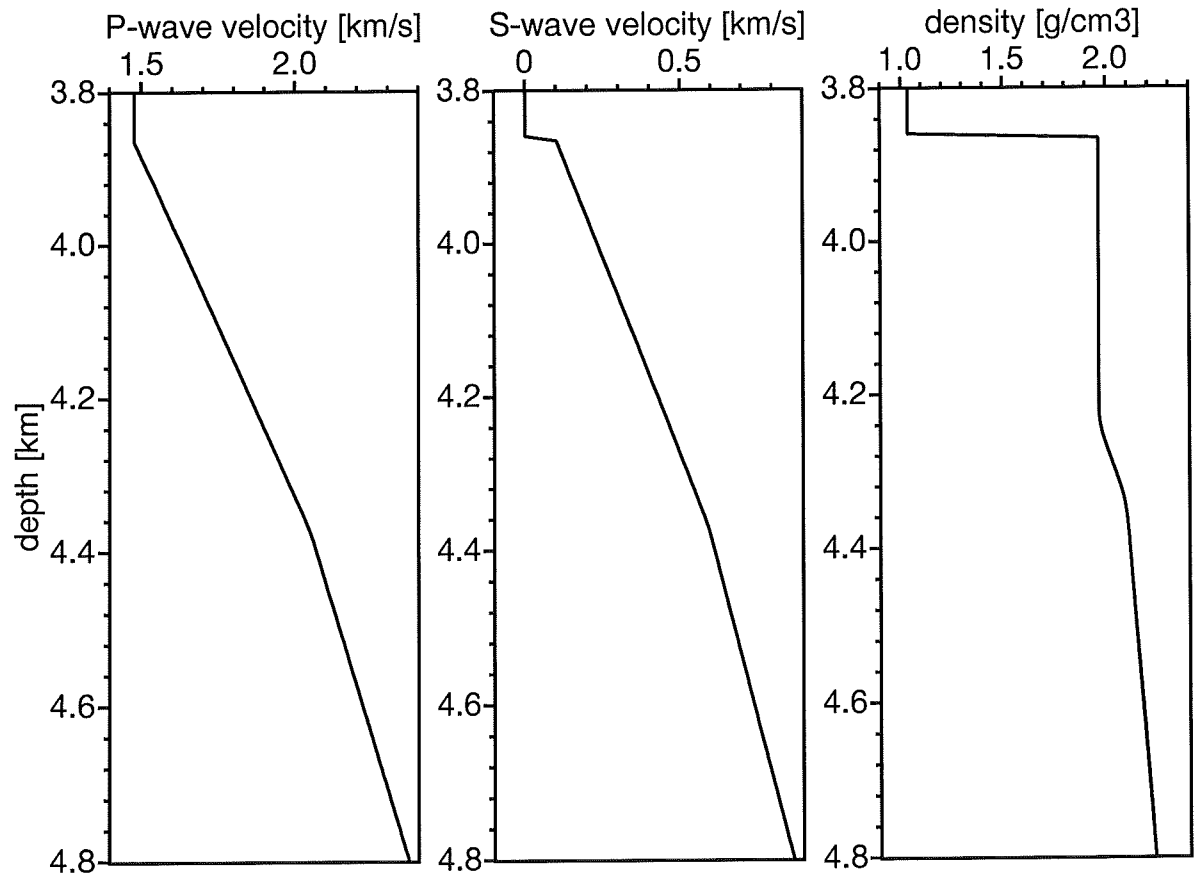

Figure 48: Starting model for the full waveform inversion at CMP 3790.

the BSR is caused by a distinct LVL, indicating the presence of free gas. The velocity structure is quite similar to that at line 1018 CMP 1126: the BSR consists of a LVL of $6-18m$ thickness having an average value of about $1.82km/s$ and a minimum value of $1.73km/s$. The BSR is less pronounced than at CMP 1126 - absolute velocity values differ between both locations. The drop of velocities from the value for V_p in starting models down to the average velocity at the BSR (which is used for estimating the amount of free gas) is $0.35km/s$ at CMP 1126 and $0.23km/s$ at CMP 3790. It is not clear, to what extent this difference is due to a lower reflectivity at the BSR at CMP 3790 or whether it is partly artificial because of problems with the starting model at this location. Velocity contrasts match better: peak-to-peak velocity differences between the maximum value in the $30m$ above the BSR and the lowest value at the BSR are $0.61km/s$ and $0.54km/s$ at lines 1018 CMP 1126 and 1017 CMP 3790, respectively.

Above the BSR, some velocity variations in the model at about $4.1-4.2km$ depth may be caused by a weak reflector at about $5.5s$ TWT (see e.g. migrated section in fig. 46 and CMP-gather in fig. 47). Velocity undulations beneath the BSR are considerably weaker than at the other locations. This indicates that such undulations are caused by a deviation of the reflectivity series at the seafloor from a mere spike function and subsequent distortions of the shape of source wavelet obtained from the seafloor reflection. The source wavelet obtained from this location probably is closest to the real source wavelets: the shape of the signal from the seafloor and layers slightly beneath it is dominated by the response from the seafloor itself. The extent of distortions of this signal, compared to the real source wavelet, is caused by the reflectivity beneath the seafloor relative to the strength of the seafloor reflection itself. Comparing real, synthetic, and residual data (fig. 50) demonstrates that in the vicinity of the BSR the V_p-structure is adequate. Computation of V_p as a function of water saturation yields a minimum concentration of 1% of free gas in the pore volume (fig. 51).

7.5 Distribution of BSRs at the central Peruvian margin

7.5.1 Reflection data from 12° S

A strong and continuous BSR can be observed at the lower slope in profiles 1017 and 1018 as shown in figs. 11 and 12. The seaward termination of the BSR in line 1017 is located almost exactly at the last landward dipping reflector which marks the landward boundary of the accretionary prism, i.e. at CMP 4230 or $17.9km$ away from the trench axis (these and the following numbers have an uncertainty of about 10 CMPs, i.e. $250m$). Landward, the BSR disappears at the middle slope at CMP 3560 ($34.6km$ from the trench axis; ref. also time section in fig. 73 for a better display of the BSR at the landward termination), where normal faults are present. No BSRs could be identified further upslope. Note that the track of line 1017 crosses the trench axis at an angle of about 25° and thus, is not exactly perpendicular to the trench axis. Therefore, distances from the trench are actually slightly lower (fig. 7) and above values have to be multiplied by a factor of about $cos(25°) = 0.9$ for comparison with other profiles.

This pattern is also found on line 1018. There, the BSR might extend slightly into the accretionary complex (CMP 790 = $12.3km$). Again, the time section in fig. 77 gives a clearer image of the BSR. It appears to be strongest beneath the lower slope terrace, which shows some landward verging thrust faults. The BSR terminates landward at CMP 1620 ($33km$ from the trench axis), which is close to a first normal fault indicating the seaward boundary of an area which is extensively covered by normal faults. Further upslope, no BSRs are present in Lima Basin.

The general pattern of the distribution of BSRs at 12° S is thus characterized by an absence of BSRs within the accretionary wedge, strong BSRs within lower slope sediments above the presumed seaward edge of the metamorphic complex and an absence further upslope. The landward termination appears to coincide with the transition from a compressional tectonic regime indicated by thrust faults at the lower slope to an extensional regime with extensive normal faulting at the middle slope.

The lack of BSRs in Lima Basin cannot be explained by the assumption that it might be too

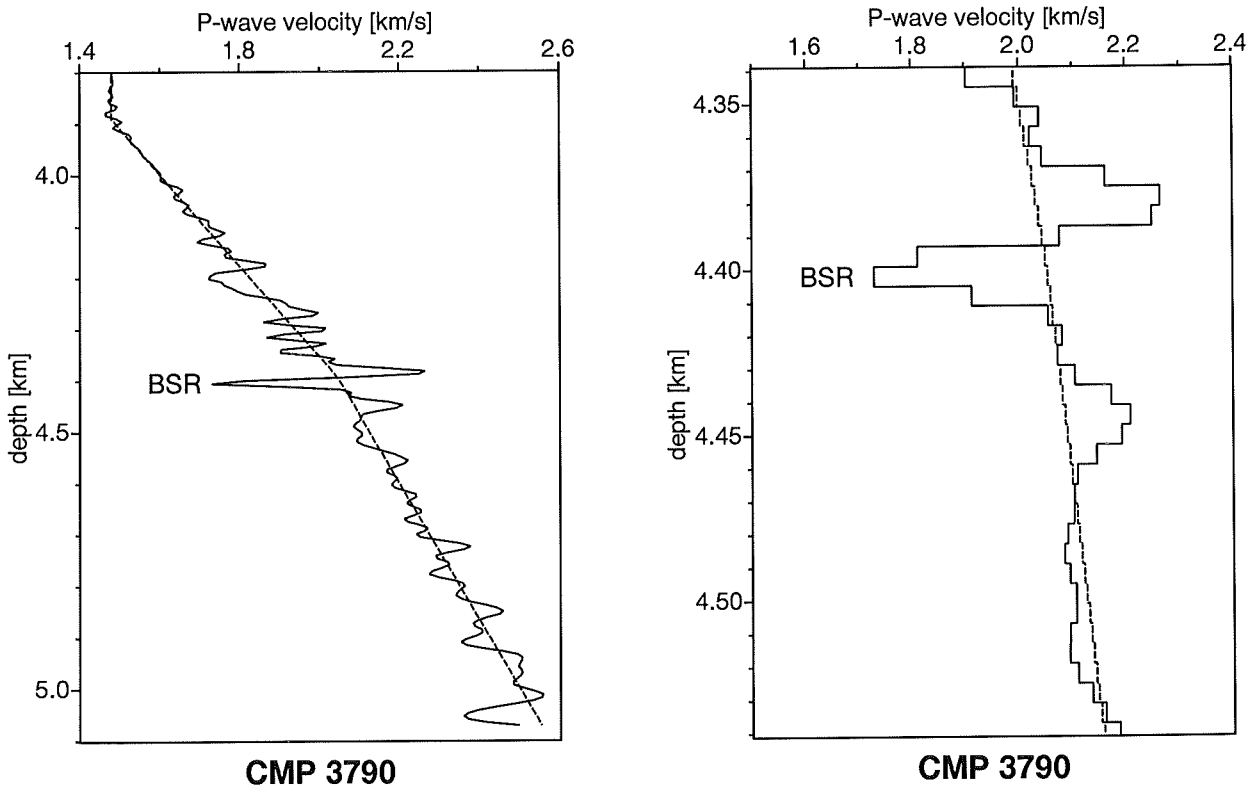

Figure 49: Velocity models obtained from full waveform inversion. The right plot shows a blow-up around the BSR. Depth intervals are $6m$. Dashed line: starting model, solid line: final model.

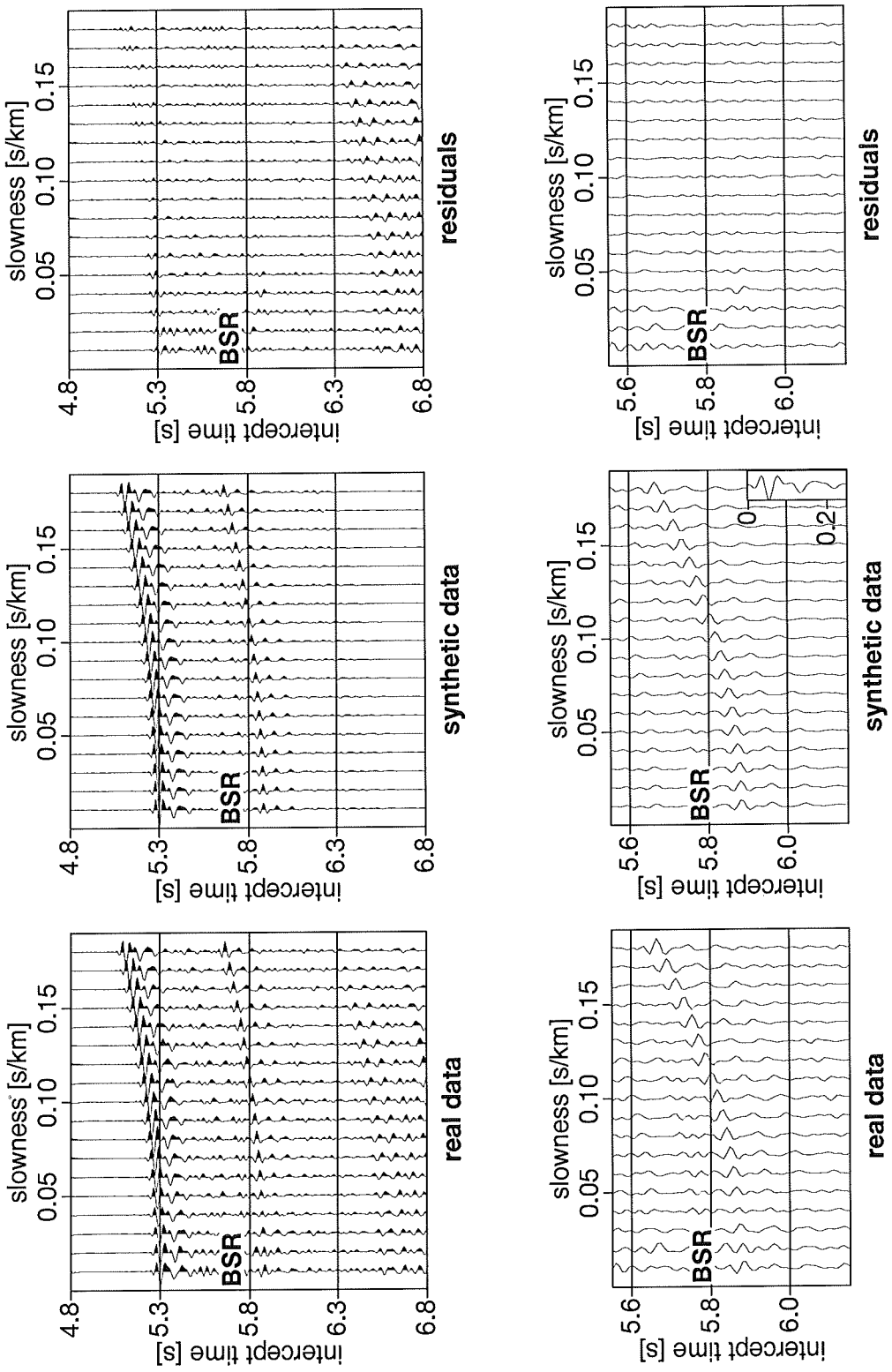

Figure 50: Real data in the (τ, p)-domain compared to synthetic data computed from the final model from the waveform inversion and residuals at CMP 3790. Lower figures: blow-up around BSR. The inset in the synthetic data displays the source signature.

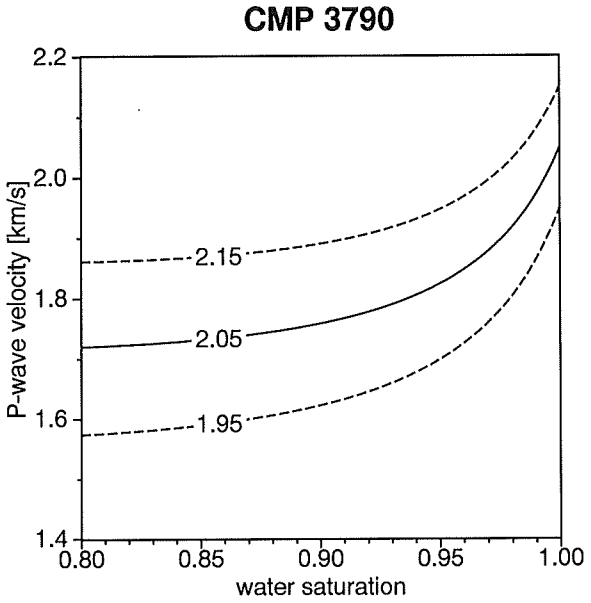

Figure 51: Compressional wave velocity as a function of water saturation at the depth of the BSR at location Peru 1017 CMP 3790. Variation of $V_{p,0}$ as given in the graph represents the approximate error margin for this modeling.

shallow and therefore be hidden by the seafloor reflection. The depth at which a BSR would be expected at $1.8km$ water depth (i.e. over the Miocene unconformity), assuming a thermal gradient of $0.05K/m$, which is a value obtained from a BSR in Yaquina Basin (ref. below) a bottom water temperature of $2°C$, hydrostatic pressure, and a pure water/methane system: it should be observed about $355mbsf$. It has to be noted, however, that Ballesteros et al. (1988) identified a BSR in th Lima Basin at approximately this distance from the trench axis in HIG line 13, a profile about $30km$ north of line 1018.

7.5.2 Reflection data from 9° S

Distribution of BSRs displays a different pattern further to the north. A pre-stacked depth migrated section re-stretched to time of the trenchward part of line CDP 2 is shown in fig. 52. In this and the following figures, time section are displayed, because BSRs are sometimes more difficult to identify in depth sections due to velocity stretching (ref. fig. 13 for comparison). A BSR can be clearly identified between CMPs 3520 and 3870 ($5.3 - 11.1km$ from the trench axis). The seaward boundary lies above the apex of a small subducted ridge. The landward termination is not that well defined, the BSR might be traced further upslope. No BSRs occur at the outer slope east of the presumed crustal boundary (fig. 13). The base of the methane HSZ beneath the lower slope basin in CDP 2 at about CMP 2900 ($21.5km$ from the trench) should be at about $605mbsf$, given a water depth of $4.2km$ and assuming a pure water/methane system as well as hydrostatic pressure. The temperature gradient was estimated at $0.04K/m$, which is the gradient at $21.5km$ from the trench axis in line 1018 (ref. section 8.1.4). This may already be within the metamorphic body, the top of which cannot be clearly delineated in the pre-stack migrated section (fig. 13). From fig. 14 it is also obvious that a BSR is present in Yaquina basin between CMPs 850 and 750 ($55.9 - 68.9km$ from the trench axis) or possibly even further upslope.

CDP 2 may be anomalous for this region because it is located across a laterally displaced basement ridge. Images of BSRs in the HIG data are poorer. Only the lower slope sections of these profiles were re-processed including pre-stack depth migration. All of these section display a similar distribution

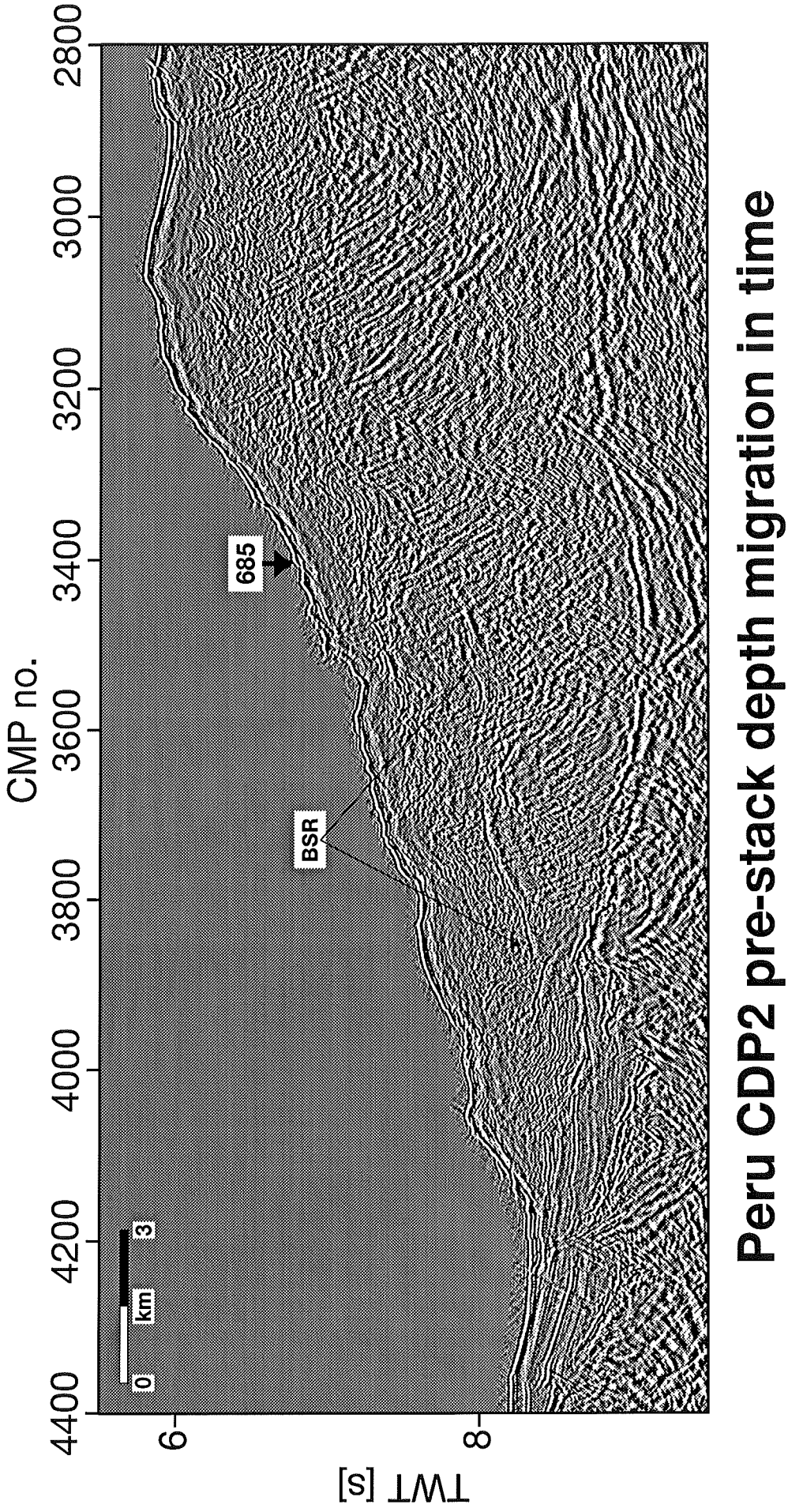

Figure 52: Pre-stack depth migrated section re-stretched to time of the seaward part of CDP 2. CMP spacing is $16.75m$. Site 685 was drilled during ODP Leg 112.

of BSRs. In HIG 2, problems with deconvolution (it was not possible to extract a proper operator for a spiking deconvolution) make it impossible to unambiguously identify BSRs (fig. 53). Probably, a BSR is displayed within the accretionary wedge (CMP 850), possibly above the western edge of the presumed metamorphic complex (CMP 1400). Identification of BSRs is easier in HIG 3 (fig. 54), where it appears as two black phases (negative with respect to the seafloor reflection) within the accretionary prism between CMPs 750 and 1130 ($4.8 - 11.7km$ from the trench axis). A BSR might also be located above the metamorphic complex (CMP 400). Data quality of line HIG 5 was better. There, the BSR can be clearly seen in the accretionary prism (fig. 55, CMPs 1100-1360, $8.7 - 13.0km$). It might be traced further landward.

The main differences between those observations and the pattern of BSR distribution at 12° S thus are (1) the presence of a BSR within the accretionary complex and (2) that BSRs are observed further upslope in Yaquina basin, whereas no BSRs can be observed in lines 1017 and 1018 or most other data across Lima Basin.

7.6 Nature of the BSR off the Nicoya Peninsula, Costa Rica line 9 CMP 1410

BSRs are present in a large area offshore Costa Rica northwest of Fisher Seamount (fig. 20). A location was selected along line 9 at which the velocity structure of the BSR was investigated. Fig. 56 displays a post-stack depth migrated section re-stretched to time around this location, CMP 1410. The BSR is characterized by its high amplitude and continuity. Both BSR and seafloor are almost horizontal there.

Two CMP-gathers, each of which consisted of 24 traces, were merged again. The resulting raw CMP-super-gather is shown in fig. 57. Amplitudes of adjacent traces varied considerably. Thus, efforts were made to recover amplitude-vs.-offset performance as described on p. 46. The data contain higher frequencies than the Peruvian data. A broad bandpass filter of $5 - 80Hz$ was applied in order to eliminate high-frequency noise. $50Hz$-noise peak had to suppressed in trace 20, to which therefore a $5 - 45Hz$ bandpass was applied.

The pre-processed CMP-gather is presented in fig. 58. For the right plot, the CMP-gather was normal-moveout (NMO)-corrected with water velocity obtained from the Monte Carlo inversion. The source signal had been created with a tuned airgun array. In the NMO-corrected gather, the direct arrival, which is a sequence of a negative and a positive half-wave starting at $3.1s$ TWT, can be clearly delineated from the ghost signal as a positive followed by a negative half-wave about $0.04s$ later. The time gap between both signals at first increases with increasing offsets, as it should be the case for increasing angles-of-incidence of the seismic ray. However, at far offsets over about $2050m$, it decreases again. The reason for this is that whereas depth sensors were integrated in the streamer, no depth control devices were attached to it (Hinz et al. 1992). According to the depth sensors, depth of the streamer was $30m$ at minimum offset, increased to a maximum depth of about $41m$ at $2100m$. The increase was steepest at the first channels. Then, it slightly decreased again to 39 m at maximum offset. These variations of streamer depth were critical for the waveform inversion, since they caused an artificial waveform-vs.-offset variation and they are in the order of magnitude of the expected thickness of a possible gas layer at the BSR.

The reflectivity series of the seafloor was again determined by finding the Wiener shaping filter which transforms the direct signal from the seafloor to the multiple signal. 21 adjacent minimum-offset traces were stacked for this purpose to increase the signal-to-noise ratio. The reflectivity series is plotted together with both direct and multiple signal in fig. 59. The reflectivity series again is dominated by a spike at the seafloor, though reflective energy is higher beneath the seafloor than at Peru 1018 CMP 1126. The main signal from seafloor and multiple are very similar. Later parts differ slightly probably due to noise, reflections beneath the seafloor or reflections from layers at the same TWT as the multiple

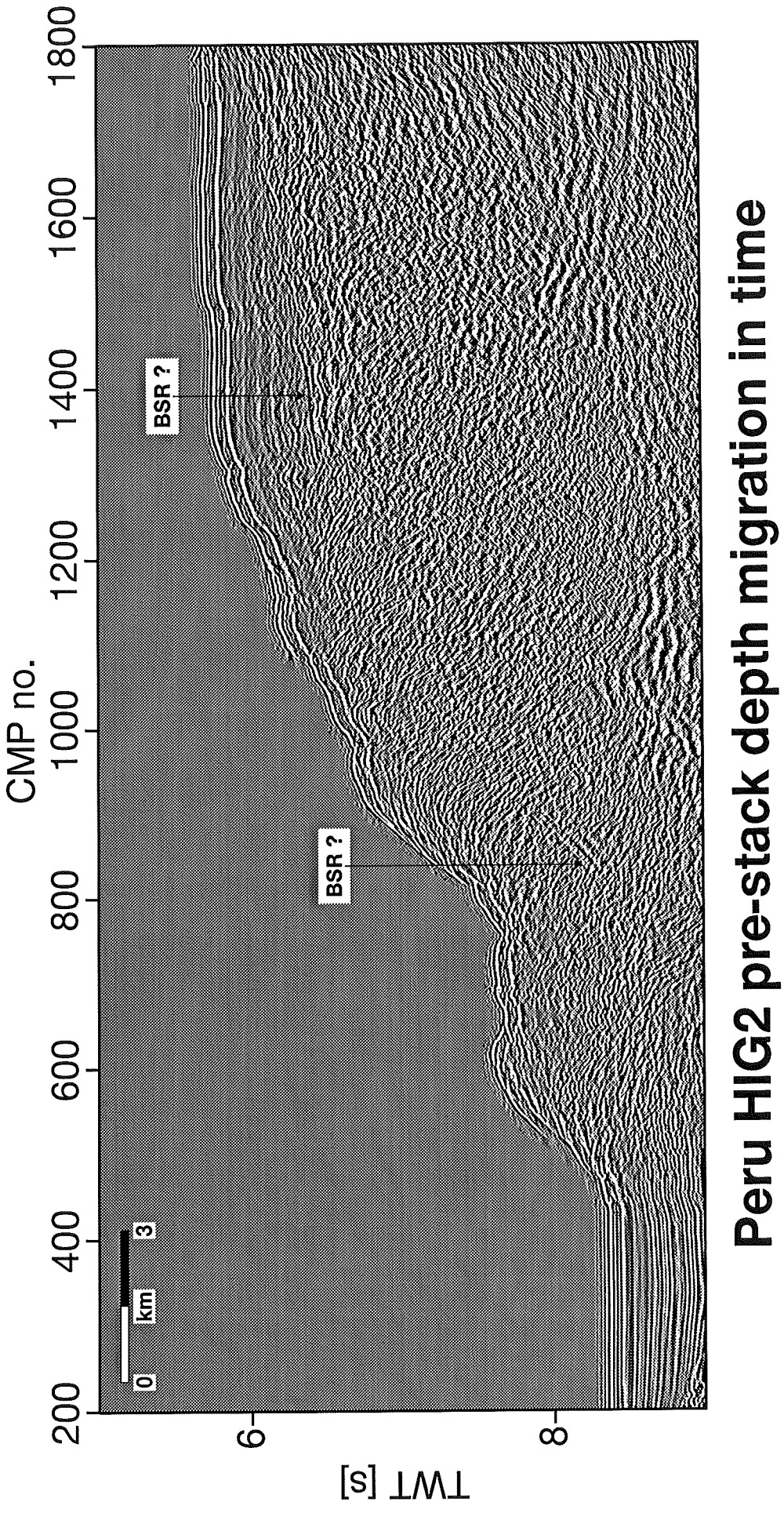

Figure 53: Pre-stack depth migrated section re-stretched to time of the seaward part of HIG 2. CMP spacing is $16.67m$.

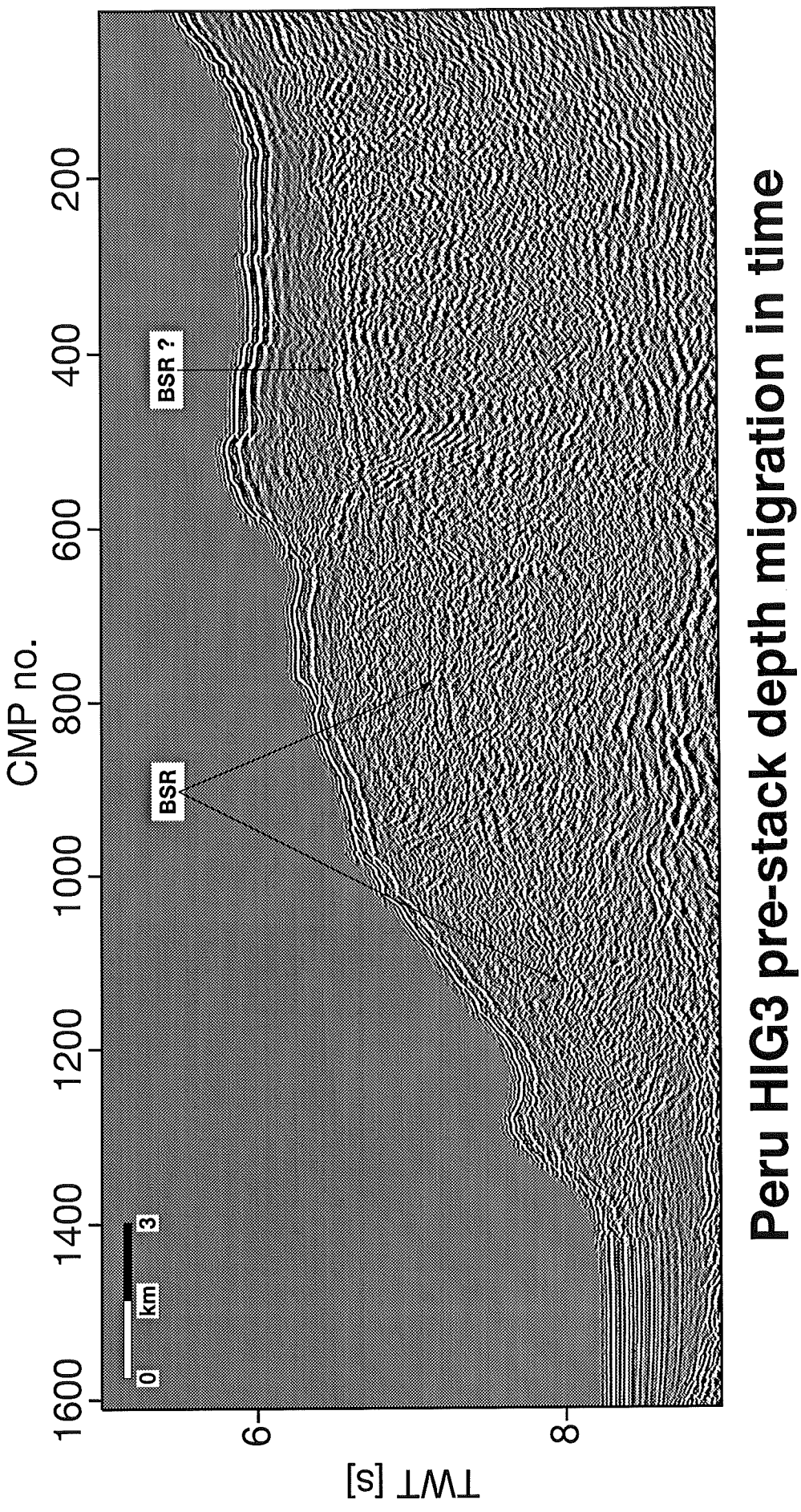

Figure 54: Pre-stack depth migrated section re-stretched to time of the seaward part of HIG 3. CMP spacing is $16.67m$.

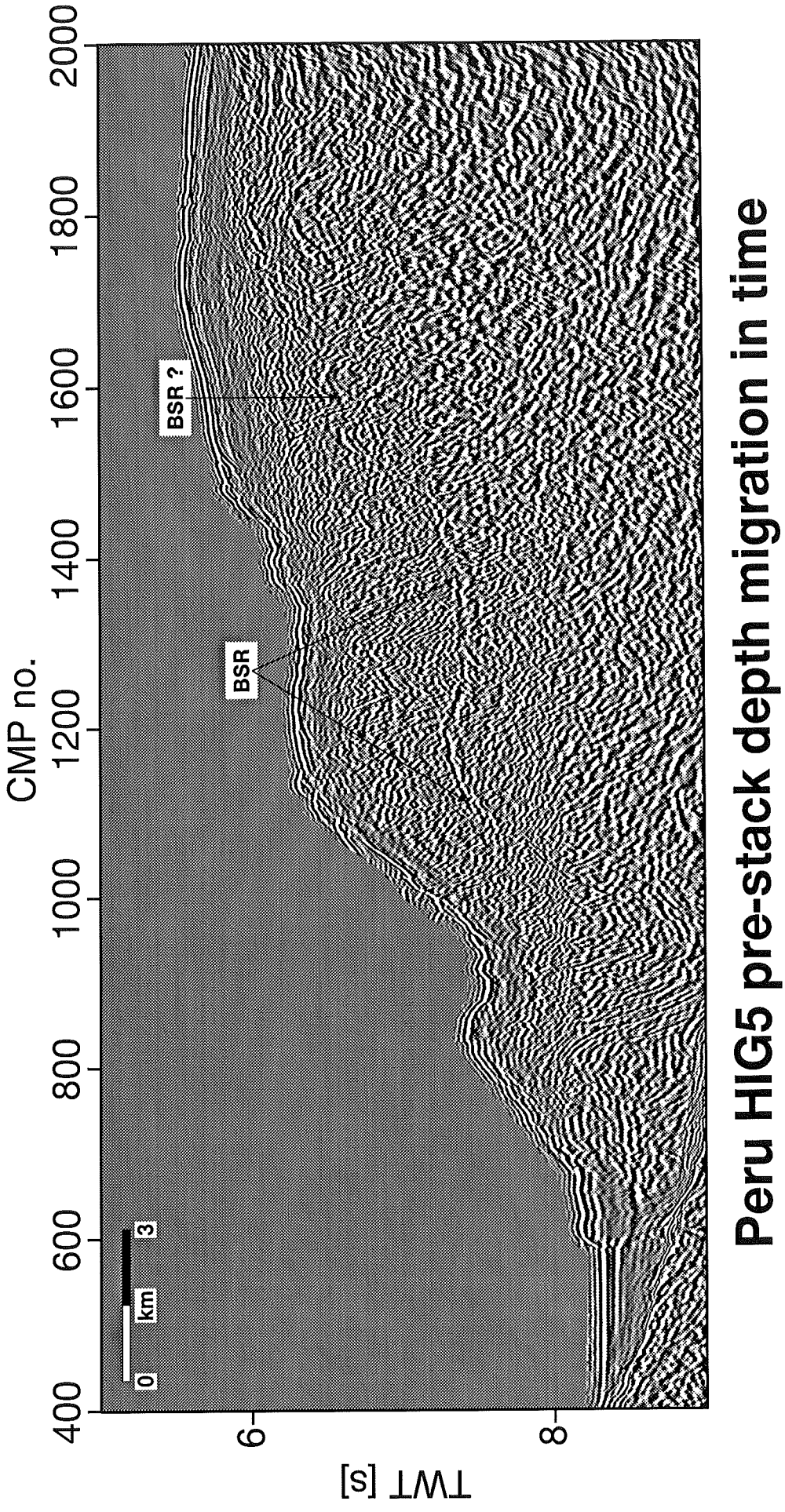

Figure 55: Pre-stack depth migrated section re-stretched to time of the seaward part of HIG 5. CMP spacing is $16.67m$.

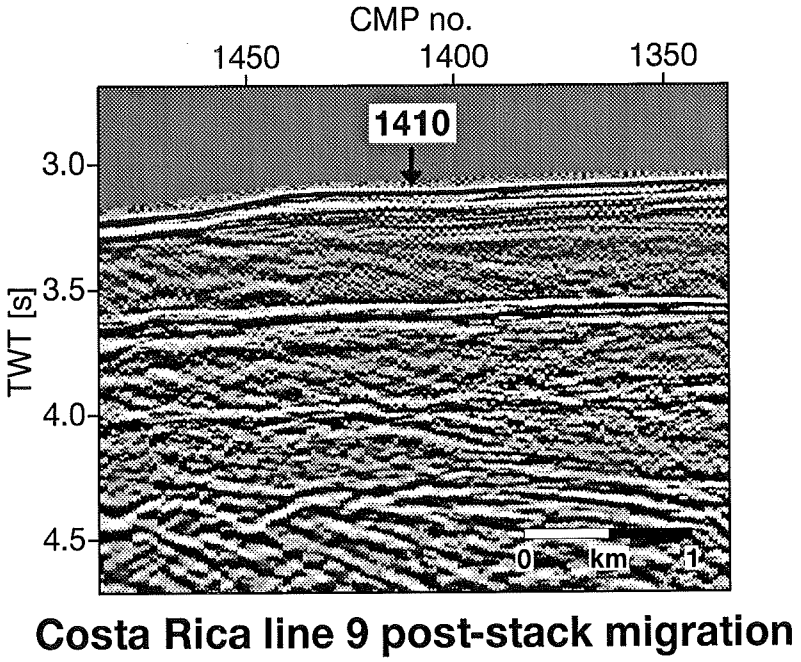

Figure 56: Post-stack depth migrated section re-stretched to time of Costa Rica line 9 around CMP 1410. Processing included spike deconvolution. Note a strong bubble pulse at about $0.2s$ beneath the seafloor. The arrow indicates the exact position of the location chosen for inversion.

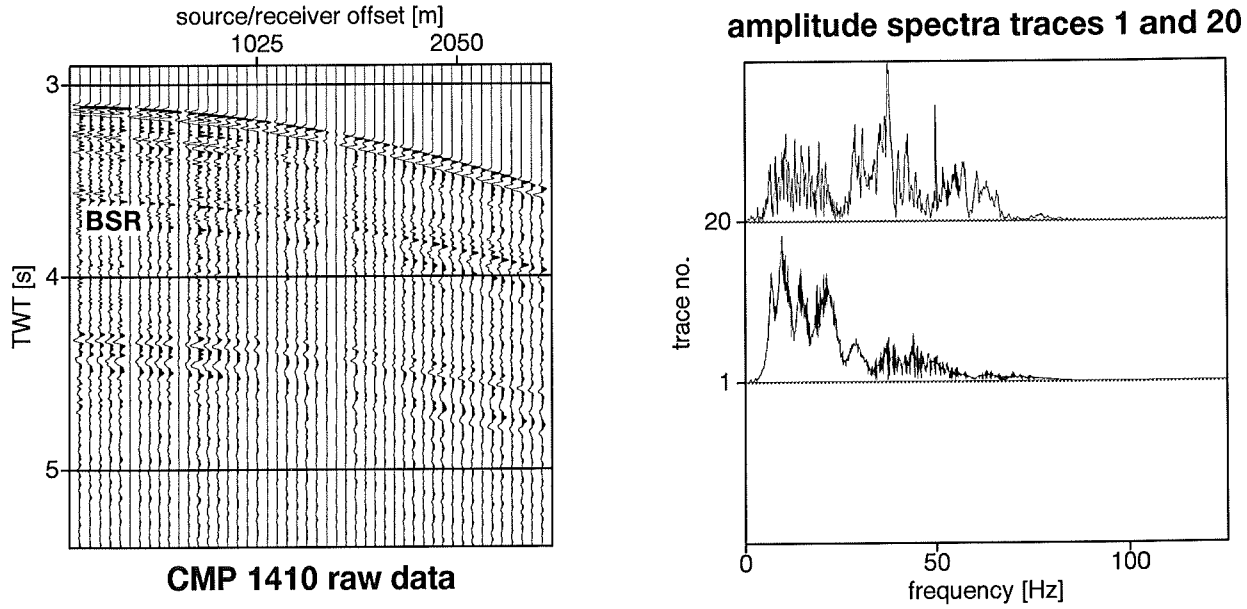

Figure 57: CMP 1410 super-gather of raw data together with amplitude spectra of two traces. No AGC. Minimum offset is $125m$, receiver spacing is $50m$. Note the remarkable differences of amplitudes in the CMP-gather. Trace 20 ($1075m$ offset) displays a distinct $50Hz$-noise peak in the amplitude spectra.

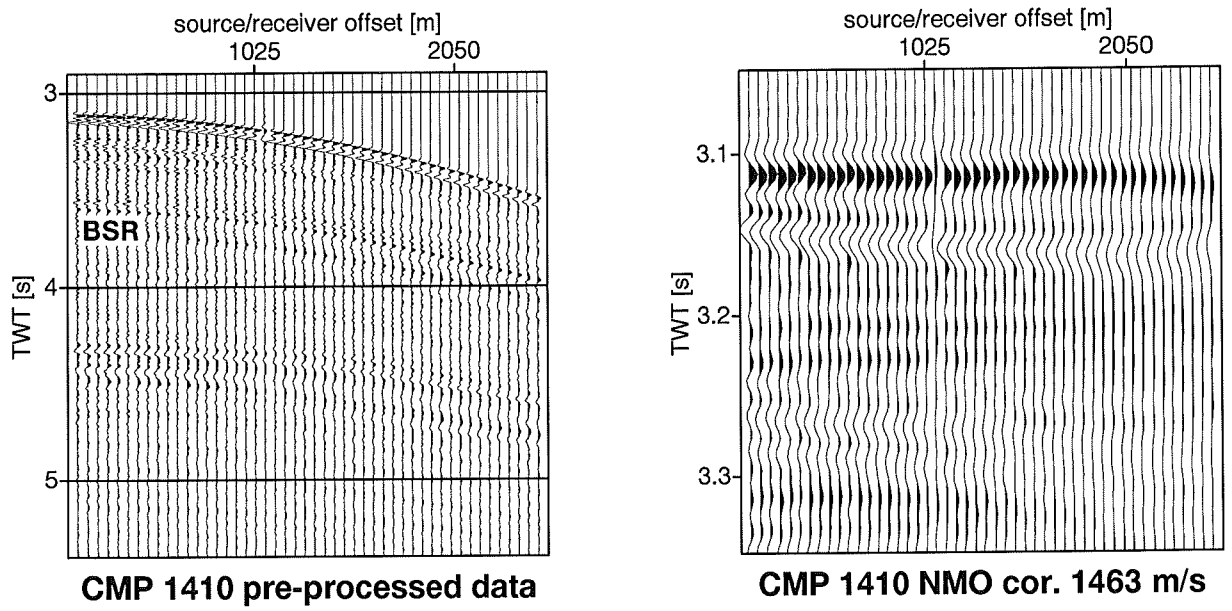

Figure 58: Pre-processed CMP 1410 super-gather. Ref. text for details about processing. No AGC. Different amplitudes and shape of signal at $1075m$ offset (trace 20) are caused by different filter parameters (ref. text). The right side shows the CMP-gather at the seafloor after NMO correction with water velocity. Water velocity is from the Monte Carlo inversion. Note that the time difference between direct and ghost signal is highest at medium offsets.

reflection from the seafloor. The seafloor itself was therefore regarded again as a single reflector, although this assumption was not as clear as for most Peru data. Reflections beneath the seafloor, however, might cause some distortions of later parts of a source wavelet, which was obtained by extracting the signal from the seafloor. The seafloor reflection coefficient was found to be 0.14. It is obvious that the source signal is a superposition of a direct arrival and a ghost signal which was reflected at the water/air-interface and arrived about $0.036s$ after the direct arrival, which is corresponding to a streamer depth of about $27m$ (depth sensors at minimum offset measured a streamer depth of $30m$).

The starting model for the full waveform inversion obtained from the Monte Carlo inversion scheme is plotted in fig. 60. If applying a simple velocity gradient between seafloor and BSR, V_p at the BSR would have exceeded the interval velocity within the layer beneath the BSR. Therefore, a gradient was determined down to a certain depth z_i between seafloor and BSR. Beneath z_i, V_p was kept constant at the interval velocity within the layer beneath the BSR. See section C.1 for details. Density at the seafloor is $1.37g/cm^3$, which is realistic compared to measurements on cores from DSDP Site 565. There, about $1.35 - 1.40g/cm^3$ were measured in cores from the first few meters beneath the seafloor, as well as a sonic velocity of about $1.50 - 1.55km/s$.

In order to minimize effects due to the variations of streamer depth, slownesses of $p = 0.06 - 0.20$ where used for the inversion. Those slownesses correspond to offsets at which the depth of streamer was relatively constant. The fine velocity structure, which is presented in fig. 61, again gives clear evidence for the presence of free gas at the BSR. The BSR is a LVL at which V_p drops from $2.00km/s$ to an average velocity of $1.76km/s$ in an $18m$ thick layer and a minimum velocity of $1.72km/s$ in a $6m$ thick depth interval. Compared to the Peru data, results appear to be less smooth. This is probably due to distortions of the source wavelet because of varying streamer depths and the higher frequency range which was used for this data set. Also, the velocity increase beneath the BSR seems to be more gradual than that in the Peru data sets. This might be real (gradient in gas concentration) or caused by differences in data

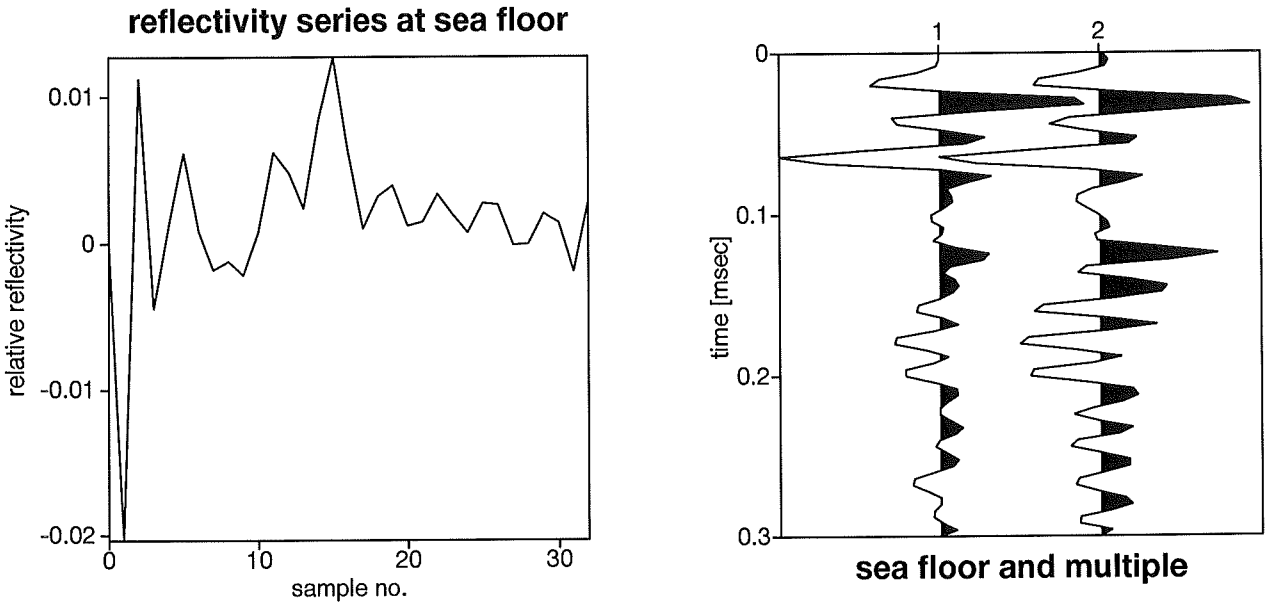

Figure 59: CMP 1410. Left: reflectivity series at the seafloor relative to the energy of the signal within the window which was chosen for the Wiener filter (left). Right: Signal from seafloor (left) and multiple (right). Signal from the multiple was multiplied by -1 and scaled such that peak-to-peak amplitudes from both seafloor and multiple are approximately the same.

acquisition. Velocity undulations beneath the BSR again probably have to be attributed to inaccuracies in later parts of the source wavelet. Velocity fluctuations beneath $\sim 3.3km$ are artifacts probably caused by reflections from the rough surface. Comparison of real, synthetic and residual energy (fig. 62) indicates an adequate model down to well below the BSR.

The data set was inverted again to test, whether inaccuracies of later parts of the source wavelet considerably affect resulting velocities at the BSR. For this purpose, a "synthetic" source wavelet, a combination of two Ricker wavelets, which have about the same main frequency as the data-derived source wavelet, was used. The second Ricker wavelet, which corresponded to the ghost signal from the sea/air interface, was superimposed to the first wavelet with a slight delay according to the depth of the streamer. The resulting velocity profile is plotted in fig. 63 together with the results presented in fig. 61 and the source wavelets for the inversions. As expected, the structure at the BSR did not change much, but undulations beneath it are stronger. A second LVL about $100m$ beneath the BSR is caused by the lack of a bubble signal in the "synthetic" source wavelet, which can be observed in the data-derived source wavelet at about $0.2s$.

Calculating V_p as a function of water saturation (fig. 64) yields a more pronounced drop of V_p at high water saturation compared to results from the Peruvian BSRs. This is due to a lower value of K_g at the lower pressures predicted at the BSR at $2.6km$ depth. The increase of the slope of the function as pressure decreases ultimately leads to the results of Domenico (1977) which were for gas under ambient conditions. A velocity of $1.76km/s$ gives a minimum concentration of $\sim$ 0.2% of free gas in the pore space. The maximum concentration would be about 4%.

7.7 Distribution of BSRs at the Costa Rican convergent margin

BSRs are wide-spread in profiles from the Costa Rican margin obtained during R/V "Sonne" Legs SO-76 and SO-81. Fig. 20 shows sections in which BSRs occur. Since processing of those lines has not yet been

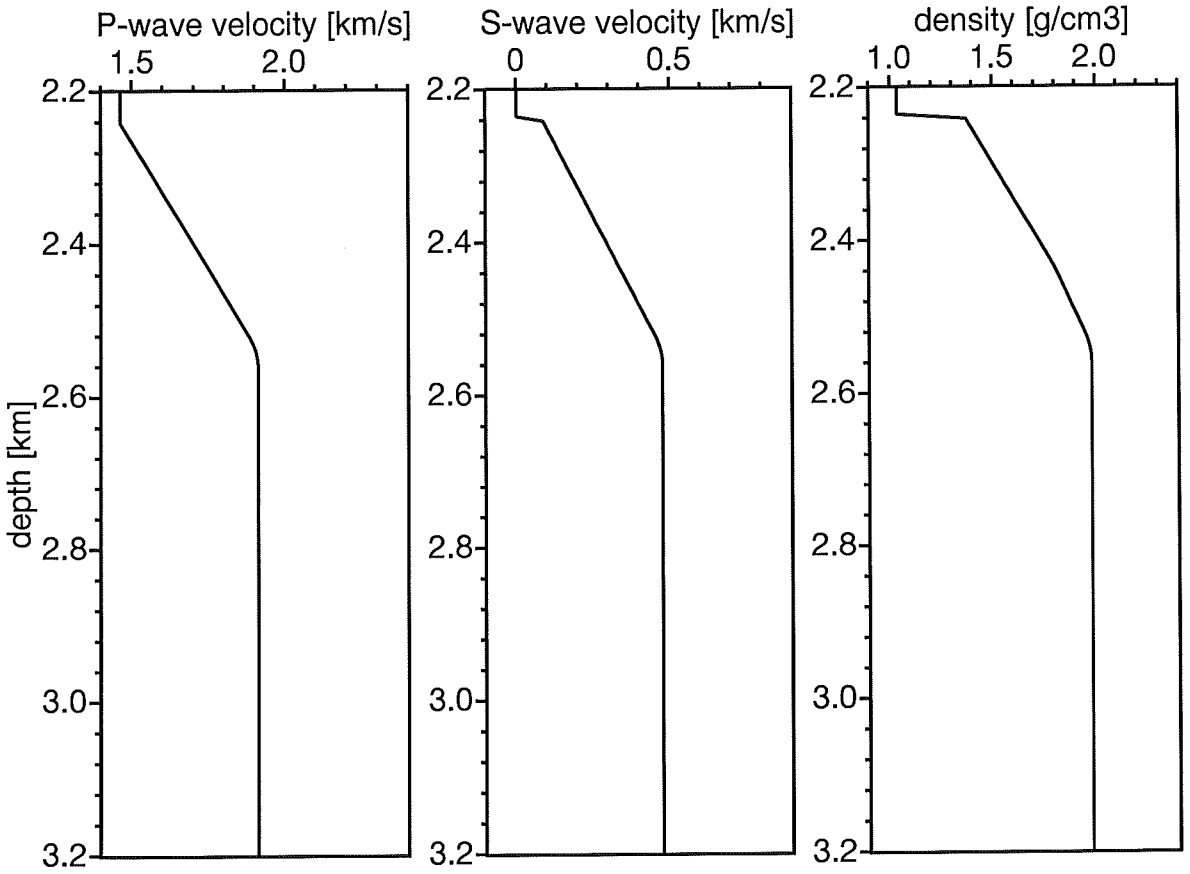

Figure 60: Starting model for the full waveform inversion CMP 1410.

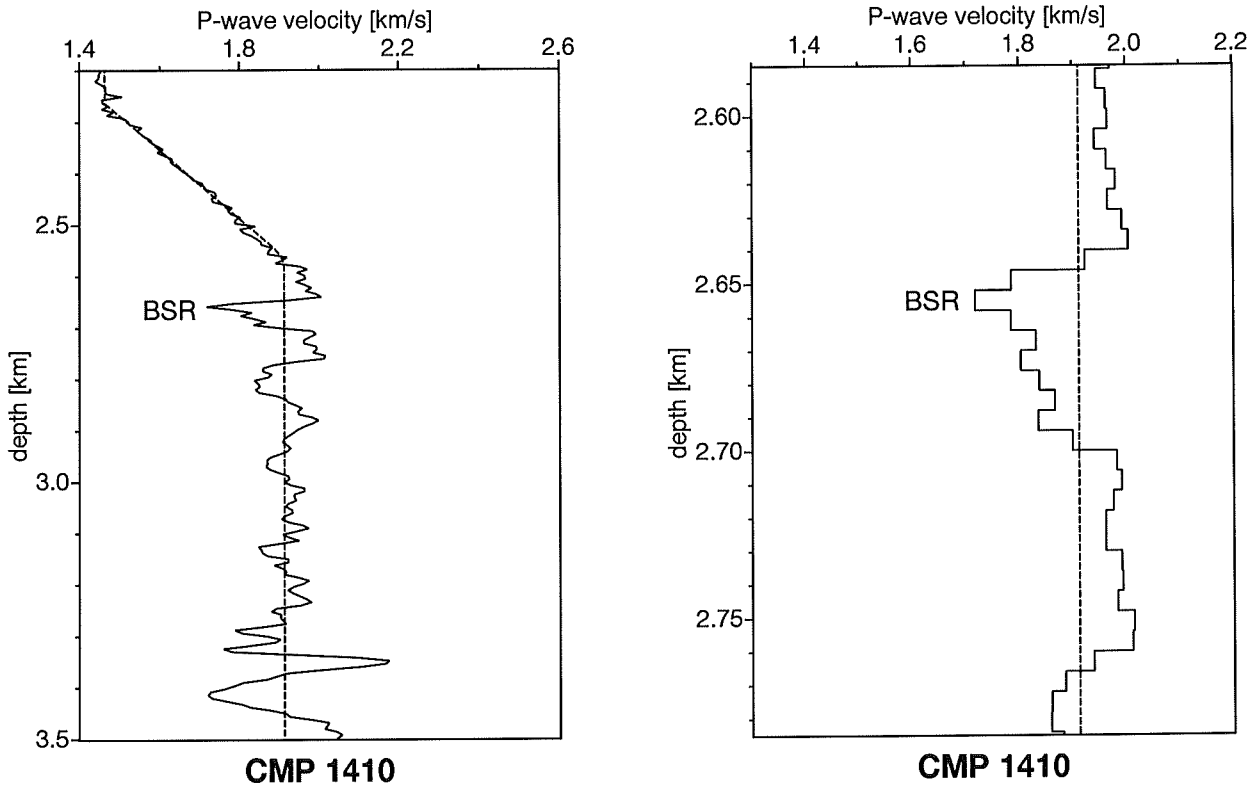

Figure 61: Velocity models obtained from full waveform inversion. The right plot shows a blow-up around the BSR. Depth intervals are $6m$. Dashed line: starting model, solid line: final model.

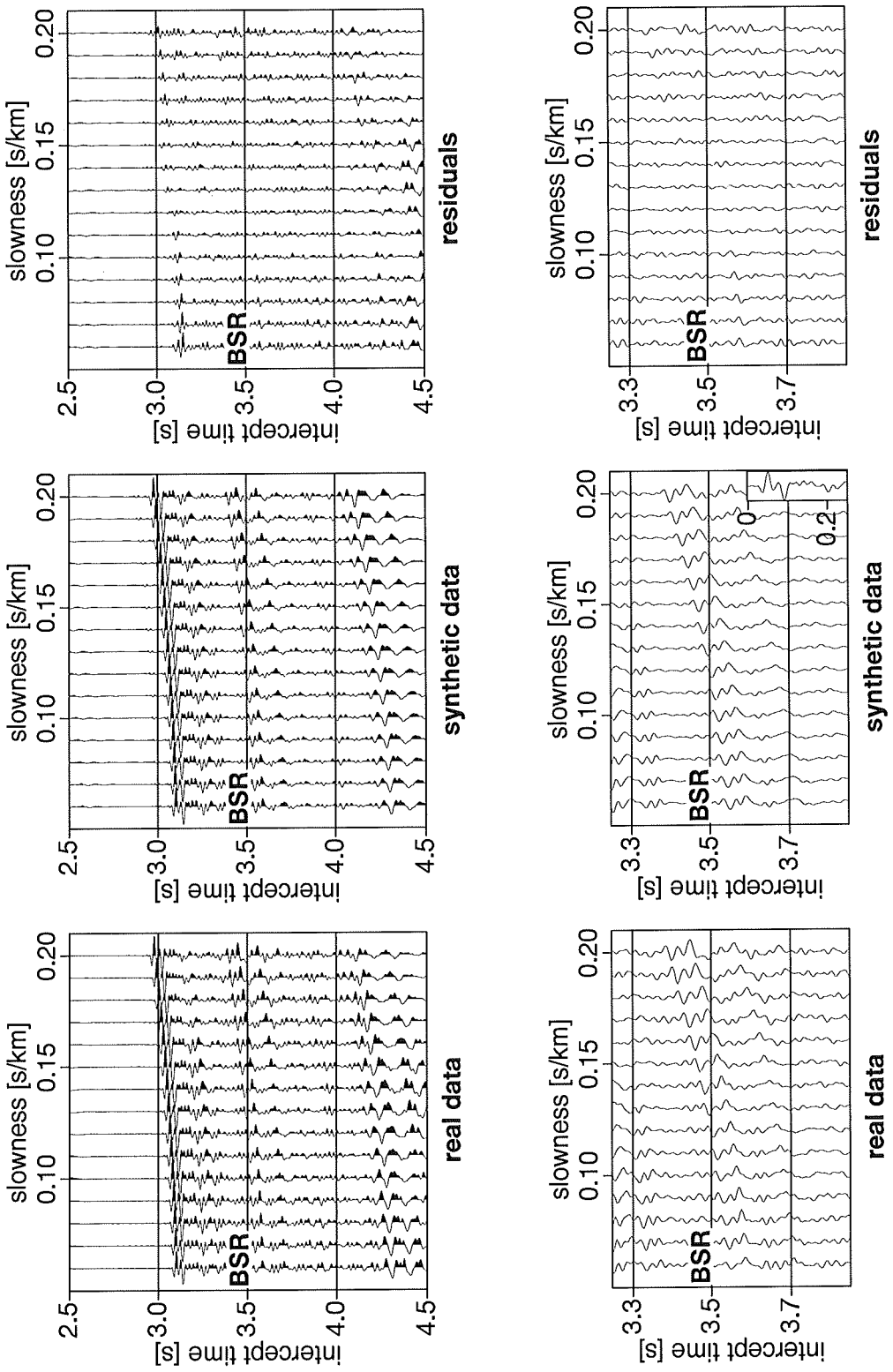

Figure 62: Real data in the (τ, p)-domain compared to synthetic data computed from the final model from the waveform inversion and residuals at CMP 1410. Lower figures: blow-up around BSR. The inset in the synthetic data displays the source signature.

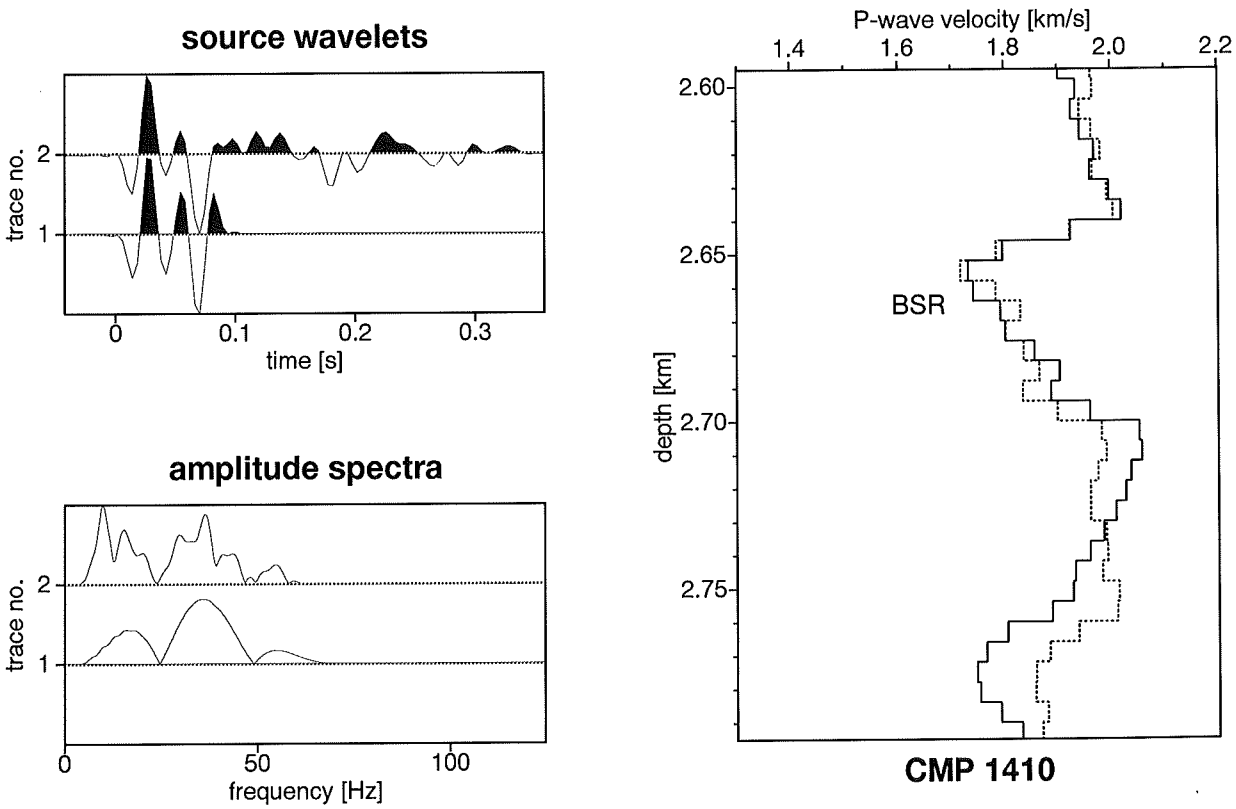

Figure 63: Left: Source wavelet derived from the data compared to the "synthetic" source wavelet (upper plots), corresponding amplitude spectra (lower plots). Right: Comparing velocity models in the vicinity of the BSR obtained from full waveform inversion using the data-derived source wavelet (dotted line) and the "synthetic" source wavelet (solid line).

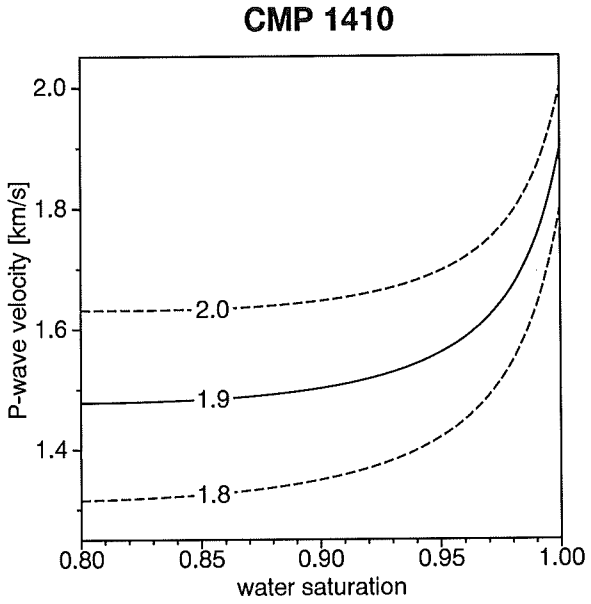

Figure 64: Compressional wave velocity as a function of water saturation at the depth of the BSR at location Costa Rica 9 CMP 1410. Variation of $V_{p,0}$ as given in the graph represents the approximate error margin for this modeling.

completed and only locations at which BSRs could be identified unambiguously are shown, this map may be incomplete.

Northwest of Fisher Seamount, in an area were a smooth Pacific Plate is being subducted, BSRs extend almost all over the region at which hydrates are stable down to close to the trench axis (see also migrated sections of lines 8 and 9, figs. 21 and 22). The BSR is absent, however, at line 15 between about the $2000m$ isobath and the trench, an area of a huge slump (Hinz et al., in press). It disappears along line 7a when moving to the northwest, into the direction of Site 565. This is consistent with observations made by Shipley et al., (1992), who did not identify BSRs in 3-d seismic data around this site.

Between Fisher Seamount and Quepos Plateau, the slope appears indented by subduction of a swath of seamounts. Areas in which slope failure caused by slumps in the trailing wake subducted seamounts took place reveal no BSRs (lines 17a, 2, and perhaps 13). BSRs are also absent between approximately above the $2000m$ isobath in the area between lines 2, 3, and 4, as well as in line 6 where it crosses those profiles, though no larger slump features can be observed from topography and BSRs are observed up to about $700m$ water depth in the other regions.

Southeast of Quepos Plateau, BSRs again are very continuous and extend over almost the whole slope region where hydrates are stable at the seafloor. An interesting feature in line 5 is that the BSR starts close to the trench axis right at the décollement. It terminates landward in rather shallow waters almost intersecting the seafloor (fig. 23).

In summary, BSRs at the Costa Rican margin northwest of Cocos Ridge are present almost wherever the phase boundary of methane hydrates is located within the sediment column, with three exceptions: (1) the northwestern edge around DSDP Site 565, (2) southeast of Fisher Seamounts in areas where slumping took place trailing subducted seamounts, and (3) in the region north of Quepos Plateau above the $2000m$ isobath.

8 Heat flux from the depth of the BSR

8.1 Heat flux at the central Peruvian margin

8.1.1 Velocity, density, and thermal conductivity

Sections of lines Peru 1017 and 1018, in which BSRs were observed, were pre-stack depth migrated with special emphasis on obtaining precise depth and velocity information. This was achieved by using a higher depth-sampling rate together with a higher sampling rate for focusing analyses compared to migrations of the whole lines for structural interpretation. In addition, a data set of 1018 was used to which a variable-norm signature deconvolution (Gray, 1979) had been applied by the U.S. Geological Survey. Higher resolution but lower penetration had been achieved by wavelet deconvolution, compared to the spike deconvolved data used for imaging the structure of the deep sub-surface.

Interval velocities between seafloor and BSR obtained from pre-stack depth migration and subsequent focusing analyses are plotted on top of the seismic time sections in figs. 65 and 66. Velocities from line 1017 are considerably above those from line 1018. It has to be kept in mind however, that focusing analysis is inaccurate in areas with dip. Line 1017 was shot downslope, whereas line 1018 was shot upslope. This might explain the velocity differences in both lines above dipping structures. The effect of an increase of interval velocities if a structure is dipping into one direction and a decrease if it dips into the other direction was observed by many 'MIGPACK' operators at GEOMAR. Eq. 48, which implies that the velocity error is independent of the direction of the dip, is only true for the single-layer case.

Both velocity models were utilized together with velocities obtained from the Monte Carlo inversions to obtain a velocity-vs.-two-way-traveltime model of the sediments above the BSR. Velocities from dipping layers were partially ignored. In particular, velocities from the western and eastern edges of line 1017 as well as from the western edge of line 1018 were not used for this function: At those locations there was a considerable dip at the BSR.

The resulting velocity function is displayed in fig. 67. It should be noted that an error in interval velocity of $100m/s$ at a water depth of $4050m$ and a depth of the BSR at $4620m$ (the situation at Peru 1018 CMP 1126) is caused by an error of only $9m/s$, i.e. 0.6%, in RMS-velocities. Conventional velocity analyses of MCS data assume an error of approximately $50m/s$ in RMS-velocities (Sheriff and Geldart, 1983). This also means that the error in total depth of the BSR caused by an velocity error of $100m/s$ also is only 0.6%, i.e. $28m$, and thus, effects due to the velocity differences displayed figs. 65 and 66 are less dramatic than it might appear from those plots.

Bulk density of the sediment column above the BSR is only relevant if lithostatic load is assumed at the BSR. Measurements in cores from ODP 112 Sites 682, 683, 685, and 688, which are located at the outer margin, were used to obtain a rough density-versus-depth function (fig. 68).

Thermal conductivity K was measured in cores from the same ODP sites, as well as during logging at Site 685 (fig. 69). Theoretically, K should increase with depth as porosity decreases. No such trend is obvious from fig. 69, however. Thus, an average value of $K = 0.878W/(m \cdot K)$ was used for further computations.

8.1.2 Estimate of heat flux at Nazca Plate

Heat flux through Nazca Plate as it enters the trench at 9° and 12° S was estimated based on its age. The age of Nazca Plate at 9° S was determined from magnetic anomalies (displayed e.g. in Huchon and Bourgois, 1990) at about $29.5Ma$. At 12° S, it is about $41.5Ma$.

Sclater et al. (1980) compiled heat flux values from the southern Pacific depending on the age of the oceanic plates. The average values were $48.1mW/m^2$ for the age interval of $20 - 35Ma$ (9° S) and

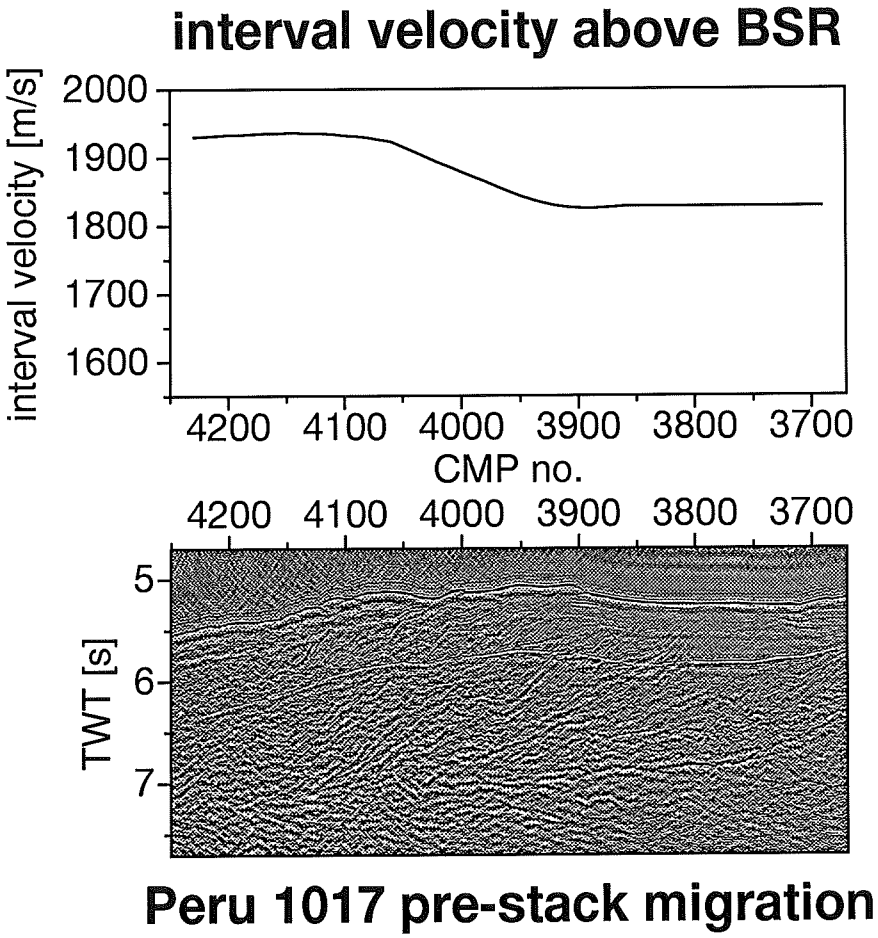

Figure 65: Velocities of the depth interval above the BSR obtained from focusing analyses during pre-stack depth migration, line 1017.

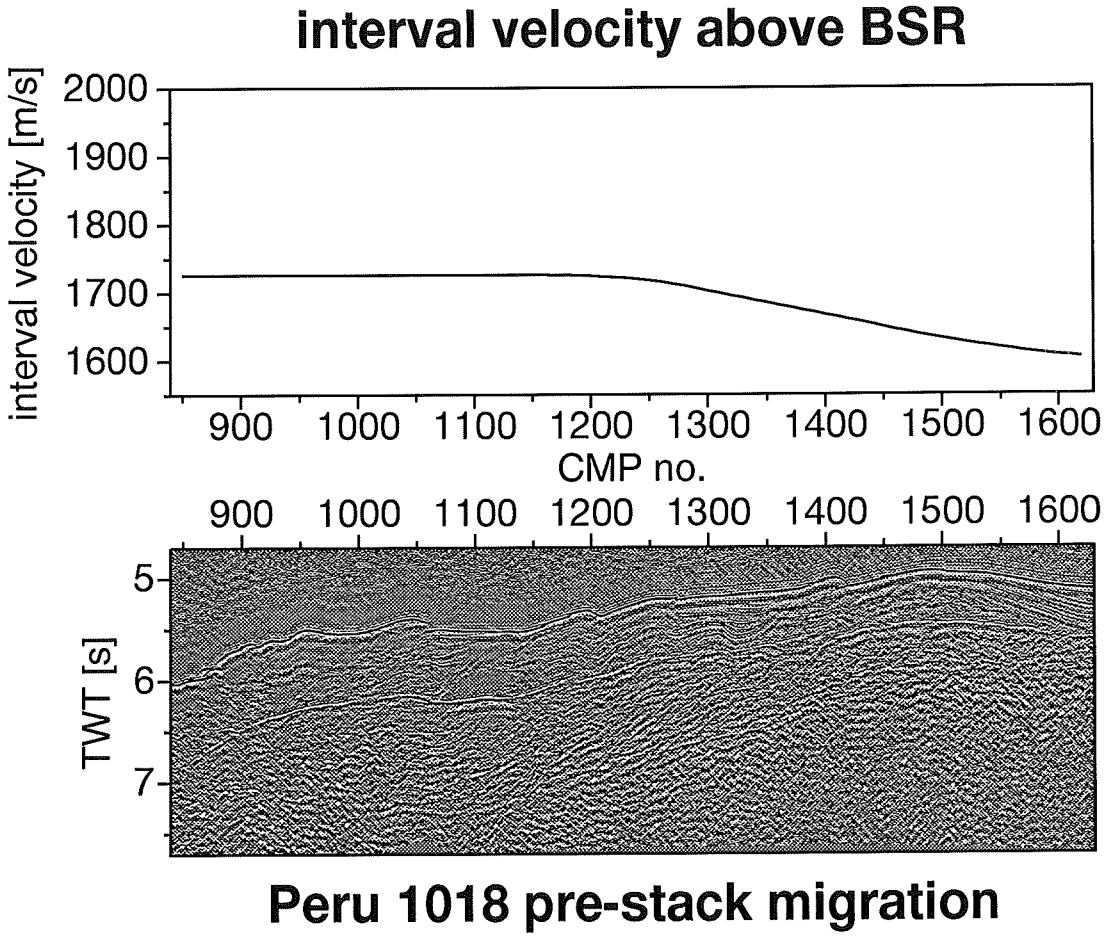

Figure 66: Velocities of the depth interval above the BSR obtained from focusing analyses during pre-stack depth migration, line 1018.

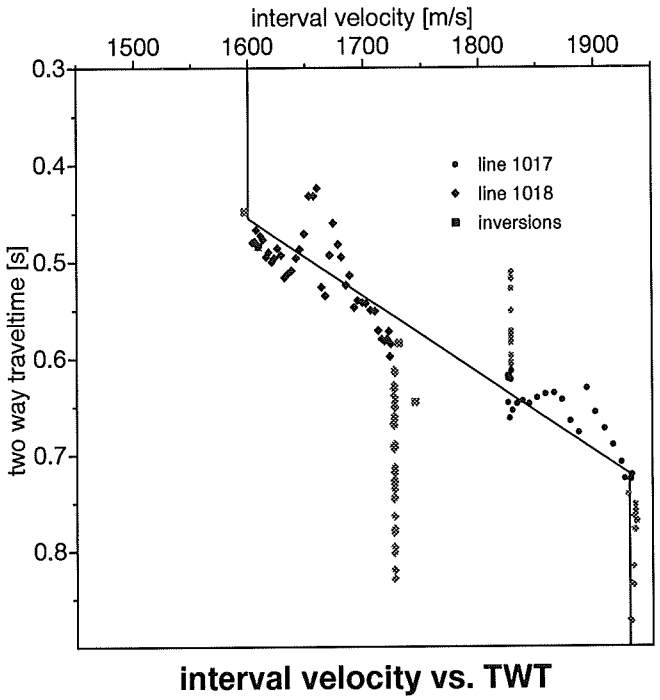

Figure 67: Interval velocities plotted against two-way-traveltime above BSRs in lines 1017 and 1018. Grey symbols denote values which were ignored for computation of the interval velocity gradient (solid line).

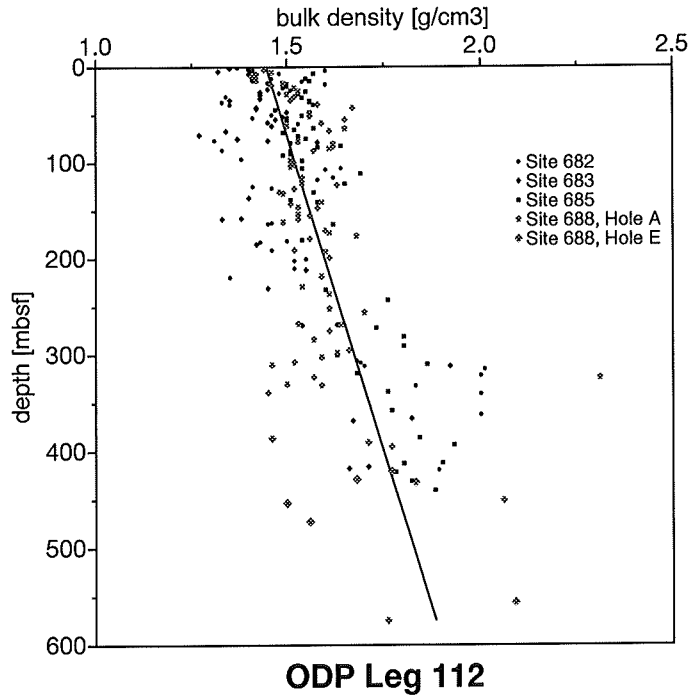

Figure 68: Bulk density in cores from ODP Leg 112 Sites 682, 683, 685, and 688, which are located at the outer Peruvian margin.

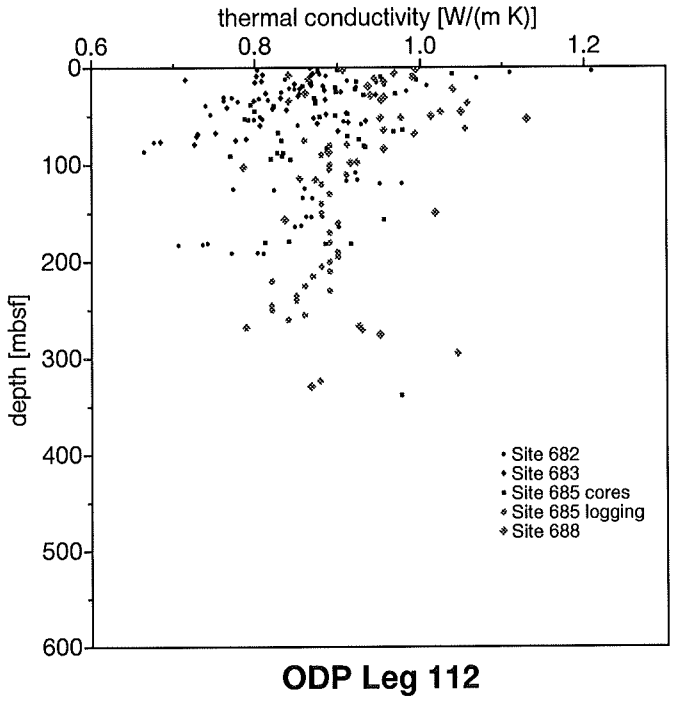

Figure 69: Thermal conductivity from ODP Leg 112 Sites 682, 683, 685, and 688, which are located at the outer Peruvian margin (from core measurements except for Site 685).

$46.0 mW/m^2$ for $35 - 52 Ma$ (12° S). These values are only rough averages, however they give at least constraints for heat flux values expected at the Nazca Plate as it enters the Peru subduction zone.

8.1.3 Heat flux from BSRs at 12° S

Line 1017

Fig. 70 displays temperature at the BSR. Hydrostatic and lithostatic pressure represent the two end-members of possible pressure at the BSR. Note that the non-normal track of line 1017 with respect to the trench axis (ref. fig. 7) was taken into account for computation of the distance from the trench by multiplying distances by $cos(25°) = 0.9$. Almost no discrepancies can be observed between temperatures obtained if using depths obtained directly from pre-stack migration instead of time picks together with a general interval velocity/TWT function. Temperatures at the BSR are roughly $1K$ higher if assuming lithostatic instead of hydrostatic pressure. The general decrease of temperature with increasing distance from the trench reflects topography and subsequent decreasing pressure at the BSR.

Errors introduced by eventual uncertainties in the velocity function are much more significant for the computation of the temperature gradient (fig. 71). The difference between values obtained from both methods for the computation of depth, i.e. time picks plus velocity function and depth picks, is highest close to the landward termination of the BSR, which can be explained by the dip of the BSR in this region (ref. fig. 65) resulting in an erroneous model for depth migration. Thus, using time picks and the general interval velocity/TWT function from fig. 67 may be more accurate than to use depth picks. Pressure at the BSR is not critical. This is due to the small relative maximum error in temperature at the BSR of $\sim 1K$ caused by inaccurate pressures at the BSR compared to the temperature difference between BSR ($\sim 25° - 27°C$) and seafloor ($2°C$). The increase of the temperature gradient towards the continent though temperature at the BSR decreases is caused by a shallower depth of the BSR beneath

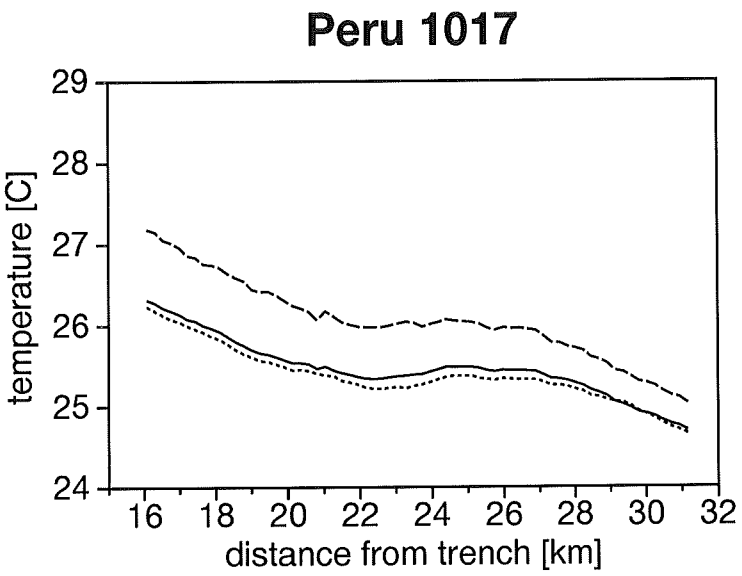

Figure 70: Temperature at the BSR along line 1017 assuming hydrostatic pressure and an interval velocity/TWT function (solid line), hydrostatic pressure and depth directly from pre-stack depth migration (dotted line), and lithostatic pressure and an interval velocity/TWT function (dashed line). Distances from the trench were corrected for the angle between the track of line 1017 and the normal to the trench axis (ref. text).

the seafloor.

Heat flux through the sediment column between BSR and seafloor is shown in fig. 72. The general increase towards the continent is consistent with results from conventional measurements (Yamano and Uyeda, 1990). Note the smooth character of the graph giving no indications for small-scale lateral variations of heat flux. The seismic section of line 1017, which was used for computing heat flux above the BSR, is displayed together with heat flux in fig. 73.

Line 1018

Temperature at the BSR along line 1018 is shown in fig. 74. The BSR could be traced closer towards the trench than in line 1017. Values as a function of distance from the trench can be well compared to those obtained from line 1017. The temperature function is relatively smooth.

Lateral variations of temperature gradient (fig. 75) and subsequently heat flux (fig. 76) can be observed between 28 and $32km$ from the trench axis. In this area, a thrust fault cuts sediments down to well beneath the BSR (fig. 77). A similar but less pronounced pattern is displayed at another thrust fault about $22km$ away from the trench. Offsets of the BSR are observed across those faults indicating that the heat flux fluctuations are not merely caused by variations in topography above the BSRs. The BSR smoothly cuts another prominent thrust fault about $19km$ away from the trench axis indicating that heat flux fluctuations in this area may be assigned mainly to a variation of sediment thickness above the BSR.

Discrepancies between heat flux obtained from picks directly in the depth domain and those from time picks together with a time-to-depth conversion using the general velocity function in fig. 67 are less pronounced than along line 1017. They are largest at the western edge of the line, where the BSR has a relatively steep dip.

In general, heat flux through the lower slope along lines 1017 and 1018 increases from $\sim 25mW/m^2$at $13km$ from the trench to $\sim 55mW/m^2$ about $33km$ away from the trench axis. These

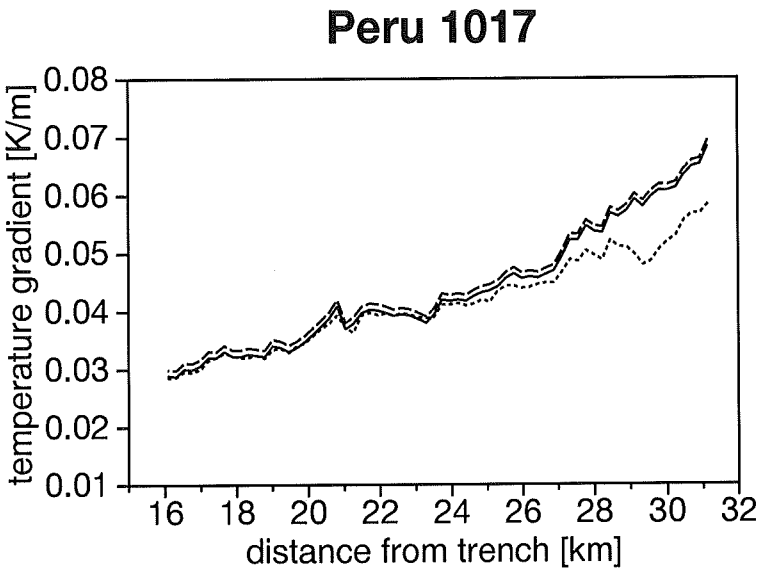

Figure 71: Temperature gradient at the BSR along line 1017 assuming hydrostatic pressure and an interval velocity/TWT function (solid line), hydrostatic pressure and depth directly from pre-stack depth migration (dotted line), and lithostatic pressure and an interval velocity/TWT function (dashed line). Distances from the trench were corrected for the angle between the track of line 1017 and the normal to the trench axis (ref. text).

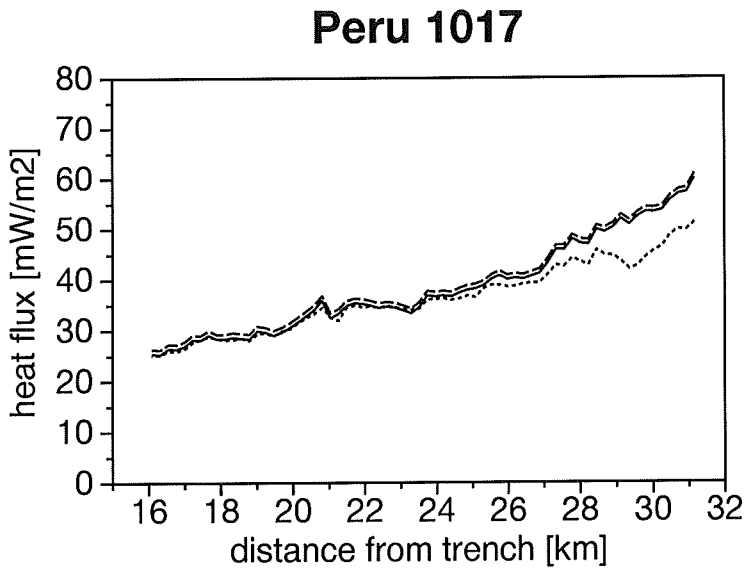

Figure 72: Heat flux above the BSR along line 1017 assuming hydrostatic pressure and an interval velocity/TWT function (solid line), hydrostatic pressure and depth directly from pre-stack depth migration (dotted line), and lithostatic pressure and an interval velocity/TWT function (dashed line). Distances from the trench were corrected for the angle between the track of line 1017 and the normal to the trench axis (ref. text).

Figure 73: Pre-stack depth migrated section in time of the part of Peru line 1017 which was used for the computation of heat flux. CMP spacing is $25m$. Heat flux is displayed below the seismic section. Distances from the trench axis were corrected for the angle between the track of line 1017 and the normal to the trench axis (ref. text).

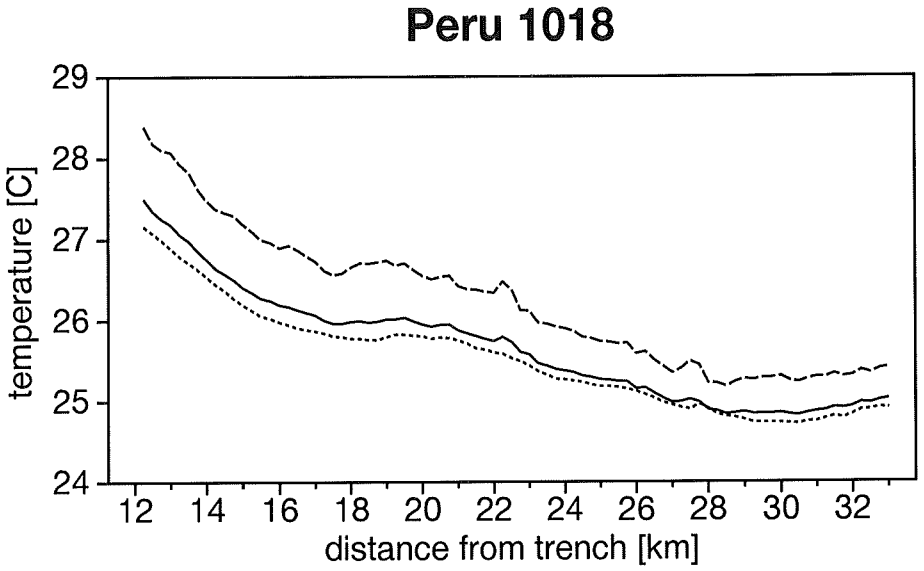

Figure 74: Temperature at the BSR along line 1018 assuming hydrostatic pressure and an interval velocity/TWT function (solid line), hydrostatic pressure and depth directly from pre-stack depth migration (dotted line), and lithostatic pressure and an interval velocity/TWT function (dashed line).

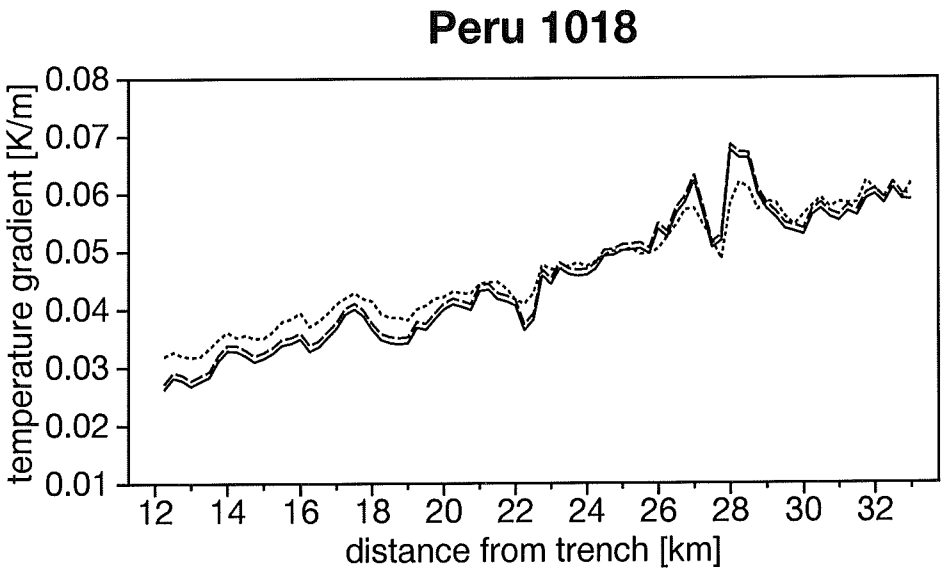

Figure 75: Temperature gradient at the BSR along line 1018 assuming hydrostatic pressure and an interval velocity/TWT function (solid line), hydrostatic pressure and depth directly from pre-stack depth migration (dotted line), and lithostatic pressure and an interval velocity/TWT function (dashed line).

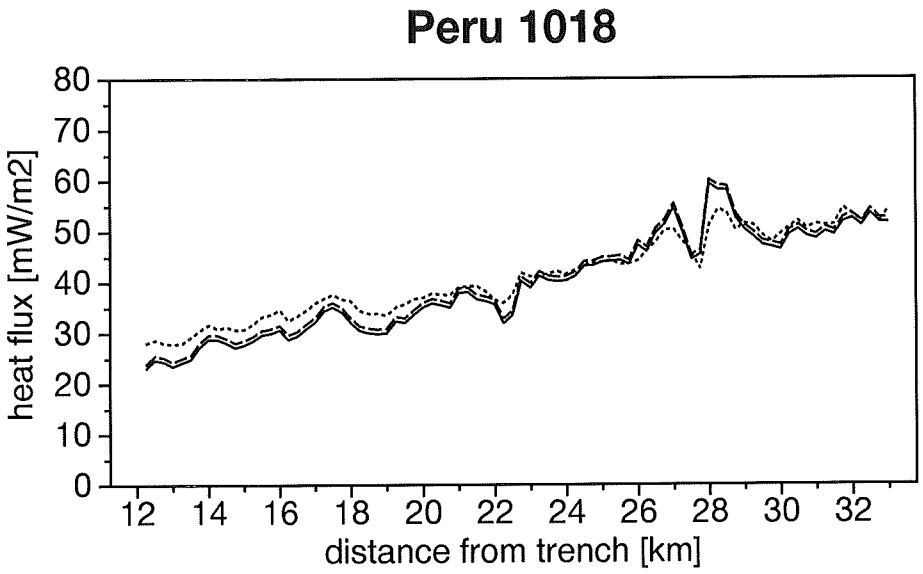

Figure 76: Heat flux above the BSR along line 1018 assuming hydrostatic pressure and an interval velocity/TWT function (solid line), hydrostatic pressure and depth directly from pre-stack depth migration (dotted line), and lithostatic pressure and an interval velocity/TWT function (dashed line).

values compare well with results from conventional heat flux measurements (ref. fig. 19). Since locations of the conventional measurements were not along the track of one of the seismic lines however, they are not suited for a more precise calibration of BSR heat flux measurements. On the other hand, heat flux obtained from bore hole temperature measurements within the first $37mbsf$ at Site 688, which is located close to the landward termination of the BSR in line 1018, is about $10mW/m^2$ lower than the BSR heat flux (p. 38 table 4).

8.1.4 Heat flux from BSRs at 9° S

BSRs occur closer to the trench in the area around 9° S. Seismic records from that area, i.e. CDP 2, HIG 2, HIG 3, and HIG 5, did not allow an accurate determination of velocities above the BSR mainly because of relatively short streamer lengths (ref. table 3 for acquisition parameters). Therefore, pre-stack depth migrated sections were re-stretched to time and TWT picks were converted to depth using the interval velocity/TWT function obtained from the two southern lines. Comparing depths of the BSR computed from time picks and the velocity function with depths obtained from pre-stack migration of line CDP 2 in Yaquina Basin, where velocity focuses were better than at the lower slope due to shallower water depths, justified this approach: At CMP 800, the BSR was at $309mbsf$, if converting time picks to depth, compared to $334mbsf$ obtained directly from the depth section. A relatively steep dip of the BSR, however, was the reason why the velocity above the BSR at this location was not taken into account for obtaining the general velocity-vs.-TWT function.

Line CDP 2

In addition to a BSR in the accretionary wedge, a BSR is present in Yaquina Basin about $56 - 58km$ away from the trench. Temperature, temperature gradient, and heat flux assuming both hydrostatic and lithostatic pressure at the BSR are plotted versus distance from the trench axis in fig. 78.

Heat flux close the trench axis is above $30mW/m^2$. There is a pronounced peak in the tem-

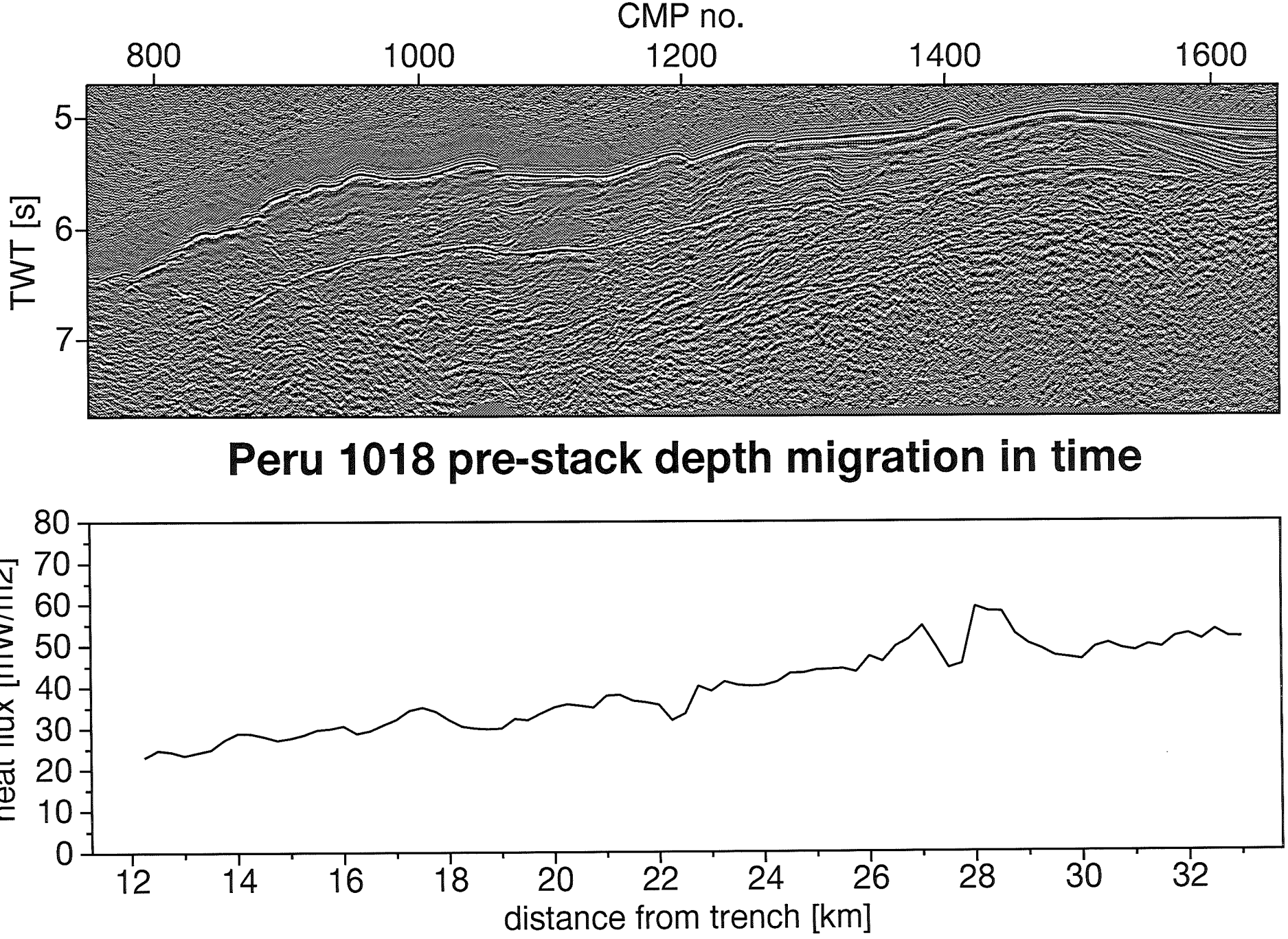

Figure 77: Pre-stack depth migrated section in time of the part of Peru line 1018 which was used for the computation of heat flux. CMP spacing is $25m$. Heat flux is displayed below the seismic section.

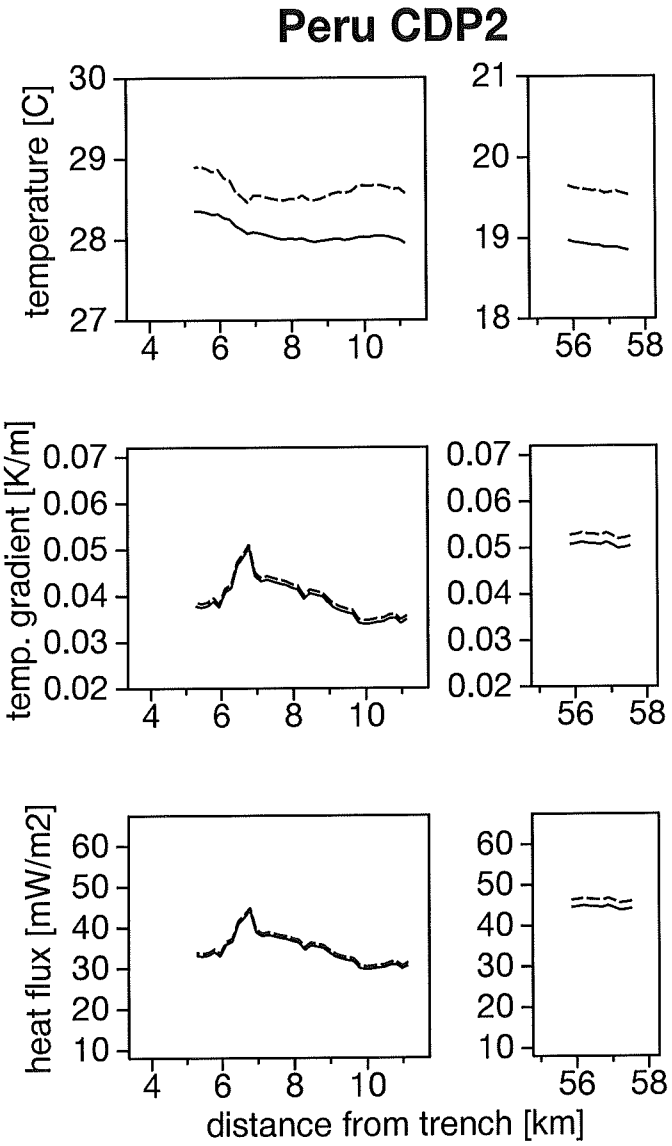

Figure 78: Temperature, temperature gradient, and heat flux from the depth of the BSR along line CDP 2 assuming hydrostatic pressure (solid line) and lithostatic pressure (dashed line). Depth of the BSR was computed from an interval velocity/TWT function obtained from lines 1017 and 1018.

perature gradient and heat flux profiles $\sim 6.8km$ away from the trench axis. This peak appears to be mainly caused by a small-scale topographic low above the BSR rather than a "pull-up" of the BSR itself. This is evident from fig. 79: TWT to the BSR does not fluctuate considerably on a small scale. This observation is supported by the smooth temperature profile, if assuming hydrostatic pressure. There might be a large-scale trend in the heat flux profile indicating an increase towards the trench axis, which is partly hidden by the distinct peak. Heat flux in Yaquina basin at $\sim 56 - 58km$ from the trench axis has been determined at $\sim 45mW/m^2$. Heat flux obtained from bore hole measurements at Site 685 is in the same range as BSR heat flux from CDP 2 (p. 38 table 4).

HIG lines
The BSR in line HIG 2 could not be identified unambiguously. Therefore, heat flux was only computed for lines HIG 3 and HIG 5. Temperature, gradient, and heat flux profiles along those lines again assuming hydrostatic and lithostatic pressure at the BSR are shown in fig. 80. All profiles are relatively smooth. There appears to be a slight increase of heat flux from ~ 30 to $\sim 35mW/m^2$ towards the trench along line HIG 3. Those values compare well with values obtained from line CDP 2. Slightly lower values of $\sim 25mW/m^2$ have been computed from line HIG 5, where the BSR occurs farther away from the trench, which may support evidence for an increase of heat flux towards the trench. Values from this line are similar to those computed at the seaward termination of the BSR, which is located at about the same distance from the trench in line 1018.

8.2 Heat flux at the Costa Rican margin

8.2.1 Velocity, density, and thermal conductivity

Offshore Costa Rica, heat flux was computed from the depth of BSRs in three seismic profiles, Costa Rica lines 5, 8, and 9 (ref. fig. 20 for locations). Only line 8 had been pre-stack depth migrated before completion of the present investigations. Fig. 81 displays migration velocities on top of the migrated section. Interval velocities between BSR and seafloor are relatively constant. They are highest at the lower slope, where BSR and seafloor are sub-horizontal. The interval velocity from the Monte Carlo inversion at CMP 1410 in line 9 is considerably higher ($1744m/s$). Therefore, an average value between the average of migration velocities and the value from inversion was used as interval velocity above the BSR (ref. eq. 52). Fig. 82 displays interval velocities from migration and the inversion as a function of TWT.

Density was computed as a function of depth beneath the seafloor based on measurements on cores from DSDP Leg 84 Site 565 (fig. 83, eq. 53). Thermal conductivity was estimated from a geometric mean relation between sea water and grain conductivity as $K = 0.94W/(m \cdot K)$ (eq. 54).

8.2.2 Heat flux

A general pattern in all of the Costa Rica lines is that the BSR gets shallower the closer to the trench, unlike in the Peruvian data. Heat flux in the western area was investigated along lines 8 and 9. In the eastern area, line 5 was used.

Line 8
Temperature, gradient and heat flux profiles as a function of distance from the trench axis along line 8 are shown in fig. 84. All functions in general are quite smooth. Slight small-scale fluctuations in thermal gradient and heat flux profiles are not reflected in TWT to the BSR indicating topography, i.e. variations of sediment thickness above the BSR, as their cause (see p. 41 fig. 21, CMPs 1000-1450). Neither uncertainties in pressure nor inaccurate velocities show a significant effect on heat flux. Heat flux

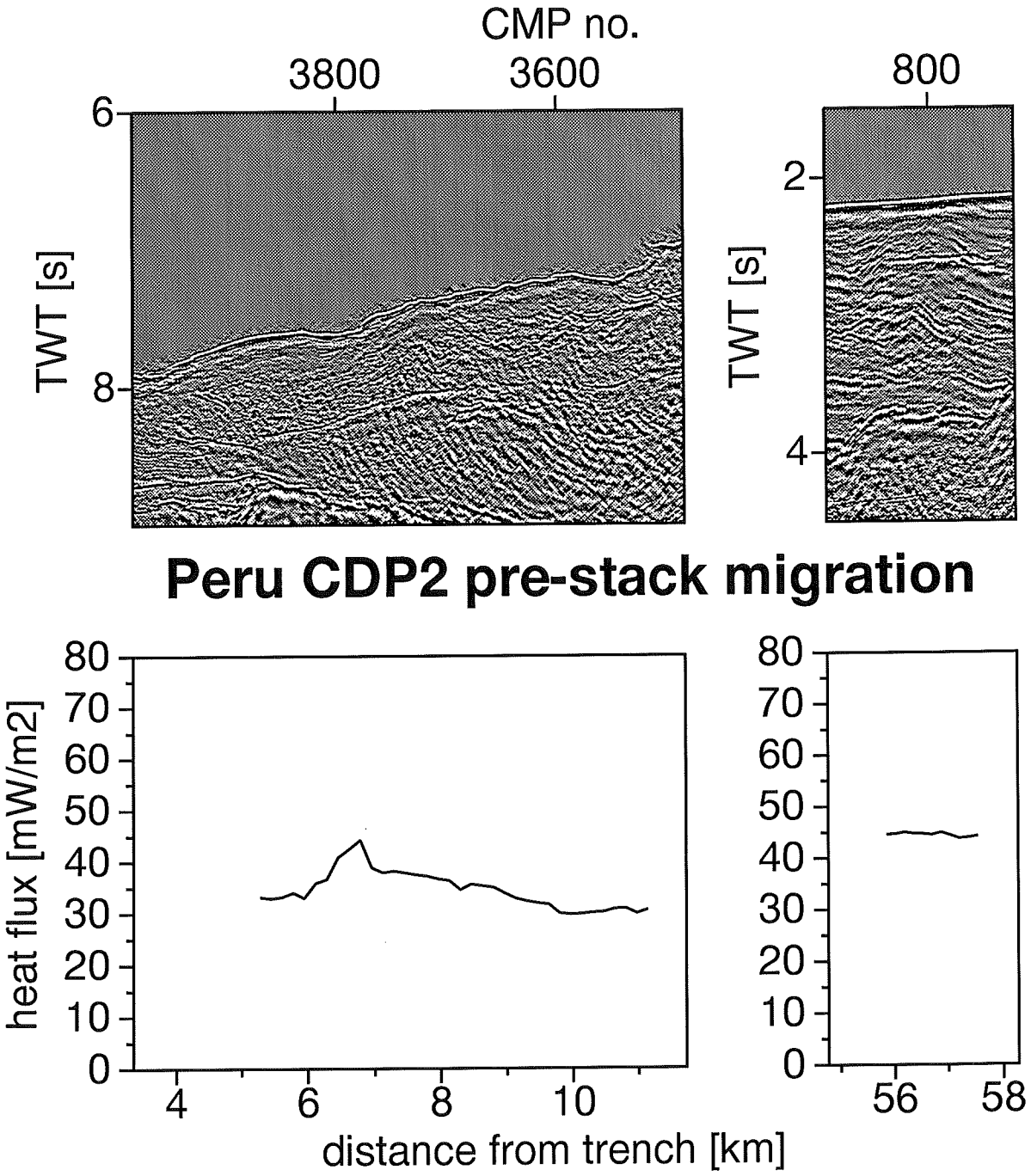

Figure 79: Pre-stack depth migrated section in time of those parts of Peru line CDP 2 which were used for the computation of heat flux. CMP spacing is 16.75m. Heat flux is displayed below the seismic sections.

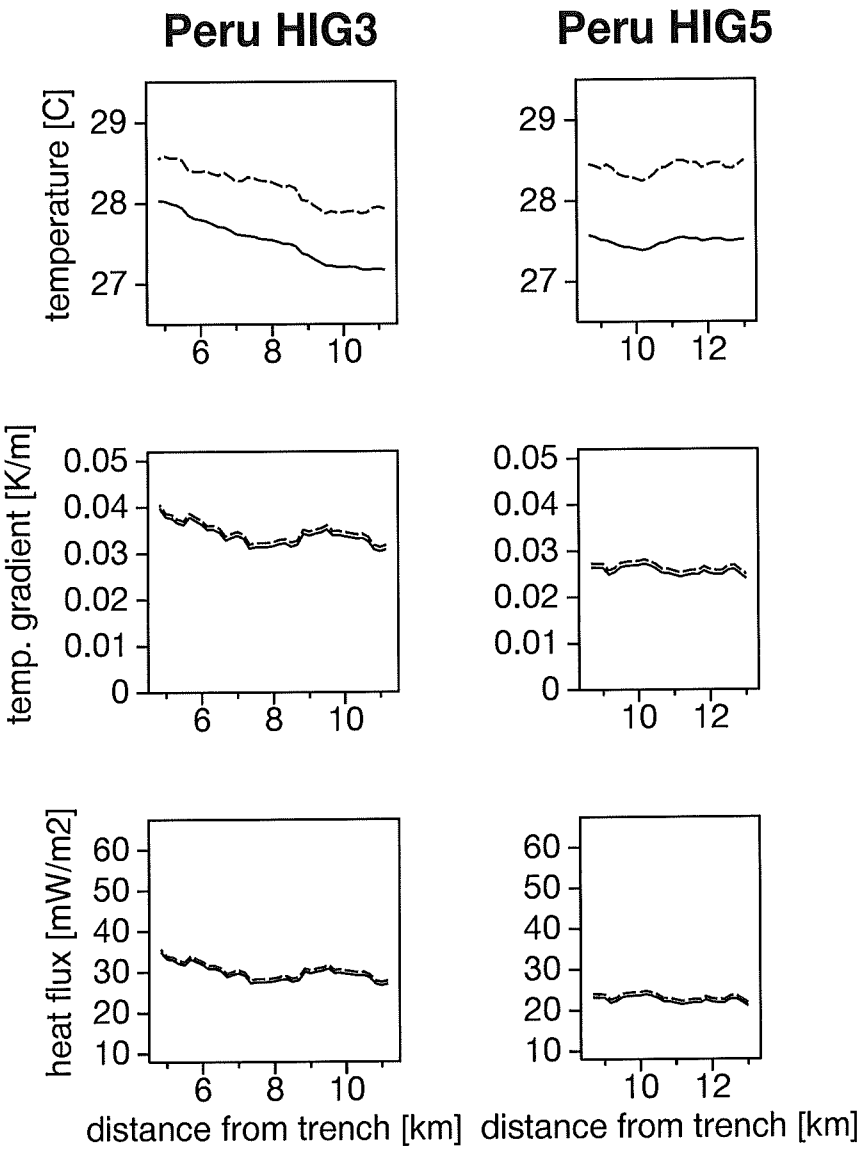

Figure 80: Temperature, temperature gradient, and heat flux from the depth of the BSR along lines HIG 3 and HIG 5 assuming hydrostatic pressure (solid line) and lithostatic pressure (dashed line). Depth of the BSR was computed from an interval velocity/TWT function obtained from lines 1017 and 1018.

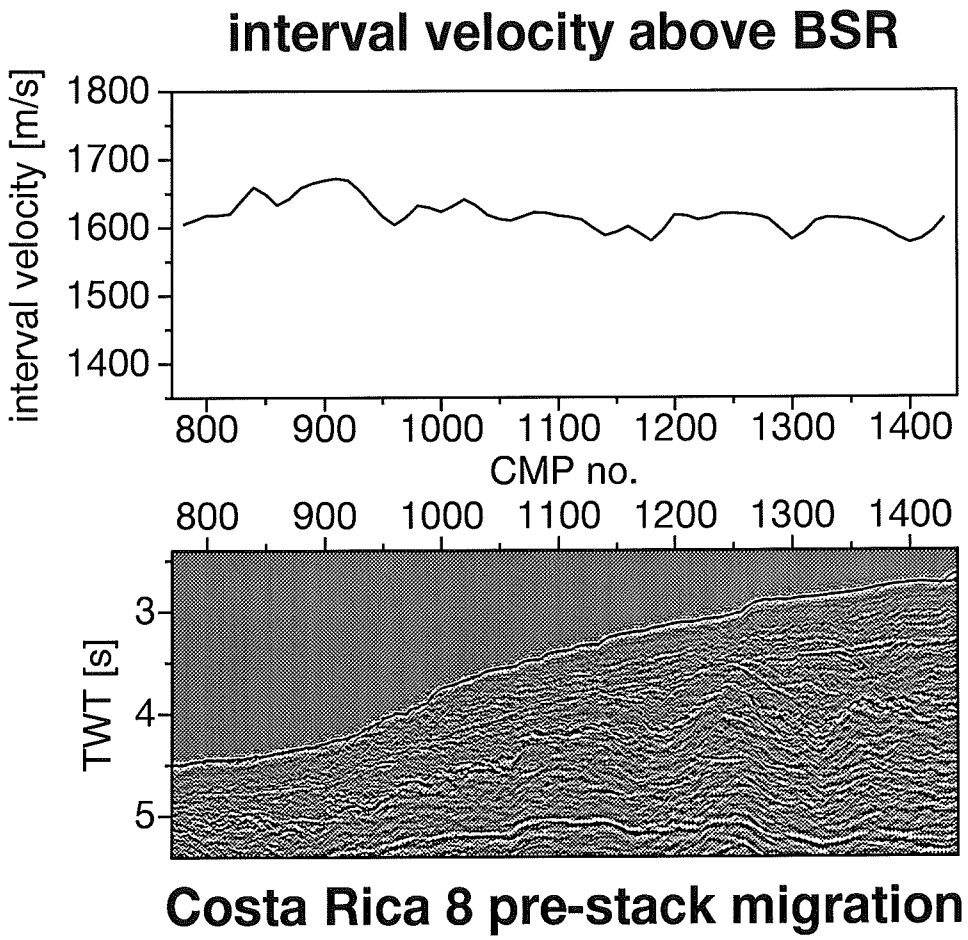

Figure 81: Velocities of the depth interval above the BSR obtained from focusing analyses during pre-stack depth migration, Costa Rica line 8.

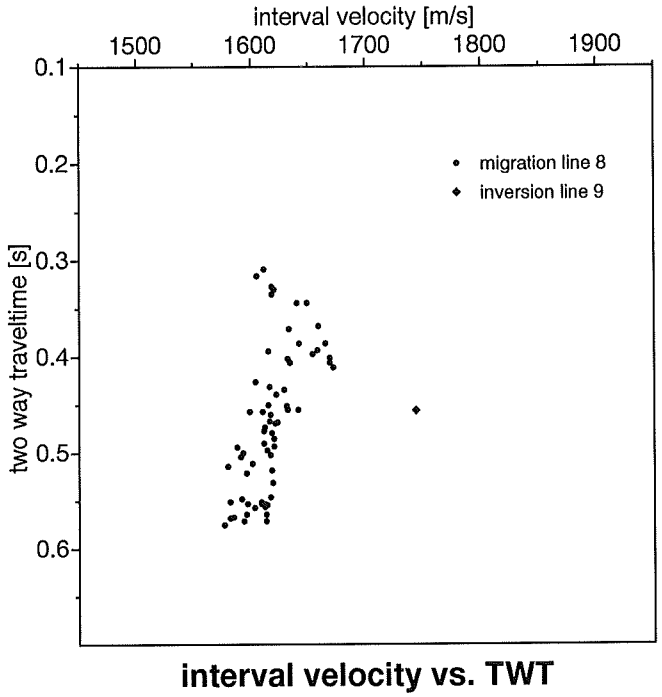

Figure 82: Interval velocities plotted against two-way-traveltime above BSRs obtained from pre-stack depth migration in line 8 and from inversion at CMP 1410 in line 9.

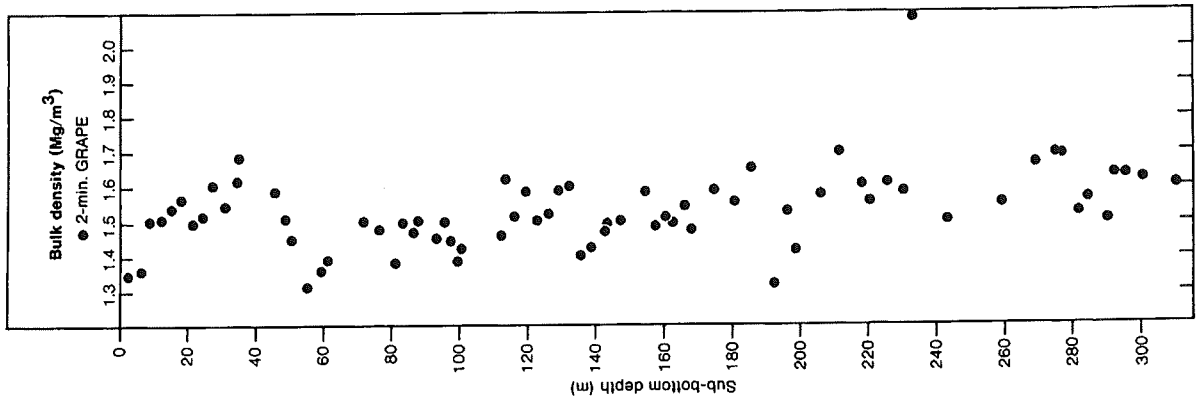

Figure 83: Bulk density in cores from DSDP Leg 84 Sites 565. From von Huene et al. (1985b)

decreases from the trench from $\sim 80mW/m^2$ towards the continent down to $\sim 40mW/m^2$. The average value between CMPs 990 and 1260 (see fig. 21) is $47.5mW/m^2$. Conventional measurements along this part of line 8 yielded an average value of $46.2mW/m^2$ (Langseth and Silver, in press). Thus, conventional and BSR heat flux compare well in this area.

Line 9
Heat flux along line 9 displays a similar pattern (fig. 85). The margin is wider than at line 8 and thus, it is difficult to compare heat flux values from both lines as a function of distance from the trench axis to each other. A variation of heat flux $\sim 22km$ away from the trench is clearly linked to topography (see p. 42 fig. 21, CMP 1530). Towards the trench, heat flux reaches values of as high as $\sim 100mW/m^2$.

Line 5
The BSR can be traced down to the décollement along line 5 (ref. fig. 23). Temperature, temperature gradient and heat flux profiles along this line are shown in fig. 86. A gap between $\sim 15 - 18km$ from the trench is caused by difficulties in identifying the BSR in this part of the section. Heat flux about $4-9km$ and $> 24km$ away from the trench axis may be inaccurate since the BSR is quite shallow in these areas and there might be interferences between signal from seafloor and BSR. This is demonstrated by the small-scale fluctuations in heat flux and temperature gradient profiles, while the temperature profile is very smooth. Heat flux close the trench axis is $\sim 100mW/m^2$. It increases up to $\sim 160mW/m^2$ about $5km$ away from the trench axis. The absolute value may be inaccurate, the pattern of an increase away from the trench however, is clearly reflected by a deeper BSR beneath the sea floor. After that, heat flux decreases again reaching values of $\sim 60mW/m^2$, which is considerably higher than at lines 8 and 9 northwest of Fisher Seamount. Values of over $\sim 150mW/m^2$ as the profile approaches the continent may be in part artifacts because the BSR is very shallow (fig. 23) and thus, the denominator for computation of the temperature gradient, i.e. depth beneath the sea floor, very small leading to relatively high errors for heat flux. Also, the assumption of $2°C$ as the bottom water temperature may be wrong in these rather shallow waters. It is obvious however, that heat flux increases towards the continent.

9 Discussion, conclusions and outlook

9.1 Inversion scheme

The 1-d full waveform inversion approach has proven to be a reliable technique for investigations of the P-wave velocity structure of thin layers. Its reliability with regard to studies of thin low velocity layers such as BSRs has been proven by drilling of ODP Site 889, where velocities from VSP logs and previous waveform inversion matched well (Singh et al., 1993; MacKay et al., 1994) .

Interval velocities between discrete horizons form the basis for a good starting model, which is required in order to reach the global minimum of the misfit function. In the present study, they were obtained by applying a Monte Carlo inversion scheme. The good match between velocities from the Monte Carlo inversion and velocities from focusing analyses during pre-stack depth migration demonstrates the accuracy of both techniques. In fact, it appears that the Monte Carlo inversion scheme might not be required if pre-stack migration is performed. On the other hand, this inversion technique is not very time-consuming and may be applied to data in the (τ, p)-domain as a test even if focusing analyses are performed. Velocities from pre-stack depth migration might be more reliable than those from the 1-d Monte Carlo inversion if slightly dipping or discontinuous layers are involved in the velocity analysis, due to the larger horizontal scale at which focusing analysis is performed.

The transformation of interval velocities into a gradient velocity model, however, is to a certain extent arbitrary. Velocities particularly in the vicinity of the BSR have to be as close to the real velocity

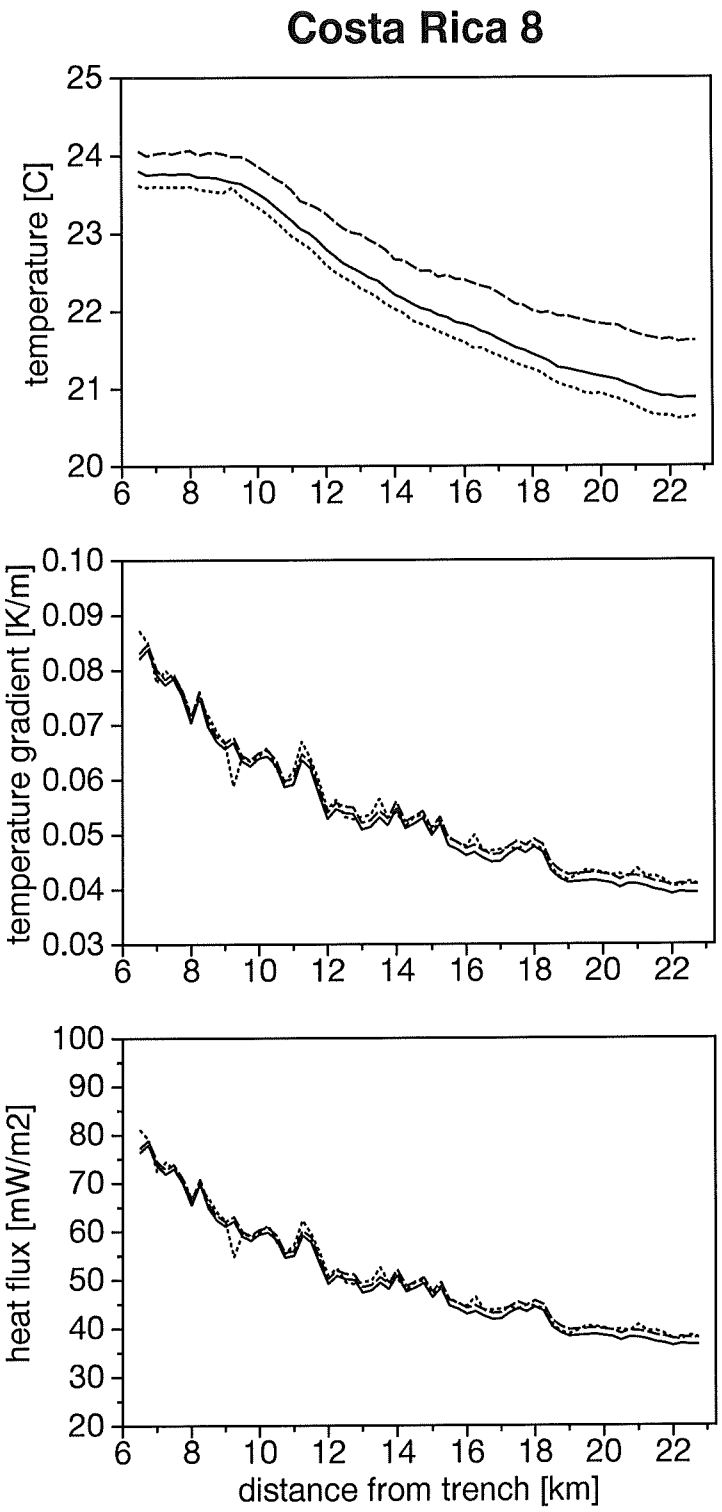

Figure 84: Temperature, temperature gradient, and heat flux from the depth of the BSR along Costa Rica line 8 assuming hydrostatic pressure together with a velocity/TWT function (solid line), hydrostatic pressure together with picks in the depth domain (dotted line), as well as lithostatic pressure and a velocity/TWT function (dashed line).

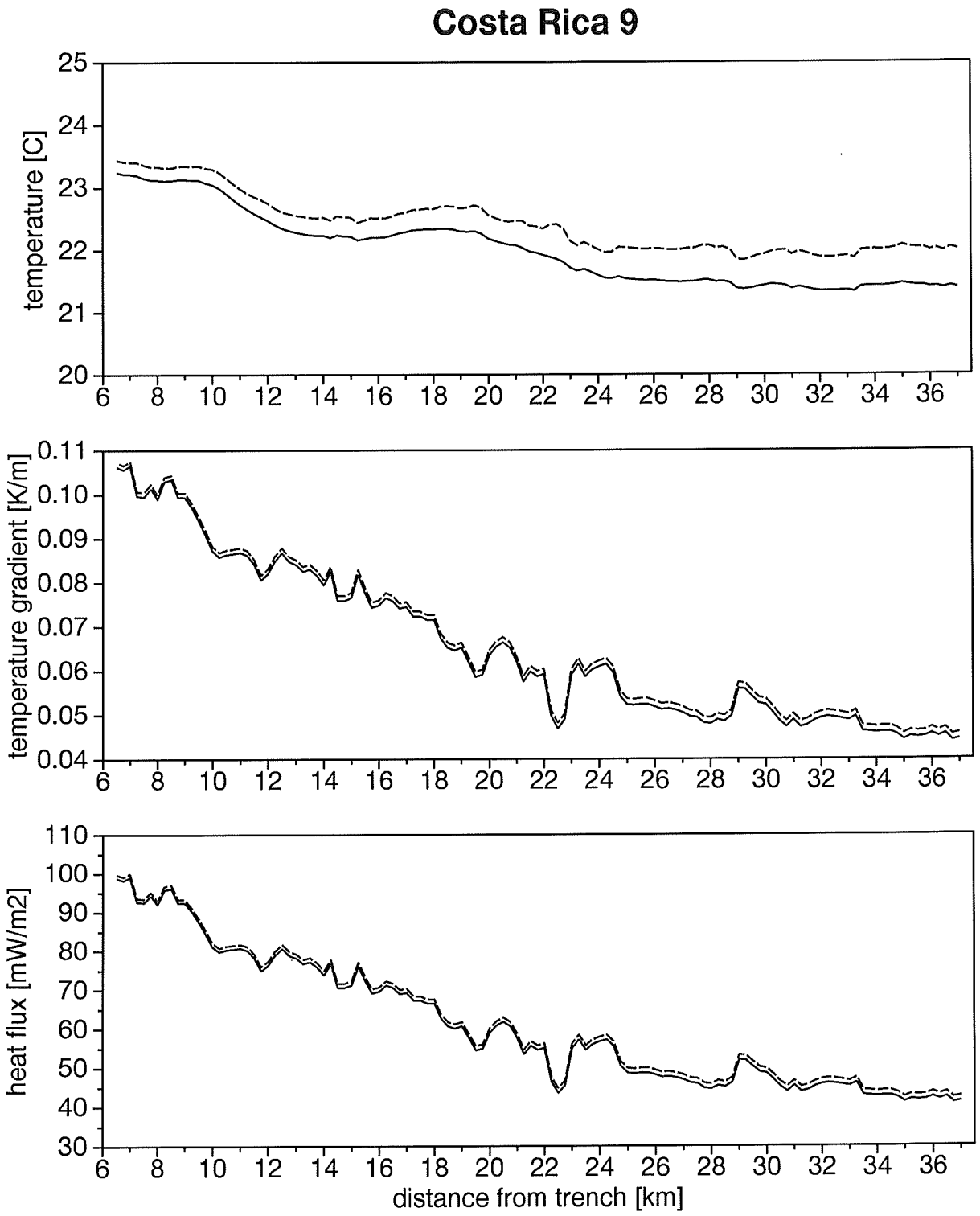

Figure 85: Temperature, temperature gradient, and heat flux from the depth of the BSR along Costa Rica line 9 assuming hydrostatic pressure (solid line) and lithostatic pressure (dashed line). Depth of the BSR was computed from time picks and an interval velocity model obtained from pre-stack migration at line 8 and a Monte Carlo inversion at line 9 CMP 1410.

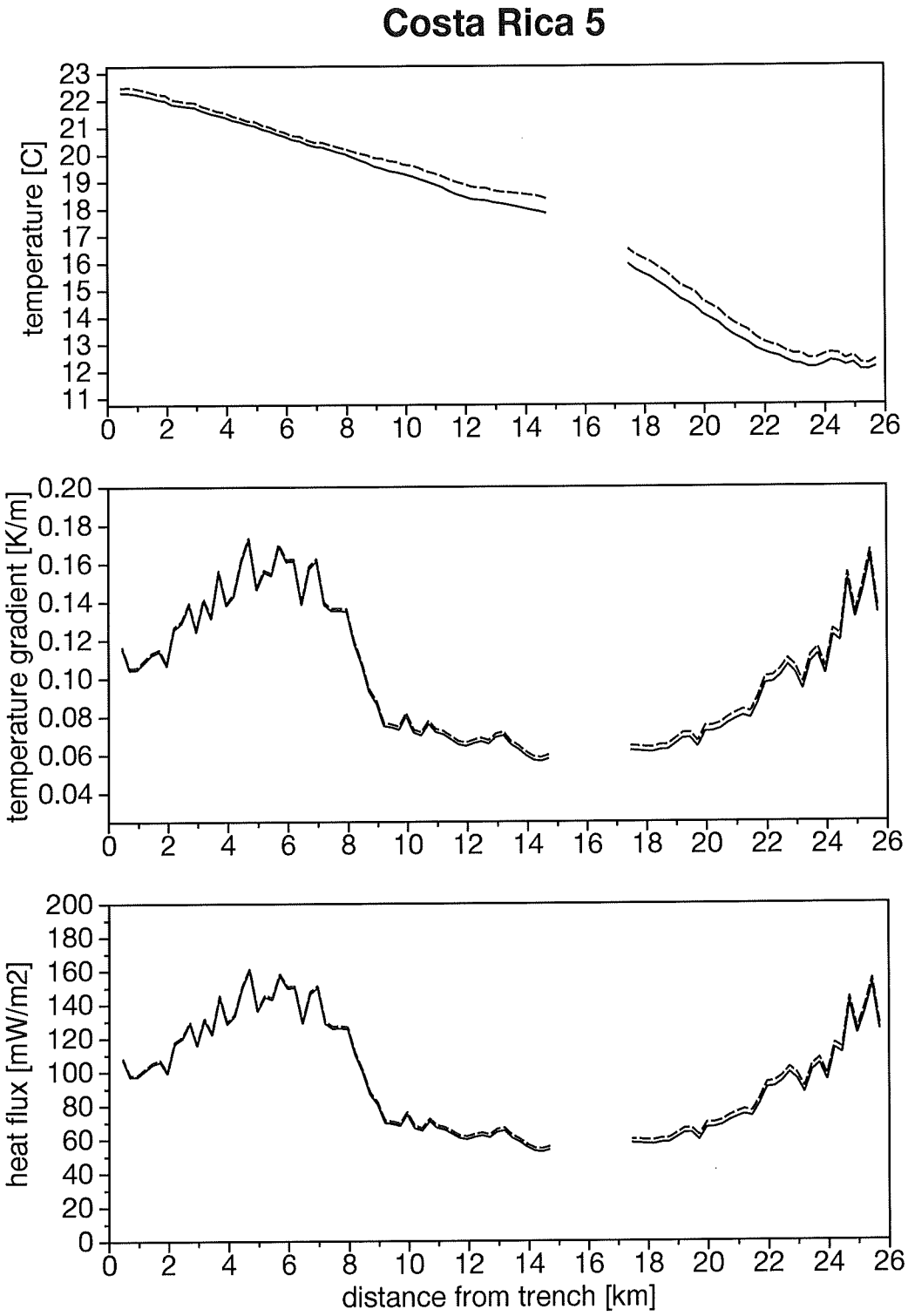

Figure 86: Temperature, temperature gradient, and heat flux from the depth of the BSR along Costa Rica line 5 assuming hydrostatic pressure (solid line) and lithostatic pressure (dashed line). Depth of the BSR was computed from time picks and an interval velocity model obtained from pre-stack migration at line 8 and a Monte Carlo inversion at line 9 CMP 1410. Note that vertical scaling differs by a factor of 2.5 compared to plots from lines 8 and 9.

structure as possible. Therefore, the positive velocity step, which is usually obtained from analysis of interval velocities above and beneath the BSR, has to be smoothed because of the negative impedance contrast observed at BSRs. A disadvantage of using velocity gradients for this purpose (followed by slight smoothing) is that the velocity at a given depth depends on the velocity assumed at the seafloor: The higher the velocity at the beginning of a depth interval the lower it will be at the end of it in order to keep traveltimes in the depth interval constant. An error in the estimate of V_p at the seafloor will thus propagate through the whole model. This may be avoided by merely applying smoothing operators to interval velocities as done e.g. by Singh et al. (1993) and Minshull et al. (1994), but this method leads to a maximum of the 1st derivative of the V_p-function at the depth of the BSR, which probably is not very close to the real Earth model at the BSR. Therefore, velocity gradients were considered to be most appropriate for the present study. Additional information such as velocities and densities at the seafloor, however, would be highly desirable and the way how to form a good starting model will depend largely on the location and the target of the inversion. On the other hand, Minshull et al. (1994) demonstrated by using different starting models in the vicinity of the BSR that the small-scale V_p-structure of the starting model is not too critical.

The lack of information regarding the other seismic properties was a general limitation during the present study. On the one hand, this is not thought to have caused much harm, since the only parameter which was expected to be considerably affected by the presence of free gas was V_p. On the other hand, some residual energy at higher slownesses (larger offsets) might be caused e.g. by inaccuracies in the estimates of V_s (and thus the Poisson's ratio), which influences reflectivity as a function of angle-of-incidence.

Another reason behind residual energy at both low and high slownesses may be inaccuracies in the source wavelet. The shape of the wavelet is expected to depend slightly on slowness, because of the increase of traveltime of the ghost signal between streamer and the air/water interface. Obtaining a good source wavelet is of course in general critical for the waveform inversion technique. As demonstrated with the Costa Rica data set however, the method is quite robust with regard to later parts of the source wavelet such as bubbles.

It is not clear in how far possible high velocity layers above BSRs, which might be caused by a higher concentration of hydrates, may be resolved by applying this technique to MCS data having a relatively low maximum offset. On the one hand, elevated velocities especially above the Peru locations 1018 CMP 1514 and 1017 CMP 3790 might be regarded at least partially as artifacts caused by the waveform inversion focusing on accommodating for a high reflection coefficient at low offsets (ref. p. 50 for details). On the other hand, such an effect is not observed in the Costa Rica data set. At Peru 1018 CMP 1594, higher velocities above the BSR are not reflected by a LVL beneath it indicating that this thin high velocity layer might be real. Minshull et al. (1994) interpreted higher velocities above the BSR obtained from waveform inversion applied to data from offshore Colombia as evidence for a hydrate saturation of $\sim$ 10% in the pore space. Although maximum offset relative to water depth was similar to that of the Peruvian data presented here, their data might have been better suited for waveform inversion due to a good shape of the tuned source wavelet. The velocity structure immediately above the BSR obtained from waveform inversion by Singh et al. (1993) at the Cascadian margin matched fairly well, although not perfectly, with velocities from VSP and sonic logs at ODP Site 889.

9.2 Geophysical nature of the BSR

Results from full waveform inversion are summarized in fig. 87. There is strong evidence from the velocity structures at the locations which were investigated for the present study that the high-amplitude negative reflections observed at BSRs are caused by the presence of a small amount of free gas which underlies hydrated sediments. Only at Peru 1018 CMP 1594, very little gas, if any, would be predicted at the BHSZ. The BSR at this location displays much lower amplitudes than at CMP 1514, where the presence

of gas is indicated from the velocity structure. A sudden decrease of reflectivity at about CMP 1580 (ref. fig. 36) may mark the transition from a BSR which involves free gas to a BSR without free gas. Both types of BSRs might intuitively be classified as "strong" and "weak BSRs" according to Lee et al. (1994) although reflection strength has not been quantified in order to test whether this classification is appropriate for the Peruvian BSRs. The sudden lateral change of the reflection coefficient is consistent with the assumption that it is caused by a transition from a zone where no free gas is trapped at the BHSZ to a zone containing free gas beneath the BHSZ: A sudden drop of V_p and thus increase of reflectivity is expected at this transition zone due to the highly non-linear negative correlation between V_p and gas content at very low concentrations. The drop of V_p at the location off Costa Rica appears to be less pronounced and the increase beneath the BSR more gradational than at most Peruvian locations, although these differences might partly be attributed to different data acquisition parameters. Subsequently, gas concentration at the BHSZ is predicted to be lower offshore Costa Rica, which is consistent with the lower amount of organic carbon found at DSDP Site 565 compared to the outer Peruvian margin.

Along line 1018, results from the present investigations in principle compare well with the earlier results of Miller et al. (1991) although their values of seismic velocities are lower. Both results give a similar velocity contrast and thickness of the low velocity layer at the BSR. Regarding different absolute values for V_p at the BSR, the velocity control around the BSR is determined more rigorously using the offset dependent waveform inversion. Interpretation of the present results yields a lower minimum assumption on the content of free gas in the pore space: Miller et al. (1991) estimated the gas content at 10% or more of pore space (porosity 65%). This discrepancy is due mainly to the lower velocities obtained from their study.

Most seismic analyses of BSRs at both active and passive continental margins also indicate the presence of free gas to produce the observed high reflectivity along a BSR, e.g. in the Gulf of Oman (White, 1979), in the Barents Sea (Andreassen et al., 1990), offshore Colombia, except for one location which displayed a relatively weak BSR (Minshull et al., 1994), at Blake Ridge (e.g. Katzman et al., 1994), Carolina Rise (e.g. Korenaga et al., 1995), and the Beaufort Sea (Andreassen et al., 1995). The model of a thin hydrate wedge above the BSR instead of gas beneath it as proposed by Hyndman and Spence (1992) based on results from AVO forward-modeling was neither confirmed by the more sophisticated waveform inversion (Singh et al., 1993) nor by drilling of Leg 146 (MacKay et al., 1994). Results from the present study of BSRs offshore Peru indicate a velocity structure similar to that from a sonic log at the BSR near the Chile triple junction which was penetrated during Leg 141. There, a $7m$ thick LVL with an average velocity of about $1.6km/s$ was drilled (Bangs et al., 1993). It might be concluded with that highly reflective BSRs commonly indicate the presence of free gas at the BHSZ.

Obviously, permeability of hydrated sediments has to be rather low in order to trap free gas. However, pore plugging by hydrates has not to be perfect to impede the upward movement of free gas: MacKay et al. (1994) point out that mobility of gas within sediments at low concentrations is relatively low. Gas permeability for gas concentrations of only a few percent is assumed to be at least three orders of magnitude less than that of the formation water (Honarpour et al, 1986). Gas at low concentrations will consequently tend to move with the pore water rather than through it (MacKay et al., 1994). As a further consequence it might theoretically in fact be possible, that free gas is trapped beneath the HSZ, however, fluids would still be able to move into it. This idea however, requires detailed investigation of the effect of hydrates in sediments on both gas and fluid flow permeability.

The amount of hydrates required to significantly decrease fluid permeability might depend on the distribution of hydrates within the sediments. Fig. 88 shows two principle end-members of hydrate distribution in the pore space. A third end-member of hydrate distribution in sediments would be macroscopically occurring hydrates (e.g. as nodules or fracture fill), in which hydrates are not confined to the pore space and replace part of the matrix material.

If hydrates form in the pore voids without grain contact, it is assumed that high concentrations

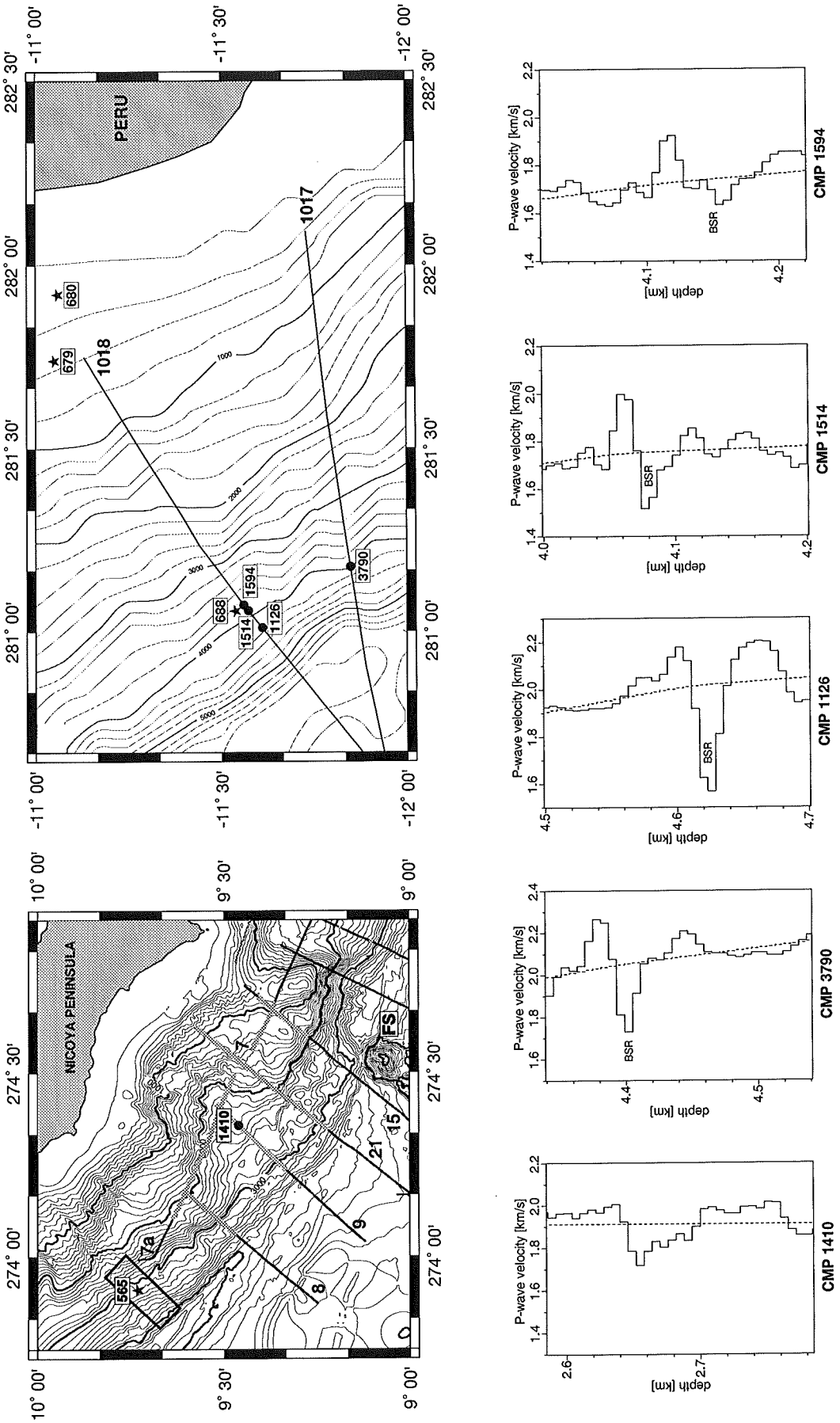

Figure 87: Compilation of the velocity structures at BSRs investigated for this study. Locations are marked by circles. Stars denote ODP and DSDP sites. Thick grey lines in the Costa Rica map (top left) mark sections of the seismic profiles in which BSRs were observed. The box around DSDP Site 565 indicates the area of a 3-d seismic experiment (Shipley et al., 1992). FS: Fisher Seamount. Bathymetry and tracks of seismic lines in the Peruvian map (right) are only approximate.

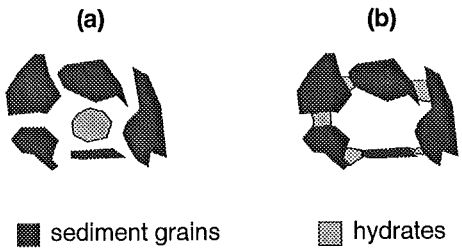

Figure 88: Possible end-members of hydrate distribution in the pore space of sediments: (a) Hydrates form without grain contact. Relatively high concentrations of hydrates are required to plug the sediment pores. (b) Hydrates form between grains. Permeability of sediments is significantly decreased even at low hydrate concentrations.

of hydrates are required to efficiently plug the sediment pores. Physical properties of the bulk sediment might be modeled by assuming unaffected grain and matrix parameters and averaging water and hydrate properties to assess pore fill properties. Lee et al. (1994) point out that if hydrates are located within the pore voids without grain contact, V_s is not expected to be significantly affected by the presence of hydrates in sediments.

On the other hand if hydrates form between grains, they may significantly decrease permeability even at low concentrations. The latter distribution is suggested for hydrated sediments around ODP Leg 146 (Cascadian margin) to explain how relatively low amounts of hydrates may impede the upward migration of fluids (MacKay et al., 1994). In this case, hydrates act as bonding agents leading to hydrate cementation and thus affecting sediment matrix properties. Hydrate cementation might lead to a considerable increase in V_s (Lee et al., 1994).

Effects of hydratization on permeability and other physical properties may be quite different, if macroscopic bodies exceeding the size of the pore voids replace part of the unhydrated bulk sediment. Then, physical properties including permeability might be computed by averaging properties of the unhydrated bulk sediment and massive hydrates.

In summary, highly reflective BSRs, although probably caused by free gas, do not necessarily imply extremely low values of fluid permeability at the BHSZ. Further investigations are required to test to what extent hydrates decrease both gas and fluid permeability. Since the assumed decrease of permeability is believed to be influenced by the distribution of hydrates in sediments, it might be of interest to test in how far physical properties, in particular V_s, depend on the distribution of hydrates. A way of constraining permeabilities of hydrated sediments might be of significance for understanding hydrate formation (i.e. to what extent possibly methane-rich fluids can move into the HSZ), as well as for predicting general fluid flow patterns in regions where hydrates occur.

9.3 Possible sources of free gas at BSRs and hydrates off Peru and Costa Rica

Two principal models have been proposed for the supply of free gas at BSRs: Methane recycling caused by decomposition of hydrates at the base of the hydrate stability zone and upward migration of methane-rich fluids. In the first case, methane is believed to be produced biogenically in situ, in the latter model, it is formed biogenically or thermogenically below the HSZ (section A.5.3).

9.3.1 Peruvian margin

Offshore Peru at 12° S, BSRs are absent in the accretionary wedge, strong BSRs can be observed at the lower slope and there is a lack of BSRs further upslope in Lima Basin. The lack in Lima Basin should not be over-interpreted, since a BSRs has been observed in HIG profiles in Lima Basin further

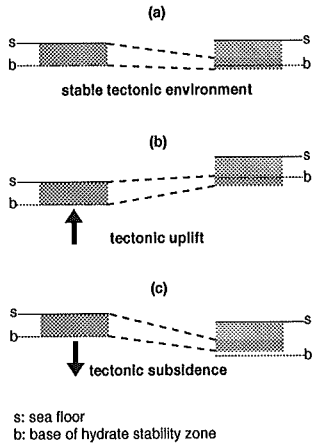

Figure 89: Tectonic control of BSR formation: An original sedimentary section assumed to contain hydrates (left-hand side, dark-shaded area) undergoes compaction together with vertical movement during sedimentation of new sediments (right-hand side, light-shaded area). Depending on whether the BHSZ moves upward relative to the base of the assumed hydrated sedimentary section, gas is expected to form from dissociation of hydrates: (a) Stable tectonic environment. Subsidence of hydrated sediment beneath the BHSZ due to compaction of underlying sediments. (b) Additional tectonic uplift. The BHSZ moves upward relative to the seafloor as pressure decreases and the phase boundary of hydrates shifts towards lower temperatures. (c) Lack of BSRs due to tectonic subsidence. The BHSZ moves downward relative to the seafloor due to an increase of pressure and a subsequent shift of the phase boundary towards higher temperatures outweighing subsidence of sediments due to compaction as in (a). Note that (c) may also suppress development of BSRs if methane is supplied from below.

north (Ballesteros et al., 1988). At 9° S, BSRs are present within the accretionary wedge and also within Yaquina Basin.

In the southern area, accretion is rapid but trench sediments are assumed to consist mostly of pelagic organic-poor sediment (Hussong et al., 1988,). The lower slope is characterized by rapid uplift (von Huene et al., in press). Lima Basin is assumed to still subside (Suess et al., 1988). Hydrates are thought to be of biogenic origin (Kvenvolden and Kastner, 1990). Sediments at the lower slope in general have a high organic carbon content (von Breymann et al., 1990) probably allowing in situ production of hydrates (ref. e.g. to model calculations for the Carolina Rise-Blake Ridge area, Paull et al., 1994). Based on the good correlation of BSR occurrence with the zone of uplift at the lower slope it is suggested that methane recycling due to uplift is the main mechanism for BSR formation in the southern area: Uplift causes a depressurization in the sediments leading to a shift of the phase boundary towards lower temperatures and thus, an upward movement of the BHSZ relative to the seafloor. Hydrates left beneath the HSZ dissociate and form free gas. Upward migrating methane, however, is expected to contribute to gas and hydrate formation, as indicated by Sr-analyses, based on which Kastner et al. (1990) conclude that some fluids must have migrated upwards from the oceanic plate possibly transporting methane produced in the sediment column beneath the HSZ upwards. The accretionary prism is inferred to be composed of organic-poor pelagic sediment perhaps not producing sufficient methane for hydrate and subsequently BSR formation. The lack of BSRs in Lima Basin along lines 1017 and 1018 may be caused by subsidence: Due to an increase of pressure, the BHSZ moves downward relative to the seafloor. Should BSRs occur further to the north and Lima Basin subside there as well, subsidence of the sediment column due to compaction probably outweighs the downward movement of the BHSZ (ref. also fig. 89).

BSRs in the relatively stable Yaquina Basin may be formed by such a subsidence due to sedimentation and compaction, which is the original model for BSR formation proposed by Claypool and

Kaplan (1974). Further investigations would be required such as a detailed small-scale analysis of local uplift/subsidence history, however, before making any final conclusions with regard to BSR formation in both Yaquina and Lima Basin. The accretionary prism in the northern area is presumed to consist mainly of turbiditic organic-rich upwelling sediments. Development of the accretionary wedge is almost complete and most of the trench sediment is currently subducted. The amount of expelled fluids is expected to be much higher than in the southern area, because (1) the trench sediment section is thicker and (2) the fraction of subducted sediments is higher (ref. fig. 17). Methane formed in presumably organic-rich sediments in the accretionary wedge driven upwards by fluids or buoyancy into the HSZ provides the best explanation for BSR formation within the accretionary wedge. Local uplift e.g. above the ridge along CDP 2 leading to methane recycling may of course contribute to the process of free gas formation.

It is concluded that both processes commonly suggested for the formation of free gas at the BHSZ operate at the outer Peruvian margin passing from hydrate dissociation as the dominant mechanism in the southern area towards gas accumulation from uprising methane as one moves north.

9.3.2 Costa Rica margin

DSDP Site 565 was drilled northwest of the study area for the present investigations in an area in which the geological setting with regard to BSR formation obviously is different since no BSRs were observed there. Therefore, it provides only limited information for the present study. Since at that time drilling through hydrates and BSRs was regarded as hazardous, drilling was stopped at Site 565 above the BHSZ because of hydrate occurrence. Therefore, composition of sediments beneath the HSZ was inferred from further above.

Features of BSR distribution, which have to be explained by BSR formation mechanisms, include the wide-spread BSR occurrence as well as the lack of BSRs (1) in areas affected by slumping, (2) north of Quepos Plateau above the $2000m$ isobath, (3) at the northwestern edge. A more detailed BSR distribution requires processing including pre-stack migration of all existing lines, after which probably other BSR occurrences may be added to fig. 20. There is only little information regarding small-scale uplift and subsidence history such that the role of tectonics in BSR formation cannot be evaluated. Fluid flow would partly depend on the nature of the rock beneath the rough surface. Thus, results presented here are preliminary.

The lack of BSRs in areas affected by slumping may be explained by an escape of free gas during slumping. The BSR might act as a zone of weakness facilitating slope failure due to a possible underconsolidation at the BHSZ and perhaps excess pore pressure at the BSR (ref. e.g. Booth et al., 1994, and fig. 94). A possible scenario which might take place during subduction of seamounts would be that at first, seamounts cause uplift of the sediment column leading to depressurization, a subsequent upward move of the BHSZ relative to the seafloor, dissociation of hydrates at the BHSZ, production of free gas and thus, excess pore pressure. Under these conditions, it may be speculated that the plane along which failure takes place is the BSR, which might lead to a sudden release of larger amounts of free gas.

Obviously time after slumping was too short for a renewed BSR formation. Assuming that the subduction of seamounts on top of the oceanic plate is the main cause for slumping and considering that a movement of seamounts of $10km$ perpendicular to the margin ($0.57cm$ in the location map fig. 20) corresponds to over $110,000a$ (plate convergence: $90mm/a$), it appears from the lack of BSRs in areas trailing subducted seamounts that BSR formation takes at least one order of magnitude longer than glaciation cycles (ref. e.g. lines 13, 17, and 17a). This would mean that BSRs offshore Costa Rica obviously have not been destroyed during glaciation because of depressurization due to sea-level fluctuations. Subsequently, the hypothesis of Paull et al. (1991), that an escape of gas from BSRs due to a decrease of sea-level during glaciation may have triggered global warming and the onset of deglaciation, might not be applicable in general to BSRs offshore Costa Rica. However, BSRs have to be identified in

an area which previously had been affected by slumping to better constrain the time required for BSR formation.

The origin of hydrates is assumed to be mainly biogenic (Kvenvolden and McDonald, 1985), however evidence is not as clear as it is for the Peruvian margin (ref. section 6.3). Also, temperature gradients from the present study indicate that thermogenic production may already begin within the accretionary prism: Assuming a temperature gradient of $0.1K/m$ in the accretionary wedge and thermogenic production starting at $\sim 100°C$, thermogenic methane may form as shallow as $\sim 1000mbsf$. Further geochemical studies are required to clearly delineate processes of methane formation.

Organic carbon content in sediments from Site 565 (0.5−2%) is lower than in sediments offshore Peru. In-situ production of methane may still take place, but the concentration of hydrates would be expected to be relatively low: The computations of Paull et al. (1994) (ref. section A.5.2) for the Blake Ridge area would roughly be appropriate for the Costa Rican margin as well. Under the assumption that only the amount of methane which exceeds saturation of pore water is available for the formation of hydrates, they concluded that the maximum amount of hydrates which could be produced in situ within a $600m$ thick HSZ from sediment containing 1% organic carbon would be $\sim 2.2 - 6.1\%$ of pore space. The presence of shallow BSRs close to the line where the base of the hydrate stability zone intersects the seafloor indicates an involvement of fluid migration in hydrate formation. High biogenic production rates of methane would be required to exceed saturation of pore water required for hydrate formation in situ before sediment subsides beneath the HSZ. The assumption of the margin wedge being composed of ophiolitic rock is not conflicting with the model of upward migrating methane-rich fluids being the main source of methane at BSRs. The presumed ophiolitic complex may be highly fractured allowing channelized fluid flow through fractures. Lateral migration of fluids along the BSR may distribute methane evenly at the BHSZ. The detection of methane while drilling the ophiolitic complex offshore Guatemala (Kvenvolden and McDonald, 1985) provides evidence that the assumption of fluids migrating through fractured serpentinite rocks is reasonable.

In summary, fluid migration appears to be involved in the formation of BSRs offshore Costa Rica. Final conclusions, however, require a better knowledge of the detailed history of tectonic uplift and subsidence, the sedimentology and chemistry down to well beneath the BHSZ, the nature of the rocks underlying the BSR, as well as information about possible fluid flow patterns.

9.3.3 Implications on hydrate formation and distribution

From the geophysical investigations of BSRs presented here, it cannot be estimated which fraction of hydrates is produced in situ, and which fraction migrates into the HSZ from below. The results from the present study indicate however, that migration of methane into the HSZ plays a major role during BSR and subsequently hydrate formation.

Some authors have suggested that such a formation mechanism for hydrates implies a thin layer of hydrated sediment having a high concentration of hydrates in the pore space above the BHSZ whereas no hydrates should be present further above (e.g. the "hydrate wedge" model suggested by Hyndman and Spence, 1992). Thus, the model of a formation of hydrates from upward migrating methane may be regarded as conflicting with hydrate occurrences at relatively shallow depths. However, two processes may lead to the presence of hydrates well above the BHSZ even if methane is merely generated below the HSZ:

- *Migration of gas within the hydrate stability zone:* If gas bubbles or supersaturated fluids are allowed to migrate some distance upward within the HSZ before they become hydrated, hydrates may start to form well within the HSZ. Once they have formed at some distance above the BHSZ leading to a decrease in permeability and thus impeding gas and fluid migration, hydrates may start forming downward (Minshull et al., 1994). The upper boundary of the hydrated sediments might then

intuitively depend largely on the permeability of the unhydrated sediment section controlling the speed of gas migration within the HSZ. This process may be particularly important in fractures and other possible paths of channelized fluid migration, where fluids are expected to travel relatively fast.

- *Downward movement of the base of the hydrate stability zone:* If the BHSZ moves gradually downward relative to the sediment column, gas trapped at the BSR will be hydrated probably leading to a relatively continuous hydrate distribution within the sediment column. In particular, this may have happened during deglaciation. Offshore Peru, subsidence of the margin after subduction of Nazca Ridge may have led to a considerable downward shift of the BHSZ.

9.4 Temperature and heat flux

9.4.1 Reliability of the method

Heat flux values obtained from the depth of the BSR assuming a pure water/methane system along the Peru lines in general compare relatively well to conventional in-situ probe and bore hole measurements. The discrepancies of bore hole measurements and BSR heat flux from Site 688 might not only be explained by inaccuracies with the BSR method. Problems with measuring temperatures in the bore hole (e.g. because of cooling from the drilling fluid) may also lead to inaccurate heat flux values. Conventional measurements were not available along the tracks of seismic lines presented in this study for an exact comparison between conventional and BSR heat flux.

Langseth and Silver (in press) measured heat flux at seven locations along the track of Costa Rica line 8 which were essentially identical with BSR heat flux. This indicates that the assumptions behind heat flux computations from the depth of BSRs off Costa Rica are reasonable.

This is not the case along all margins as demonstrated by WSTP measurements at ODP Leg 146 sites (Westbrook et al., 1994). However, as long as interpretation of heat flux obtained from the depth of BSRs focuses on relative lateral fluctuations, this method appears to be reliable. Computations of temperature, temperature gradient, and heat flux in section 8 also underline that this method is quite robust regarding geophysical inaccuracies (e.g. velocity and density). The key factor for calibration appears to be the composition of hydrates and the resulting (p, T)-conditions at the phase boundary.

9.4.2 Peruvian margin

Southern area

Heat flux obtained from BSR at the lower slope along lines 1017 and 1018 is displayed in fig. 90. Values increase relatively steadily from the accretionary wedge towards the continent. Two sources may contribute to that increase: (1) Metamorphic rock of continental affinity is believed to underly the sediment column, which may produce radiogenic heat. (2) Heat production from friction between the subducted plate and the metamorphic complex may increase as more fluids are expulsed from the subducted sediments and the load of the overburden increases towards the continent. Relatively high basal friction at the Peruvian margin would be consistent with results from sandbox modeling (Kukowski et al., 1994).

Heat flux fluctuations across two thrust faults ($28-32$ and $\sim 22km$ from the trench axis) along line 1018 are reflected by variations in depth of the BSR. Thus, they might give evidence for paths of uprising warm fluids. On the other hand, the character of the BSR across another thrust fault $\sim 19km$ away from the trench indicates that slight heat flux fluctuations there are mainly caused by variation of topography of the seafloor (see p. 94).

Northern area

Yamano and Uyeda (1990) underline the large difference between theoretically determined temperature

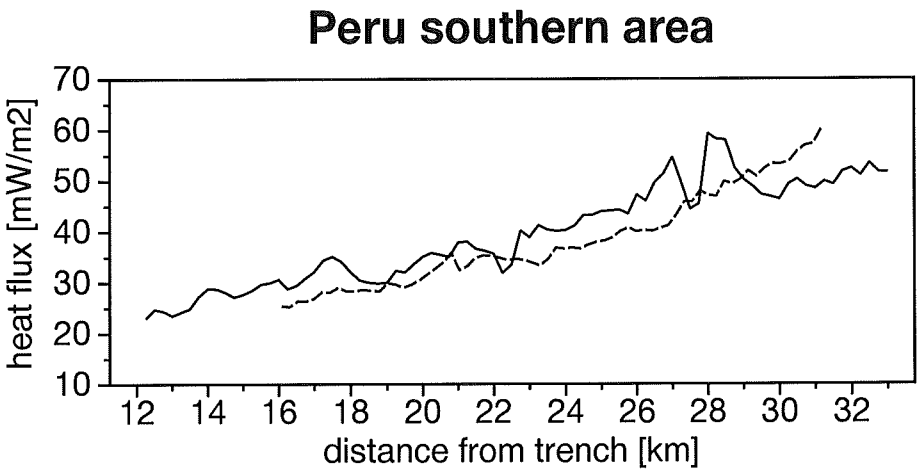

Figure 90: Heat flux vs. distance from the trench axis along lines 1017 (dashed line) and 1018 (solid line).

at the Nazca Plate based on its age, which they suggest should be $\sim 80mW/m^2$ at 12° S $\sim 90mW/m^2$ at 9° S, and their measurements in the trench. The estimates in section 8.1.2, which are based on relatively old measurements compiled by Sclater et al. (1980) are considerably lower ($\sim 48.1mW/m^2$ at 9° S) and in the same range as the values obtained from BSR heat flux close to the trench axis (fig. 91). Obviously, part of the discrepancy between theoretical and real heat flux values are caused by processes which take place at the oceanic plate before it enters the subduction zone. The "sea water heat exchange" suggested by Langseth et al. (1992) (ref. section 6.4) could be a possible cooling mechanism.

There appears to be a slight decrease of heat flux with increasing distance from the trench axis in the accretionary wedge (fig. 91). This can be explained by a geometrical effect: As BSR and seafloor approach the warmer oceanic plate, the vertical distance between isotherms above the BSR is expected to decrease, i.e. the temperature gradient increases. Another mechanism leading to elevated heat flux closer to the trench might be fluid expulsion from the subduction zone.

A peak of heat flux in line CDP 2 about $6.8km$ away from the trench is mainly caused by a topographic low at this location which is demonstrated by the lack of a "pull-up" of the BSR and subsequently a smooth temperature profile. Thus, temperature at the BSR was not fully accommodated for the higher loss of heat through the thinner overburden sediment which would result in a downward shift of isotherms. This observation may be regarded as evidence for a lateral flow of fluids along the base of the hydrate stability zone: an increase in heat loss is compensated by a supply of warm fluids moving beneath the layer of hydrated sediments. Fluid flow along the BHSZ would also be consistent with the BSR formation model proposed for this area. Further studies, in particular numerical modeling, are being performed to quantify the effect of fluid flow on the thermal regime within the accretionary wedge (Kukowski, in prep.).

Values in Yaquina Basin of $\sim 45mW/m^2$ indicate that heat flux increases again from the accretionary wedge towards the continent. This pattern is consistent with the increase observed in the two southern lines.

9.4.3 Margin off Costa Rica

Again, results from the Costa Rican margin are preliminary: Pre-stack depth processing of some of these lines is still being performed, velocity analyses were available only from line 8, and heat flux was only

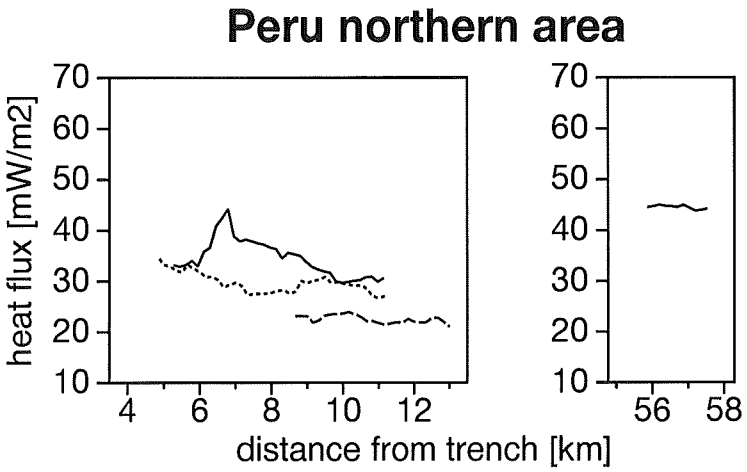

Figure 91: Heat flux vs. distance from the trench axis along lines CDP 2 (solid line) and HIG 3 (dotted line) and HIG 5 (dashed line).

computed from the depth of BSRs along three lines.

Fig. 92 displays a compilation of results from those lines. Since the margin is considerably wider in the northwestern area (lines 8 and 9), values from line 5 as a function from the trench axis cannot be directly compared to values at the northwestern part of the study area. Heat flux at the toe of the accretionary prism could only be computed along line 5. An increase of heat flux from ~ 100 to $\sim 160 mW/m^2$ is observed. In all three lines, heat flux decreases at the lower and middle slope towards the continent. Heat flux at the seaward termination of lines 8 and 9 is approximately $80 mW/m^2$ and $100 mW/m^2$, respectively. Minimum values of $\sim 60 mW/m^2$ along line 5 appear to be higher than those obtained from the northern parts of lines 8 and 9 (~ 35 and $\sim 40 mW/m^2$, respectively). However, there is a gap in the BSR along line 5 in which values may be lower. Heat flux increases again towards the continent along line 5.

Thus, the general pattern of heat flux across the margin appears to be an increase of heat flux to very high values at the toe of the accretionary wedge, a decrease across the lower and upper slope followed by another increase close to the shelf. Two other observations are a possibly higher heat flux in the southeastern area (line 5) compared the northwestern area (lines 8 and 9) as well as a decrease of heat flux to the northwest from line 9 towards line 8. The latter two observations should be confirmed by investigations along other seismic lines before making any final conclusions.

Small-scale variations of heat flux are clearly linked to topography, as the TWT to the BSR does not display any significant fluctuations. This may indicate lateral migration of fluids along the BHSZ, similar to the Peruvian margin.

High heat flux at the lower slope can be explained by a relatively hot oceanic plate. Theoretical heat flux based on the age of the oceanic plate ($\sim 20 Ma$) of $\sim 100 mW/m^2$ (Klitgord and Mammerickx, 1982) compare well to BSR heat flux close to the trench. A decrease of heat flux towards the continent may be explained by a stretching of isotherms as the hot oceanic plate bends downward and the overburden thickens. Fluid expulsion would be another mechanism which could explain much of the heat flux pattern off Costa Rica. Subduction at the margin appears to be highly efficient (e.g. von Huene et al., 1985b). Most of the trench sediment is subducted and thus, a large amount of fluids may be expelled. An increase of heat flux from the trench towards the accretionary wedge (as in line 5) followed by a decrease along the lower slope can be explained by such a process. Heat flux would be highest where fluid flux from below

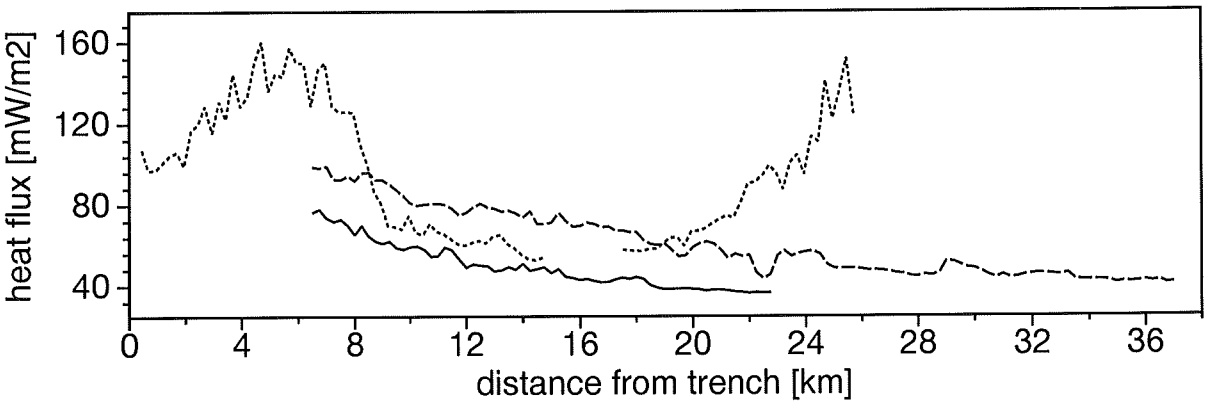

Figure 92: Heat flux vs. distance from the trench axis along Costa Rica lines 5 (dotted line) 8 (solid line) and 9 (dashed line).

is strongest. However, making any conclusions would require more detailed investigations, in particular thermal modeling. Wang et al. (1995) investigated (among others) a similarly rapid decrease of heat flux landward from the trench axis offshore southwestern Japan by applying time-dependent thermal modeling and were not able to find a quantitatively satisfactory model for this phenomenon.

BSR heat flux along line 8 close to the trench axis differs considerably to probe measurements conducted by Langseth and Silver (in press) at the trench and the accretionary prism about $30km$ northwest of line 8. They reported values of $\sim 10 - 30mW/m^2$ increasing slightly towards the continent. This significant difference may be attributed to two factors:

- *Difference in BSR heat flux and conventional measurements:* If temperature does not increase linearly with depth, heat flux computed from temperature measurements within the first few meters of the seafloor are expected to differ from measurements that average the temperature gradient over a range of tens to hundreds of meters, such as BSR heat flux. In the present case, the temperature gradient directly beneath the seafloor must be considerably lower than the average temperature gradient between seafloor and BSR.

- *Sharp decrease of heat flux towards the northwest:* This explanation might be supported by the apparent decrease of heat flux close to the trench axis about the same distance ($\sim 8km$) away from it between line 9 and line 8. Also, Langseth and Silver (in press) determined average heat flux along a part of line 8 as $\sim 46.2mW/m^2$. Further to the northwest, where they measured the low values close to the trench, heat flux was determined along a transect from the trench axis up to almost $30km$ away from the trench axis. No values over $40mW/m^2$, have been reported (ref. fig. 24). If the assumption of a rapid decrease towards the northwest is true, production from the heat source (or one of the heat sources) must change considerably.

Deploying heat flux probes close to the trench axis along lines 8 and 9 would allow to discriminate between these two hypotheses. Additional conventional measurements would also allow to further calibrate BSR heat flux allowing a more accurate determination of heat flux above the wide-spread BSRs at this margin. In general, a more detailed knowledge of the structure, the tectonic history, and fluid flow patterns is required to better explain the heat flux patterns at the Costa Rican margin.

9.5 Outlook

Waveform inversion

Full waveform inversion might be used on a much larger scale for high resolution velocity analyses of MCS data from areas where major horizons are layered almost horizontally. Its applicability to crustal data was demonstrated by Minshull and Singh (1993) by applying a combination of modeling and waveform inversion to expanding spread profiles over the oceanic crust at the Blake Spur Fracture Zone.

An accurate source wavelet is a pre-requisite for investigating waveform. Problems introduced by an slowness-dependence of the receiver ghost arrival might be addressed by separating direct and ghost signals prior to the inversion and merge both signals again during inversion with a slowness dependent delay. The method of obtaining the source wavelet might in general be improved e.g. by applying maximum likelihood inversion techniques to the data. These methods, such as the variable norm deconvolution technique (Gray, 1979), are based on the assumption that the real Earth reflectivity function consists of a limited number of spikes above a certain noise level. They may be used only to obtain a good source wavelet without deconvolving the data. However, recording of the far-field from the source e.g. using a moored hydrophone certainly leads to a better (i.e. closer to the real waveform of the source) source signature as input for waveform inversion.

With regard to BSR investigations, the small-scale lateral variation of reflectivity at BSRs cannot be investigated by merely applying the full waveform inversion due to its 1-d approach. However, this might be achieved by combining this pre-stack inversion with a post-stack (or neartrace) inversion technique, which requires a much better a priori knowledge of the background velocity model (e.g. Hampson and Russell, 1985). A problem with stacking is that because of AVO effects, amplitude performance of stacked data will only be a poor approximation to that of zero-offset data. Therefore, techniques to preserve amplitudes during stacking (e.g. partial stacking) have to be applied before inverting post-stack data.

The assumption of one-dimensionality is a major limitation of the full waveform inversion method. Dip moveout (DMO) corrections before transforming into the (τ, p)-domain might help to correct for slight dips (e.g. Hale, 1991). Waveforms might be affected by DMO processing and thus, such techniques may not be suitable. The use of a 2-d forward modeling part during inversion, which would mean not to work in the (τ, p)-domain any more, might be more appropriate in the long run. Since computation of the Fréchet derivatives would also be affected, such a change would both require major coding efforts and lead to considerably more computing time. Also, it would be quite difficult to incorporate structure while updating the model.

The full waveform inversion scheme has already been adapted to OBH geometry (Korenaga, Minshull, Singh, pers. com., 1995). This allows to also account for post-critical reflections providing better constraints on the velocity structure above the BSR. Investigations of pre-critical reflections at large offsets and post-critical reflections might also allow collection of additional information about the other seismic properties, in particular ρ and V_s. With regard to ρ, it should be tested whether impedance is not a better parameter to invert for than V_p. The inversion scheme might be modified to invert for V_s in addition to V_p by allowing V_s to be varied as a second free parameter. This might lead to a highly unstable solution, partly because V_p has a much stronger influence on the reflectivity than V_s. It might be a better approach to first invert for an optimum V_p-model followed by an inversion for shear waves to improve AVO performance. If necessary, this procedure might be repeated until a good fit is achieved. A better constraint on V_s would be highly desirable because of the presumed effect which hydrate cementation may have on S-wave velocity. However, a technique to invert for shear waves would be of interest for seismic wide-angle investigations on a much broader scale.

Heat flux from the depth of BSRs
BSRs have been observed in a large number of seismic profiles. It is highly desirable to improve the method to determine heat flux from the depth of the BSR, since these results would considerably augment to existing heat flux measurements at continental margins. Enhancement of this technique would include the development of processing techniques to reliably identify BSRs even in lower-quality data. Most emphasis, however, should be laid on finding ways to calibrate this technique regarding (p, T)-conditions at the phase boundary. Combining probe measurements with BSR heat flux appears to be a feasible method, as demonstrated along Costa Rica line 8. Hyndman et al. (1992) performed similar temperature calibration from ODP downhole measurements at the Peruvian margin, the Japan Nankai margin and the Blake-Bahama Outer Ridge.

Identification and quantification of hydrates
Until now, most hydrate occurrences are inferred from BSRs in seismic profiles. In order to refine the global methane quantity, an indirect method for the detection of hydrates would be desirable. Seismic methods appear to be most suitable for this purpose, if combined with detailed knowledge of chemistry and geology behind hydrate formation and distribution. Electrical measurements may play an additional role since resistivity is different from that of pore water. The impact of hydrates on slope stability is not yet fully understood. Although obviously not yet economically viable, a development of production techniques of methane from hydrates appears to be of interest in the long range.

Studies of oceanic hydrates in the near future will certainly focus on results from ODP Leg 164 in late 1995, during which extensive studies of hydrated sediments and the BSR at Blake Outer Ridge and Carolina Rise are planned. ODP Leg 170 planned for late 1996 offshore Costa Rica should give valuable information about hydrates at convergent margins and in particular about the involvement of fluid flow in hydrate formation and distribution. Laboratory measurements of physical properties of hydrated sediments (among others: V_p, V_s, electric conductivity, and shear strength), which have started at the U.S. Geological Survey (Winters et al., 1995) are expected to significantly contribute to the knowledge of how hydrates affect sediment properties. Some particular question which might be addressed during geological hydrate research in the near future are as follows:

- *Geological and chemical conditions for BSR and hydrate formation:* This knowledge would be especially helpful in both constraining regions of potential hydrate occurrences and discriminating between regions in which BSRs would be expected at the BHSZ from those where hydrates may occur without being "marked" by a BSR. Some questions regarding BSR formation comprise (1) the minimum hydrate concentration required to trap free gas at the BHSZ, (2) if there are certain sediment types (porosity, permeability) in which BSRs form preferably, (3) in how far fracturing through the HSZ may impede the formation of BSRs, (4) how fluid flow influences the formation or destruction of BSRs. Questions about the formation mechanisms of natural hydrates would include (1) the efficiency of methane production, (2) the minimum methane saturation required for hydrate formation, (3) effects of trace gases, ions, and other pore water components as well as eventually grain components, (4) the time and activation energy required for hydrate formation, (5) further development of methods to delineate sources of hydrate production including ways to discriminate between in-situ production and hydrate formation from uprising fluids. Sedimentological problems would especially comprise (1) the distribution of hydrates in the pore space (2) the role of hydrates as bonding agent as well as inhibitor for other cementation processes, (3) mechanisms which might lead to the occurrence of macroscopic, i.e. at least nodular natural hydrates, (4) sediment types which might preferably contain hydrates (e.g. permeability and porosity requirements), and (5) the processes behind amplitude blanking.

- *Geophysical investigation of BSRs and hydrates:* Investigations of BSRs beneath hydrate layers have so far mostly focussed on investigating their V_p-structure using standard seismic reflection

data. A move towards higher frequencies would be highly desirable as has been demonstrated by results from multichannel deep-towed data from the Blake Ridge area (Wood et al., 1995) and from combined OBH and single-channel high-frequency data (e.g. Katzman et al., 1994; Korenaga et al., 1995; Bobsien, 1995; Spence et al., in press). Efforts for the identification and eventually quantification of hydrates themselves have concentrated on elevated V_p and amplitude blanking. Again, higher frequency data would significantly contribute to such investigations, as shown in deep-tow data from Blake Ridge (Rowe et al., 1995) as well as the combined OBH/single channel data (e.g. Katzman et al., 1994). V_s may be another important parameter for this purpose, since hydrate cementation may result in a strong increase of V_s. Shear wave logging is therefore planned to be conducted in Leg 164 bore holes. However, it is still difficult to perform in-situ measurement of V_s in marine sediments. Electric conductivity might also be used for identifying and quantifying hydrates. Combining measurements of the geophysical parameters which are thought to be most sensitive to the presence of hydrates, i.e. V_p, V_s, seismic quality factors, and electric conductivity, may be regarded as the ultimate goal for hydrate detection. Laboratory investigations are required to calibrate these methods and make them reliable.

- *Hydrates and "global change":* As pointed out by Kvenvolden (1993) as well as Englezos and Hatzikiriakos (1994), continental hydrates and hydrates in shallow arctic waters are assumed to be most vulnerable with regard to a temperature increase related to the greenhouse effect. In this context, thermal modeling is essential to test, how long a temperature signal at the surface or the seafloor requires to reach hydrated sediments and the BHSZ, and how long decomposition may be delayed due to activation energy. Englezos and Hatzikiriakos (1994) performed some modeling studies addressing these problems. Another question which should be addressed in this context is, if, how and to which extent methane from the –compared to continental hydrates– huge amount of oceanic hydrates may penetrate the water column and finally reach the atmosphere.

It is obvious from the scatter in the estimated amount of methane stored in hydrates listed in table 1 that there is a desire for more precise information about hydrate quantities. Combining geophysical methods with geological and geochemical constraints may be an approach towards improving knowledge of global hydrate distribution.

10 Acknowledgments

These investigations would not have been performed without the support from many persons, too many to list them all.

In particular, I would like to thank Prof. Roland von Huene for his supervision. He enthusiastically encouraged me to do this Ph.D. research, provided valuable support and fruitful discussion. The help from his encyclopedic knowledge about the geology of convergent margins cannot be overestimated.

I also would like to thank Prof. Erwin Suess for his valuable support regarding geochemical aspects of this work and Prof. Dietrich Ristow for fruitful discussion with regard to seismic questions.

This study would not have been accomplished without a stay at Bullard Laboratories/British Institutions Reflection Profiling Syndicate, Univ. of Cambridge, U.K., from July until December 1993. I would like to thank both institutions as a whole for their great hospitality and the smooth manner how they enabled me to use their facilities and provided me any support I could think of.

Supervision by Dr. Tim Minshull and Dr. Satish Singh, Univ. Cambridge, was essential for my Ph.D. studies. Their patience in guiding me through the waveform inversion technique, their expertise and ideas regarding both inversion and hydrate related problems and the many discussions I had with them during my stay in Cambridge as well as during some later visits and via the Internet, was extremely valuable for me. I also would like to thank them for providing the inversion and many other useful codes.

Dr. Nina Kukowski contributed to this study by fruitful discussion especially related to fluid and heat flow and gave me valuable assistance regarding organizational aspects.

Among the many other person I have to thank for their support are Dr. Cesar Ranero for letting me use some of the Costa Rica data which he had processed as well as discussing results from this area, Drs. Rüdiger Kunze, Willi Weinrebe and Dave Lynness for their help and their patience in the many computer related questions which I had both at the GEOMAR and at Bullard Labs., Dirk Klaeschen for assisting me with processing and 'MIGPACK' problems, Dr. Klaus Regenauer-Lieb for his enthusiasm particularly in improving the computer environment at the Graduiertenkolleg at GEOMAR/Univ. Kiel, Jun Korenaga for providing an enhanced (τ, p)-conversion routine, and John Miller for his help regarding data acquisition parameters and other processing steps of some of the Peru data. Marc-André Gutscher carefully corrected the English of some sections of this thesis. Oliver Ruoff checked some of the formulas in the appendix.

The Deutsche Forschungsgemeinschaft provided a travel grant to Cambridge as well as personal funding until June 1993 within the grant Hu-470. I was awarded a Ph.D. scholarship by the Deutsche Forschungsgemeinschaft within the Graduiertenkolleg "Dynamik globaler Kreisläufe im System Erde" (headed by Prof. Hans-Ulrich Schmincke) which covered my personal expenses after June 1993. Travel grants under this scheme also enabled me to participate in two meetings of the American Geophysical Union, for which I am particularly grateful.

Lines Peru 1017 and 1018 were acquired by Shell Oil Co. (The Hague), who I have to thank for the use of their data. I also would like to thank the Bundesanstalt für Geowissenschaften und Rohstoffe for use of some of the Costa Rica data. Peru lines HIG 2-5 were acquired by the Hawaii Institute of Geophysics - thanks in particular to Dr. Brian Taylor and Dr. Gregory Moore.

I am among the growing number of geophysicists who are indebted to the Colorado School of Mines and the Gas Research Institute for freely distributing 'SEISUNIX', which turned out to be a very useful tool for seismic data processing. Thank you to Jack K. Cohen and his colleagues for developing and maintaining this package. Some of the plots have been made using 'GMT' software. Thanks to P. Wessel and W. H. F. Smith.

Thank you all at the Dept. of Oceanic Geodynamics, the Graduiertenkolleg and at "Bullard" for the good atmosphere during and after work.

References

[1] K. Andreassen, P. E. Hart, and A. Grantz. Seismic studies of a bottom simulating reflection related to gas hydrate beneath the continental margin of the Beaufort Sea. *J. Geophys. Res.*, 100:12659–12673, 1995.

[2] K. Andreassen, K. Hogstad, and K. A. Berteussen. Gas hydrate in the southern Barents Sea, indicated by a shallow seismic anomaly. *First Break*, 8:235–245, 1990.

[3] P. W. Atkins. *Physical chemistry*, pages 1–1022. Oxford University Press, 1978.

[4] F. Audebert and J.-P. Diet. A focus on focusing. In *52nd EAEG Meeting in Copenhagen, Denmark, expanded abstracts*, pages 107–108. European Association of Exploration Geophysicists, May 1990.

[5] M. W. Ballesteros, G. F. Moore, B. Taylor, and S. Ruppert. Seismic stratigraphic framework of the Lima and Yaquina forearc basins, Peru. In E. Suess and R. von Huene et al., editors, *Proc. Ocean Drill. Program Initial Rep.*, volume 112, pages 77–90, Washington, D.C., 1988. U.S. Printing Office.

[6] N. L. Bangs, D. S. Sawyer, and X. Golovchenko. Free gas at the base of the gas hydrate zone in the vicinity of the Chile triple junction. *Geology*, 21:905–908, 1993.

[7] M. A. Biot. Theory of propagation of elastic waves in a fluid-saturated porous solid, I. low-frequency range. *J. Acoust. Soc. Am.*, 28:168–178, 1956a.

[8] M. A. Biot. Theory of propagation of elastic waves in a fluid-saturated porous solid, II. high-frequency range. *J. Acoust. Soc. Am.*, 28:178–191, 1956b.

[9] M. Bobsien. *Entwicklung und Einsatz eines Hoch-Frequenz-Ozean-Boden-Hydrophons zur hochauflösenden Bestimmung von Kompressionswellengeschwindigkeit in Sedimenten.* PhD thesis, SFB 313, Univ. Kiel, 1995.

[10] J. S. Booth, W. J. Winters, and W. P. Dillon. Circumstantial evidence of gas hydrates and slope failure associations on the United States Atlantic continental margin. In E. D. Sloan, J. Happle, and M. A. Hnatow, editors, *International conference on natural gas hydrates*, volume 715, pages 487–489, New York, 1994. Plenum Press.

[11] J. M. Brooks, A. L. Anderson, R. Sassen, I. R. MacDonald, M. C. K. II, and N. L. Guinasso. Hydrate occurrences in shallow subsurface cores from continental slope sediments. In E. D. Sloan, J. Happle, and M. A. Hnatow, editors, *International conference on natural gas hydrates*, volume 715, pages 381–391, New York, 1994. Plenum Press.

[12] J. M. Brooks, M. C. Kennicutt, R. R. Bidigare, and R. A. Fay. Hydrates, oil seepage, and chemosynthetic ecosystems on the Gulf of Mexico slope. *Eos, Trans. Am. Geophys. Union*, 66:106, 1985.

[13] S. C. Cande. Nazca-South American plate interactions since 50 my B.P. In D. M. Hussong, S. P. Dang, L. D. Kulm, R. W. Couch, and T. W. C. Hilde, editors, *Atlas of the Ocean Margin Program, Peru continental margin, Region IV*, pages 1–14, Woods Hole, MA, 1985.

[14] J. P. Castagna, M. L. Batzle, and R. L. Eastwood. Relationships between compressional-wave and shear-wave velocities in clastic silicate rocks. *Geophysics*, 50:571–581, 1985.

[15] C. H. Chapman. Generalized Radon transforms and slant stacks. *Geophys. J. Roy. Astr. Soc.*, 66:445–453, 1981.

[16] G. W. Claypool and I. R. Kaplan. The origin and distribution of methane in marine sediments. In I. R. Kaplan, editor, *Natural gases in marine sediments*, pages 99–139, New York, 1974. Plenum Press.

[17] R. W. Clayton and R. H. Stolt. A Born-WKBJ inversion method for acoustic reflection data. *Geophysics*, 46:1559–1567, 1981.

[18] E. Denelle, Y. Dezard, and J. J. Raoult. 2-D prestack depth migration in the (S-G-W)-domain. In *56th SEG Meeting in Houston, expanded abstracts*, page 37. Society of Exploration Geophysicists, September 1986.

[19] G. Dietrich, K. Kalle, W. Krauss, and G. Siedler. *Allgemeine Meereskunde*, pages 1–593. Gebrüder Borntraeger, Berlin, 1975.

[20] M. Dietrich and F. Kormendi. Perturbation of the plane-wave reflectivity of a depth-dependent elastic medium by weak inhomogeneities. *Geophys. J. Int.*, 100:203–214, 1990.

[21] W. P. Dillon, M. W. Lee, and D. F. Coleman. Identification of marine hydrate in situ and their distribution off the Atlantic coast of the United States. In E. D. Sloan, J. Happle, and M. A. Hnatow, editors, *International conference on natural gas hydrates*, volume 715, pages 364–380, New York, 1994. Plenum Press.

[22] V. M. Dobrynin, P. Y. Korotayev, and D. V. Plyuschev. Gas hydrates: a possible energy resource. In R. F. Meyer and J. C. Olson, editors, *Long-term energy resources*, pages 727–729, Boston, 1981. Pitman.

[23] C. R. Dodson and M. B. Standing. API drilling and production practice. *Am. Petr. Inst.*, page 173, 1944.

[24] S. N. Domenico. Effect of brine-gas mixture on velocity in an unconsolidated sand reservoir. *Geophysics*, 41:882–894, 1976.

[25] S. N. Domenico. Elastic properties of unconsolidated porous sand reservoirs. *Geophysics*, 42:1339–1368, 1977.

[26] D. H. Ehhalt. How has the atmosphere concentration of CH_4 changed ? In F. S. Rowland and I. S. A. Isaksen, editors, *The changing atmosphere*, volume 7 of *Dahlem Workshop Report*, pages 25–32, Berlin, Germany, 1988.

[27] P. Englezos and S. G. Hatzikiriakos. Environmental aspects of clathrate hydrates. In E. D. Sloan, J. Happle, and M. A. Hnatow, editors, *International conference on natural gas hydrates*, volume 715, pages 270–282, New York, 1994. Plenum Press.

[28] I. G. Ferguson, G. K. Westbrook, M. G. Langseth, and G. P. Thomas. Heat flow and thermal models of the Barbados ridge and accretionay complex. *J. Geophys. Res.*, 98:4121–4142, 1993.

[29] T. J. Galloway, W. Ruska, and P. S. Kobayashi. Experimental measurement of hydrate numbers for methane and ethane and comparison with theoretical values. *Ind. Eng. Chem. Fundam.*, 9:237–243, 1970.

[30] F. Gassmann. Über die Elastizität poröser Medien. *Vierteljahreszeitschrift der Naturforschenden Gesellschaft in Zürich*, 96:1–23, 1951.

[31] J. Geertsma. Velocity-log interpretation: The effect of rock bulk compressibility. *Soc. Pet. Eng. J.*, 1:235–248, 1961.

[32] G. D. Ginsburg, R. A. Guseynov, A. A. Dadashev, G. A. Ivanov, S. A. Kazantsev, V. A. Soloviev, E. V. Telepnev, R. Y. Askeri-Nasirov, A. D. Yesikov, V. I. Maltseva, Y. G. Mashirov, and I. Y. Shabayeva. Gas hydrates in the southern Caspian sea. *Int. Geol. Rev.*, 34:765–782, 1994.

[33] V. Gornitz and I. Fung. Potential distribution of methane in the world's oceans. *Global Biogeochem. Cycles*, 8:333–347, 1994.

[34] W. C. Gray. *Variable norm deconvulution.* PhD thesis, Stanford Univ., 1979.

[35] D. Hale. *Dip moveout processing*, volume 4 of *Course note series*, pages 1.1–5.13. Society of Exploration Geophysicists, Tulsa, OK, 1991.

[36] E. L. Hamilton. Sound velocity-density relations in sea-floor sediments and rocks. *J. Acoust. Soc. Am.*, 43:366–377, 1978.

[37] R. D. Hammond and J. R. Gaither. Anomalous seismic character - Bering Sea shelf. *Geophysics*, 48:590–605, 1983.

[38] D. Hampson and B. H. Russell. Maximum-likelihood seismic inversion. In *National CSEG meeting*, page 16, Calgary, Alberta, 1985. Canadian Society of Exploration Geophysicists. abstract.

[39] S. M. Henrichs and W. S. Reeburgh. Anaerobic mineralization of marine sediment organic matter: rates and role of anaerobic processes in oceanic carbon economy. *Geomicrobiol. J.*, 5:191–237, 1987.

[40] S. G. Henry and H. N. Pollack. Terrestial heat flow above the Andean subduction zone in Peru and Bolivia. *J. Geophys. Res.*, 93:15153–15162, 1988.

[41] R. P. V. Herzen. Heat flow values from the southeastern Pacific. *Nature*, 183:882–883, 1959.

[42] R. P. V. Herzen and S. Uyeda. Heat flow through the eastern Pacific ocean floor. *J. Geophys. Res.*, 68:4219–4250, 1963.

[43] R. Hesse. Diagenesis #11: early diagenetic pore water/sediment interaction: modern offshore basins. *Geoscience Canada*, 14:165–195, 1986.

[44] R. Hey. Tectonic evolution of the Cocos-Nazca spreading center. *Geol. Soc. Am. Bull.*, 88:1404–1420, 1977.

[45] F. Hilterman. Seismic lithology - elastic moduli to seismic velocity. GECO-PRAKLA course notes.

[46] K. Hinz and scientific crew. Geoscientific investigation off Costa Rica, PACOMAR II. Internal Report Archiv-Nr. 110/48, Tagebuch-Nr. 12.212/92, Bundesanstalt für Geowissenschaften und Rohstoffe, Hannover, 1992.

[47] K. Hinz, R. von Huene, C. R. Ranero, and the PACOMAR Working Group. Tectonic structure of the convergent Pacific margin offshore Costa Rica from multichannel seismic reflection data. *Tectonics*, in press.

[48] M. Honarpour, L. Koederitz, and A. H. Harvey. *Relative permeability of petroleum reservoirs*, pages 1–143. CRC Press, Boca Raton, FL, 1986.

[49] P. Huchon and J. Bourgois. Subduction-induced fragmentation of the Nazca Plate off Peru: Mendaña fracture zone and Trujillo trough revisited. *J. Geophys. Res.*, 95:8419–8436, 1990.

[50] J. M. Hunt. *Petroleum geochemistry and geology*, page 1. W. H. Freeman, San Francisco, 1990.

[51] D. M. Hussong, T. B. R. IV, and W. A. Bartlett. SeaMARC II sonar imagery and bathymetry of the Nazca Plate and Peru Forearc, ODP Leg 112. In E. Suess and R. von Huene et al., editors, *Proc. Ocean Drill. Program Initial Rep.*, volume 112, pages 125–130, Washington, D.C., 1988. U.S. Printing Office.

[52] D. M. Hussong and K. L. Wipperman. Vertical movement and tectonic erosion of the continental wall of the Peru-Chile trench near $11^0 30'$ s latitude. In L. D. Kulm, J. Dymond, E. J. Dasch, and D. M. Hussong, editors, *Nazca Plate: Crustal formation and Andean convergence*, volume 154 of *Geol. Soc. Am. Mem.*, pages 71–85, 1981.

[53] D. R. Hutchinson, M. W. Lee, C. A. Scholz, A. J. Golmshtok, and A. H. Johnson. Lake Baikal: Gas hydrate character in an active rift lake. In *Suppl. to Eos, 25 Apr. 1995, AGU Spring Meeting*, page 164, 1995.

[54] R. D. Hyndman and E. E. Davis. A mechanism for the formation of methane hydrate and seafloor bottom-simulating reflectors by vertical fluid expulsion. *J. Geophys. Res.*, 97:7025–7041, 1992.

[55] R. D. Hyndman, J. P. Foucher, M. Yamano, A. Fisher, and S. T. of Ocean Drilling Program Leg 131. Deep sea bottom-simulating reflectors: calibration of the hydrate stability field as used for heat flow estimates. *Earth Planet. Sci. Lett.*, 109:289–302, 1992.

[56] R. D. Hyndman and G. D. Spence. A seismic study of methane hydrate marine bottom simulating reflectors. *J. Geophys. Res.*, 97:6683–6698, 1992.

[57] G. A. Jeffrey and R. K. McMullan. *Progress in inorganic chemistry*, pages 43–108. Marcel Bekker Inc., New York, 1967.

[58] M. Kastner, H. Elderfield, J. B. Martin, E. Suess, K. A. Kvenvolden, and R. E. Garrison. Diagenesis and interstitial water-chemistry at the Peruvian continental margin - major constituents and strontium isotopes. In *Proc. Ocean Drill. Program Sci. Results*, volume 112, pages 413–440, Washington, D.C., 1990. U.S. Printing Office.

[59] M. Kastner, K. A. Kvenvolden, and M. J. Whiticar. Relation between pore fluid chemistry and gas hydrates associated with bottom-simulating reflectors at the Cascadia margin, Sites 889 and 892. In *Proc. Ocean Drill. Program Sci. Results*, volume 146, Washington, D.C., in press. U.S. Printing Office.

[60] D. L. Katz. Depths with frozen gas fields may be expected - footnotes. *J. Petrol. Tech.*, 24:557, 1972.

[61] R. Katzman, W. S. Holbrook, and C. K. Paull. Combined vertical-incidence and wide-angle seismic study of a gas hydrate zone, Blake Ridge. *J. Geophys. Res.*, 99:17975–17995, 1994.

[62] B. L. N. Kennett and N. J. Kerry. Seismic waves in a stratified half space. *Geophys. J. Roy. Astr. Soc.*, 57:557–583, 1979.

[63] H. Kiefte, M. J. Clouter, and R. E. Gagnon. Determination of acoustic velocities of clathrate hydrates by Brillouin spectroscopy. *J. Phys. Chem.*, 89:3103–3108, 1985.

[64] K. Klitgord and J. Mammerickx. northern East Pacific Rise: Magnetic anomaly and bathymetric framework. *J. Geophys. Res.*, 87:6725–6750, 1982.

[65] R. Kobayashi and D. L. Katz. Methane hydrates at high pressure. *J. Petrol. Tech.*, 1:66–70, 1949.

[66] J. Korenaga, W. S. Holbrook, and C. K. Paull. Combined vertical-incidence and wide-angle seismic study of a gas hydrate zone, Carolina Rise. In *Suppl. to Eos, 25 Apr. 1995, AGU Spring Meeting*, page 164, 1995.

[67] F. Kormendi and M. Dietrich. Non-linear waveform inversion of plane-wave seismograms in stratified elastic media. *Geophysics*, 56:664–674, 1991.

[68] N. Kukowski. Modeling coupled heat and fluid transport in the accretionary complex off Peru. *Earth Planet. Sci. Lett.*, in prep.

[69] N. Kukowski, R. von Huene, J. Malavieille, and S. E. Lallemand. Sediment accretion against a buttress beneath the Peruvian continental margin at 12° s as simulated with sandbox modeling. *Geol. Rundschau*, 83:1–10, 1994.

[70] L. D. Kulm, R. A. Prince, and S. Dang. Drill hole stratigraphy, dredge lithologies, and sample locations. In D. M. Hussong, S. P. Dang, L. D. Kulm, R. W. Couch, and T. W. C. Hilde, editors, *Atlas of the Ocean Margin Program, Peru continental margin, Region IX*, page 18, Woods Hole, MA, 1985.

[71] L. D. Kulm, T. M. Thornburg, E. Suess, J. Resig, and P. Fryer. Clastic, diagenetic, and metamorphic lithologies of a subsiding continental block: central Peru forearc. In E. Suess and R. von Huene et al., editors, *Proc. Ocean Drill. Program Initial Rep.*, volume 112, pages 91–107, Washington, D.C., 1988. U.S. Printing Office.

[72] B. Kvamme. Mechanisms for initiation of hydrate from liquid water. In E. D. Sloan, J. Happle, and M. A. Hnatow, editors, *International conference on natural gas hydrates*, volume 715, pages 307–310, New York, 1994. Plenum Press.

[73] K. A. Kvenvolden. Methane hydrate - a major reservoir of carbon in the shallow geosphere ? *Chem. Geol.*, 71:41–51, 1988.

[74] K. A. Kvenvolden. Gas hydrates - geologic perspective and global change. *Rev. Geophys.*, 31:173–187, 1993.

[75] K. A. Kvenvolden. Natural gas hydrate occurrence and issues. In E. D. Sloan, J. Happle, and M. A. Hnatow, editors, *International conference on natural gas hydrates*, volume 715, pages 233–246, New York, 1994. Plenum Press.

[76] K. A. Kvenvolden, T. J. Frank, and M. Golan-Bac. Hydrocarbon gases in tertiary and quaternary sediments offshore Peru - results and comparisons. In *Proc. Ocean Drill. Program Sci. Results*, volume 112, pages 505–516, Washington, D.C., 1990. U.S. Printing Office.

[77] K. A. Kvenvolden and M. Kastner. Gas hydrates of the Peruvian outer continental margin. In *Proc. Ocean Drill. Program Sci. Results*, volume 112, pages 517–526, Washington, D.C., 1990. U.S. Printing Office.

[78] K. A. Kvenvolden and T. J. McDonald. Gas hydrates of the Middle America trench - Deep Sea Drilling Project Leg 84. In R. von Huene and J. A. et al., editors, *Initial Rep. Deep Sea Drill.*, volume 84, pages 667–682, Washington, D.C., 1985. U.S. Printing Office.

[79] E. Landa, P. Thore, V. Sorin, and Z. Koren. Interpretation of velocity estimates from coherency inversion. *Geophysics*, 56:1377–1383, 1991.

[80] M. G. Langseth. Calibration of the BSR on the Costa Rican margin. *Geophys. Res. Lett.*, in prep.

[81] M. G. Langseth, K. Becker, R. P. V. Herzen, and P. Schultheiss. Heat and fluid flux through sediment on the western flank of the Mid- Atlantic Ridge: A hydrogeological study of North Pond. *Geophys. Res. Lett.*, 19:517–520, 1992.

[82] M. G. Langseth and M. A. Hobart. A marine geothermal study over deformed sediments of the subduction complex off Oregon and Washington. *Eos, Trans. Am. Geophys. Union*, 65:1089, 1984. Abstract.

[83] M. G. Langseth and E. Silver. The convergent margin off the Nicoya Peninsula - a region of exceptionally low heat flow. -, in press.

[84] L. Lebedev. Tectonic features of the shale diapirs and mud volcano distribution in sediments of the Caspian, Black and Azov seas. In *Gas in marine sediments*, Nioz, Texel, Netherlands, September 1994. The shallow gas group. abstract.

[85] M. W. Lee, D. R. Hutchinson, W. F. Agena, W. P. Dillon, J. J. Miller, and B. A. Swift. Seismic character of gas hydrates on the southeastern U.S. continental margin. *Mar. Geophys. Res.*, 16:163–184, 1994.

[86] M. W. Lee, D. R. Hutchinson, W. P. Dillon, J. J. Miller, W. F. Agena, and B. A. Swift. Method of estimating the amount of in situ gas hydrates in deep marine sediments. *Mar. and Petrol. Geol.*, 10:493–506, 1993.

[87] P. Lonsdale and K. D. Klitgord. Structure and tectonic history of the eastern Panama Basin. *Geol. Soc. Am. Bull.*, 89:981–999, 1978.

[88] M. E. MacKay, R. D. Jarrard, G. K. Westbrook, and R. D. Hyndman. Origin of bottom simulating reflectors: Geophysical evidence from the Cascadia accretionary prism. *Geology*, 22:459–462, 1994.

[89] Y. F. Makogon. Natural gas hydrates: the state of study in teh USSR and perspectives of its use. In *Third chemical congress of North America*, June 1988. abstract.

[90] Y. F. Makogon, F. A. Trebin, A. A. Trofimuk, V. P. Tsarev, and N. V. Cherskiy. Detection of a pool of natural gas in solid (hydrated gas) state. *Doklady Academy Science USSR, Earth Science Section*, 196:197–200, 1972.

[91] R. G. Markl, G. M. Bryan, and J. I. Ewing. Structure of the Blake-Baham Outer Ridge. *J. Geophys. Res.*, 75:4539–4555, 1970.

[92] D. R. Marshall, S. Saito, and R. Kobayashi. Hydrates at high pressure. *AIChE J*, 10:734–740, 1964.

[93] A. McAuley. Prestack inversion with plane-layer point-source modelling. *Geophysics*, 50:77–89, 1985.

[94] H. D. McLeod and J. M. Campbell. Natural gas hydrates at pressures to 10,000 psia. *J. Petrol. Tech.*, 13:590, 1961.

[95] C. D. Mets, R. G. Gordon, D. F. Argus, and S. Steins. Current plate motions. *Geophys. J. Int.*, 101:425–478, 1990.

[96] R. F. Meyer. Gas hydrates. In R. F. Meyer and J. C. Olson, editors, *Long-term energy resources*, pages 713–726, Boston, 1981. Pitman.

[97] R. F. Meyer. Speculations on oil and gas resources in small fields and unconventional deposits. In R. F. Meyer and J. C. Olson, editors, *Long-term energy resources*, pages 49–72, Boston, 1981. Pitman.

[98] J. J. Miller, M. W. Lee, and R. von Huene. An analysis of a reflection from the base of a gas hydrate zone off Peru. *Am. Assoc. Pet. Geol. Bull.*, 75:910–924, 1991.

[99] T. A. Minshull and S. C. Singh. Shallow structure of oceanic crust in the western North Atlantic from seismic waveform inversion and modelling. *J. Geophys. Res.*, 98:1777–1792, 1993.

[100] T. A. Minshull, S. C. Singh, and G. K. Westbrook. Seismic velocity structure at a gas hydrate reflector, offshore western Colombia, from full waveform inversion. *J. Geophys. Res.*, 99:4715–4734, 1994.

[101] T. A. Minshull and R. S. White. Sediment compaction and fluid migration in the Makran accretionary prism. *J. Geophys. Res.*, 94:7387–7402, 1989.

[102] T. A. Minshull, R. S. White, P. J. Barton, and J. S. Collier. Deformation at plate boundaries around the Gulf of Oman. *Mar. Geol.*, 104:265–277, 1992.

[103] G. F. Moore and B. Taylor. Structure of the Peru forearc from mulitchannel seismic-reflection data. In E. Suess and R. von Huene et al., editors, *Proc. Ocean Drill. Program Initial Rep.*, volume 112, pages 71–76, Washington, D.C., 1988. U.S. Printing Office.

[104] D. C. Noble, E. H. McKee, and F. Megard. Early Tertiary "Incaic" tectonism, uplift, and volcanic activity, Andes of central Peru. *Geol. Soc. Am. Bull.*, 90(I):903–907, 1979.

[105] W. J. Ostrander. Plane wave reflection coefficients for gas sands at nonnormal angles of incidence. *Geophysics*, 49:1637–1648, 1984.

[106] B. I. Pandit and M. S. King. Elastic wave propagation in propane gas hydrates. In H. M. French, editor, *Fourth Canadian permafrost conference*, pages 335–352. Canadian National Research Council, 1982.

[107] C. K. Paull, W. U. III, and W. S. Borowski. Sources of biogenic methane to form marine gas hydrates. In E. D. Sloan, J. Happle, and M. A. Hnatow, editors, *International conference on natural gas hydrates*, volume 715, pages 393–409, New York, 1994. Plenum Press.

[108] C. K. Paull, W. Ussler, and W. P. Dillon. Is the extent of glaciation limited by marine gas-hydrates ? *Geophys. Res. Lett.*, 18:432–434, 1991.

[109] J. Philipp. *Bestimmung der Kompressions- und Scherwellengeschwindigkeit mariner Sedimente an Kastenlotkernen: Entwicklung einer Meßapparatur und Vergleich mit sedimentologischen Parametern.* PhD thesis, Inst. Geophysik, Univ. Kiel, 1989.

[110] R. H. Pilger and D. W. Handschuhmacher. The fixed hotspot hypothesis and the origin of the Easter-Sala y Gomez-Nazca trace. *Geol. Soc. Am. Bull.*, 92:437–446, 1981.

[111] E. Polak and G. Ribière. Note sur la convergence de méthodes de diréction conjugées. *Revue Fr. Inf. Rech. Oper.*, 16:35–43, 1969.

[112] P. M. Rodger. The stability of gas hydrates. *J. Phys. Chem.*, 94:6080, 1990.

[113] M. M. Rowe, K. M. Fisher, and J. F. Gettrust. Geophysical evidence for pathways of gas escape from submarine gas hydrates. In *Suppl. to Eos, 25 Apr. 1995, AGU Spring Meeting*, page 163, 1995.

[114] M. M. Rowe and J. F. Gettrust. Faulted structure of the bottom simulating reflector on the Blake Ridge, western North Atlantic. *Geology*, 21:833–836, 1993.

[115] M. M. Rowe and J. F. Gettrust. Methane hydrate content of Blake Outer Ridge sediments. In E. D. Sloan, J. Happle, and M. A. Hnatow, editors, *International conference on natural gas hydrates*, volume 715, pages 492–494, New York, 1994. Plenum Press.

[116] F. Santosa and W. W. Symes. *An analysis of least-squares velocity inversion*, pages 1–154. Number 4 in geophysical monograph series. Society of Exploration Geophysicists, Tulsa, OK, 1989.

[117] J. G. Sclater, C. Jaupart, and D. Galson. The heat flow through oceanic and continental crust and the heat loss of the earth. *Rev. Geophys. Space Phys.*, 18:269–311, 1980.

[118] R. E. Sheriff and L. P. Geldart. *Exploration seismology*, volume 1, pages 1–253. Cambridge University Press, Cambridge, U.K., 1982.

[119] R. E. Sheriff and L. P. Geldart. *Exploration seismology*, volume 2, pages 1–221. Cambridge University Press, Cambridge, U.K., 1983.

[120] T. H. Shipley, M. H. Houston, R. T. Buffler, F. J. Shaub, K. J. McMillen, J. W. Ladd, and J. L. Worzel. Seismic evidence for widespread possible gas hydrate horizons on continental slopes and rises. *Am. Assoc. Pet. Geol. Bull.*, 63:2204–2213, 1979.

[121] T. H. Shipley, P. L. Stoffa, and D. F. Dean. Three-dimensional seismic imaging of the Costa Rica accretionary prism: Structural diversity in a small volume of the lower slope. *J. Geophys. Res.*, 97:4439–4459, 1992.

[122] S. C. Singh and T. A. Minshull. Velocity structure of a gas hydrate reflector at Ocean Drilling Program Site 889 from a global seismic waveform inversion. *J. Geophys. Res.*, 99:24221–24233, 1994.

[123] S. C. Singh, T. A. Minshull, and G. D. Spence. Velocity structure of a gas hydrate reflector. *Science*, 260:204–207, 1993.

[124] E. D. Sloan. *Clathrate hydrates of natural gases*, pages 1–641. Marcel Bekker Inc., New York, 1990.

[125] E. D. Sloan and F. Fleyfel. A molecular mechanism for gas hydrate nucleation. *AIChE J.*, 37:1281–1292, 1991.

[126] G. D. Spence, T. A. Minshull, and C. Fink. Seismic studies of methane gas hydrate, offshore Vancouver Island. In *Proc. Ocean Drill. Program Sci. Results*, volume 146, Washington, D.C., in press. U.S. Printing Office.

[127] E. Suess, R. von Huene, and et al. *Proc. Ocean Drill. Program Initial Rep. - Site Reports*, volume 112, chapter 2, pages 1–738. U.S. Printing Office, Washington, D.C., 1988.

[128] A. Tarantola. Inversion of seismic reflection data in the acoustic approximation. *Geophysics*, 49:1259–1266, 1984.

[129] A. Tarantola and B. Valette. Generalized nonlinear problems solved using the least squares criterion. *Rev. Geophys. Space Phys.*, 20:219–232, 1982.

[130] F. W. Taylor. The greenhouse effect and climate change. *Rep. Prog. Phys.*, 54:881–981, 1991.

[131] A. A. Trofimuk, N. V. Cherskiy, and V. P. Tsarev. The role of continental glaciation and hydrate formation on petroleum occurrences. In R. F. Meyer, editor, *Future supply of nature-made petroleum and gas*, pages 919–926, New York, 1977. Pergamon Press.

[132] B. E. Tucholke, G. M. Bryan, and J. I. Ewing. Gas-hydrate horizons detected in seismic profile data from the western North Atlantic. *Am. Assoc. Pet. Geol. Bull.*, 61:698–707, 1977.

[133] V. K. Verma, J. H. Hand, and D. L. Katz. Gas hydrates from liquid hydrocarbons (methane-propane-water-system). In *AICHE-VTG Joint Meeting, Munich, abstracts*, page 10, September 1974.

[134] M. T. von Breymann, K.-C. Emeis, and A. Camerlenghi. Geochemistry of sediments from the Peru upwelling area: results from Sites 680, 682, 685, and 688. In *Proc. Ocean Drill. Program Sci. Results*, volume 112, pages 491–503, Washington, D.C., 1990. U.S. Printing Office.

[135] R. von Huene, J. Bialas, E. R. Flueh, B. Cropp, T. Csernok, E. Fabel, J. Hoffmann, K. Emeis, P. Holler, G. Jeschke, C. M. Leandro, I. F. Peréz, J. S. Chavarria, A. H. Florez, D. Z. Escobedo, R. León, and O. L. Barrios. Morphotectonics of the Pacific convergent margin of Costa Rica. In P. Mann, editor, *Geologic and tectonic development of the Caribbean plate boundary in southern Central America*, volume 295, pages 291–308. Geol. Soc. Am., 1995.

[136] R. von Huene and J. A. et al. *Initial Rep. Deep Sea Drill. Proj.*, volume 84, pages 1–967. U.S. Printing Office, Washington, D.C., 1988.

[137] R. von Huene, L. D. Kulm, and J. Miller. Structure of the frontal part of the Andean convergent margin. *J. Geophys. Res.*, 90:5429–5442, 1985.

[138] R. von Huene and J. Miller. Migrated multichannel seismic-reflection records across the Peru continental margin. In E. Suess and R. von Huene et al., editors, *Proc. Ocean Drill. Program Initial Rep.*, volume 112, pages 109–124, Washington, D.C., 1988. U.S. Printing Office.

[139] R. von Huene, I. A. Pecher, and M.-A. Gutscher. Development of the accretionary prism along Peru and material flux after subduction of Nazca Ridge. *Tectonics*, in press.

[140] R. von Huene, E. Suess, N. Kukowski, I. A. Pecher, W. Rabbel, and K. A. Kvenvolden. Drilling the Peruvian convergent margin for geophysical determination of gas hydrate properties, investigating vertical tectonism and quantification of fluid flow. ODP proposal, submitted to JOIDES Planning Office, 1995. unpubl.

[141] R. von Huene, E. Suess, and L. . S. Scientists. Ocean Drilling Program Leg 112, Peru continental margin: Part 1, tectonic history. *Geology*, 16:934–938, 1988.

[142] K. Wang, R. D. Hyndman, and M. Yamano. Thermal regime of the Southwest Japan subduction zone: effects of age history of the subducting plate. *Tectonophysics*, 248:53–69, 1995.

[143] F. Warner. Absolute reflection coefficients from deep seismic reflections. *Tectonophysics*, 173:15–23, 1990.

[144] G. K. Westbrook, B. Carson, R. J. Musgrave, and et al. *Proc. Ocean Drill. Program Initial Rep.*, volume 146, pages 1–611. U.S. Printing Office, Washington, D.C., 1994.

[145] E. Whalley. Speed of longitudinal sound in clathrate hydrates. *J. Geophys. Res.*, 85:2539–2542, 1980.

[146] R. S. White. Gas hydrate layers trapping free gas in the gulf of oman. *Earth Planet. Sci. Lett.*, 42:114–120, 1979.

[147] R. B. Whitmarsh and P. R. Miles. In situ measurements of shear-wave velocity in ocean sediments. In J. M. Hovem, M. D. Richardson, and R. D. Stoll, editors, *Shear waves in marine sediments*, pages 321–328, Dordrecht, The Netherlands, 1991. Kluwer Academic Publishers.

[148] W. J. Winters, J. S. Booth, D. H. Mason, and R. F. C. amd W. P. Dillon. Laboratory testing of gas hydrates in marine sediments. In *Suppl. to Eos, 25 Apr. 1995, AGU Spring Meeting*, page 165, 1995.

[149] W. T. Wood, M. M. Rowe, and J. F. Gettrust. Very high resolution 2-d seismic modeling of the base of methane hydrate in the Blake Ridge. In *Suppl. to Eos, 25 Apr. 1995, AGU Spring Meeting*, page 164, 1995.

[150] W. T. Wood, P. L. Stoffa, and T. H. Shipley. Quantitative detection of methane hydrate through high resolution seismic velocity analysis. *J. Geophys. Res.*, 99:9681–9695, 1994.

[151] R. E. Wyman. Petrogeophysics, the interrelationships of petrophysics, geology and geophysics. In *Stratigraphic interpretation of seismic data*, AAPG continuing education, pages 1–106. Am. Assoc. Pet. Geol, 1982.

[152] M. Yamano and S. Uyeda. Heat flow. In A. E. M. Naim, F. G. Stehli, and S. Uyeda, editors, *The ocean basins and margins: the Pacific Ocean*, volume 7B, pages 523–557, New York, 1988. Plenum Press.

[153] M. Yamano and S. Uyeda. Heat-flow studies in the peru subduction zone. In *Proc. Ocean Drill. Program Sci. Results*, volume 112, pages 653–661, Washington, D.C., 1990. U.S. Printing Office.

[154] M. Yamano, S. Uyeda, Y. Aoki, and T. H. Shipley. Estimates of heat flow derived from gas hydrates. *Geology*, 10:339–343, 1982.

[155] S. Ye, E. R. Flueh, A. Stavenhagen, G. Leandro, R. von Huene, and K. Hinz. Crustal structure of the subduction zone off Costa Rica derived from OBS refraction and wide-agle reflection seismic data. *Tectonics*, in press.

[156] K. Zoeppritz. Über Reflexion und Durchgang seismischer Wellen durch Unstetigkeitsflächen. In *Über Erdbebenwellen VII B*, volume K1, pages 57–84. Nachr. der königl. Ges. der Wiss. zu Göttingen, 1919.

A Gas hydrates in sediments

A.1 Chemistry of gas hydrates

Gas hydrates are ice-like crystalline structures of a water lattice with cavities which contain guest gases. They are bonded by Van der Waals forces under low temperature and moderate pressures. The guest molecule is necessary to support the cavity. In the natural environment, methane is the most common guest molecule (Sloan, 1990).

There are two relevant structures of hydrates in nature, structure I and structure II, which consist of a combination of three types of cavities. These cavities are a pentagonal dodecahedron (5^{12}, where 5 is the number of edges, 12 is the number of faces), a tetrakaidecahedron ($5^{12}6^2$), and a hexakaidecahedron ($5^{12}6^4$). Ref. fig. 93 for further illustration. Structure I hydrate is composed of a combination of 5^{12} and $5^{12}6^2$ cavities, whereas structure II hydrate consists of 5^{12} linked with $5^{12}6^4$ cavities. Table 6 displays geometrical features of both hydrate structures.

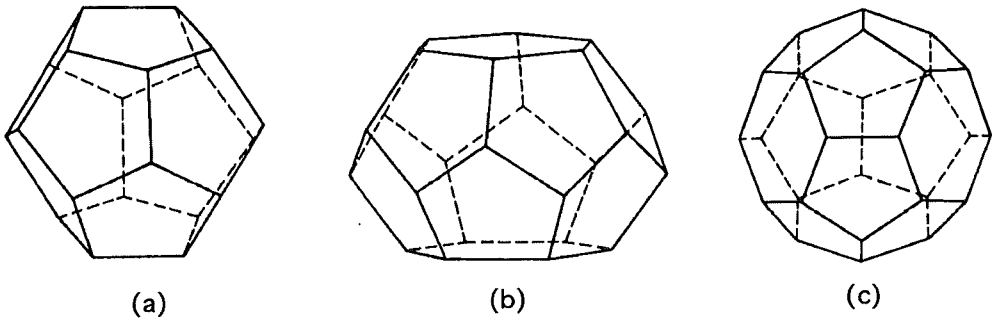

Figure 93: Three cavities in gas clathrate hydrates: (a) 5^{12}, (b) $5^{12}6^2$, (c) $5^{12}6^4$. From Sloan (1990) after Jeffrey and McMullan (1967).

Hydrate crystal structure	I	I	II	II
Cavity	small	large	small	large
Description	5^{12}	$5^{12}6^2$	5^{12}	$5^{12}6^4$
Number of cavities/structure	2	6	16	8
Average cavity radius [Å]	3.91	4.33	3.902	4.683
Variation in radius [%] (1)	3.4	14.4	5.5	1.73
Coordination number (2)	20	24	20	28

Table 6: Geometry of hydrate cavities. (1) Variation in distance of oxygen atoms from center of cage, (2) Number of oxygens at the periphery of each cavity. After Sloan (1990), Jeffrey and McMullan (1967).

The maximum radius of the space available for guest molecules in each cavity can be computed by subtracting the Van der Waals radius of the water molecule (1.45 Å) from the average cavity radius in table 6. If the ratio of the radius of a guest molecule relative to the radius of the cavity is greater than 1, the guest molecule cannot fit into the cavity without distortion. If this ratio is lower than about 0.77, the molecular attractive forces cannot sufficiently support the cavity structure (Sloan, 1990). Table 7 shows the guest molecule to cavity size ratio of some known natural hydrate formers. Note that this table is only true if assuming simple hydrate formers, i.e. without admixture of other gases. Under this assumption, guest molecules from smaller cavities also enter the larger cages. If small amounts of other gases are added as guest molecules, the choice of the structure may change: Sloan (1990) predicts, that the addition of 0.5% propane to methane should suffice to cause hydrate to change from structure I to

Hydrate crystal structure:	I	I	II	II
	5^{12}	$5^{12}6^2$	5^{12}	$5^{12}6^4$
N_2	0.833	0.712	*0.836*	*0.634*
O_2	0.853	0.729	*0.856*	*0.649*
CH_4	*0.886*	*0.757*	0.889	0.675
H_2S	*0.931*	*0.795*	0.934	0.708
CO_2	1.041	*0.889*	1.044	0.792
C_2H_6	1.118	*0.955*	1.122	0.851
$c-C_3H_6$	1.178	*1.007*	1.182	*0.897*
$(CH_2)_3O$	1.240	*1.059*	1.244	*0.943*
C_3H_8	1.276	1.090	1.280	*0.971*
$i-C_4H_10$	1.321	1.128	1.325	*1.005*

Table 7: Ratio of the sizes of hydrate forming molecular diameters relative to cavity diameters. Cavity diameters take account for the water radii of 1.45$\AA$. Experimentally observed occupancies by simple hydrate formers are marked in italic. After Sloan et al. (1990).

structure II.

Hypotheses for nucleation of hydrates in liquid water include those of Rodger (1990) and Sloan and Fleyfel (1991). The first theory assumes that hydrate formers are initially adsorbed on a liquid (or solid) water phase. Cavities may be formed by condensation of additional water molecules onto this surface around the guest molecule. Sloan (1990) suggests that clusters form around the soluted guest molecules followed by joining of these clusters, agglomeration and finally crystal growth. A brief comparison of both theories is given by Kvamme (1994). See Sloan (1990) for a detailed treatise about the kinetics of gas hydrate nucleation and crystal growth.

Hydrates can store large amounts of methane. The ratio of gas to water molecules in structure I hydrate is $1 : 5\frac{3}{4}$, leading to 164 volumes of methane under ambient conditions per volume of methane hydrate (e.g. Kvenvolden, 1993). Usually however, the fractional occupancy of the smaller cavities of structure I hydrates is reported to be between 0.7 and 0.9 (Sloan, 1990).

Stability of hydrates is considerably more pressure dependent than that of ice. Fig. 1 displays the phase diagram of pure methane hydrate together with assumed thermal gradients in the two regions of the world, where hydrates are stable in the subsurface: permafrost regions (referred to as continental hydrate) and deep sea sediments (oceanic hydrates). Adding other trace gases or ions to the system yields a shift of the phase boundary. Addition of NaCl and N_2, e.g. shifts the phase boundary towards lower temperatures, whereas admixture of CO_2, H_2S, and higher-molecular-weight hydrocarbons cause a shift into the opposite direction (ref. e.g. Kvenvolden, 1993). The addition of a small amount of propane, which causes a change from structure I to II, leads to a pronounced shift of the hydrate stability phase diagram towards higher temperatures: Less than half the pressure is required at a given temperature to stabilize structure II hydrates than structure I hydrates (Sloan, 1990).

A.2 Chemical markers of hydrates in sediments

The formation of hydrates leads to an exclusion of ions, since ions are too large to fit into hydrate cages and they compete with hydrates for the available water molecules. Consequently, hydrates formed from salt water, are expected to be depleted of Cl^--ions, whereas the water around them would be enriched. The depletion of chloride ions in sediment cores is therefore one of the main chemical indicators for the occurrence of hydrates. It should be cautioned however, that there are other reasons to find a decrease of Cl^- in marine sediments, such as a transformation of opal, filtration, and clay mineral authigenesis (e.g. Kastner et al., in press).

A second chemical indicator of hydrates is a fractionation of O isotopes. The enrichment factor α of ^{18}O, defined by

$$\alpha \equiv \frac{(^{18}O/^{16}O)_{solid}}{(^{18}O/^{16}O)_{liquid}} \quad ,$$

was measured as $\alpha = 1.0026$, which is similar to that of ice (Sloan, 1990).

A.3 Physical properties of hydrates and hydrated sediments

Most physical properties of hydrates resemble those of ice, with two prominent exceptions: Thermal conductivity of hydrates is close to the conductivity of water, the relative dielectric constant is lower than that of both substances. Table 8 gives a compilation of physical properties of structure I hydrates compared to properties of ice and water.

	water	ice	hydrate
Compressional wave velocity $[km/s]$	1.47	3.8	$3.3 - 3.8$
Shear wave velocity $[km/s]$	0	2.0	~ 1.7
Thermal conductivity $[W/(m \cdot K)]$	$0.59 - 0.56$	$1.5 - 2.5$	~ 0.5
Density $[g/cm^3]$	1.035	0.917	~ 0.92
Electric resistivity $[\Omega \cdot m]$	~ 0.3	$10 - 1000$	~ 150

Table 8: Physical properties of structure I methane hydrate compared to those of water and ice. Properties of structure II hydrates appear to be similar to those of structure I hydrates. Thermal conductivity of water is for a salinity of $0 - 4\%$, temperature of $17.5°C$, and ambient pressure (from Dietrich et al., 1975). Other properties of water assume a salinity of 3.5%, a temperature of $4°C$, and ambient pressure (from Dietrich et al., 1975). Density of ice assumes fresh water ice without inclusion of air molecules (from Dietrich et al., 1975). Thermal conductivity and electric properties of ice give possible ranges for natural ice (from Dietrich et al., 1975). Seismic velocities of ice are from Pandit and King (1982). See text regarding gas hydrate properties. Gas hydrate properties compiled mainly after Sloan (1990).

P-wave velocity of marine hydrates were first calculated by Whalley at al. (1980) at $3.8km/s$, they were measured in the laboratory by Kiefte et al. (1985) at $3.3km/s$, $3.7km/s$, and $3.35km/s$ for methane, propane, and hydrogen sulfide hydrates, respectively. Ship-board laboratory measurements were performed at a massive hydrate sample at DSDP Leg 84 Site 570. Laboratory data and sonic logging through this massive gas hydrate layer drilled allowed a determination of V_p as $\sim 3.6km/s$ (von Huene et al., 1985b). Density was determined while logging this bore hole as $1.04 - 1.06g/cm^3$, which was the apparent density and was corrected for the presence of methane to $0.92 - 0.93g/cm^3$. Electric resistivity was also measured in situ at this site as $\sim 150\Omega \cdot m$. Measurement of S-wave velocity has so far only been reported by Pandit and King (1982).

Sediments in which hydrates replace part of the pore water, are subsequently assumed to have higher seismic velocities than their non-hydrated counterparts. It might be difficult to quantify this elevation in velocities, partly because in addition to the mere replacement of pore water by hydrates, hydrates might be involved in cementation between grains, a process which especially affects V_s (e.g. Lee et al., 1994). Density and thermal conductivity are not assumed to be affected significantly, whereas electric properties are expected to change considerably. Permeability is another factor which is assumed to be strongly influenced by hydrates. The replacement of pore water by hydrates probably causes a significant decreases of permeability due to an expected pore pluggage by solid hydrates. However so far, no quantitative measurements of this effect are available. The changes of physical properties are expected to be different if hydrates also replace part of the sediment matrix (nodular and more massive hydrates) as well as for hydrates in permafrost regions, where hydrates replace solid ice.

A.4 Implications on sedimentological properties

If solid hydrates replace part of the liquid water in the pore space they are expected to inhibit the sedimentological processes of consolidation and mineral cementation (e.g. Kvenvolden, 1993). On the other hand, hydrates themselves can act as cementation agents between grains leading to an increase in stiffness of the sediments as long as they remain within the HSZ.

In seismic profiles from the Blake Outer Ridge so-called amplitude blanking is observed from reflectors above the BSR: amplitudes of reflections from a lithological boundary which crosses the BHSZ are considerably weaker above the BSR than beneath it (e.g. Dillon et al., 1994). This effect might be attributed to the impact of hydrates on sedimentology (ref. also section A.6.1).

A.5 Formation mechanisms for methane, hydrates, and BSRs

A.5.1 Formation of methane

Two models are proposed for the generation of methane and other hydrate forming gases, a thermogenic and a biogenic formation. The thermogenic formation is the common mechanism for the production of hydrocarbon gases (e.g. Hunt, 1979). Hydrocarbon gases are formed by a catagenesis process at temperatures above $\sim 100°C$.

Claypool and Kaplan (1974) proposed the process of biogenic methane production which involves microbial organisms and can take place at seafloor temperatures. It involves six stages as described by Hesse (1986). Organic matter is assumed to contain carbon, nitrogen and phosphorus in the ratio 106 : 16 : 1. After deposition, the matter is oxidized by dissolving oxygen. The second stage is characterized by a reduction of organic matter by nitrates. Beneath this zone, sulfate reduction takes places until in the next stage, methane is generated by carbonate reduction. Sloan (1990) summarizes the overall production of methane in these stages as:

$$(CH_2O)_{106}(NH_3)_{16}(H_3PO_4) \rightarrow 53CO_2 + 53CH_4 + 16NH_3 + H_3PO_4 \quad .$$

Paull et al. (1994) note that the CO_2 may be reduced further if there is a sufficient supply of hydrogen:

$$CO_2 + 4H_2 \rightarrow CH_4 + 2H_2O \quad .$$

The next two stages described by Hesse (1986) are no longer part of the actual biogenic formation mechanism of methane. They include the fermentation stage which still involves bacteria until finally the stage of thermogenic methane generation is reached. This process of biogenic methane production may only take place in ventilated basins. Hesse (1986) also describes a modification of this process which might be true for euxinic basins.

A.5.2 Models for the formation of hydrates in sediments

Whereas biogenic formation of methane may take place both in situ within the HSZ and beneath it, thermogenic methane must move upward into the HSZ in order to have a supply of a hydrate former. Hydrates of thermogenic and biogenic origin can be delineated mainly by two features. During thermogenic generation of methane, a considerable amount of higher-molecular-weight hydrocarbons is produced. The ratio of methane to ethane plus propane ($C_1/(C_2 + C_3)$) is expected to be above 1000 for pure biogenic hydrocarbon gases and below 100 for merely thermogenically formed gases (Sloan, 1990).

During the fourth stage of biogenic methane production, considerable fractionation of carbon isotopes takes place. The ratio difference relative to PDB, which is defined by

$$\delta^{13}C \equiv \left(\frac{(^{13}C/^{12}C)}{(^{13}C/^{12}C)_{PDB}} - 1 \right) \cdot 10^3 \quad ,$$

is expected to be in the range of −85% and −55% in biogenic methane (Sloan, 1990), whereas it is between −60% and −20% in thermogenic methane. Consequently, other carbon containing offspring products, such as CO_2, are expected to be enriched in ^{13}C. ^{34}S- and D-isotopes are also fractionated in biogenic production.

It is commonly believed that pore water has to be fully saturated with methane before natural hydrates can nucleate (e.g. Sloan, 1990; Paull et al., 1994; Brooks et al., 1994). It is still not clear if hydrates form from dissolved gas at equilibrium or supersaturation (e.g. Claypool and Kaplan, 1974) or in a two-phase system involving free gas. The latter model, which is preferred by many investigators (e.g. Sloan, 1990; Paull et al., 1994) implies, that only the amount of methane which exceeds saturation is available for the formation of hydrates. Thus, there has to be a relatively large amount of methane in the pore water, before hydrates start to form. Two end-member models have been proposed: (1) A biogenic in situ generation of methane and (2) a biogenic or thermogenic production beneath the BSR and subsequent upward migration of methane.

Biogenic generation of methane is expected to yield a gradual increase of methane concentration beneath the sulfate reduction zone. Subsequently, in-situ formation of hydrates will lead to an increase of hydrate content with depth starting at the depth where methane concentration exceeds solubility. The assumption that only methane in excess of saturation is available for hydrates to form, requires a relatively high carbon content in sediments. Sloan (1990) postulates a minimum organic carbon concentration of 0.5%. Paull et al. (1994) computed the maximum amount of hydrates which could be produced by sediment containing 1% carbon estimating that only half of the total organic carbon is available for microorganisms (Henrichs and Reeburgh, 1987), assuming the BHSZ at $600mbsf$, and adapting physical properties to a sediment column representative for the Carolina Rise-Blake Ridge area. From the sedimentary carbon budget they concluded that at most 6.1% of pore space could be filled with hydrates, whereas the upper limit was 2.2% if depth-extrapolating modern microbial production rates. The concentration expected from geophysical investigations is in the range between 5% (Katzman et al., 1994) and 35% (Rowe and Gettrust, 1994). Therefore, an additional source of methane appears to be required according to Paull et al. (1994). They also mention that in-situ formation becomes less probable the shallower the depth of the BHSZ.

Generation of methane formed either thermogenically or biogenically beneath the BHSZ implies upward migration of methane into the HSZ either as bubbles or dissolved in fluids. The model for biogenic methane generation beneath the BHSZ postulates fluids to be enriched with methane as they move upward through the zone of biogenic methane generation until saturation is reached (e.g. Paull et al., 1994). Then either bubbles will form or fluids become supersaturated. Hydrates may form from methane bubbles driven by buoyancy or migrating together with fluids into the HSZ. Alternatively, they might be extracted from supersaturated fluids entering the stability zone. Hyndman and Davis (1992) postulate that supersaturation might not even be necessary to form hydrates from pore fluids. A consequence of this model is that only a relatively thin layer of hydrate bearing sediment with a sharp base and a gradational top is expected to be located at the BHSZ (Hyndman and Spence, 1992). The formation mechanism of hydrates from thermogenic methane would be similar.

A combination of both models of methane supply for hydrate formation is of course possible. A third mechanism may play an important role for hydrate concentration with depth, methane recycling (Paull et al., 1994). If the BHSZ moves upward relative to hydrated sediments or hydrated sediments are depressed beneath the BHSZ, hydrates will decompose and form methane, which is expected to move back into the stability zone. Hence, concentration of hydrates is presumably elevated at the BHSZ.

Once hydrates have formed in sediments, they might undergo some consolidation process (Sloan et al., 1990). Hydrates have been found (1) finely disseminated, (2) as small nodules having a diameter of less than $\sim 5cm$, (3) as layers separated from sediment layers, and (4) as massive hydrates such as at DSDP Site 570, where a $1.05m$ long hydrate sample was recovered (von Huene et al., 1985b). Brooks

et al. (1985) proposed that hydrates consolidate from being disseminated in the pore space to becoming more massive. This assumption was based on the observation that in the Gulf of Mexico the content of thermogenic methane increases the more massive the hydrate sample. They interpreted thermogenic methane concentration as an indicator for the maturity of hydrates in this region. They also underlined, however, that a number of other factors may influence hydrate formation such as faulting of sediments. Fracturing may be responsible for the massive hydrate sample recovered at DSDP Site 570 (von Huene et al., 1985b).

It should be mentioned, that hydrates may also form from crude oils which contain only few hydrate formers: Water denudes crude oil from its lighter components by hydrate formation, increasing viscosity of the remaining oil (Katz, 1972).

A.5.3 Possible formation mechanisms for BSRs

Formation mechanisms for BSRs are closely linked to hydrate formation. The presence of free gas at BSRs is not required, but possible, if hydrates form exclusively from methane which is extracted from uprising fluids (Hyndman and Spence, 1992). If hydrates are formed in situ however, free gas is expected at the BHSZ: The oversaturation of pore fluids with methane within the HSZ, which is presumed to be required for in-situ formation of hydrates, leads to the development of free gas beneath the stability zone. However, free gas can only be trapped beneath the HSZ, if hydrate concentration is high enough to decrease permeability sufficiently and impede the upward movement of free gas and fluids. On the other hand, MacKay et al. (1994) stress that at low concentrations, mobility of gas is relatively low (Honarpour et al., 1986) and gas might even be trapped at relatively high permeabilities.

One of the sources of free gas, if present at the BSR, may be upward migrating bubbles or supersaturated fluids, which are trapped beneath the HSZ. The hydrate layer itself is another potential gas source by dissociation of methane at the BHSZ, which is equivalent to the process of methane recycling (Paull et al., 1994) as described in section A.5.2.

Three mechanisms might lead to a dissociation of hydrates at BSRs: (1) In a stable tectonic environment with high sedimentation, hydrated sediments may subside beneath the BHSZ due to sedimentation and compaction of sediments below the HSZ (Claypool and Kaplan, 1974). (2) Temperatures may increase in the sediment column. Such a temperature increase caused by rising temperatures of bottom water after deglaciation may be one of the causes for BSRs around ODP Leg 146 sites at the Cascadian margin (Westbrook et al., 1994). (3) Pressure at the BHSZ may decrease e.g. due to uplift shifting the phase boundary towards lower temperatures. Such a mechanism was postulated for BSR formation in the area of ODP Leg 141 at the Chilean margin (Bangs et al., 1993).

It should be mentioned, that in silicate-rich sediments, a different type of "BSRs" has been observed: A high-impedance cross-cutting reflection may be produced by a diagenetic alteration from opal-A to opal-CT or opal-CT to quartz in diatomaceous sediments (e.g. Hammond and Gaither, 1983). These reflections are characterized by a positive impedance contrast due to an increase in both velocity and density.

A.6 Identification and quantification of oceanic hydrates in sediments

Geological and geographical constraints for the extent of hydrates in sediments include that sediments have to be within the hydrate stability zone, and that a source for a sufficient amount of methane must exist. Brooks et al. (1994) succeeded in finding a number of shallow hydrate sites primarily by investigating seismic data in order to closely look at geology and to locate faults as possible fluid paths - an approach which is similar to that behind exploration for oil.

A.6.1 Seismic methods

The most obvious marker for oceanic hydrates is the presence of BSRs. However, by far not all hydrates which have been recovered were located above BSRs. In fact, DSDP Site 570, during which the so far largest hydrate body was drilled, was purposely located away from BSRs because of possible hazards that might result from drilling through hydrate and gas containing zones (von Huene et al., 1985b).

P-wave velocity may be an appropriate parameter to identify and possibly quantify hydrates in sediments. The most common approach to estimate the effect of hydrates in the pore space on V_p is to apply a time average equation (e.g. Minshull et al., 1994):

$$\frac{1}{V_b} = \frac{1}{V_w} + \frac{1}{V_h} \quad ,$$

where V_b denotes the P-wave velocity of the bulk sediment, V_w of the unhydrated water saturated sediment, and V_h the velocity of pure hydrate.

Hyndman and Davis (1992) suggested a semi-quantitative approach: They assumed that replacing pore water by hydrates has the same effect as increasing the fraction of the matrix material, i.e. decreasing porosity, and obtained the resulting velocity from an empirical velocity/porosity function from their study area, the Cascadian margin.

Both approaches require velocity calibration from an unhydrated reference sediment. With regard to other seismic parameters, bulk density is not assumed to change because of hydrates unless hydrates replace part of the sediment matrix. There appears to be a lack of knowledge regarding the effect of hydrates on V_s and the seismic quality factors Q_p and Q_s. However, laboratory investigations of these and other physical parameters such as electric properties and shear strength in hydrated sediments have been started (Winters et al., 1995).

Amplitude blanking was also proposed as a parameter for hydrate quantification. However, the process controlling amplitude blanking is not yet understood. In most regions above BSRs, no blanking effects could be observed. Moreover, similar high-resolution velocity analyses of wide-angle data from hydrated layers at Blake Ridge (Katzman et al., 1994), where strong amplitude blanking is displayed, and the adjacent Carolina Rise (Korenaga et al., 1995), where no significant blanking was observed, yielded similar velocity structures. Assuming that this indicates a similar concentration of hydrates, the assumption that blanking is caused by hydrate cementation is not consistent with these results (Korenaga et al., 1995). Thus where occurring, amplitude blanking might only be an appropriate parameter for hydrate quantification after proper calibration (e.g. Dillon et al., 1994) or in conjunction with other parameters such as velocities (e.g. Lee et al., 1993).

A.6.2 Drilling oceanic hydrates: Evidence from cores and logging

Macroscopically visible hydrates, i.e. nodular and more massive hydrates, in sediment cores could be identified mostly as white (e.g. Site 570, von Huene et al. 1985b), sometimes yellowish (a number of shallow hydrates in the Gulf of Mexico, e.g. Brooks et al. 1994) to dark grey (Site 685 offshore Peru, Suess et al., 1988) ice-like substances, which exhibit coldness to the touch. Decomposition on board ship leads to bubbling at the edges. Evidence for disseminated hydrates comes from an unusual release of gas from hydrate bearing sediment cores (e.g. Site 565 off Costa Rica, von Huene et al., 1985b).

Identification and quantification of gas hydrates in sediment cores is mainly based on indirect evidence, since much of the hydrate originally stored in sediments is believed to decompose during core recovery. Gas production from dissociation of hydrates and subsequent expansion during depressurization leads to gas expansion voids which are regarded as an indicator for hydrates (e.g. ODP Leg 146, Westbrook et al., 1994). Decomposition of hydrates is an endothermic process resulting in a decrease of temperature in the surrounding sediments. Low temperatures between $-0.9°$ and $-1.4°C$ in cores from Leg 146 Site

889 were attributed to hydrates. Important chemical markers are chlorinity and ^{13}C-fractionation. Efforts to quantify the in-situ content of hydrates from measurements on sediment cores from Leg 146 have been made primarily based on chlorinity (Kastner et al., in press) and temperature balances (Westbrook et al., 1994).

Layered or massive hydrates can be clearly delineated in geophysical logs. Logs through the massive hydrate body at DSDP Site 570 were characterized by a decrease in density (~ 1.7 to $\sim 1.1 gm/cm^3$), increase in P-wave velocity (~ 2.0 to $\sim 3.6 km/s$), and increase in resistivity ($1-3$ to $\sim 150 \Omega m$) (von Huene et al., 1985b). Density values are uncorrected apparent densities, thus the discrepancy with table 8. If disseminated within the pore space, density might not decrease significantly, since hydrates replace pore water having a density of only $1.035 g/cm^3$. The other parameters are expected to change according to the hydrate saturation. See also table 8 for hydrate properties. Quantification of hydrates might be based on such variations of physical properties. However, calibration from an unhydrated reference section might be required.

A.7 Significance of natural gas hydrates

A.7.1 Potential energy reservoir

Methane hydrates represent a huge potential energy source. Some estimates of the volumes of methane stored in natural hydrates are listed in table 1. McIver (1981) and Meyer (1981) computed the possible amount of methane by considering thermodynamic conditions together with other factors such as the availability of methane. Gornitz and Fung (1994) calculated the range of the potential amount of methane stored in oceanic hydrates based on the two methane formation theories (biogenic and thermogenic) using estimates of geothermal gradients, porosity, pore fill chemistry and other constraints from recent literature. They stress that the actual amount is most likely to be close to the lower boundary of the resulting range of $26.4 - 139.1 \cdot 10^{15} m^3$. Kvenvolden (1988) used a different approach by extrapolating an estimate of the hydrate amount off northern Alaska to the total length of continental margins worldwide, resulting in an estimated volume of $18 \cdot 10^{15} m^3$ of methane stored in oceanic hydrates. Though more than one order of magnitude apart, there appears to be some convergence of the values listed in table 1. The work of Dobrynin et al. (1981), which suggested hydrate volumes about two order of magnitudes higher, assumed that hydrates form wherever thermodynamic conditions are favorable (Sloan, 1990).

Dissociation of hydrates in order to produce methane is an endothermic process, i.e. energy has to be supplied according to the 1st Law of Thermodynamics. However, the overall energy balance is favorable: energy obtained from methane stored in hydrates is 15 times greater than the energy required for dissociation (Sloan, 1990). The key problem regarding production of methane from hydrate layers is "mobilization" of methane from solid hydrates, i.e. dissociation of in-situ hydrates. Three processes have been proposed (e.g. Kvenvolden, 1994). (1) thermal stimulation leading to melting of hydrates, (2) depressurization, and (3) a shift of the phase boundary towards lower temperatures by injection of inhibitors.

Development of the Siberian Messoyakha gas hydrate field is the only example for methane production from gas hydrates (Makogon et al., 1972). Whereas depressurization was used for long-term dissociation of hydrates, the inhibition of methanol mixtures yielded significant short-term increases in production of gas (Makogon, 1988). Injection of inhibitors however, make commercial production of gas from this field currently prohibitively expensive (Kvenvolden, 1994).

A.7.2 Geologic hazard and slope stability

It is believed that hydrates might significantly inhibit the process of consolidation and mineral cementation (ref. section A.4). Continued sedimentation may lead to a burial of hydrated sediments beneath the

HSZ. Hydrates, which might have acted as metastable bonding agents within the HSZ, dissociate leaving layers of underconsolidated sediments at the BHSZ. Additionally, excess pore pressure may build up at this depth due to continued formation of free gas in conjunction with a low permeability of the hydrated sediments above. An upward movement of the BHSZ e.g. resulting from an increase of bottom water temperature might accelerate this process (ref. also section A.5.3). Thus, the BHSZ acts as a potential zone of weakness, which might lead to huge slumps triggered e.g. by gravitational loading or seismicity (Kvenvolden, 1994).

There is strong evidence of slope failure being associated with hydrates offshore the southeastern U.S. coast. Fig. 94 displays the distribution of slumps in this area together with hydrate distribution. Locations of slides obviously concentrate slightly seaward of the line at which the hydrate stability zone intercepts the seafloor, though the gentle dip of the seafloor of $< 6°$ at these depths would indicate a relatively stable slope (Booth et al., 1994).

Other possible geologic risk factors which might be linked with hydrates are submarine mud volcanos such as in the Caspian Sea (Ginsburg et al., 1992) and the Black Sea (Lebedev, 1994). The effect of hydrates on sediment stability is also of interest for offshore engineering (e.g. Brooks et al., 1994).

A.7.3 Hydrates and environment

Gas hydrates have been linked with environmental problems mainly because methane is a strong greenhouse gas. Its global warming potential is 21 times that of carbon dioxide (Taylor, 1991). Its concentration is believed to have increased from 0.8 to $1.72ppmv$ since the industrial revolution (Ehhalt, 1988) and accounts for about 15% of the current warming effect (Englezos and Hatzikiriakos, 1994). Rough estimates that the amount of methane trapped in gas hydrates is about 3000 times the amount in the atmosphere (Kvenvolden, 1993) underline the potential role which hydrates could play in amplifying or damping temperature changes.

Two effects linked to climate change may affect the stability of natural hydrates: (1) A temperature increase may lead to a release of hydrates from permafrost regions on-shore or in shallow water. (2) A rise of the sea level associated with such a temperature increase would increase pressure in oceanic sediments and thus shift the BHSZ downward, i.e. make hydrates more stable (e.g. Kvenvolden, 1993).

Englezos and Hatzikiriakos (1994) modeled the impact of a temperature increase at the Earth's surface on hydrate layers in permafrost regions. They assumed the base of the permafrost at $280m$ beneath the surface and that no hydrate may be stored within the permafrost (i.e. above $280m$ beneath the surface). Their results indicate that for the presumed worst-case-scenario, a temperature rise of $0.08K/a$, it will take at least 100 years before hydrates start to decompose. Kvenvolden (1994) suggests that polar continental shelves might be most vulnerable with regard to methane release from hydrates due to an increase of bottom water temperature. According to Kvenvolden (1994), supporting evidence for this suggestion came from a cruise north of Oliktok Point, Alaska, during which methane concentration beneath the ice was measured. It was found to be $6 - 28$ times greater than the atmospheric equilibrium concentration. On the other hand, it has to be noted that only a relatively small amount of methane is trapped in continental hydrates (table 1). Other possible sources of anthropogenic methane appear to be much more significant: Kvenvolden (1994) estimated that only $\sim 1\%$ of the amount of anthropogenic methane released into the atmosphere might be related to gas hydrates.

A different scenario has been proposed for oceanic hydrates at outer continental margins. Paull et al. (1991) suggested that decreasing sea levels during glaciation could have triggered the release of large amounts of methane from hydrates caused by an upward shift of the BHSZ as pressure decreases. This might have resulted in global warming and the onset of deglaciation. For methane released from hydrates to contribute to the methane concentration in the atmosphere, however, methane bubbles have to travel through the water column without being dissolved (e.g. Kvenvolden, 1994).

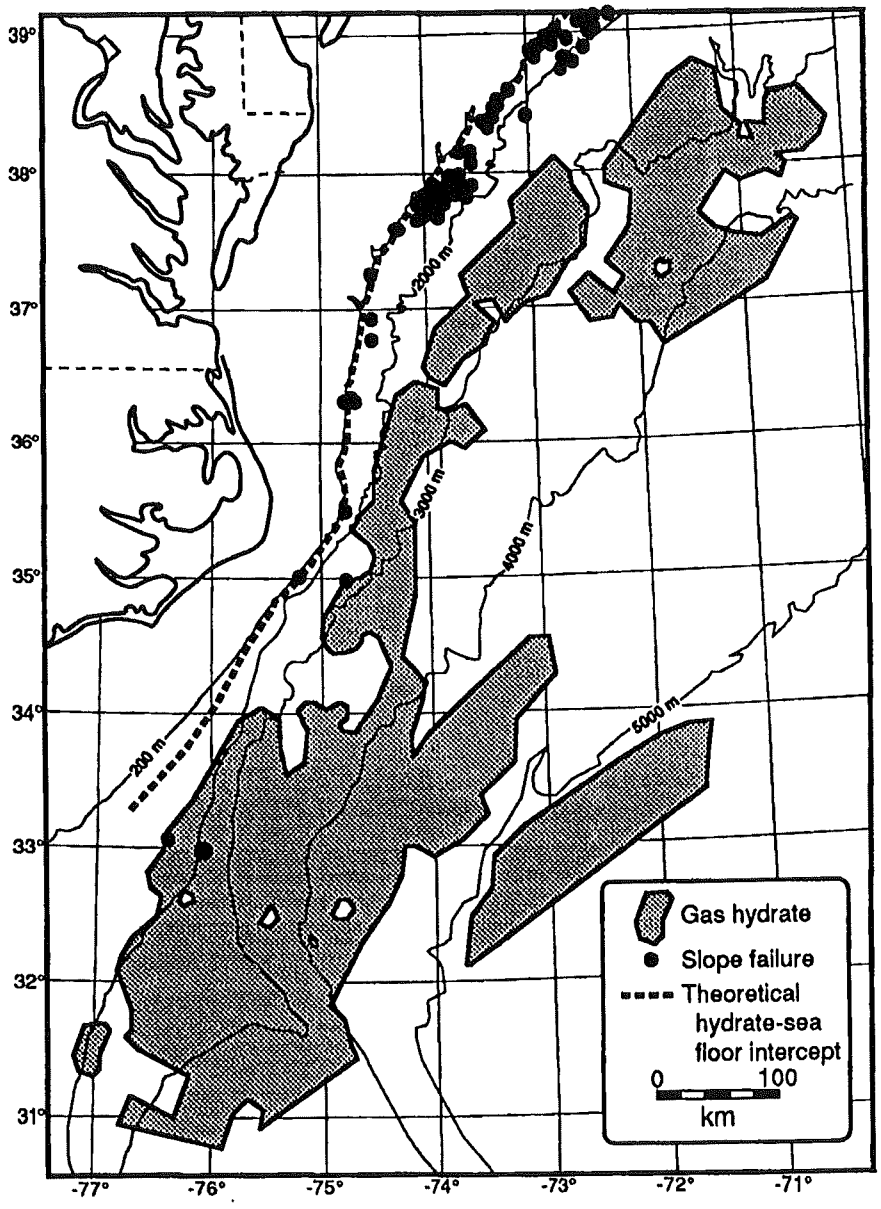

Figure 94: Map of locations of slumps and hydrates off the U.S. Atlantic coast. From Booth et al. (1994).

B Amplitude corrections

B.1 Determination of the energy from the seafloor

Traces within a CMP-gather were first NMO corrected. Then the cross correlation between adjacent traces within a window of n samples around the seafloor (typically $0.2s$) was computed as:

$$\varphi_{i,i+1}(k) = \sum_{j=1}^{n} A_i(j) A_{i+1}(j+k) \tag{14}$$

where $\varphi_{i,j}(k)$ denotes the k'th sample of the cross correlation function between the i'th and j'th trace, $A_i(j)$ the amplitude of the j'th sample of the i'th trace. Traces where then shifted such that $\varphi_{i,i+1}(k)$ is maximum for $k = 0$. After that, energies of the i'th trace within a window of n samples around the seafloor were computed as $E_i = \varphi_{i,i}(0)$. Note, that the cross correlation function was not normalized, which therefore strictly is the covariance function and which allowed a computation of energies using the same routine.

B.2 Computation of theoretical energies

As a next step, the theoretical energy-versus-offset function was computed normalized to the average energy of the CMP-gather taking into account geometrical spreading, directivities, and amplitude-versus-angle-of-incidence performance.

Geometrical spreading effects in the water column was accounted for according to Sheriff and Geldart (1982) by:

$$\frac{E_i}{E_j} = \left(\frac{S_j}{S_i}\right)^2 \tag{15}$$

where E_i denotes the energy from the seafloor reflection in the i'th trace having a travel path of length S_i (applying eq. 15 to energies from seafloor and multiple yields eq. 9).

B.2.1 Directivities

Directivity effects were computed for source array, receiver array, source ghost and receiver ghost according to Sheriff and Geldart (1982). The directivity factor F is defined by:

$$F = \frac{A_{real}}{A_{point}} \tag{16}$$

where A_{real} is the real amplitude, A_{point} the amplitude which would be expected for point sources and receivers at zero depth beneath the sea level (i.e. without ghost). Source and receiver array directivities can be computed as:

$$F_a = \left| \frac{sin\left(n\pi\frac{\Delta x}{\lambda} \cdot sin\left(\Theta\right)\right)}{n \cdot sin\left(\pi\frac{\Delta x}{\lambda} \cdot sin\left(\Theta\right)\right)} \right| \tag{17}$$

where n is the number of array elements, Δx the distance between adjacent elements, λ the seismic wavelength, and Θ the angle-of-incidence. Ghost directivities (at far distances) can be accounted for by:

$$F_g = 2 \cdot sin\left(2\pi\frac{z}{\lambda} cos\left(\Theta\right)\right) \tag{18}$$

where z is the source or receiver depth. Note, that using this procedure, varying phase shifts with offset are not taken into account. Such phase shifts would be expected, since the wavelet from a single reflection in fact is a composition of two signals, the real signal arriving from below the hydrophone and the ghost from the sea surface. The composite signal may change with increasing offset (the ghost arriving later), since the angle-of-incidence (and thus, the difference in travel paths for ghost and direct signal) increases.

The total directivity effect is the product of all single directivities. Note, that F is computed for amplitudes. F^2 would be the equivalent value for energies. The seismic wavelength λ was computed from water velocity and the main frequency obtained from amplitude spectra.

The data themselves were directivity corrected in the (ω, p)-domain before entering the waveform inversion (ref. fig. 4). The source wavelet was obtained from the seafloor reflection in the (τ, p)-gather. Thus, phase shifts in the signal from the seafloor with increasing offset due to an increasing angle-of-incidence were averaged out.

B.2.2 Reflectivity versus angle-of-incidence

The Zoeppritz equations (Zoeppritz, 1919) allow a computation of the reflection and transmission coefficients of a horizon as a function of angle-of-incidence for P- and S-waves ($\Theta_{p,1}$, $\Theta_{s,1}$), as well as contrasts in P-wave velocities ($V_{p,1}$, $V_{p,2}$), S-wave velocities ($V_{s,1}$, $V_{s,2}$), and densities (ρ_1, ρ_2). They can be written as:

$$\begin{pmatrix} sin(\Theta_{p,1}) & cos(\Theta_{s,1}) & -sin(\Theta_{p,2}) & cos(\Theta_{s,2}) \\ -cos(\Theta_{p,1}) & sin(\Theta_{s,1}) & -cos(\Theta_{p,2}) & -sin(\Theta_{s,2}) \\ sin(2\Theta_{p,1}) & \frac{V_{p,1}}{V_{s,1}} cos(2\Theta_{s,1}) & \frac{\rho_2 V_{s,2}^2 V_{p,1}}{\rho_1 V_{s,1}^2 V_{p,2}} sin(2\Theta_{p,2}) & -\frac{\rho_2 V_{s,2} V_{p,1}}{\rho_1 V_{s,1}^2} cos(2\Theta_{s,2}) \\ cos(2\Theta_{s,1}) & -\frac{V_{s,1}}{V_{p,1}} sin(2\Theta_{s,1}) & -\frac{\rho_2 V_{p,2}}{\rho_1 V_{p,1}} cos(2\Theta_{s,2}) & -\frac{\rho_2 V_{s,2}}{\rho_1 V_{p,1}} sin(2\Theta_{s,2}) \end{pmatrix} \cdot \begin{pmatrix} R_p \\ R_s \\ T_p \\ T_s \end{pmatrix} = \begin{pmatrix} -sin(\Theta_{p,1}) \\ -cos(\Theta_{p,1}) \\ sin(2\Theta_{p,1}) \\ -cos(2\Theta_{s,1}) \end{pmatrix} \tag{19}$$

$\Theta_{p,2}$ and $\Theta_{s,2}$ are the angles of transmission for shear and compressional waves, R_p and R_s denote the reflection coefficients for P- and S-waves, respectively, T_p and T_s transmission coefficients.

Densities and P-wave velocities directly beneath the seafloor were computed from the zero-offset reflection coefficient assuming that the impedance contrast is merely due to a jump in density. Shear wave velocity at the seafloor was obtained from Castagna et al. (1985).

C Starting model

C.1 Gradient velocity model

Interval velocities for compressional waves obtained from the Monte Carlo inversion could not be used as an adequate long-wavelength velocity model for the waveform inversion. This is due to the sharp (i.e. high frequency) velocity contrasts at the picked horizons, especially at the BSR, which would introduce artifacts. Instead of smoothing the interval velocity model with a low-pass filter (running average operator), as done previously e.g. by Singh et al. (1993) and Minshull et al. (1994), the interval velocity model was first transformed into a gradient velocity model such that for the depth interval $[z_1, z_2]$ with an interval velocity $V_{p,1}$

$$V_p(z) = V_{p,0} + g \cdot z \qquad \text{and} \qquad \int_{z_1}^{z_2} \frac{1}{V_p(z)} dz = \frac{z_2 - z_1}{V_{p,1}} \tag{20}$$

where $V_{p,0}$ is the highest velocity from the velocity interval above, g is the velocity gradient. In case that $V_p(z)$ exceeds the interval velocity $V_{p,2}$ of the layer beneath the interval $[z_1, z_2]$, a depth z_i was determined such that:

$$V_p(z) = \begin{cases} V_{p,0} + g \cdot z \quad \text{for} \quad z_1 < z \leq z_i \\ V_p(z_i) = V_{p,0} + g \cdot z_i = V_{p,2} \\ V_p(z) = V_{p,2} \quad \text{for} \quad z_i < z \leq z_2 \end{cases} \qquad \text{and} \qquad \int_{z_1}^{z_2} \frac{1}{V_p(z)} dz = \frac{z_2 - z_1}{V_{p,1}} \tag{21}$$

z_i was searched by a linear search algorithm. This was done to avoid an artificial long-wavelength velocity inversion.

A gradient model was chosen, since even after smoothing, interval velocity models lead to a relatively strong increase of background velocities in the vicinity of the BSR, if the interval velocity

beneath it is considerably higher than that above it. This increase in velocity at the BSR is certainly not a realistic starting model considering the negative reflection coefficient at BSRs.

C.2 Density and shear wave velocity

Water density was set to $\rho_w = 1035 kg/m^3$. Density of the seafloor was computed from the zero-offset seafloor reflection coefficient R assuming that this is merely caused by a step in density. Then, bulk density of the sediment ρ_s can be computed from water velocity (V_w) and ρ_w as:

$$\rho_s = \rho_w \frac{1+R}{1-R} \quad . \tag{22}$$

Hamilton's relation (1978) between V_p and ρ for silt, clays, turbidites and mudstone shales was used to estimate ρ_s at greater depths:

$$\rho(V_p) = \begin{cases} 14.8 \cdot V_p - 21014 & \text{for } V_p \leq 1524 m/s \quad , \\ 1.135 \cdot V_p - 190 & \text{for } 1524 m/s < V_p \leq 2007 m/s \quad \text{and} \\ 917 + 0.744 \cdot V_p - 8 \cdot 10^{-5} \cdot V_p^2 & \text{for } V_p > 2007 m/s \quad . \end{cases} \tag{23}$$

Units are m/s for velocities and kg/m^3 for densities. Density of the sediment column was set to the density of the seafloor ρ_s down to the depth where ρ obtained from eq. 23 became higher than ρ_s.

Shear wave velocities were obtained from Castagna's et al. (1985) relation between V_s and V_p for clastic silicate sediments:

$$V_s(V_p) = \frac{1}{1.16}(V_p - 1360) \tag{24}$$

Again, units are m/s. Assuming $V_p = 1480 m/s$, V_s at the seafloor is $100 m/s$. This is a realistic value compared to in-situ measurements in deep sea sediments in the Northeast Atlantic and the Norwegian Sea (Whitmarsh and Miles, 1991)

D Elastic waves in porous media

D.1 Homogeneous media

Assuming an ideally elastic homogeneous medium, velocities of seismic waves within this medium can be computed as:

$$V_p = \sqrt{\frac{K + \frac{4}{3}\mu}{\rho}} \tag{25}$$

and

$$V_s = \sqrt{\frac{\mu}{\rho}} \tag{26}$$

where K is the bulk modulus, μ the shear modulus. Thus, V_p, V_s, and ρ fully describe a homogeneous elastic medium. The assumption of an elastic medium implies that no loss of energy occurs, i.e. seismic quality factors Q are infinite. The Poisson's ratio, which is often used to identify gas layers (e.g. Ostrander, 1984), is defined by:

$$\sigma = \frac{\left(\frac{V_p}{V_s}\right)^2 - 2}{2 \cdot \left(\left(\frac{V_p}{V_s}\right)^2 - 1\right)} \quad . \tag{27}$$

D.2 Porous media

Biot (1956a) derived equations for elastic properties of porous media. Gassmann (1951) showed that the compressional modulus of the bulk material can be expressed by

$$K = K_b + \frac{\left(1 - \frac{K_b}{K_s}\right)^2}{\left(1 - \Phi - \frac{K_b}{K_s}\right)\frac{1}{K_s} + \frac{\Phi}{K_f}} \quad . \tag{28}$$

Φ is the porosity, indices b, s, f denote matrix (approximately dry bulk rock), solid material, and pore fluid, respectively. Assuming an ideal liquid as a pore fluid (i.e. no viscosity), no shear stress can be transmitted through the fluid and thus, the shear modulus of the system is that of the matrix:

$$\mu = \mu_b \quad . \tag{29}$$

Bulk density can be easily computed as:

$$\rho = \Phi\rho_f + (1 - \Phi)\rho_s \quad . \tag{30}$$

Using these parameters for eq. 25 gives the zero-frequency approximation of the Biot-Geertsma equation (Biot, 1956a, Geertsma, 1961) :

$$V_p = \sqrt{\frac{K_b + \frac{4}{3}\mu_b + \frac{\left(1 - \frac{K_b}{K_s}\right)^2}{\left(1 - \Phi - \frac{K_b}{K_s}\right)\frac{1}{K_s} + \frac{\Phi}{K_f}}}{\rho}} \quad . \tag{31}$$

This equation can be applied to partially saturated media by adjusting properties of the pore fluid. Density again is a weighted average of both components:

$$\rho_f = S_w\rho_w + (1 - S_w)\rho_g \quad , \tag{32}$$

where S_w denotes water saturation and the indices w and g are for water and gas, respectively. The bulk modulus of the pore fill can be computed as a weighted average of its reciprocals, the compressibilities C, by:

$$\frac{1}{K_f} = C_f = S_w C_w + (1 - S_w)C_g \quad . \tag{33}$$

Strictly, eq. 31 can only be applied to model seismic properties of porous media, if the pore fluid is firmly coupled to the pore wall (which is equivalent to a zero-frequency), gas and liquid are uniformly distributed in the pores, shear modulus is not affected by the pore fluid, and pore shapes are spheroidal. Refer also to section D.5 for more details and the limitations of this Biot-Geertsma model.

The properties of solid material, water, and gas are known from the literature or can be derived. The compressibility of water at standard temperature is pressure dependent and well approximated by a linear relation (Dodson and Standing, 1944):

$$\frac{1}{K_w} = C_w\left[\frac{ft^2}{pndl}\right] = 7.1343 \cdot 10^{-10}\frac{ft^2}{pndl} - 2.0717 \cdot 10^{-14}\frac{ft^2}{pndl \cdot psi}P_p\,[psi] \tag{34}$$

where P_p is the pore pressure, which is equivalent to

$$\frac{1}{K_w} = C_w\left[\frac{m^2}{N}\right] = 4.7940 \cdot 10^{-10}\frac{m^2}{N} - 2.0191 \cdot 10^{-18}\frac{m^2}{N \cdot Pa}P_p\,[Pa]$$

in SI units ('[·]' denotes units). Density of water at standard temperatures then can be computed after e.g. Domenico (1977):

$$\rho_w\left[\frac{lbs}{ft^3}\right] = \rho_{w,0}\left[\frac{lbs}{ft^3}\right] \cdot exp\left(7.1343\frac{1}{psi} \cdot 10^{-10}P_p\,[psi] - 2.0717\frac{1}{psi^2} \cdot 10^{-14}P_p^2\,[psi^2]\right) \tag{35}$$

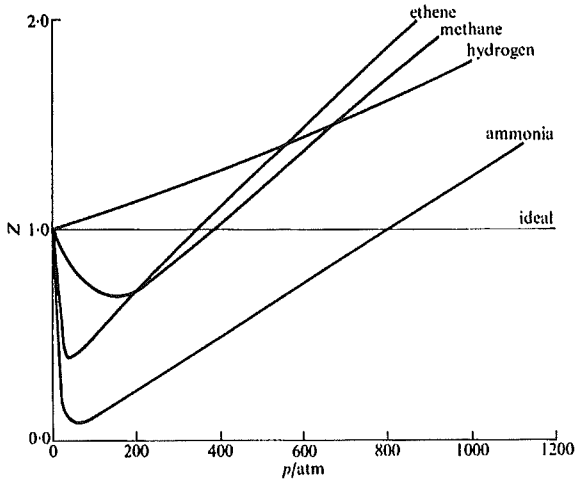

Figure 95: Compression factor Z for a variety of gases, from Atkins (1978).

where $\rho_{w,0}$ denotes the brine density under standard conditions. This is equivalent to

$$\rho_w \left[\frac{kg}{m^3}\right] = \rho_{w,0} \left[\frac{kg}{m^3}\right] \cdot exp\left(1.0347 \frac{1}{Pa} \cdot 10^{-13} P_p\,[Pa] - 4.3580 \frac{1}{Pa^2} \cdot 10^{-22} P_p^2\,[Pa^2]\right)$$

in SI unit.

Refer also to section D.3 for gas properties, and tables 10 and 11 for the other quantities used in our calculations. A method for estimating matrix moduli is described in section D.4.

D.3 Physical properties of methane gas

D.3.1 Deviation from ideal gas and density

According to e.g. Atkins (1978), the gas equation for ideal gases can be written as:

$$\frac{pV_m}{RT} = Z \tag{36}$$

where p denotes pressure, V_m molar volume, R the gas constant, T temperature, and Z the compression factor. $Z = 1$ for real gases. Values for Z may differ considerably from 1 at higher pressures, as displayed in fig. 95 ($1atm = 1.013250 \cdot 10^5 Pa$).

Thus, density of a gas at a given pressure and constant temperature can be computed from density at standard pressure ρ_0 as

$$\rho(P) = \frac{\rho_0}{Z(P)} \frac{P}{P_0} \tag{37}$$

assuming ideal gas at standard pressure. Density of methane (CH_4) at standard conditions can be obtained from its molar mass as $\rho_0 = 0.714 \frac{kg}{m^3}$.

D.3.2 Bulk modulus

The dynamic (i.e. adiabatic) compressibility C, the reciprocal of the bulk modulus K, of a gas is defined by:

$$\frac{1}{K} = C = -\frac{1}{V} \cdot \left.\frac{\partial V}{\partial P}\right|_{S=const.} \tag{38}$$

where S denotes entropy. Assuming adiabatic compression of gas changes the (ideal) gas equation to

$$p \cdot V^\gamma = const. \tag{39}$$

with $\gamma = 1.4$ for air and $\gamma = 1.67$ for an ideal 1-molecular gas (e.g. Atkins, 1978). In the present study, $\gamma = 1$ was chosen (i.e. isothermal compression was assumed as an approximation), since values for Z according to eq. 36 were not available for adiabatic compression.

Hilterman(unpubl.) gives values for dynamic K of methane for three pressure values from Wyman (1982), which are listed in table 9. Solving eq. 38 by applying eq. 36 allows computing bulk moduli for other pressures if the bulk modulus K_1 is known for pressure P_1:

$$K_2 = K_1 \cdot \frac{Z_1}{Z_2}\frac{T_1}{T_2}\left(\frac{P_2}{P_1}\right)^2 \quad . \tag{40}$$

If assuming adiabatic compression and $\gamma = 1.4$ for air, the factor $(P_2/P_1)^2$ changes to $(P_2/P_1)^{1.7}$. This would change K of methane at location Peru 1018 CMP 1126 by about 10% (if assuming that values for Z are correct), which therefore was estimated to be the error margin for the determination of K for gases. The model calculations show that other parameters are by far more critical (ref. fig. 35). Moreover, the validity of the approach chosen for the present investigations can be tested by computing the other K values in table 9 from one value: Differences are in the order of $1 - 2\%$. It should be noted,

Pressure [atm]	K [10^9Pa]
63.9	0.0063
191.8	0.0208
319.6	0.0383

Table 9: Dynamic bulk modulus K of methane, after Wyman (1982). $1atm = 10132.50Pa$.

that values for K_g at higher pressure are considerably above those at ambient conditions. Experimental results from Domenico (1977) are from measurements at standard pore pressures. They are often quoted in the context of estimating gas content in sediments at greater depths (for BSRs e.g. Bangs et al., 1993), though they might not be appropriate for those conditions. Domenico himself (1977) gives a formula to adjust pore fill properties at ambient conditions to higher pressures.

D.4 Modeling P-wave velocity versus water saturation

The main problem of estimating V_p in a porous medium from eq. 31 are estimates of the matrix properties K_b and μ_b, which can be described as properties of the structure itself. Approximately, they can be regarded as being the properties of the dry rock (more accurately: properties of the dry rock in a vacuum). This approximation is based on the assumption, that in eq. 31 K and μ_b by far dominate V_p, if the rock is filled with gas. This is due to the fact that K_g, and thus, K_f at ambient conditions is very low compared to the other moduli.

Matrix properties cannot be easily computed from the properties of the solid material. However, for partially saturated sediments, it is possible to compute them, if both V_p and V_s are known at a given saturation. This is due to the fact, that matrix properties are not affected by water saturation in the pore space. A modification of a method described by Hilterman (unpubl.) was chosen.

Densities of pore fill and bulk sediment, ρ_f, and ρ can be computed from eqs. 32 and 30, respectively, as well as compressibility of the pore fill C_b from eq. 33. Modifying eq. 31 then yields

$$K_b = \frac{1}{C_b} = \left(1 - \frac{-B + \sqrt{B^2 - 4AC}}{2A}\right) \cdot K_s \tag{41}$$

where

$$A \equiv S - 1 \quad ,$$

$$B \equiv \Phi S \left(\frac{K_s}{K_f} - 1 \right) - S + \frac{M}{K_s} \quad ,$$

$$C \equiv -\Phi \left(S - \frac{M}{K_s} \right) \left(\frac{K_s}{K_f} - 1 \right) \quad ,$$

and

$$S \equiv 3 \cdot \frac{1 - \sigma_b}{1 + \sigma_b} \quad ,$$

$$M \equiv V_p^2 \rho \quad .$$

K_s denotes the bulk modulus of the solid material, σ_b is the Poisson's ratio as defined by eq. 27. Note, that it is the Poisson's ration of the matrix (or approximately, dry rock). The (matrix) shear modulus μ_b can then be computed as:

$$\mu_b = \frac{3}{4} K_b (S - 1) \quad . \tag{42}$$

Hilterman (unpubl.) suggested using an assumed value of σ_b, as well as a known value of V_p at a given saturation for such computations. For the investigations presented here, it was thought that an estimate of V_s at a given saturation would give better constrained results than a mere assumption of σ_b. Values of V_p and V_s from the long-wavelength velocity model were thus used as velocity values at full water saturation. A linear search algorithm was applied to eqs. 41 and 42 to determine σ_b such that V_p and V_s at full saturation match velocity values from the background model.

D.5 Limitations

A general limitation for estimating the amount of free gas from seismic velocities using eq. 31 is the sharp drop of V_p within the first few percent of gas saturation, whereas it changes only little for higher gas content. This drop is due to the fact that even at low gas content in the pore space the bulk modulus of the pore fill computed from eq. 33 is largely dominated by the very low values of K_g compared to K_w. Thus as a matter of principle, predicting gas content from V_p is only feasible for low percentages of gas. The drop in V_p at low concentrations becomes less dramatic (and thus, gas concentration can be estimated up to higher values), if K_g increases due to higher pressure.

The zero-frequency approximation of the Biot-Geertsma equation (eq. 31) assumes that there is no relative movement between pore fluid and matrix, i.e. there is perfect coupling between those two media. A coupling factor k was introduced to account for such movements at higher frequencies, which transforms eq. 31 into

$$V_p = \sqrt{\frac{K_b + \frac{4}{3}\mu + \frac{\frac{\Phi \rho_b}{k \rho_f} \left(1 - \frac{K_b}{K_s}\right) \left(1 - \frac{K_b}{K_s} - \frac{2\Phi}{k}\right)}{\left(1 - \Phi - \frac{K_b}{K_s}\right) \frac{1}{K_s} + \frac{\Phi}{K_f}}}{\rho \left(1 - \frac{\rho_f}{\rho_b} \frac{\Phi}{k}\right)}} \tag{43}$$

and is equivalent to the infinite-frequency equation of Biot (1956b). For $k = \infty$, i.e. perfect coupling, eq. 43 is identical with eq. 31. It is difficult to assess values for k, which may also be frequency dependent. Domenico (1977), estimated k-values from experiments on Ottawa sand as a function of differential pressure (P_d). He showed that k increases with P_d from near 1.0 at low pressure to a value between 2 and 3 at $5000psi$ ($345kPa$) (ref. fig. 96). Constraining k for the model sediment used in the present study would be highly arbitrary. Minshull et al. (1994) used a coupling factor of 2.5 as an average value from Domenico. However, Domenico's results are from seismic measurements on sands at about $200kHz$. Thus, the ratio of seismic wavelength over mean pore diameter is several orders of magnitude lower than for the reflection seismic data used here, because both wavelengths are much shorter and because the mean pore diameter is higher than for the clayey to silty sediments off Peru and Costa Rica. Intuitively it is probable that the higher this ratio, the lower the relative movement between pore fill and matrix, and thus, the higher the degree of coupling. Therefore, perfect coupling was assumed.

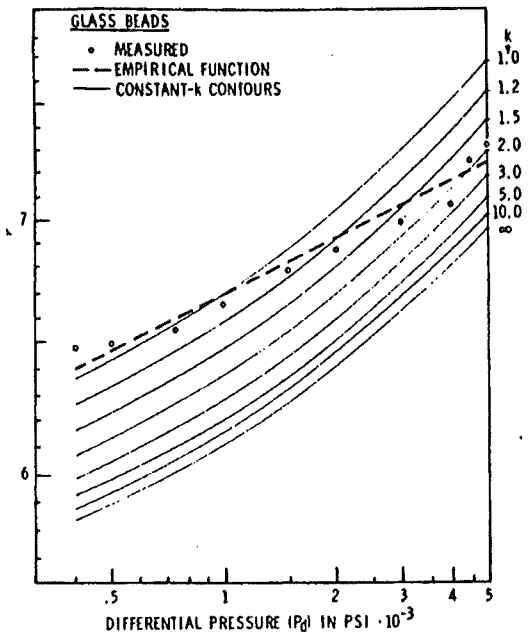

Figure 96: Estimating the coupling factor in Ottawa sand as a function of differential pressure by comparison of theoretical and measured relation of P- and S-wave velocities with differential pressure, from Domenico (1977).

By using a version of eq. 31 in which V_p and V_s at full saturation are used as input values, a coupling factor might also have partly been accounted for by changing matrix properties in a way that observed velocities matched modeled velocities at full saturation, and thus compensated for an eventual coupling effect by adjusting matrix properties. It is also possible that the coupling factor introduced by Domenico (1977) partly compensated for erroneous assumptions on matrix properties.

The assumption that gas and liquid are uniformly distributed in the pore space is another limitation of this model. According to Domenico (1976), gas tends to first occupy larger pores. Then, bulk moduli of the fill of these pores would drop according to eq. 32, whereas other pores would not be affected. In this case, bulk modulus (or better compressibility) of the sediment would be a weighted average of sediment with full water saturation and partially saturated sediment similar to eq. 32. This would result in a considerably less dramatic drop of V_p at low gas concentration. In fact, Domenico (1976) observed such an effect, which he attributed to an uneven distribution of gas in the pore space of his Ottawa sand samples (fig. 97). He used a new technique for injecting a brine-gas mixture to achieve a more uniform distribution of gas in the samples for the experimental results published in 1977, which much better fitted theoretical results.

Quantities used for modeling V_p as a function of water saturation are listed in tables 10 and 11.

E Pre-stack depth migration

The 2-d pre-stack depth migration package 'MIGPACK' combines a pre-stack depth migration based on a downward continuation of the wavefield in the source-receiver-frequency domain and a focusing analysis to determine errors in the velocity model used for the migration. See Denelle et al. (1986) Audebert and Diet (1990) for a detailed description.

Migration is performed by applying a phase shift operator together with a diffraction (or focusing) operator. Downward movement of source (or receiver) from $z = 0$ to $\bar{z_1}$ is performed by the phase shift operator, which reduces traveltime t to $\bar{t} = \bar{z_1}/V$ assuming a velocity V of the medium (this

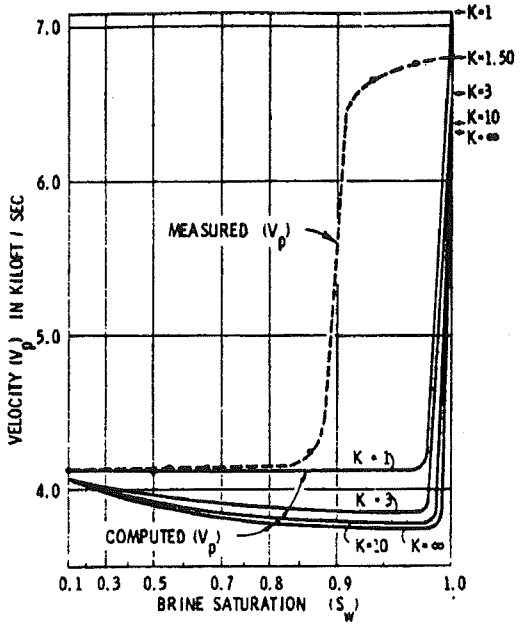

Figure 97: Measured and computed P-wave velocities in an Ottawa sand specimen, from Domenico (1976).

Location	P[atm]	T[K]	Z	Φ[%]
Peru 1018-1126	484.5	299.15	1.17	55
Peru 1018-1514	425.7	298.05	1.06	65
Peru 1017-3790	459.4	298.55	1.12	60
C.Rica 9-1410	276.5	294.65	0.80	65

Table 10: Quantities for modeling V_p as a function of water saturation: pressure (P), temperature (T), deviation from ideal gas (Z), and porosity (Φ). T is from the phase boundary of methane hydrates. Values for Φ are estimated from measurements on ODP Leg 112 Site 688 and DSDP Leg 84 Site 565. $1atm = 10132.50Pa$. Z as a function of pressure is from Atkins (1978).

Location	ρ_s	ρ_w	ρ_g	K_s	K_w	K_g	$V_{p,0}$	$V_{s,0}$
Peru 1018-1126	2.65	1.035	0.296	40	2.1	0.089	1.90-2.10	0.58
Peru 1018-1514	2.65	1.035	0.287	40	2.1	0.076	1.65-1.85	0.34
Peru 1017-3790	2.65	1.035	0.293	40	2.1	0.083	1.95-2.15	0.60
C.Rica 9-1410	2.65	1.035	0.247	40	2.1	0.043	1.80-2.00	0.48

Table 11: Quantities for modeling V_p as a function of water saturation: densities of sediment, water, and gas (ρ_s, ρ_w, ρ_g, in $10^3 kg/m^3$), bulk moduli of sediment, water, and gas (K_s, K_w, K_g, in $10^9 Pa$), P- and S-wave velocity at full saturation ($V_{p,0}$, $V_{s,0}$, in km/s. Density values and bulk moduli are from Domenico (1977) and computed from formulas given above. Variation of $V_{p,0}$ represents the estimated error margin.

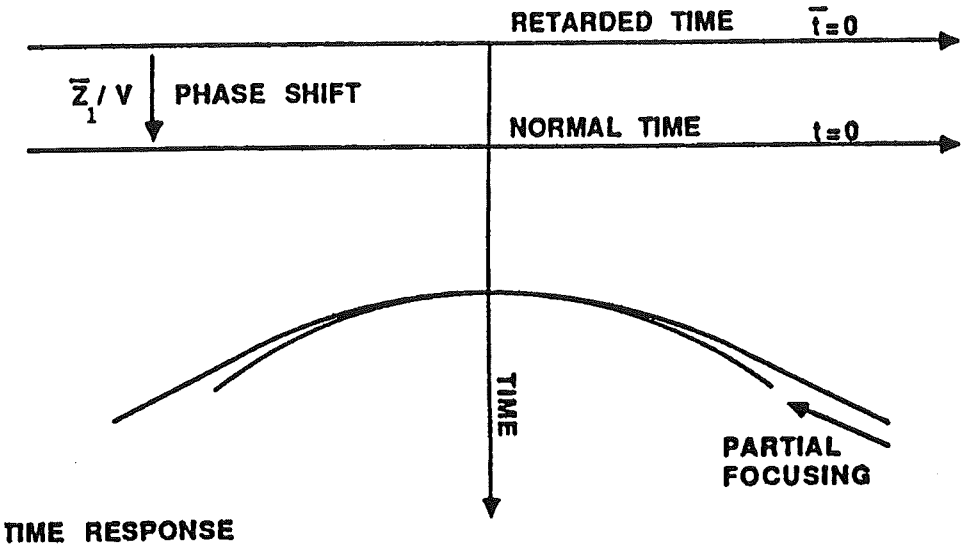

Figure 98: Phase shift and diffraction operator during downward movement of shot or receivers (from Denelle et al., 1986).

operator is applied in the frequency domain, in which the downward shift results in a phase shift). The diffraction operator sums energy along diffraction trajectories resulting in partial focusing (fig. 98).

The effect of these operations on a reflection in the shot or receiver gather at depth z_R is illustrated by fig. 99 (note that this procedure can be applied alternatively to both shot-domain and geophone-domain as third dimension). Starting at $\bar{z} = 0$, if the velocity V is correct, more energy is focussed at zero offset the more $\bar{z}$ approaches z_R. Focusing is perfect at $\bar{z} = z_R$. If V is too high (fig. 100), the diffraction operator focuses the energy at a shallower depth than the exact depth (steepness of diffraction hyperbola), whereas the phase shift operator moves reflections deeper than the actual depth (computation of depth from TWT). Thus, the exact depth is between the focusing depth $\bar{Z}_f$ and the migration depth $\bar{Z}_m$. Similarly, if V is too low, $\bar{Z}_f$ is too deep and $\bar{Z}_m$ is too shallow.

Assuming horizontal layering, the following relations allow an estimate of the depth (and subsequently, velocity) error as

$$Z_R V = \bar{Z}_f V_m \qquad \text{and} \qquad \frac{Z_R}{V} = \frac{\bar{Z}_m}{V_m} \tag{44}$$

leading to

$$Z_R = \sqrt{\bar{Z}_m \bar{Z}_f} \quad , \tag{45}$$

which, for small velocity errors, is approximated by

$$Z_R = \frac{\bar{Z}_m + \bar{Z}_f}{2} \qquad \text{or} \qquad Z_R - \bar{Z}_m = \frac{\bar{Z}_f - \bar{Z}_m}{2} \quad . \tag{46}$$

This means that for small velocity errors, the depth error is half the focusing error, which can be used for computing first order depth and velocity errors from the focusing analysis (ref. fig. 101). If velocity is a function of depth, a mathematical relation between $\bar{Z}_f$, Z_R, and $\bar{Z}_m$ is not as straightforward as in eq. 45. It can be shown, however, that assuming horizontal layering, the relative error of a depth interval $\Delta z_i/z_i$ is a linear function of $(\Delta V_i/V_i)^2$, where $\Delta V_i/V_i$ is the relative error in interval velocities. A first order depth and velocity error for this layer can then be obtained as a linear approximation from the slope of a line joining two neighboring picks, as demonstrated in fig. 102. The slope of this line is defined

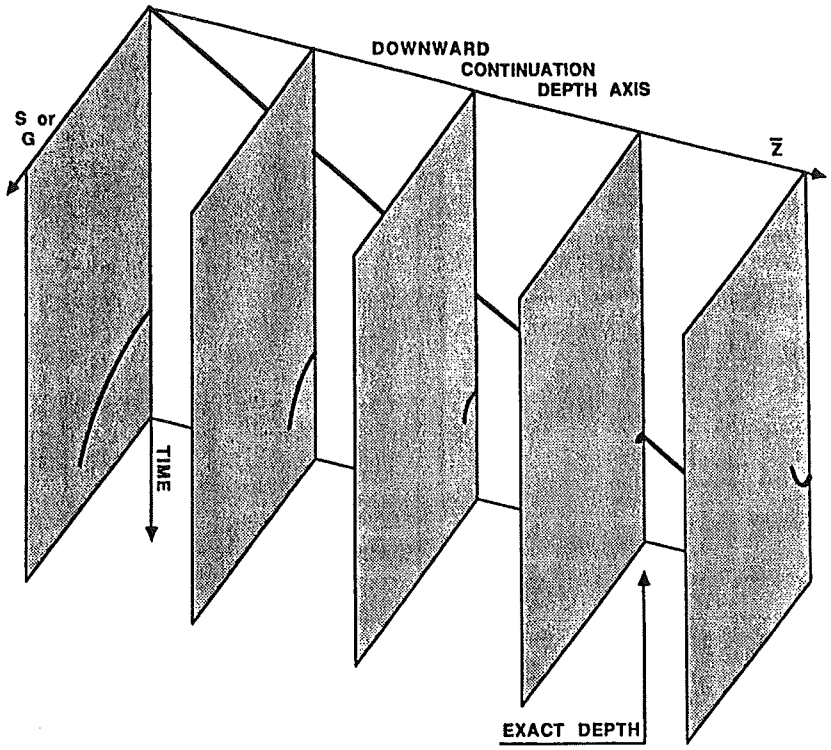

Figure 99: Downward continuation of shot (S) or receivers (G) along $\bar{t}$ (thick line) assuming a correct velocity (after Denelle et al., 1986).

by:

$$\Delta V_i = \frac{\Delta z_i}{t_i} \tag{47}$$

where t_i is the (one way) traveltime through this layer.

The usual procedure for migrating reflection seismic data is to iteratively obtain a velocity model of the subsurface. A 0th migration is performed assuming a constant velocity model for the whole data set (water velocity for marine data). Then, a focusing analysis at the first reflection beneath the seafloor is performed to obtain velocities of the first sediment layer (focuses at the seafloor should be correct, unless there are problems with geometry information). These velocities are used to update the velocity model by extending velocities of the first sediment layer downward. Then, another migration is started. After that, focusing errors for a deeper layer are determined etc. This procedure of migration, focusing analysis, and updating velocity models is repeated down to the bottom of the section. This way, harmful cumulative effects for deeper layers are avoided by obtaining correct velocities of the overlying layers.

The assumption of horizontal layering during focusing analysis might cause some systematic velocity errors for dipping layers: Assuming a constant velocity model and down to a reflection with a slight dip α, eq. 46 changes to:

$$Z_R - \bar{Z_m} = cos^2(\alpha) \cdot \frac{\bar{Z_f} - \bar{Z_m}}{2} \quad . \tag{48}$$

This has to be taken into account when determining velocities above slightly dipping reflectors - such as the BSR in most cases. Then, only focuses of sections of the lines where the BSR is almost horizontal should be considered for a velocity analysis.

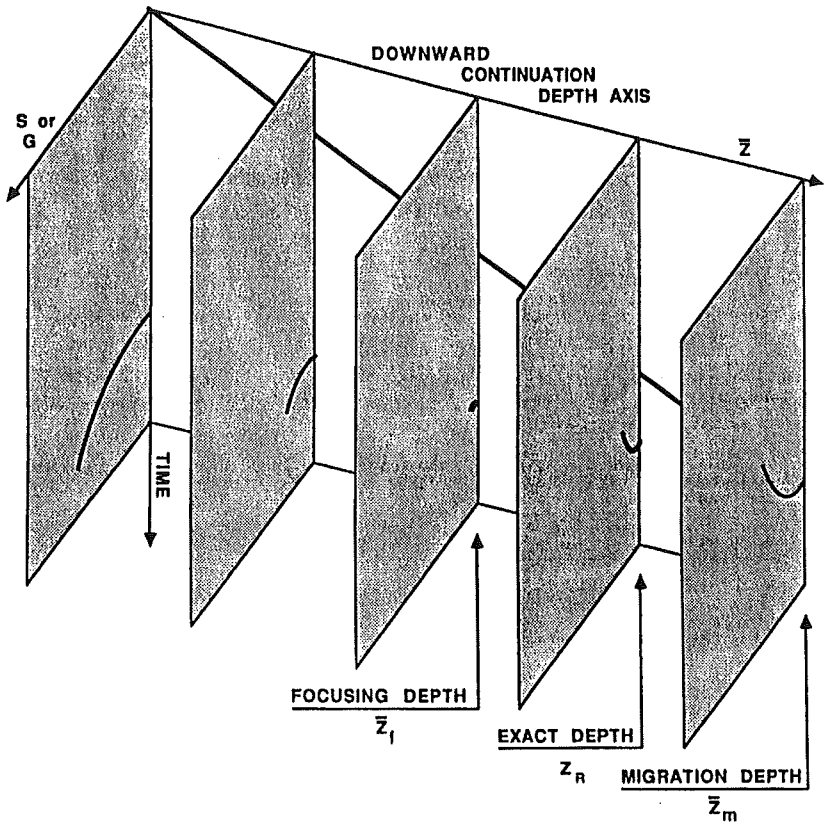

Figure 100: Downward continuation of shot or receivers assuming a velocity V_m which is higher then the actual velocity V in the medium (after Denelle et al., 1986).

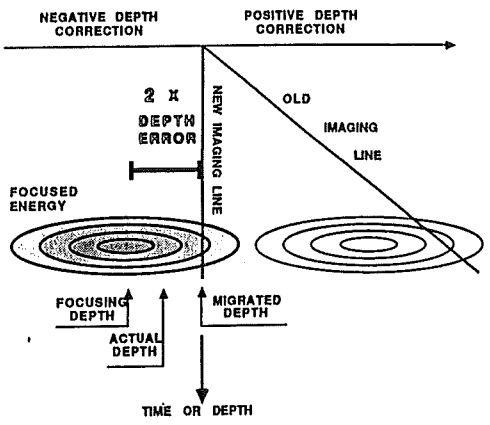

Figure 101: Obtaining the first order depth error from focusing analysis for a single layer case - the old imaging line $\bar{t} = \bar{z}/V$ is transformed to a vertical line (after Denelle et al., 1986).

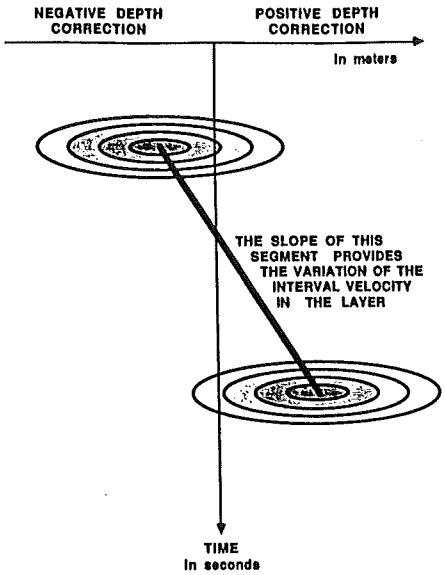

Figure 102: Obtaining the first order interval velocity and depth error from focusing analysis (from Denelle et al., 1986).

F Phase boundary of methane hydrate

The temperature at the depth of the BSR was determined from the phase boundary of hydrates in a pure water/methane system. Experimental values were used from Galloway et al. (1970), Kobayashi and Katz (1949), Marshall et al. (1964), McLeod and Campbell (1961), and Verma et al. (1974), compiled by Sloan (1990). A logarithmical fit curve was calculated to compute temperature as a function of pressure, as illustrated in fig. 103. The formula for the logarithmic fit which was used for determining temperature at the BSR as a function of pressure is:

$$T = 289.0K + 18.31K \cdot (log_{10}(P) - 1.145) \quad , \tag{49}$$

where T denotes temperature in K, P pressure in MPa.

A program enclosed to the book by Sloan (1990) ('CSMHYD') does not allow to compute phase diagrams for pressures above about $30MPa$, which is the reason why eq. 49 was used. The assumption of a pure methane/water-system may not be completely correct. According to Kvenvolden and Kastner (1990), less than 1% of higher-order hydrocarbons are present in hydrates off Peru as hydrate forming gases. However, both salinity and CO_2 may influence the phases boundary. Whereas NaCl is expected to shift the phase boundary towards lower temperatures, adding CO_2 has the opposite effect (ref. e.g. Kvenvolden, 1993). Thus, both effects may partly outweigh each other. More data for both the effects on the hydrate/water-phase boundary due to the addition of other substances and for the chemical composition of hydrates off Peru and Costa Rica would be required to obtain a more accurate phase diagram.

G Miscellaneous parameters and equations

The velocity-vs.-TWT function used for determining the depth of BSRs in the Peruvian data obtained from fig. 67 is:

$$V_{int}(t_2) = \begin{cases} 1600m/s & \text{for } t_2 \leq 0.455s \quad , \\ 1033.4m/s + 1245.3m/s^2 \cdot t_2 & \text{for } 0.455s < t_2 < 0.720s \quad \text{and} \\ 1930m/s & \text{for } t_2 \geq 0.720s \quad . \end{cases} \tag{50}$$

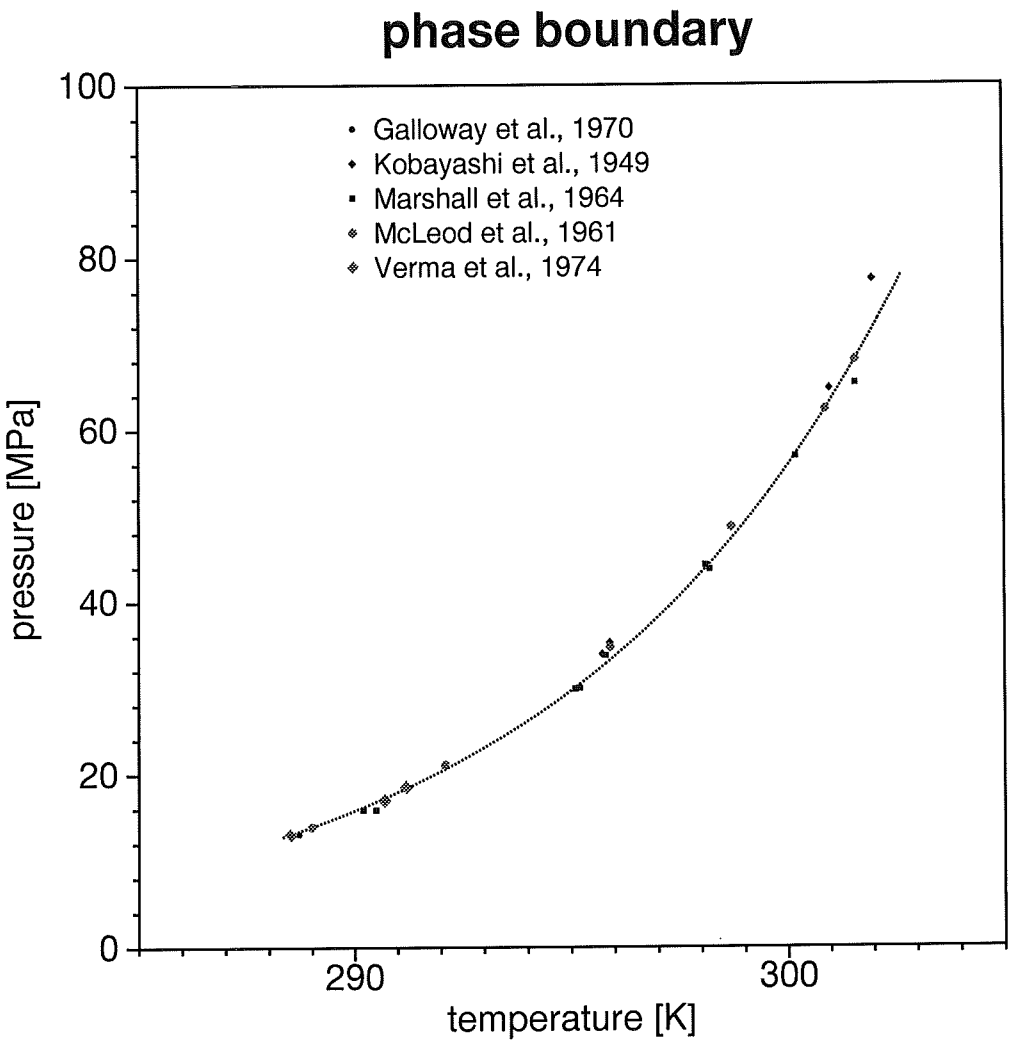

Figure 103: Experimental values for the phase boundary of hydrates in a pure water/methane-system. The logarithmic curve represents the approximation which was used for the present investigations.

V_{int} denotes interval velocity in m/s, t_2 two-way-traveltime in s.

Density as a function of depth beneath the seafloor at the outer Peruvian margin (fig. 68) was determined as

$$\rho(z_{bsf}) = 1.446\frac{g}{cm^3} + 7.579 \cdot 10^{-4}\frac{g}{cm^3 \cdot m} \cdot z_{bsf} \quad , \tag{51}$$

where ρ is the bulk density in g/cm^3, z_{bsf} the depth beneath the seafloor in m.

It is obvious from the graphs that correlation is relatively poor, which is not surprising, since those plots average physical properties over a large area and a number of strata between about 0 and $600mbsf$.

Interval velocity above the BSR offshore Costa Rica was estimated from velocities obtained from pre-stack depth migration of line 8 and the long-wavelength velocity model from the Monte Carlo inversion at CMP 1410 in line 9. The average of the average values of migration velocities ($1617m/s$) and the value from the inversion ($1744m/s$) was computed as:

$$V_{int} = 1681m/s \quad . \tag{52}$$

This compares well with velocities from pre-stack depth migration of line 8 at the lower slope, where both BSR and seafloor are relatively horizontal (fig. 81).

Density as a function of depth at DSDP Site 565 (fig. 83) was approximated as

$$\rho(z_{bsf}) = 1.400\frac{g}{cm^3} + 6.452 \cdot 10^{-4}\frac{g}{cm^3 \cdot m} \cdot z_{bsf} \quad , \tag{53}$$

where ρ is the bulk density in g/cm^3, z_{bsf} the depth beneath the seafloor in m.

Average thermal conductivity of the sediment down to the BSR was estimated as a function of porosity as:

$$log_{10}K = \Phi log_{10}K_w + (1 - \Phi)log_{10}K_g \tag{54}$$

(e.g. Langseth, in prep.) where K_w is the conductivity of the sea water (assumed as $0.6W/(m \cdot K)$), K_g is the grain conductivity (assumed as $2.7W/(m \cdot K)$), and Φ is the porosity (average porosity above BSR assumed as 70% based on physical properties at Site 565). This method yields an average value of $K = 0.94W/(m \cdot K)$, which is a realistic value. Certainly, further calibration would be desirable.

H Abbreviations and symbols

Common abbreviations and symbols used in the text are listed in tables 12 and 13.

Abbreviation	meaning
AGC	automatic gain control
AVO	amplitude versus offset
BHSZ	base of the hydrate stability zone
BSR	bottom simulating reflector
CMP	common mid point
DSDP	Deep Sea Drilling Project
MCS	multichannel seismic
HIG	Hawaii Institute of Geophysics
HSZ	hydrate stability zone
LVL	low velocity layer
mbsf	meters beneath the seafloor
OBH	ocean bottom hydrophone
OBS	ocean bottom seismometer
ODP	Ocean Drilling Program
PDB	standard sample of Peedee Belemite
ppmv	parts per million volumes
VSP	vertical seismic profiling
WHOI	Woods Hole Oceanographic Institution
WSTP	water-sampling temperature profile

Table 12: Table of common abbreviations used in the text. Some abbreviations, which have not been referred to more frequently, are not listed here but explained in the text

Symbol	meaning	units	remarks
C	compressibility	m^2/N, $ft^2/pndl$	indices as for K $1ft^2/pndl = 0.6719690m^2/N$
K	compressional modulus	Pa	
K_b	K of the matrix	Pa	
K_f	K of the pore fill (water and gas)	Pa	
K_g	K of gas	Pa	
K_s	K of the sediment grains	Pa	
K_w	K of water	Pa	
p	pressure	Pa, atm	$1atm = 1.013250 \cdot 10^5 Pa$
Q_p	seismic quality factor for P-waves describing attenuation	–	
Q_s	seismic quality factor for S-waves	–	
T	temperature	K, C	$273.15K = 0°C$
V	volume (velocity)	m^3 (m/s)	velocity only in section E
V_p	compressional wave velocity)	m/s, km/s	
V_s	shear wave velocity	m/s, km/s	
z	depth	m, km	
Z	deviation from ideal gas	–	
μ	dynamic shear modulus	Pa	indices as for K
Φ	porosity	–, %	
ρ	density	g/cm^3, kg/m^3, lbs/ft^3	indices as for K, $1lbs/ft^3 = 16.01846kg/m^3$

Table 13: Table of common symbols together with units used in the text. Some symbols, which have not been referred to more frequently, are not listed here but explained in the text. Non-metric units are only given for converting values quoted from literature.

List of Figures

1 Simplified phase diagram of hydrates in a pure water/methane-system adapted to typical situations expected in permafrost (A) and in deep sea sediments (B). This diagram qualitatively demonstrates that hydrates are stable within sediments in these two regions (grey areas). Pressure was converted to depth assuming hydrostatic pore pressure. From Sloan (1990) after Kvenvolden (1988). 9

2 Worldwide locations of known and inferred hydrates. Squares: continental hydrates, circles: oceanic hydrates, inferred from BSRs, diamonds: locations where oceanic hydrates have been recovered. From Kvenvolden (1994). 10

3 Compressional wave velocity structure of the BSR according to two principal models (a) not involving and (b) involving the presence of free gas. The free gas model may be a combination of two end-member models, a first-order velocity contrast at the base of the BSR (left) or a gradual increase of velocity beneath the BSR (right). Note that a much higher velocity, and thus presumably hydrate concentration, is required above the BSR than if assuming free gas at the BSR in order to produce a given reflectivity. 12

4 Flow pattern of the inversion strategy. 18

5 Flow pattern of the waveform inversion. The model update is performed using a conjugate gradient technique. 21

6 Determination of heat flux from the depth of the BSR. Instead of converting TWT to the BSR to depth using a velocity function, depth of the BSR could also be picked from pre-stack depth migrated sections at 12° S (ref. text for details). 22

7 Location of drill sites and seismic lines at the Peruvian convergent margin. NP: Nazca Plate, MFZ: Mendaña Fracture Zone, LB: Lima Basin, TB: Trujillo Basin, YB: Yaquina Basin. Locations of seismic lines are only approximate due to a lack of exact navigational data. Tracks of CDP1 and 1018 are almost identical except at the lower slope, where CDP1 is located slightly north of 1018. Circles denote drill sites, numbered sites are ODP Leg 112 sites, Ballena and Delfin are industry sites. HIG2-5, CDP2, 1017, and 1018 are reflection seismic profiles. 24

8 Movement of Nazca Ridge from north to south along the margin based on the assumption that its topography mirror-images that of Tuamotu Ridge. Insets show paleobathymetric reconstructions at ODP Leg 112 Sites 679, 684, and 688. The lines in the insets display water depth as a function of age at these sites (dashed lines indicate that the exact age is uncertain). The shaded areas show the topography of Tuamotu Ridge along a trajectory beneath the corresponding ODP sites. Slightly modified from von Huene et al. (in press). 25

9 Columnar sections of ODP Leg 112 drill sites along the southern transect. From von Huene et al. (1988). 26

10 Columnar sections of ODP Leg 112 and industry drill sites along the northern transect. The line drawing is from a time section of CDP 2. From von Huene et al. (1988). 27

11 Pre-stack depth migrated section of the seaward part of Peru line 1017. CMP spacing is $25m$, vertical exaggeration is 3, AGC window is $1s$. The numbered arrow indicates the location at which the velocity structure of the BSR was investigated. 29

12 Pre-stack depth migrated section of the seaward part of Peru line 1018. CMP spacing is $25m$, vertical exaggeration is 3, AGC window is $1s$. Numbered arrows indicate locations at which the velocity structure if the BSR was investigated. Site 688 was drilled during ODP Leg 112. 30

13 Pre-stack depth migrated section of the seaward part of Peru line CDP 2. CMP spacing is $16.75m$, vertical exaggeration is 3, AGC window is $1s$. Sites 685 and 683 were drilled during ODP Leg 112. The location of the crustal boundary is relatively well constrained. Note the subducted ridge beneath the accretionary wedge. 32

14 Pre-stack depth migrated section of the landward part of Peru line CDP 2. CMP spacing is $16.75m$, vertical exaggeration is 3, AGC window is $1s$. Site 683 was drilled during ODP Leg 112. 33

15 Line drawings of coherent reflectors from the profiles from the lower slope area at 9° S. The higher velocity buttress is shown in gray. From von Huene et al. (in press). 34

16 Four stages of the development of an accretionary wedge. The elapsed time after subduction corresponds to distance along the margin from the present location of the crest of Nazca Ridge, i.e. 15° S. The stage of $1 - 2m.y.$ is inferred. From von Huene et al. (in press). 35

17 Top: Fraction of accreted and subducted sediments per m.y. as a function of distance from the crest of Nazca ridge and subsequently elapsed time after its subduction. Squares indicate approximate positions of the seismic lines (from left to right: 1017, 1018, CDP 1, HIG 2, HIG 5, HIG 3) used for these computations. CDP 2 was not suitable for volumetric considerations due to distortions caused by subduction of a small ridge. After von Huene et al. (in press). 36

18 Seismic model at the BSR used by Miller et al. (1991)for investigating the velocity structure at the BSR. Thickness of the presumed gas layer was varied in order to obtain an optimum fit of real and synthetic data. 37

19 Compilation of heat flow values vs. distance from the trench obtained from heat flow probe measurements and in Leg 112 bore holes (stars). Closed and open triangles represent data obtained in 1985 and 1986, respectively, circles denote values from other measurements (Von Herzen, 1959; Von Herzen and Uyeda, 1963; Henry and Pollack, 1988). Crosses mark values obtained from the depth of the BSR. From Yamano and Uyeda (1990). 38

20 Tectonic setting, bathymetry, tracks of seismic lines, and occurrence of BSRs offshore Costa Rica. CR: Cocos Ridge, FS: Fisher Seamount, QP: Quepos Plateau. Site 565 was drilled during DSDP Leg 84 and the surrounding box denotes the location of a 3-d data set (Shipley et al., 1992). Lines mark tracks of seismic profiles acquired during "Sonne" cruise SO-76 and SO-81. Processing of lines 12, 12a, and 14 (in grey) has not yet been finished. Thick grey lines indicate sections in which BSRs could clearly be identified. The velocity structure of the BSR in line 9 was investigated at CMP 1410. After Hinz et al. (in press). 40

21 Pre-stack depth migrated section re-stretched to time of the landward part of Costa Rica line 8. CMP spacing is $25m$, AGC window is $1s$. Site 565, the location of which is projected into this line, was drilled during DSDP Leg 565. After Hinz et al.(in press). 41

22 Post-stack depth migrated section re-stretched to time of the landward part of Costa Rica line 9. CMP spacing is $25m$, AGC window is $1s$. After Hinz et al.(in press). 42

23 Post-stack time migrated section of the seaward part of Costa Rica line 5. CMP spacing is $25m$, AGC window is $1s$. After Hinz et al.(in press). 43

24 Heat flux vs. distance from the trench off the Nicoya Peninsula. The locations are approximately in the area of the seismic 3-d survey. Individual measurements are shown as dots, means of groups of measurements at a given distance from the trench axis as squares. Triangles are measurements obtained during dives of D/V "Alvin". Error bars are from computation of standard deviations. From Langseth and Silver (in press). 45

25 Temperature profile within oceanic crust cooled by the "sea water heat exchange" mechanism. From Langseth and Silver (in press). 45

26 Pre-stack depth migrated section re-stretched to time of Peru line 1018 around CMP 1126. Processing included signature deconvolution. The AGC window is $1s$. The arrow indicates the exact position of the location chosen for inversion. 47

27 Neartrace and CMP 1126 super-gather of raw data. No AGC was applied for plotting. The arrow in the neartrace indicates the exact position of the location chosen for inversion. 47

28 Left: Energies of the seafloor reflection together with the theoretical energy-versus-offset function (dashed line). Right: Amplitude spectra of neartrace and fartrace. 48

29 Pre-processed CMP-gather together with (τ, p)-gather. Refer text for details about processing. No AGC was applied for plotting. 49

30 CMP 1126. Left: reflectivity series at the seafloor relative to the energy of the signal within the window which was chosen for the Wiener filter (left). Right: Signal from seafloor (left) and multiple (right). The signal from the multiple was multiplied by -1 and scaled such that peak-to-peak amplitudes from both seafloor and multiple are approximately the same. 49

31 Starting velocity model for CMP 1126. (a) 50 random models for the Monte Carlo inversion. (b) Models after 50 Monte Carlo steps. (c) Models after Simplex optimization. (d) Resulting interval velocity model (solid) and gradient model (dashed). (e) Velocity histograms for steps (a) (grey line) and (c) (black line) in the layer above the BSR. The velocity bin is $0.01km/s$. (f) Velocity histograms for steps (a) (grey line) and (c) (black line) in the layer below the BSR. The velocity bin is $0.01km/s$. 51

32 Starting model for the full waveform inversion at CMP 1126. Values for Q are constant: $Q_p = 10000$ in the water column, $Q_p = 200$ and $Q_s = 100$ in the sediment. 52

33 Velocity models obtained from full waveform inversion (top). The right plot shows a blow-up around the BSR. Depth intervals are $6m$. Dashed line: starting model, dotted line: final model from the low-frequency runs, solid line: final model using the whole frequency range. Development of the misfit function (bottom) using low frequencies (left) and all frequencies (right). Misfits in the two plots are not comparable with each other because of different scaling of the data. 53

34 Real data in the (τ, p)-domain compared to synthetic data computed from the final model from the waveform inversion and residuals (real minus synthetic data) at CMP 1126. Lower figures: blow-up around BSR. The inset in the synthetic data displays the source signature. 55

35 Compressional wave velocity as a function of water saturation. Variation with (a) $V_{p,0}$, (b) $V_{s,0}$ (b), (c) Φ, and (c) K_g (d). Values for those properties are given in the graphs, units: $V_{p,0}$, $V_{s,0}$ in km/s, Φ in percent, and K_g in $10^7 Pa$. Those variations represent the approximate error margins for the assumed model parameters. Variation of other parameters did not significantly affect the V_p-versus-water saturation function. Note, that water saturation is given in percent of pore volume, not of the bulk sediment. 56

36 Pre-stack depth migrated section re-stretched to time of Peru line 1018 around CMPs 1514 and 1594. Processing included signature deconvolution. The AGC window is $1s$. The arrows indicate the exact positions of the locations chosen for inversion. 57

37 Left: CMP 1514 super-gather after pre-processing, no AGC. Right: Signals from seafloor and multiple, the multiple was multiplied by -1 and scaled such that peak-to-peak amplitudes from both direct and multiple signal are approximately the same. 57

38 Starting model for the full waveform inversion at CMP 1514. 58

39 Velocity models obtained from full waveform inversion. The right plot shows a blow-up around the BSR. Depth intervals are $6m$. Dashed line: starting model, solid line: final model. 59

40 Real data in the (τ, p)-domain compared to synthetic data computed from the final model from the waveform inversion and residuals at CMP 1514. Lower figures: blow-up around BSR. The inset in the synthetic data displays the source signature. 60

41 Compressional wave velocity as a function of water saturation at the depth of the BSR at locations Peru 1018 CMPs 1514 and 1594. Variation of $V_{p,0}$ as given in the graph represents the approximate error margin for this modeling. 61

42 Left: CMP 1594 super-gather after pre-processing. Right: Signals from seafloor and multiple, the multiple was multiplied by -1 and scaled such that peak-to-peak amplitudes from both direct and multiple signal are approximately the same. 61

43 Starting model for the full waveform inversion at CMP 1594. 62

44 Velocity models obtained from full waveform inversion. The right plot shows a blow-up around the BSR. Depth intervals are $6m$. Dashed line: starting model, solid line: final model. 63

45 Real data in the (τ, p)-domain compared to synthetic data computed from the final model from the waveform inversion and residuals at CMP 1594. Lower figures: blow-up around BSR. The inset in the synthetic data displays the source signature, which is from CMP 1514. 64

46 Pre-stack depth migrated section re-stretched to time of Peru line 1017 around CMP 3790. Processing included spiking deconvolution. The AGC window is $1s$. The arrow indicates the exact position of the location chosen for inversion. 65

47 Left: CMP 3790 super-gather after pre-processing. Right: Signals from seafloor and multiple, the multiple was multiplied by -1 and scaled such that peak-to-peak amplitudes from both direct and multiple signal are approximately the same. 66

48 Starting model for the full waveform inversion at CMP 3790. 66

49 Velocity models obtained from full waveform inversion. The right plot shows a blow-up around the BSR. Depth intervals are $6m$. Dashed line: starting model, solid line: final model. 68

50 Real data in the (τ, p)-domain compared to synthetic data computed from the final model from the waveform inversion and residuals at CMP 3790. Lower figures: blow-up around BSR. The inset in the synthetic data displays the source signature. 69

51 Compressional wave velocity as a function of water saturation at the depth of the BSR at location Peru 1017 CMP 3790. Variation of $V_{p,0}$ as given in the graph represents the approximate error margin for this modeling. 70

52 Pre-stack depth migrated section re-stretched to time of the seaward part of CDP 2. CMP spacing is $16.75m$. Site 685 was drilled during ODP Leg 112. 71

53 Pre-stack depth migrated section re-stretched to time of the seaward part of HIG 2. CMP spacing is $16.67m$. 73

54 Pre-stack depth migrated section re-stretched to time of the seaward part of HIG 3. CMP spacing is $16.67m$. 74

55 Pre-stack depth migrated section re-stretched to time of the seaward part of HIG 5. CMP spacing is $16.67m$. 75

56 Post-stack depth migrated section re-stretched to time of Costa Rica line 9 around CMP 1410. Processing included spike deconvolution. Note a strong bubble pulse at about $0.2s$ beneath the seafloor. The arrow indicates the exact position of the location chosen for inversion. 76

57 CMP 1410 super-gather of raw data together with amplitude spectra of two traces. No AGC. Minimum offset is $125m$, receiver spacing is $50m$. Note the remarkable differences of amplitudes in the CMP-gather. Trace 20 ($1075m$ offset) displays a distinct $50Hz$-noise peak in the amplitude spectra. 76

58 Pre-processed CMP 1410 super-gather. Ref. text for details about processing. No AGC. Different amplitudes and shape of signal at $1075m$ offset (trace 20) are caused by different filter parameters (ref. text). The right side shows the CMP-gather at the seafloor after NMO correction with water velocity. Water velocity is from the Monte Carlo inversion. Note that the time difference between direct and ghost signal is highest at medium offsets. 77

59 CMP 1410. Left: reflectivity series at the seafloor relative to the energy of the signal within the window which was chosen for the Wiener filter (left). Right: Signal from seafloor (left) and multiple (right). Signal from the multiple was multiplied by -1 and scaled such that peak-to-peak amplitudes from both seafloor and multiple are approximately the same. 78

60 Starting model for the full waveform inversion CMP 1410. 79

61 Velocity models obtained from full waveform inversion. The right plot shows a blow-up around the BSR. Depth intervals are $6m$. Dashed line: starting model, solid line: final model. 80

62 Real data in the (τ, p)-domain compared to synthetic data computed from the final model from the waveform inversion and residuals at CMP 1410. Lower figures: blow-up around BSR. The inset in the synthetic data displays the source signature. 81

63 Left: Source wavelet derived from the data compared to the "synthetic" source wavelet (upper plots), corresponding amplitude spectra (lower plots). Right: Comparing velocity models in the vicinity of the BSR obtained from full waveform inversion using the data-derived source wavelet (dotted line) and the "synthetic" source wavelet (solid line). 82

64 Compressional wave velocity as a function of water saturation at the depth of the BSR at location Costa Rica 9 CMP 1410. Variation of $V_{p,0}$ as given in the graph represents the approximate error margin for this modeling. 83

65 Velocities of the depth interval above the BSR obtained from focusing analyses during pre-stack depth migration, line 1017. 85

66 Velocities of the depth interval above the BSR obtained from focusing analyses during pre-stack depth migration, line 1018. 86

67 Interval velocities plotted against two-way-traveltime above BSRs in lines 1017 and 1018. Grey symbols denote values which were ignored for computation of the interval velocity gradient (solid line). 87

68 Bulk density in cores from ODP Leg 112 Sites 682, 683, 685, and 688, which are located at the outer Peruvian margin. 87

69 Thermal conductivity from ODP Leg 112 Sites 682, 683, 685, and 688, which are located at the outer Peruvian margin (from core measurements except for Site 685). 88

70 Temperature at the BSR along line 1017 assuming hydrostatic pressure and an interval velocity/TWT function (solid line), hydrostatic pressure and depth directly from pre-stack depth migration (dotted line), and lithostatic pressure and an interval velocity/TWT function (dashed line). Distances from the trench were corrected for the angle between the track of line 1017 and the normal to the trench axis (ref. text). 89

71 Temperature gradient at the BSR along line 1017 assuming hydrostatic pressure and an interval velocity/TWT function (solid line), hydrostatic pressure and depth directly from pre-stack depth migration (dotted line), and lithostatic pressure and an interval velocity/TWT function (dashed line). Distances from the trench were corrected for the angle between the track of line 1017 and the normal to the trench axis (ref. text). 90

72 Heat flux above the BSR along line 1017 assuming hydrostatic pressure and an interval velocity/TWT function (solid line), hydrostatic pressure and depth directly from pre-stack depth migration (dotted line), and lithostatic pressure and an interval velocity/TWT function (dashed line). Distances from the trench were corrected for the angle between the track of line 1017 and the normal to the trench axis (ref. text). 90

73 Pre-stack depth migrated section in time of the part of Peru line 1017 which was used for the computation of heat flux. CMP spacing is $25m$. Heat flux is displayed below the seismic section. Distances from the trench axis were corrected for the angle between the track of line 1017 and the normal to the trench axis (ref. text). 91

74 Temperature at the BSR along line 1018 assuming hydrostatic pressure and an interval velocity/TWT function (solid line), hydrostatic pressure and depth directly from pre-stack depth migration (dotted line), and lithostatic pressure and an interval velocity/TWT function (dashed line). 92

75 Temperature gradient at the BSR along line 1018 assuming hydrostatic pressure and an interval velocity/TWT function (solid line), hydrostatic pressure and depth directly from pre-stack depth migration (dotted line), and lithostatic pressure and an interval velocity/TWT function (dashed line). 92

76 Heat flux above the BSR along line 1018 assuming hydrostatic pressure and an interval velocity/TWT function (solid line), hydrostatic pressure and depth directly from pre-stack depth migration (dotted line), and lithostatic pressure and an interval velocity/TWT function (dashed line). 93

77 Pre-stack depth migrated section in time of the part of Peru line 1018 which was used for the computation of heat flux. CMP spacing is $25m$. Heat flux is displayed below the seismic section. . 94

78 Temperature, temperature gradient, and heat flux from the depth of the BSR along line CDP 2 assuming hydrostatic pressure (solid line) and lithostatic pressure (dashed line). Depth of the BSR was computed from an interval velocity/TWT function obtained from lines 1017 and 1018. 95

79 Pre-stack depth migrated section in time of those parts of Peru line CDP 2 which were used for the computation of heat flux. CMP spacing is $16.75m$. Heat flux is displayed below the seismic sections. 97

80 Temperature, temperature gradient, and heat flux from the depth of the BSR along lines HIG 3 and HIG 5 assuming hydrostatic pressure (solid line) and lithostatic pressure (dashed line). Depth of the BSR was computed from an interval velocity/TWT function obtained from lines 1017 and 1018. 98

81 Velocities of the depth interval above the BSR obtained from focusing analyses during pre-stack depth migration, Costa Rica line 8. 99

82 Interval velocities plotted against two-way-traveltime above BSRs obtained from pre-stack depth migration in line 8 and from inversion at CMP 1410 in line 9. 100

83 Bulk density in cores from DSDP Leg 84 Sites 565. From von Huene et al. (1985b) 100

84 Temperature, temperature gradient, and heat flux from the depth of the BSR along Costa Rica line 8 assuming hydrostatic pressure together with a velocity/TWT function (solid line), hydrostatic pressure together with picks in the depth domain (dotted line), as well as lithostatic pressure and a velocity/TWT function (dashed line). 102

85 Temperature, temperature gradient, and heat flux from the depth of the BSR along Costa Rica line 9 assuming hydrostatic pressure (solid line) and lithostatic pressure (dashed line). Depth of the BSR was computed from time picks and an interval velocity model obtained from pre-stack migration at line 8 and a Monte Carlo inversion at line 9 CMP 1410. 103

86 Temperature, temperature gradient, and heat flux from the depth of the BSR along Costa Rica line 5 assuming hydrostatic pressure (solid line) and lithostatic pressure (dashed line). Depth of the BSR was computed from time picks and an interval velocity model obtained from pre-stack migration at line 8 and a Monte Carlo inversion at line 9 CMP 1410. Note that vertical scaling differs by a factor of 2.5 compared to plots from lines 8 and 9. 104

87 Compilation of the velocity structures at BSRs investigated for this study. Locations are marked by circles. Stars denote ODP and DSDP sites. Thick grey lines in the Costa Rica map (top left) mark sections of the seismic profiles in which BSRs were observed. The box around DSDP Site 565 indicates the area of a 3-d seismic experiment (Shipley et al., 1992). FS: Fisher Seamount. Bathymetry and tracks of seismic lines in the Peruvian map (right) are only approximate. 107

88 Possible end-members of hydrate distribution in the pore space of sediments: (a) Hydrates form without grain contact. Relatively high concentrations of hydrates are required to plug the sediment pores. (b) Hydrates form between grains. Permeability of sediments is significantly decreased even at low hydrate concentrations. 108

89 Tectonic control of BSR formation: An original sedimentary section assumed to contain hydrates (left-hand side, dark-shaded area) undergoes compaction together with vertical movement during sedimentation of new sediments (right-hand side, light-shaded area). Depending on whether the BHSZ moves upward relative to the base of the assumed hydrated sedimentary section, gas is expected to form from dissociation of hydrates: (a) Stable tectonic environment. Subsidence of hydrated sediment beneath the BHSZ due to compaction of underlying sediments. (b) Additional tectonic uplift. The BHSZ moves upward relative to the seafloor as pressure decreases and the phase boundary of hydrates shifts towards lower temperatures. (c) Lack of BSRs due to tectonic subsidence. The BHSZ moves downward relative to the seafloor due to an increase of pressure and a subsequent shift of the phase boundary towards higher temperatures outweighing subsidence of sediments due to compaction as in (a). Note that (c) may also suppress development of BSRs if methane is supplied from below. 109

90 Heat flux vs. distance from the trench axis along lines 1017 (dashed line) and 1018 (solid line). . . 113

91 Heat flux vs. distance from the trench axis along lines CDP 2 (solid line) and HIG 3 (dotted line) and HIG 5 (dashed line). . . . 114
92 Heat flux vs. distance from the trench axis along Costa Rica lines 5 (dotted line) 8 (solid line) and 9 (dashed line). . . . 115
93 Three cavities in gas clathrate hydrates: (a) 5^{12}, (b) $5^{12}6^2$, (c) $5^{12}6^4$. From Sloan (1990)after Jeffrey and McMullan (1967). . . . 127
94 Map of locations of slumps and hydrates off the U.S. Atlantic coast. From Booth et al. (1994). . . . 136
95 Compression factor Z for a variety of gases, from Atkins (1978). . . . 141
96 Estimating the coupling factor in Ottawa sand as a function of differential pressure by comparison of theoretical and measured relation of P- and S-wave velocities with differential pressure, from Domenico (1977). . . . 144
97 Measured and computed P-wave velocities in an Ottawa sand specimen, from Domenico (1976). . . . 145
98 Phase shift and diffraction operator during downward movement of shot or receivers (from Denelle et al., 1986). . . . 146
99 Downward continuation of shot (S) or receivers (G) along $\bar{t}$ (thick line) assuming a correct velocity (after Denelle et al., 1986). . . . 147
100 Downward continuation of shot or receivers assuming a velocity V_m which is higher then the actual velocity V in the medium (after Denelle et al., 1986). . . . 148
101 Obtaining the first order depth error from focusing analysis for a single layer case - the old imaging line $\bar{t} = \bar{z}/V$ is transformed to a vertical line (after Denelle et al., 1986). . . . 148
102 Obtaining the first order interval velocity and depth error from focusing analysis (from Denelle et al., 1986). . . . 149
103 Experimental values for the phase boundary of hydrates in a pure water/methane-system. The logarithmic curve represents the approximation which was used for the present investigations. . . . 150

List of Tables

1 Estimates of the amount of methane stored in hydrates worldwide. Compiled mainly after Sloan et al. (1990). . . . 11
2 Estimated distribution of organic carbon in the Earth. Dispersed organic carbons such as kerogen and bitumen are not included. From Kvenvolden (1993). . . . 11
3 Data acquisition parameters of seismic lines from offshore Peru which were used for these investigations. CMP spacing of the HIG lines has been re-sampled to half the original spacing by trace interpolation to avoid spatial aliasing during pre-stack migration. . . . 28
4 Heat flux from temperatures at Sites 685 and 688. Temperature at 0 mbsf is the bottom-water temperature. After Yamano and Uyeda (1990). . . . 38
5 Data acquisition parameters of seismic lines from offshore Costa Rica acquired during "Sonne" Legs SO-76 and 81. . . . 39
6 Geometry of hydrate cavities. (1) Variation in distance of oxygen atoms from center of cage, (2) Number of oxygens at the periphery of each cavity. After Sloan (1990), Jeffrey and McMullan (1967).127
7 Ratio of the sizes of hydrate forming molecular diameters relative to cavity diameters. Cavity diameters take account for the water radii of 1.45Å. Experimentally observed occupancies by simple hydrate formers are marked in italic. After Sloan et al. (1990). . . . 128
8 Physical properties of structure I methane hydrate compared to those of water and ice. Properties of structure II hydrates appear to be similar to those of structure I hydrates. Thermal conductivity of water is for a salinity of $0-4\%$, temperature of $17.5°C$, and ambient pressure (from Dietrich et al., 1975). Other properties of water assume a salinity of 3.5%, a temperature of $4°C$, and ambient pressure (from Dietrich et al., 1975). Density of ice assumes fresh water ice without inclusion of air molecules (from Dietrich et al., 1975). Thermal conductivity and electric properties of ice give possible ranges for natural ice (from Dietrich et al., 1975). Seismic velocities of ice are from Pandit and King (1982). See text regarding gas hydrate properties. Gas hydrate properties compiled mainly after Sloan (1990). . . . 129
9 Dynamic bulk modulus K of methane, after Wyman (1982). $1atm = 10132.50Pa$. . . . 142
10 Quantities for modeling V_p as a function of water saturation: pressure (P), temperature (T), deviation from ideal gas (Z), and porosity (Φ). T is from the phase boundary of methane hydrates. Values for Φ are estimated from measurements on ODP Leg 112 Site 688 and DSDP Leg 84 Site 565. $1atm = 10132.50Pa$. Z as a function of pressure is from Atkins (1978). . . . 145

11 Quantities for modeling V_p as a function of water saturation: densities of sediment, water, and gas (ρ_s, ρ_w, ρ_g, in $10^3 kg/m^3$), bulk moduli of sediment, water, and gas (K_s, K_w, K_g, in $10^9 Pa$), P- and S-wave velocity at full saturation ($V_{p,0}$, $V_{s,0}$, in km/s. Density values and bulk moduli are from Domenico (1977)and computed from formulas given above. Variation of $V_{p,0}$ represents the estimated error margin. 145

12 Table of common abbreviations used in the text. Some abbreviations, which have not been referred to more frequently, are not listed here but explained in the text 152

13 Table of common symbols together with units used in the text. Some symbols, which have not been referred to more frequently, are not listed here but explained in the text. Non-metric units are only given for converting values quoted from literature. 152

GEOMAR REPORTS

1 GEOMAR FORSCHUNGSZENTRUM FÜR MARINE GEOWISSENSCHAFTEN DER CHRISTIAN-ALBRECHTS-UNIVERSITÄT ZU KIEL
BERICHT FÜR DIE JAHRE 1987 UND 1988. 1989. 71 + 6 pp.
In German

2 GEOMAR FORSCHUNGSZENTRUM FÜR MARINE GEOWISSENSCHAFTEN DER CHRISTIAN-ALBRECHTS-UNIVERSITÄT ZU KIEL
JAHRESBERICHT / ANNUAL REPORT 1989. 1990. 96 pp.
In German and English

3 GEOMAR FORSCHUNGSZENTRUM FÜR MARINE GEOWISSENSCHAFTEN DER CHRISTIAN-ALBRECHTS-UNIVERSITÄT ZU KIEL
JAHRESBERICHT / ANNUAL REPORT 1990. 1991. 212 pp.
In German and English

4 ROBERT F. SPIELHAGEN
DIE EISDRIFT IN DER FRAMSTRASSE WÄHREND DER LETZTEN 200.000 JAHRE. 1991. 133 pp.
In German with English summary

5 THOMAS C. W. WOLF
PALÄO-OZEANOGRAPHISCH-KLIMATISCHE ENTWICKLUNG DES NÖRDLICHEN NORDATLANTIKS SEIT DEM SPÄTEN NEOGEN
(ODP LEGS 105 UND 104, DSDP LEG 81). 1991. 92 pp.
In German with English summary

6 SEISMIC STUDIES OF LATERALLY HETEROGENOUS STRUCTURES - INTERPRETATION AND MODELLING OF SEISMIC DATA.
Edited by ERNST R. FLUEH
Commission on Controlled Source Seismology (CCSS), Proceedings of the 8th Workshop Meeting, held at
Kiel - Fellhorst (Germany), August 27-31, 1990. 1991. 359 pp.
In English

7 JENS MATTHIESSEN
DINOFLAGELLATEN-ZYSTEN IM SPÄTQUARTÄR DES EUROPÄISCHEN NORDMEERES: PALÖKOLOGIE UND PALÄO-OZEANOGRAPHIE. 1991. 104 pp.
In German with English summary

8 DIRK NÜRNBERG
HAUPT- UND SPURENELEMENTE IN FORAMINIFERENGEHÄUSEN - HINWEISE AUF KLIMATISCHE UND OZEANOGRAPHISCHE ÄNDERUNGEN
IM NÖRDLICHEN NORDATLANTIK WÄHREND DES SPÄTQUARTÄRS. 1991. 117 pp.
In German with English summary

9 KLAS S. LACKSCHEWITZ
SEDIMENTATIONSPROZESSE AM AKTIVEN MITTELOZEANISCHEN KOLBEINSEY RÜCKEN (NÖRDLICH VON ISLAND). 1991. 133 pp.
In German with English summary

10 UWE PAGELS
SEDIMENTOLOGISCHE UNTERSUCHUNGEN UND BESTIMMUNG DER KARBONATLÖSUNG IN SPÄTQUARTÄREN SEDIMENTEN DES ÖSTLICHEN
ARKTISCHEN OZEANS. 1991. 106 pp.
In German with English summary

11 FS POSEIDON - EXPEDITION 175 (9.10.-1.11.1990)
175/1: OSTGRÖNLÄNDISCHER KONTINENTALRAND (65° N)
175/2: SEDIMENTATION AM KOLBEINSEYRÜCKEN (NÖRDLICH VON ISLAND)
Hrsg. von J. MIENERT und H.-J. WALLRABE-ADAMS. 1992. 56 pp. + app.
In German with some English chapters

12 GEOMAR FORSCHUNGSZENTRUM FÜR MARINE GEOWISSENSCHAFTEN DER CHRISTIAN-ALBRECHTS-UNIVERSITÄT ZU KIEL
JAHRESBERICHT / ANNUAL REPORT 1991. 1992. 152 pp.
In German and English

13 SABINE E. I. KÖHLER
SPÄTQUARTÄRE PALÄO-OZEANOGRAPHISCHE ENTWICKLUNG DES NORDPOLARMEERES UND EUROPÄISCHEN NORDMEERES ANHAND VON
SAUERSTOFF- UND KOHLENSTOFF- ISOTOTPENVERHÄLTNISSEN DER PLANKTISCHEN FORAMINIFERE
Neogloboquadrina pachyderma (sin.). 1992. 104 pp.
In German with English summary

14 FS SONNE - FAHRTBERICHT SO 78 PERUVENT: BALBOA, PANAMA - BALBOA, PANAMA, 28.2.1992-16.4.1992
Hrsg. von ERWIN SUESS. 1992. 120 pp.
In German with some English chapters

15 FOURTH INTERNATIONAL CONFERENCE ON PALEOCEANOGRAPHY (ICP IV): SHORT- AND LONG-TERM GLOBAL CHANGE:
RECORDS AND MODELLING 21-25 SEPTEMBER 1992, KIEL/GERMANY
PROGRAM & ABSTRACTS. 1992. 351 pp.
In English

16 MICHAELA KUBISCH
DIE EISDRIFT IM ARKTISCHEN OZEAN WÄHREND DER LETZTEN 250.000 JAHRE. 1992. 100 pp.
In German with English summary

17 PERSISCHER GOLF: UMWELTGEFÄHRDUNG, SCHADENSERKENNUNG, SCHADENSBEWERTUNG AM BEISPIEL DES MEERESBODENS; ERKENNEN
EINER ÖKOSYSTEMVERÄNDERUNG NACH ÖLEINTRÄGEN. Schlußbericht zu den beiden BMFT-Forschungsvorhaben 03F0055 A+B. 1993. 108 pp.
In German with English summary

18 TEKTONISCHE ENTWÄSSERUNG AN KONVERGENTEN PLATTENRÄNDERN / DEWATERING AT CONTINENTAL MARGINS.
Hrsg. von / ed. by ERWIN SUESS. 1993. 106 + 32 + 68 + 16 + 22 + 38 + 4 + 19 pp.
Some chapters in English, some in German

19 THOMAS DICKMANN
DAS KONZEPT DER POLARISATIONSMETHODE UND SEINE ANWENDUNGEN AUF DAS SEIMISCHE VEKTORWELLENFELD IM WEITWINKELBEREICH. 1993. 121 pp.
In German with English summary

20 GEOMAR FORSCHUNGSZENTRUM FÜR MARINE GEOWISSENSCHAFTEN DER CHRISTIAN-ALBRECHTS-UNIVERSITÄT ZU KIEL
JAHRESBERICHT / ANNUAL REPORT 1992. 1993. 139 pp.
In German and English

21 KAI UWE SCHMIDT
PALYNOMORPHE IM NEOGENEN NORDATLANTIK - HINWEISE ZUR PALÄO-OZEANOGRAPHIE UND PALÄOKLIMATOLOGIE. 1993. 104 + 7 + 41 pp.
In German with English summary

22 UWE JÜRGEN GRÜTZMACHER
DIE VERÄNDERUNGEN DER PALÄOGEOGRAPHISCHEN VERBREITUNG VON *BOLBOFORMA* - EIN BEITRAG ZUR REKONSTRUKTION UND DEFINITION VON WASSERMASSEN IM TERTIÄR.1993. 104 pp.
In German with English summary

23 RV PROFESSOR LOGACHEV - Research Cruise 09 (August 30 - September 17, 1993): SEDIMENT DISTRIBUTION ON THE REYKJANES RIDGE NEAR 59°N
Edited by H.-J. WALLRABE-ADAMS & K.S. LACKSCHEWITZ. 1993. 66 + 30 pp.
In English

24 ANDREAS DETTMER
DIATOMEEN-TAPHOZÖNOSEN ALS ANZEIGER PALÄO-OZEANOGRAPHISCHER ENTWICKLUNGEN IM PLIOZÄNEN UND QUARTÄREN NORDATLANTIK. 1993. 113 + 10 + 25 pp.
In German with English summary

25 GEOMAR FORSCHUNGSZENTRUM FÜR MARINE GEOWISSENSCHAFTEN DER CHRISTIAN-ALBRECHTS-UNIVERSITÄT ZU KIEL
JAHRESBERICHT / ANNUAL REPORT 1993. 1994. 69 pp.
In German and English

26 JÖRG BIALAS
SEISMISCHE MESSUNGEN UND WEITERE GEOPHYSIKALISCHE UNTERSUCHUNGEN AM SÜD-SHETLAND TRENCH UND IN DER BRANSFIELD STRASSE - ANTARKTISCHE HALBINSEL. 1994. 113 pp.
In German with English summary

27 JANET MARGARET SUMNER
THE TRANSPORT AND DEPOSITIONAL MECHANISM OF HIGH GRADE MIXED-MAGMA IGNIMBRITE TL, GRAN CANARIA: THE MORPHOLOGY OF A LAVA-LIKE FLOW. 1994. 224 pp.
In English with German summary

28 GEOMAR LITHOTHEK. Edited by JÜRGEN MIENERT. 1994. 12 pp + app.
In English

29 FS SONNE - FAHRTBERICHT SO 97 KODIAK-VENT: KODIAK - DUTCH HARBOR - TOKYO - SINGAPUR, 27.7. - 19.9.1994
Hrsg. von ERWIN SUESS. 1994.
Some chapters in German, some in English

30 CRUISE REPORTS:
RV LIVONIA CRUISE 92, KIEL-KIEL, 21.8.-17.9.1992: GLORIA STUDIES OF THE EAST GREENLAND CONTINENTAL MARGIN BETWEEN 70° AND 80°N
RV POSEIDON PO200/10, LISBON-BREST-BREMERHAVEN, 7.-23.8.1993: EUROPEAN NORTH ATLANTIC MARGIN: SEDIMENT PATHWAYS, PROCESSES AND FLUXES
RV AKADEMIK ALEKSANDR KARPINSKIY, KIEL-TROMSØ, 5.-25.7.1994: GAS HYDRATES ON THE NORTHERN EUROPEAN CONTINENTAL MARGIN
Edited by JÜRGEN MIENERT. 1994.
In English; report of RV AKADEMIK ALEKSANDR KARPINSKIY cruise in English and Russian

31 MARTIN WEINELT
BECKENENTWICKLUNG DES NÖRDLICHEN WIKING-GRABENS IM KÄNOZOIKUM - VERSENKUNGSGESCHICHTE, SEQUENZSTRATIGRAPHIE, SEDIMENTZUSAMMENSETZUNG. 1994. 85 pp.
In German with English summary

32 GEORG A. HEISS
CORAL REEFS IN THE RED SEA: GROWTH, PRODUCTION AND STABLE ISOTOPES. 1994. 141 pp.
In English with German summary

33 JENS A.HÖLEMANN
AKKUMULATION VON AUTOCHTHONEM UND ALLOCHTHONEM ORGANISCHEM MATERIAL IN DEN KÄNOZOISCHEN SEDIMENTEN DER NORWEGISCHEN SEE (ODP LEG 104). 1994. 78 pp.
In German with English summary

34 CHRISTIAN HASS
SEDIMENTOLOGISCHE UND MIKROPALÄONTOLOGISCHE UNTERSUCHUNGEN ZUR ENTWICKLUNG DES SKAGERRAKS (NE NORDSEE) IM SPÄTHOLOZÄN. 1994.
In German with English summary

35 BRITTA JÜNGER
TIEFENWASSERERNEUERUNG IN DER GRÖNLANDSEE WÄHREND DER LETZTEN 340.000 JAHRE.
DEEP WATER RENEWAL IN THE GREENLAND SEA DURING THE PAST 340,000 YEARS.1994. 6 + 109 pp.
In German with English summary

36 JÖRG KUNERT
UNTERSUCHUNGEN ZU MASSEN- UND FLUIDTRANSPORT ANHAND DER BEARBEITUNG REFLEXIONSSEISMISCHER DATEN AUS DER KODIAK-SUBDUKTIONSZONE, ALASKA. 1995. 129 pp.
In German with English summary

37 CHARLOTTE M. KRAWCZYK
DETACHMENT TECTONICS DURING CONTINENTAL RIFTING OFF THE WEST IBERIA MARGIN: SEISMIC REFLECTION AND DRILLING CONSTRAINTS. 1995. 133 pp.
In English with German summary

38 CHRISTINE CAROLINE NÜRNBERG
BARIUMFLUSS UND SEDIMENTATION IM SÜDLICHEN SÜDATLANTIK - HINWEISE AUF PRODUKTIVITÄTSÄNDERUNGEN IM QUARTÄR. 1995. 6 + 108pp.
In German with English summary

39 JÜRGEN FRÜHN
TEKTONIK UND ENTWÄSSERUNG DES AKTIVEN KONTINENTALRANDES SÜDÖSTLICH DER KENAI-HALBINSEL, ALASKA. 1995. 93 pp.
In German with English summary

40 GEOMAR FORSCHUNGSZENTRUM FÜR MARINE GEOWISSENSCHAFTEN DER CHRISTIAN-ALBRECHTS-UNIVERSITÄT ZU KIEL
JAHRESBERICHT / ANNUAL REPORT 1994. 1995.
In German and English

41 FS SONNE - FAHRTBERICHT / CRUISE REPORT SO 103 CONDOR 1 B: VALPARAISO-VALPARAISO, 2.-21.7.1995.
Hrsg. von ERNST R. FLUEH. 1995. 140 pp.
Some chapters in German, some in English

42 R/V PROFESSOR BOGOROV CRUISE 37: CRUISE REPORT "POSETIV": Vladivostok - Vladivostok, September 23 - October 22, 1994.
Edited by CHRISTOPH GAEDICKE, BORIS BARANOV and EVGENIY LELIKOV. 1995. 48 + 33 pp.
In English

43 CHRISTOPH GAEDICKE
DEFORMATION VON SEDIMENTEN IM NANKAI-AKKRETIONSKEIL, JAPAN. BILANZIERUNG TEKTONISCHER VORGÄNGE ANHAND VON SEISMISCHEN PROFILEN UND ERGEBNISSEN DER ODP-BOHRUNG 808. II + 89 pp.
In German with English summary

44 MARTIN ANTONOW
SEDIMENTATIONSMUSTER UM DEN VESTERIS SEAMOUNT (ZENTRALE GRÖNLANDSEE) IN DEN LETZTEN 250.000 JAHREN. 1995.
In German with English summary

45 INTERNATIONAL CONGRESS: CORING FOR GLOBAL CHANGE - ICGC '95. KIEL, 28 - 30 June, 1995.
Edited by JÜRGEN MIENERT and GEROLD WEFER. 1996.
In English

46 JENS GRÜTZNER
ZUR PHYSIKALISCHEN ENTWICKLUNG VON DIAGENETISCHEN HORIZONTEN IN DEN SEDIMENTBECKEN DES ATLANTIKS. 1995. 96 pp.
In German with English summary

47 INGO A. PECHER
SEISMIC STUDIES OF BOTTOM SIMULATING REFLECTORS AT THE CONVERGENT MARGINS OFFSHORE PERU AND COSTA RICA. 1996.
In English with German summary

48 XIN SU
DEVELOPMENT OF LATE TERTIARY AND QUATERNARY COCCOLITH ASSEMBLAGES IN THE NORTHEAST ATLANTIC. 1996. 120 pp. + 7 pl.
In English with German summary

49 FS SONNE - FAHRTBERICHT / CRUISE REPORT SO 108 ORWELL: SAN FRANCISCO - ASTORIA, 14.4. - 23.5.1996
Edited by ERNST R. FLUEH and MICHAEL A. FISHER. 1996.